# Aeroelastic Behavior of Bird-Damaged Fan Blades Using a Coupled CFD/CSD Framework

by

Eric Raymond Muir

A dissertation submitted in partial fulfillment
of the requirements for the degree of
Doctor of Philosophy
(Aerospace Engineering)
in the University of Michigan
2014

Doctoral Committee:

Professor Peretz P. Friedmann, Chair
Professor Carlos E. Cesnik
Assistant Professor Karthik Duraisamy
Professor Bogdan Epureanu
Assistant Professor Krzysztof J. Fidkowski

---

I lovingly dedicate this dissertation to Lisa, my source of strength and inspiration.

## *ACKNOWLEDGMENTS*

This dissertation marks a significant milestone in my formal education and development as an engineer. Its completion would not have been possible without the influence of many people.

First, I would like to sincerely thank my advisor Professor Peretz Friedmann for his friendship and guidance throughout my undergraduate and graduate studies. His high standards for precise and original work pushed the limits of my ability and will benefit me throughout my career. I also value my many interactions with the Aerospace faculty, whose dedication to teaching and passion for the aerospace industry have inspired me to continually strive for my best. I am especially grateful to the members of my doctoral committee, Professor Carlos Cesnik, Professor Karthik Duraisamy, Professor Bogdan Epureanu, and Professor Krzysztof Fidkowski, for their thoughtful critique of this work. I would also like to express appreciation for the kindness and helpfulness of the Aerospace Department staff, especially Denise Phelps, Dave McLean, and Cindy Enoch, whose assistance has made life as a graduate student that much easier.

I would like to acknowledge two Pratt & Whitney engineers for providing outstanding advise and insight into this very relevant and challenging problem area. Specifically, it has been a pleasure to collaborate with Ed Gallagher, Principal Engineer – Aero/Thermo, and Bill Graves, Principal Engineer – Materials/Structures. I appreciate your patience while I became familiar with the bird strike problem, and I am thankful for the many comments and suggestions you have offered during the course of this investigation. You have contributed in a significant way to the success of this project.

A significant portion of my research was performed using the ANSYS engineering simulation software suite. The ANSYS support team has been extremely helpful in addressing any questions in the use of their code. I especially thank Michael Tooley from the Waterloo, ON office for his personalized assistance in getting the fluid-structure interaction calculations underway. Furthermore, I would like to acknowledge support from several members of the College of Engineering's Center for Advanced Computing staff, namely Bennet Fauber, Amadi Nwankpa, and Brock Palen, for your professional and timely support of the College's high performance computing capabilities.

I am blessed with many friends, both at the University of Michigan and elsewhere, who have significantly influenced who I am today. From weekend camping trips, to casual get-togethers, to in-depth lunch discussions, they provided a nice break from the rigors of my research and I will always cherish the many laughs and memories. I am particularly grateful for the camaraderie with those in my research group: Michael Chia, Dr. Bryan Glaz, Dr. Ahbijit Gogulapati, Daning Huang, Dr. Nicolas Lamorte, Dr. Li Liu, Dr. Ashwani Padthe, and Puneet Singh. You all have been a valuable source of information, mentorship, and reassurance throughout our years together.

Finally, I owe immense gratitude to my family. My parents, Ron and Denise, set me down a path to success and happiness and outfitted me with the tools to complete the journey. Without them I would not be where I am today, and I am forever grateful for their never-ending love and encouragement. Last but certainly not least, I thank my wife Lisa for her unwavering love, devotion, and support. She has patiently and unselfishly supported my *many* endeavors despite the demands and challengers of her own career. She is my greatest source of strength and inspiration in all aspects of life.

# TABLE OF CONTENTS

# LIST OF FIGURES

Figure

# LIST OF TABLES

Table

# LIST OF ABBREVIATIONS

**1B** 1st Bending Mode

**2B** 2nd Bending Mode

**3B** 3rd Bending Mode

**1T** 1st Torsion Mode

**2T** 2nd Torsion Mode

**ALE** Arbitrary Lagrangian-Eulerian

**ATM** Automatic Topology and Meshing

**CAD** Computer Aided Design

**CFD** Computational Fluid Dynamics

**CSD** Computational Structural Dynamics

**CPU** Central Processing Unit

**FAA** Federal Aviation Administration

**FAR** Federal Aviation Regulation

**FE** Finite Element

**FEM** Finite Element Method

**FFT** Fast Fourier Transformation

**FSI** Fluid Structure Interaction

**RAM** Random Access Memory

**RANS** Reynolds-averaged Navier-Stokes

**RBF** Radial Basis Function

**RBFN** Radial Basis Function Network

**RMS** Root Mean Square

**RPM** Revolutions Per Minute

# LIST OF SYMBOLS

| | |
|---|---|
| $c$ | Structure damping coefficient |
| $C$ | Sutherland's constant |
| $C_P$ | Specific heat at constant pressure |
| $C_V$ | Specific heat at constant volume |
| $C_w$ | Log-layer constant |
| $C_{\epsilon 1}$, $C_{\epsilon 2}$, $C_\mu$, $\sigma_k$, $\sigma_\epsilon$ | $k-\epsilon$ turbulence model parameters |
| $e$ | Specific internal energy |
| $E$ | Elastic modulus |
| $F_x$ | $x$-component of total aerodynamic force acting on blade |
| $F_y$ | $y$-component of total aerodynamic force acting on blade |
| $F_z$ | $z$-component of total aerodynamic force acting on blade |
| $g_M$ | Generalized degree of freedom of the $M^{\text{th}}$ structural mode |
| $h$ | Specific enthalpy |
| $k$ | Turbulence kinetic energy |
| $\dot{m}$ | Mass flow rate |
| $\dot{m}_R$ | Referred mass flow rate |
| $N_1 \ldots N_8$ | Hexahedral element shape functions |
| $N_b$ | Number of fan blades |
| $N_D$ | Number of RBFN driver points |
| $N_{Nodes}$ | Number of nodes per element |
| $N_p$ | Number of data points |
| $N_r$ | Number of circumferential bands |
| $P$ | Static pressure |
| $P^T$ | Total pressure |
| $Pr$ | Prandtl number |
| $Pr_T$ | Turbulent Prandtl number |
| $PR$ | Total pressure ratio |
| $r_r$ | Center radius of circumferential band |
| $R$ | Ideal gas constant |
| $S_f$ | Surface of fluid control volume |
| $S_{LE}$ | Circumferential deformation of leading edge due to bird damage |
| $t$ | Time |
| $\Delta t_f$ | Fluid solver time step |
| $\Delta t_s$ | Structural solver time step |
| $T$ | Static temperature |
| $T_0$ | Sutherland's reference temperature |

| | |
|---|---|
| $T^T$ | Total temperature |
| $V_t$ | Velocity tangent to fluid boundary |
| $V_\tau$ | Fiction velocity |
| $V^+$ | Near wall tangential velocity |
| $V_f$ | Volume of fluid control volume |
| $V_{f\text{ref}}$ | Reference volume for CFD mesh displacement |
| $V_s$ | Volume of structural element |
| $y^+$ | Dimensionless distance from fluid boundary |
| $\mathbf{A}$ | RBF fitting coefficients |
| $\mathbf{B}$ | Strain-displacement matrix |
| $\mathbf{c}$ | Structural element damping matrix |
| $\mathbf{C}$ | Global damping matrix |
| $\mathbf{D}$ | Compliance matrix |
| $\mathbf{f}$ | External applied force |
| $\mathbf{f_a}$ | Nodal applied force vector for FEM element |
| $\mathbf{f_\Omega}$ | Nodal centrifugal force vector for FEM element |
| $\mathbf{F}$ | Vector of inviscid flux terms |
| $\mathbf{F_a}$ | Assembled applied force vector |
| $\mathbf{F}_{\text{aero}}$ | Assembled aerodynamic force vector |
| $\mathbf{F_f}^n$ | Aerodynamic force vector on $n$-th node of CFD mesh |
| $\mathbf{k}$ | Structural element stiffness matrix |
| $\mathbf{K}$ | Global stiffness matrix |
| $\mathbf{m}$ | Structural element mass matrix |
| $\mathbf{M}$ | Global mass matrix |
| $\mathbf{N}$ | Vector of element shape functions |
| $\mathbf{n_a}$ | Control volume surface normal |
| $\mathbf{q}$ | Heat flux |
| $\mathbf{q_T}$ | Turbulent heat flux |
| $\mathbf{r}$ | Radius vector |
| $\mathbf{R}$ | Newton-Raphson residual vector |
| $\mathbf{S}_{\text{cfg}}$ | Centrifugal body force |
| $\mathbf{S}_{\text{Cor}}$ | Coriolis body force |
| $\mathbf{S_M}$ | Momentum source |
| $\mathbf{u} = \{u_1, u_2, u_3\}^T$ | Nodal displacement vector for FEM element |
| $\mathbf{U}$ | Assembled nodal displacement vector |
| $\mathbf{V} = \{V_1, V_2, V_3\}^T$ | Fluid velocity |
| $\mathbf{V}^R$ | Fluid velocity in rotating frame |
| $\mathbf{w}$ | Structural displacement vector |
| $\mathbf{x} = \{x, y, z\}^T$ | Position vector |
| $\mathbf{x}^d$ | RBFN driver point |
| $\mathbf{x}^e$ | RBFN evaluation point |

*Greek Symbols*

| | |
|---|---|
| $\alpha$ | HHT-$\alpha$ time-integration parameter |
| $\beta$ | HHT-$\alpha$ time-integration parameter |

| | |
|---|---|
| $\vartheta$ | Advection scheme parameter |
| $\gamma$ | HHT-$\alpha$ time-integration parameter |
| $\gamma_f = {}^{C_P}/_{C_V}$ | Ratio of specific heats |
| $\Gamma_{\text{eff}}$ | Diffusivity of representative passive scalar |
| $\Gamma_M$ | CFD mesh diffusivity |
| $\Gamma_T = {}^{\mu_T}/_{Pr_T}$ | Turbulent diffusivity |
| $\epsilon$ | Turbulence eddy dissipation |
| $\zeta$ | Bulk viscosity of fluid |
| $\kappa$ | Thermal conductivity |
| $\kappa_w$ | von Karman constant |
| $\lambda$ | Cross-sectional twist angle of undamaged blade |
| $\lambda_D$ | Cross-sectional twist of bird damaged blade |
| $\mu$ | Dynamic viscosity |
| $\mu_{\text{eff}} = \mu + \mu_T$ | Effective viscosity |
| $\mu_T$ | Turbulent viscosity |
| $\mu_0$ | Sutherland's reference viscosity |
| $\nu$ | Poisson's ratio |
| $\rho$ | Fluid density |
| $\rho_s$ | Structure density |
| $\tau_w$ | Fluid boundary shear stress |
| $\phi$ | RBF |
| $\varphi$ | Representative passive scalar |
| $\Omega$ | Engine Rotation Speed |
| $\boldsymbol{\varepsilon}$ | Elastic strain vector |
| $\boldsymbol{\sigma}$ | Structural stress vector |
| $\boldsymbol{\varsigma}$ | Deformation field from bird damage |
| $\hat{\boldsymbol{\varsigma}}$ | RBF interpolant of the deformation field from bird damage |
| $\boldsymbol{\tau}$ | Viscous stress tensor |
| $\boldsymbol{\tau_T}$ | Turbulent stress tensor |
| $\boldsymbol{\Phi}_M$ | Mode shape deformation of the $M^{\text{th}}$ structural mode |
| $\boldsymbol{\Psi}$ | CFD mesh displacement |
| $\boldsymbol{\Omega} = \{0, 0, \Omega\}^T$ | Engine rotation vector |

*Coordinate Systems*

| | |
|---|---|
| $< r, \theta, z >$ | Global cylindrical coordinate system |
| $< x, y, z >$ | Global Cartesian coordinate system |
| $< \xi, \eta, \zeta >$ | Element-fixed coordinate system |

*Subscripts*

| | |
|---|---|
| $B$ | Evaluated at the bypass duct outlet |
| $i$, $j$, $k$ | Index notation indices, $i, j, k = 1, 2, 3$ |
| $ip$ | Evaluated at integration point |
| $l$, $m$ | Row/column indices |
| $M$ | Structural mode number |
| $STD$ | Standard atmosphere conditions |

*Superscript*

| | |
|---|---|
| $n$ | CFD or FEM node number |

*Operators*

| | |
|---|---|
| $\bar{}$ | Area-averaging within a circumferential band |
| $\delta$ | Variational operator |
| $\boldsymbol{\delta}$ | Kronecker delta, $\delta_{i=j} = 1$, $\delta_{i \neq j} = 0$ |
| $\|\| \, \|\|$ | Euclidean norm, i.e. $\|\|x\|\| = \sqrt{x_1^2 + x_2^2 + \cdots + x_n^2}$ |

*Units* [ ]

| | |
|---|---|
| deg | Degrees |
| in | Inch |
| ft | Feet |
| GB | Gigabyte |
| GHz | Gigahertz |
| lb | Pounds of mass |
| lbf | Pounds of force |
| mol | Mole |
| psf | Pounds of force per square foot |
| R | Rankine |
| RPM | Revolution per minute |
| s | Seconds |

# ABSTRACT

**Aeroelastic Behavior of Bird-Damaged Fan Blades Using a Coupled CFD/CSD Framework**

**by**

**Eric Raymond Muir**

**Chair: Professor Peretz P. Friedmann**

Bird strike is a growing concern in the design of modern high-bypass turbofan engines. Predicting the aeroelastic behavior of a bird-damaged fan blade represents a significant barrier in the development of improved-efficiency turbofan engines. In this dissertation, the aeroelastic response of a bird-damaged fan stage at the inlet of a high-bypass ratio turbofan engine is examined using a combined computational fluid dynamics (CFD) and computational structural dynamics framework. The damaged fan contains a sector of 5 damaged blades obtained from accurate numerical simulation of the bird impact. Unsteady aerodynamic and aeroelastic response calculations are performed at 100%, 75%, and 60% take-off thrust conditions to investigate the role of engine speed on the fan response.

A CFD-based aerodynamic model is utilized to perform the steady and unsteady aerodynamic calculations for the undamaged and damaged fan. An automated mesh deformation scheme using radial basis function interpolation is developed to generate a high quality

computational mesh for the damaged geometry. The steady calculations of the damaged fan predict significant flow loss with the fan operating near stall where unsteadiness is significant. The unsteady calculations of the damaged fan exhibit a periodic behavior dominated by the progression and regression of a stall cell that produces significant unsteady aerodynamic loads on the fan blades.

The aerodynamic model is coupled with a finite element based structural dynamics model to perform both one-way forced response and fully-coupled aeroelastic response calculations. The undamaged blades downstream of the damaged sector exhibit the greatest structural response that is dominated by the first bending mode. When compared to the forced response calculation, the aeroelastic response includes increased participation of the higher structural modes, especially for the damaged blades, that grow in time or exhibit beating. Examination of the work exerted by the aerodynamic forces suggests that the growth in amplitude of the higher modes may result from aeroelastic instability.

This study provides substantial contribution toward improved understanding of the bird strike problem and demonstrates the feasibility of performing aeroelastic response calculations of a bird-damaged fan. The results illustrate the importance of aeroelastic coupling when predicting the post bird strike fan response.

# CHAPTER 1

# Introduction, Background, and Objectives

In-flight collision with birds, denoted "bird strike", is a hazard that has plagued the operation of civilian and military aircraft since the early days of aviation. The Wright Brothers recorded the first bird strike event when flying over Huffman Prairie in Dayton, OH on September 7, 1905, "Orville...flew 4,751 meters in 4 minutes 45 seconds, four complete circles. Twice passed over fence into Beard's cornfield. Chased flock of birds for two rounds and killed one which fell on top of the upper surface and after a time fell off when swinging a sharp curve" [1]. The first fatal bird strike occurred on April 3, 1912 when Calbraith Rodgers, flying a Wright Pusher, struck a flock of sea gulls and plunged into the sea near Long Beach, California [1]. More recently on January 15, 2009, United Airways flight 1549 struck a flock of Canada geese on initial climb out from LaGuardia Airport causing the pilot to ditch the aircraft into the Hudson River after complete loss of engine power [1]. In the period between 1990 and 2008, over 89,000 wildlife strikes were reported to the Federal Aviation Administration (FAA) with 97.4% of these strikes involving birds [1]. The annual bird strike related costs incurred by the US commercial aviation industry is estimated to exceed 650 million US dollars [2, 3]. Bird strike incidents and the associated cost are projected to rise each year as a result of increasing air traffic and growing bird

populations near airports.

All forward-facing structures of an aircraft are vulnerable to bird strikes, and typical damage includes cracked windshields, dented leading edges and nose cones, and failure of the propulsion system [4]. The structural and aerodynamic damage caused by bird strikes can affect the airworthiness of the aircraft and potentially result in catastrophic accidents. Although most bird strike incidences are far less severe, the downtime and repair associated with even minor bird damage incurs significant costs. Furthermore, bird strikes occur primarily during takeoff and landing due to the tendency of birds to congregate in the vicinity of the ground. The low altitude at which bird strikes typically occur limits recovery options and enhances the risk due to bird strike. Therefore, robustness to bird strike damage is a driving factor in the design, testing, and certification of modern aircraft.

The modern high-bypass ratio turbofan engine, depicted in Fig. 1.1, is particularly susceptible to failure due to bird strike. Turbofan engines achieve far greater propulsive efficiency compared to their turbojet predecessors thanks to the large, internal, ducted fan. The turbofan is composed of four primary components, as shown in Figure 1.1: the fan, the compressor (high-pressure and low-pressure), the combustor, and the turbine (high-pressure and low-pressure). The compressor, combustor, and turbine constitute the engine core whose primary purpose is to spin the fan by shafts that connect the fan, compressor, and turbine. The propulsive efficiency of turbofans is proportional to the area of the fan, motivating designs with a large intake area covered by fan blades that increases the chance of bird strikes. Furthermore, the thin, low aspect ratio, low camber fan blades used in modern turbofans are structurally and aerodynamically optimized for efficiency at normal operating conditions, and bird damage induces off-design operation [5]. Therefore,

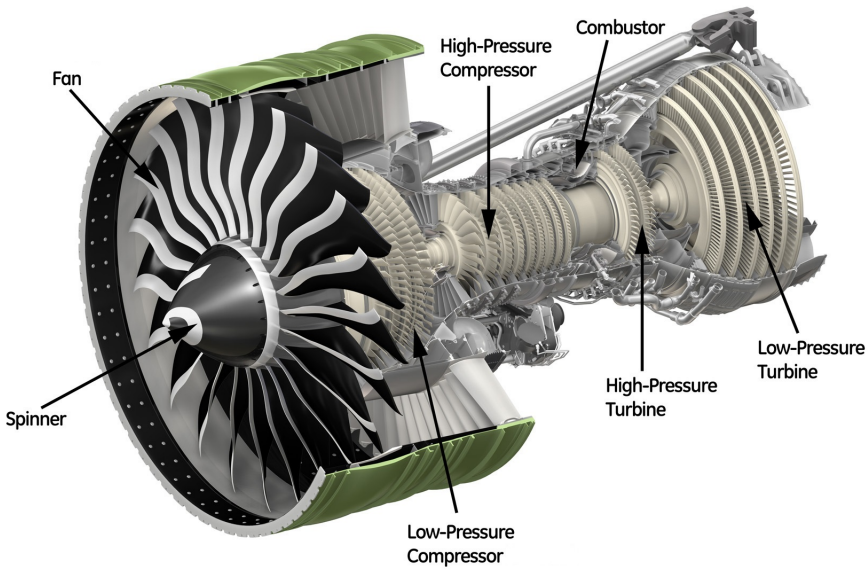


Figure 1.1: General Electric GE90-115B turbofan.

turbofan designs represent a sophisticated trade-off between structural integrity, propulsive efficiency, and robustness under bird strike.

The FAA mandates comprehensive standards for bird strike resistance [1, 6, 7]. Engine certification requires successful demonstration of compliance with Federal Aviation Regulation (FAR) Part 33 in which a bird is fired with an air cannon at a test stand mounted, running engine. During bird-strike, the bird hits the fan blades, fragments, and propagates through the engine core and bypass duct. The impact can cause substantial deformation of the blade leading edge combined with bending and twist of the blade [8]. Furthermore, the unsteady aerodynamic loading caused by bird damage coupled with the structural dynamics induce a complex aeroelastic response problem. Predicting the aeroelastic behavior of a bird-damaged fan blade represents a significant design barrier in the development of improved-efficiency turbofan engines [9].

Numerical simulations provide a cost effective means for assessing the aerodynamic

loading and aeroelastic behavior of a damaged fan. However, the combined aerodynamic and structural dynamic modeling of a bird-damaged fan assembly, where the damage is typically isolated to a sector of blades, is a complex problem. Computational Structural Dynamics (CSD) based on the Finite Element Method (FEM) are typically used to model the bird impact and resulting structural response since it can represent complex material behavior and nonlinear geometric deformations [10–16]. Computational Fluid Dynamics (CFD) is required to accurately capture the complex flow phenomena associated with bird damaged turbofans [17, 18]. Reliable CSD and CFD methods exist to compute the bird impact, structural dynamic response, and unsteady aerodynamic loads of a damaged fan blade. However, due to the computational times required for CFD methods, the structural and aerodynamic computations are typically performed separately in an uncoupled manner. Therefore, the aeroelastic effects that may be important in the bird strike problem are not properly accounted for.

This dissertation investigates the aeroelastic behavior of a bird damaged commercial turbofan using a computational aeroelasticity framework for improved understanding of the bird-strike problem. The following sections provide background information pertaining to bird strike certification testing and turbomachinery aeroelasticity together with a review of previous studies relevant to the bird strike problem.

## 1.1 Engine Certification for Bird Strike

The FAA regulations under FAR §33.76 specify bird ingestion testing requirements and procedures for jet engine certification [7]. The FAA certification tests are conducted on a

test-stand mounted engine operating at 100% takeoff thrust. The diameter of the engine inlet determines the required bird strike test conditions. For the modern, commercial turbofan engines considered in this study, three tests are mandated: the single large bird impact test, the medium flocking bird test, and the single largest medium bird test. These conditions are clarified later in this section.

The single large bird impact test verifies that an engine can be safely shutdown after ingestion of a large bird without endangering the airworthiness of the aircraft. For an engine with inlet diameter between 51.6 inches and 87.7 inches, the single large bird test involves ingestion of a 6 pound bird at an impact speed of 200 knots. The strike location must correspond to the most critical exposed location of the fan, as determined with appropriate component tests and/or analysis performed by the engine manufacturer. The FAR §33.76 mandates that ingestion of a single large bird must not result in any of the following:

1. Non-containment of high-energy debris.
2. Concentration of toxic products in the engine bleed air intended for the cabin sufficient to incapacitate crew or passengers.
3. Significant thrust in the opposite direction to that commanded by the pilot.
4. Uncontrolled fire.
5. Failure of the engine mount system leading to inadvertent engine separation.
6. Complete inability to shut down the engine.

The aerodynamic and aeroelastic response of the damaged fan is not a factor for single large bird tests since there exists no requirements for continued operation after ingestion. There-

fore, numerical prediction of the post bird strike behavior of the damaged configuration resulting from large bird impact tests is not considered in this study.

The medium flocking bird test simulates a flock encounter and requires ingestion of one 2.5 pound bird and three 1.5 pound birds for an engine with inlet diameter between 51.6 inches and 57.9 inches. The 2.5 pound bird is aimed at the flow path leading to the core duct, one of the 1.5 pound birds is aimed at the most critical exposed location of the fan as determined by the engine manufacturer, and the remaining 1.5 pound birds are evenly distributed over the engine face. The single largest medium bird test requires ingestion of a 2.5 pound bird at the most critical location outboard of the flow path leading to the core duct. The bird-damaged engine resulting from either of these tests must not result in the conditions listed for the single large bird test or any of the following:

1. A sustained engine thrust loss not to exceed 25%.

2. Unacceptable deterioration of engine handling requirements.

3. The engine to be shut down during the required demonstration of continued operation after bird strike, referred to as the run-on demonstration.

The run-on demonstration required by the medium flocking bird test and the single largest medium bird test consists of a series of throttle movements that simulate an emergency landing sequence. Figure 1.2 provides a throttle "skyline" chart that describes the sequence of throttle settings for the run-on demonstration. The test begins at flight idle, which is denoted by 0% take-off thrust in Fig. 1.2. Next, the throttle is increased to the 100% take-off thrust throttle setting and the bird(s) are ingested. Throttle movement is not permitted within 2 minutes of the bird ingestion. During this time, the thrust loss result-

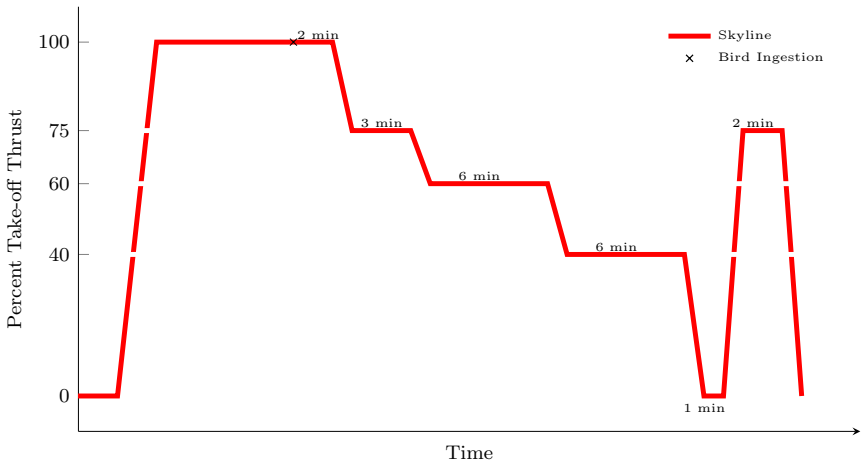


Figure 1.2: Throttle "skyline" chart for run-on demonstration.

ing from the bird damage is measured, and it must not exceed 25%. The throttle is then decreased to the 75% take-off thrust throttle setting and held for 3 minutes. The throttle is adjusted to 60% take-off thrust and held for 6 minutes and then to the 40% take-off thrust throttle setting for 6 minutes. Subsequently, the throttle is set to approach idle setting for 1 minute, followed by 2 minutes at the 75% take-off thrust throttle setting, followed by idle and engine shutdown.

Assuming the fan blades withstand the initial impact, the minimum thrust requirement and run-on demonstration of the medium bird tests are particularly challenging. Aerodynamic disturbances caused by the bird damage, such as flow separation, vortex shedding, and shock oscillations, can result in sustained thrust loss. Furthermore, these aerodynamic disturbances also introduce significant unsteady aerodynamic forces that can lead to high levels of vibratory stress and eventual fatigue failure of the blades during the run-on demonstration. The single largest medium bird test often results in the most substantial damage since the 2.5 pound bird impacts the blade at an outer span location. The difficulties posed by the single largest medium bird test motivate the damaged fan configuration and operating

conditions considered in this study. Thus, the bird-damage represents that resulting from a single largest medium bird test in which a 2.5 pound bird is ingested at take-off conditions with a strike location of 70%span. The unsteady aerodynamic behavior and aeroelastic response is evaluated at the 100%, 75%, and 60% take-off thrust throttle settings, which correspond with the first three throttle settings of the run-on demonstration.

## 1.2 Review of Turbomachinery Aeroelasticity

Aeroelasticity is the field of study pertaining to the behavior of an elastic body in an airstream, wherein there is significant reciprocal interaction or feedback between the structural deformation and fluid flow [19]. Modern aeroelasticity involves the interactions of several disciplines including aerodynamics, inertia, elasticity, thermal effects, and controls, as illustrated by Fig. 1.3(a). Aeroelastic behavior in fan blades involves the triad of aerodynamics, interia, and elasticity, the interaction of which may lead to undesirable structural vibrations or instabilities [20]. The interactions between these three disciplines constitute the base of the hexahedron shown in Fig. 1.3(a), isolated in Fig. 1.3(b) and denoted as Collar's triangle.

Aeroelastic problems in turbomachinery occur when the interaction of the aerodynamics and structural dynamics results in vibrations with sustained or increasing amplitudes [21]. Excessive blade vibrations can lead to significant fatigue stresses and eventual blade failure [22]. Due to the importance of the problem, a substantial body of research dealing with turobmachinery aeroelasticity exists. References [23] and [24] provide a comprehensive review of the early approaches for unsteady aerodynamic and aeroelastic stud-

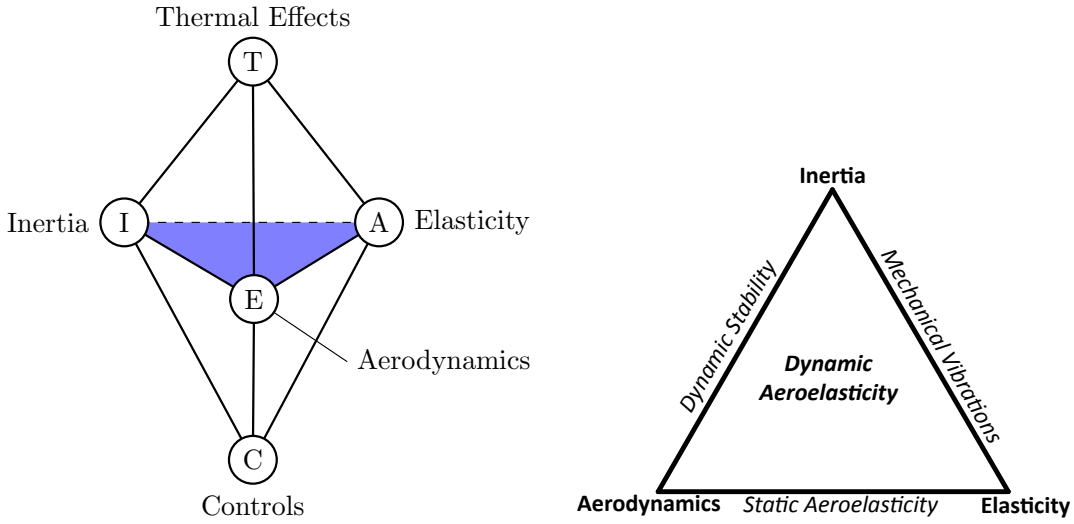


(a) Hexahedron of aeroelastic interactions.

(b) Collar's triangle.

Figure 1.3: Interactions in modern aeroelasticity.

ies in axial-flow turbomachinery. References [21, 25–27] review aeroelastic phenomenon associated with modern turbomachinery and provide an overview of current analysis approaches. A concise review of aeroelasticity relevant to the large, axial fans of turbofan engines is provided in the following subsections. Section 1.2.1 details the aeroelastic phenomena of primary interest to fan blade designers, namely static aeroelasticity, forced response, and flutter. Section 1.2.2 reviews numerical methods employed to model the structural dynamic and aerodynamic environments in turbomachinery aeroelastic studies. Section 1.2.3 discusses the manner in which the structural dynamic and aerodynamic models are coupled for aeroelastic response calculations. This section also describes several computational studies that performed an aeroelastic study of large, axial fans.

### 1.2.1 Aeroelastic Behavior of Fan Blades

Static aeroelasticity describes the time-independent interaction between the aerodynamic and elastic forces and neglects inertial effects [25]. During operation, fan blades are subject

to centrifugal and aerodynamic forces that cause the blades to deform elastically from their non-rotating geometry. Static aeroelastic equilibrium calculations are typically performed to determine the non-rotating geometry from the optimal blade shape when the engine is running [27]. The "running" blade shape represents the deformed blade geometry resulting from equilibrium of the aerodynamic and centrifugal forces during engine operation. The deformation includes global twisting, denoted "untwist", and bending, denoted "lean", of the blades along with uncambering of the blade cross-sections [25]. The fan blade geometry is designed for optimal efficiency at this condition, and the non-rotating blade geometry is calculated by removal of the aerodynamic and centrifugal loads from this state.

Forced response is a subset of dynamic aeroelasticity in which the structural dynamic response results from unsteady aerodynamic forces that are independent of the blade motion [28]. The fan blade structural response to the unsteady aerodynamic forces may contribute further unsteadiness to the aerodynamic environment; however, the aerodynamics are not solely dependent on the blade response. Sources of the unsteady aerodynamic forces include inlet distortions, vortex shedding, upstream-traveling pressure waves propagating from downstream compressor rows, or unsteady flow separation and reattachment [21, 25]. The frequencies of the periodic aerodynamic forcing often occur at integer multiples of the engine rotational speed, called engine orders [21, 25, 27].

Rotating stall and surge are two common aerodynamic instabilities that drive forced response vibrations in fans [25, 29, 30]. During a rotating stall event, a flow disturbance causes the suction-side boundary layer of a blade to separate, partially or totally blocking the downstream passage. The flow blockage causes the incoming flow to be diverted to the adjacent blade passages resulting in a decreased angle of attack for the currently stalled

blade and an increased angle of attack for the downstream blade. The decreased angle of attack causes the flow to reattach to the separated blade, and the increased angle of attack causes the downstream blade to stall. The resulting region of stalled flow, denoted a stall cell, typically propagates opposite the direction of rotation at 1/5 to 1/2 the engine rotation speed and encompasses only 2 or 3 blades. Rotating stall is often the precursor to the more severe flow instability of surge, which is a self-excited compression system phenomenon characterized by large pressure ratios and fluctuating mass flow rates of the compression system [25, 31].

Flutter is a self-excited, dynamic aeroelastic instability that results from continuous, reciprocal interaction of the elastic, inertial, and aerodynamic forces of the system. In contrast to forced response vibrations, the aerodynamic forces that sustain the blade motion are solely dependent on that motion [28]. During flutter, the coupled aerodynamic and structural dynamic response of the vibrating fan blades is characterized by negative damping of the system producing an unstable oscillatory response with growing amplitudes. The onset of flutter is typically a linear phenomenon; however, nonlinear fluid mechanics is essential in determining the limit cycle response [21]. The common types of flutter include classical supersonic (unstalled) flutter, high-incidence (stalled) flutter, supersonic positive-incidence flutter, and negative-incidence (choke) flutter. Classical supersonic flutter can occur at design operating conditions, while the others occur at off-design conditions with high-incidence flutter having the highest frequency of occurrence [28].

Flutter in turbomachinery is fundamentally different from the frequency coalescence flutter characteristic of fixed-wing aircraft structures. In frequency coalescence flutter, two structural modes become coupled through aerodynamic forces and the frequencies of these

modes coalesce near the onset of flutter [21, 32, 33]. In turbomachinery, the coupling between the fluid and structure tends to be relatively small due to the high mass ratios, and the structural modes usually do not coalesce [21, 27]. As a result, flutter in turbomachinery is often presented as a single degree of freedom event in which a single blade vibratory mode shape and frequency, typically the first bending or first torsion, are nearly unchanged by the unsteady aerodynamic forces acting on the blades [21]. However, the likelihood of a coupled-mode flutter is increased in modern designs where fan blades tend to be thinner and more heavily loaded in an effort to improve aerodynamic efficiency [27]. In both single and coupled degree-of-freedom flutter, the unsteady aerodynamic forces resulting from the blade vibration introduce negative aerodynamic damping into the system producing an unstable structural response.

### 1.2.2 Aerodynamic and Structural Dynamic Modeling

The unsteady aerodynamic environment in turbofan engines with large axial fans is complex. The desire for high fuel-efficiency requires designs with very thin, low camber fan blades that are prone to flow separation at high incidence angles [5]. Furthermore, large fans operate with relative flow velocities ranging from subsonic at the blade hub to supersonic at the blade tip, resulting in a complex, three-dimensional shock structure [22, 26]. Shock position is influenced by the blade profile, tip clearance, and the splitter configuration that separates the core and bypass duct [34]. Furthermore, shock oscillation may influence fan aeroelastic response [5, 34]. Other flow phenomena associated with large fans include leading edge bow shocks, standing normal shocks, shock/boundary layer interaction, flow separation, and time-dependent wake [35, 36]. The unsteady aerodynamic

analyses for turbomachinery aeroelastic predictions must capture these complex flow features for a wide range of three-dimensional geometries.

Time-domain solutions for turbomachinery aerodynamics have progressed through a gamut of fluid models with increasing fidelity and complexity, such as: full-potential, linearized-Euler, Euler, and, Reynolds-averaged Navier-Stokes (RANS) solutions. Classical models based on simplifying assumptions such as inviscid, incompressible, and irrotational flow were common among early semi-analytical aerodynamic analyses for turbomachinery. However, the restrictions associated with these assumptions limited their usefulness for aeroelastic applications involving transonic flow where nonlinearities and compressibility are important [27]. Furthermore, two-dimensional cascade theories, such as Whitehead's theory (Ref. [37, 38]), historically used in compressor and turbine aerodynamic calculations neglect the important three-dimensional aerodynamic features of fans [26]. Linearized potential and Euler equations are useful in calculating the time-dependent, inviscid flows in a computationally efficient manner; however, the applicability of these methods to aeroelastic analysis is limited since linearization may fail to accurately capture important flow features such as shock oscillations and time-dependent flow separation [27]. To overcome this limitation, the nonlinear potential and Euler equations can be solved using a time-accurate discretization of the unsteady terms [27]. Furthermore, viscous effects in the boundary layer can be included through the use of viscous-inviscid interaction where additional equations are used to model turbulence near the boundary [39]. References [21, 26–28, 40] provide a thorough review of the large array of aerodynamic theories applicable to turbomachinery.

Currently, unsteady RANS solvers, which account for flow unsteadiness and viscous

effects, represent the state-of-the-art in industrial scale turbomachinery aerodynamic and aeroelastic calculations. Typically, the finite volume form of the RANS equations is solved, often with multiple grids and local time-stepping techniques [27]. The finite-volume method is favored over a finite-difference formulation due to its applicability to complex three-dimensional geometries without the need for grid transformations [27]. It is impractical to solve the Navier-Stokes equations on a sufficiently fine mesh to capture the small eddies required for accurate representation of turbulence; therefore, simplified turbulence models and laminar-to-turbulent flow transition methods are utilized. There exists an abundance of turbulence and transition models available, each with their own assumptions and limitations.

The structural dynamic models used in turbomachinery aeroelastic analyses are exclusively Finite Element (FE)-based and are solved in either the time-domain or the frequency domain [21]. Fans are designed such that all blades are identical yielding a perfectly "tuned" structural system exhibiting cyclic symmetry. In a tuned fan, all blades are assumed to be identical and either a single blade cantilevered at the hub or a "pie-sliced" section of the bladed disk is modeled using periodic boundary conditions [21]. Structural imperfections in the blade due to randomness associated with manufacturing, uneven wear of the fan blades, or foreign-object damage (i.e. bird damage) alters the natural frequencies of each blade and destroys the cyclic symmetry of the fan. The loss of symmetry due to structural disorder is referred to as structural mistuning and can significantly affect the behavior of a fan [21]. The presence of structural mistuning requires the entire fan stage to be modeled resulting in a significant increase in the size of the structural model and a corresponding increase in computational resources. In addition, when hub flexibility is

significant relative to that of the blades, it is essential that the structural model also include the hub disk to capture the structural coupling of the individual fan blades. However, fan blades of modern high bypass ratio commercial turbofans are significantly more flexible than the hub disks; therefore, the hub flexibility is often neglected and the fan blades are modeled as individual blades cantilevered at the hub [18].

### 1.2.3 Aeroelastic Coupling

The following provides a concise overview of the modern methods typically employed in turbomachinery aeroelastic response calculations. References [27] and [25] provide a thorough review of prior contributions to the field of turbomachinery aeroelasticity and emphasize two primary methods used for aeroelastic response calculations: the "classical" which ignores the interaction between the fluid and structure and the integrated approach which attempts to account for it. Forced response and prescribed motion flutter calculations utilize the classical aeroelasticity method in which the fluid and structure remain uncoupled. In the fully integrated method, the fluid and structural domains are combined using either a monolithic or partitioned framework.

#### 1.2.3.1 Forced Response Calculations

Forced response calculations typically utilize a "classical" or one-way coupled approach to calculate the effect of the unsteady flow field on the structural response [25, 27, 28]. In this approach, the aerodynamic calculations are performed first for a rigid geometry. Subsequently, the unsteady aerodynamic forces are extracted and applied on the structural dynamic model of the blade. The aerodynamic model is not affected by with the structural

response, thus the feedback mechanism of the structural response on the unsteady aerodynamic loading is not captured. Sometimes this is deemed to be adequate when the forced response is dominated by the inherent unsteadiness of the aerodynamics. Static aeroelasticity calculations are also performed using one-way coupling to obtain the running blade geometry. For these calculations, a steady aerodynamic calculation is carried out for a rigid geometry, and the steady aerodynamic forces are applied to a static structural model of the blade that also includes centrifugal effects due to rotation.

A benefit of the one-way coupled approach is the ability to perform the aerodynamic calculations and structural dynamic calculations separately. The CFD-based aerodynamic models typically require time-steps that are often much smaller than the time-step required by the CSD model [41]. Performing the calculations separately allows each solver to be run using the ideal time-step thereby reducing the computational expense of the coupled calculations. Furthermore, the one-way coupled approach permits modifications to the CSD model to be explored using the same unsteady aerodynamic forces. This allows trend studies to investigate different blade materials, blade root designs, and FE modeling parameters and mesh density.

Breard et al. [22] coupled a time-accurate, nonlinear, viscous, unsteady flow model with a FE-based structural model for the prediction of fan forced response to inlet distortion. The study also examined the effect of the blade structural response on the unsteady pressure distribution and concluded that the unsteady aerodynamic loading is sensitive to blade motion for certain modes (first torsion and second bending modes). Sayma et al. [42] coupled a linear modal-based structural model with a Favre-averaged Navier-Stokes solver to assess the role of blade response on the forced response of several turbomachinery components.

These studies demonstrate that the influence of the blade motion on the aerodynamic forcing may be important in forced response vibrations.

#### 1.2.3.2 Prescribed Motion Flutter Calculations

Flutter calculations were traditionally performed using a prescribed motion technique [25, 27, 28]. In this approach, a periodic blade motion is prescribed in the aerodynamic solver, where the blade motion is based on the mode shapes and frequencies from a free-vibration structural analysis of a cantilevered blade. The same mode shape and frequency is prescribed for each blade, and a constant phase angle is specified between adjacent blades. Unsteady aerodynamic calculations are performed with the prescribed blade motion until a periodic solution is obtained. The aeroelastic stability is inferred based on the nature of the aerodynamic work calculated over one period of the solution [39, 43]. Negative aerodynamic work implies an energy transfer from the blade to the flow and indicates a stable response. Positive aerodynamic work implies an energy transfer from the flow to the blade and indicates an unstable response. The prescribed motion technique requires a number of educated guesses as to the modes and phase angles needed, and significant computer resources are required to explore all combinations of modes, phase angles, and operating conditions [44]. However, this approach also neglects the feedback mechanism between the aerodynamic response and the structural motion that may be important for coupled mode flutter.

Aotsuka et al. [45] examined transonic stall flutter of a fan using a RANS solver that accommodates a dynamic aerodynamic mesh. Harmonic oscillations of the blade were prescribed based on the mode shapes obtained from a free-vibration analysis of a blade, and

the flutter point was identified by calculating the aerodynamic work. It was observed that the aerodynamic work at the shock impingement point has positive value, the aerodynamic work downstream of the shock has negative value, and stability is determined by a balance of the aerodynamic work terms. Isomura et al. [5] employed a quasi three-dimensional thin-shear-layer Navier-Stokes equation solver to investigate the role of shock wave/boundary layer interaction in the flutter mechanism of the a modern transonic fan blade in the first bending mode. The flutter mechanism was identified as shock oscillation and the laminar-to-turbulent transition point in the unsteady aerodynamic calculations was important.

#### 1.2.3.3 Fully-Coupled Aeroelastic Response Calculations

Increases in computational power have enabled dynamic aeroelastic calculations, including flutter calculations, to be performed using an integrated or two-way coupled approach that combines the aerodynamic and structural dynamic models [25, 27, 28, 46]. This approach utilizes either a monolithic or partitioned framework to fully capture the reciprocal interaction of the unsteady aerodynamics and structural dynamics [47, 48]. Monolithic methods solve the aerodynamic and structural dynamic models simultaneously at each time-step. This is accomplished using the same integrator through discretizing the fluid and structural domains into a single Arbitrary Lagrangian-Eulerian (ALE) system [49]. The ALE approach differs from the partitioned methods in which separate aerodynamic and structural dynamic computations are performed within each time-step and exchange of information between the two solvers occurs at the end of the time-step. Within each time-step of the partitioned approach, the aerodynamic forces are transferred to the structural model at the wetted surface, and the corresponding structural displacements are transferred back to the

aerodynamic model. Various time-marching techniques exist that vary from fully explicit schemes to fully implicit schemes, the latter being the most efficient [41]. Partitioned methods are commonly used due to the ease of implementation when off-the-shelf aerodynamic and structural dynamic solvers are available. The transfer of data between the solvers at node points for the two systems that do not coincide is a challenging problem that requires sophisticated mapping and interpolation techniques [41, 50, 51].

Carstens et al. [52] coupled an unsteady RANS solver to a linear modal representation of the structure to assess the aeroelastic stability of a fan in the transonic regime. A partitioned approach is utilized where the aerodynamic and structural dynamic models are integrated separately in the time domain and their interaction is calculated with a coupling algorithm. It was determined that the energy transfer from the fluid to the structure was dominated by oscillating shocks and shock-boundary layer interaction. Vahdati et al. [39] examined seven different three-dimensional part-speed flutter prediction methodologies including linearized and nonlinear inviscid and viscous calculations for both a single blade passage and a full fan wheel. All aerodynamic methods use the same viscous steady flow and differ only in the treatment of unsteady flow. The structural model consists of a linear modal representation of the entire fan stage. Two mechanisms for part-speed stall flutter were identified: aeroacoustic effects where viscous effects are not important and classical stall flutter where viscous effects dominate. In addition, the shock region had a stabilizing effect, and the separation area behind the shock was destabilizing. Vahdati et al. [53] also explored mechanisms for wide-chord fan blade flutter using a three-dimensional RANS solve coupled with a linear modal representation of the structure. The flutter mechanism was identified as flow separation that created significant unsteadiness behind the shock and

caused the phase of the unsteady pressure to be in phase with the blade motion.

## 1.3 Review of Bird Strike Studies

A review of the studies pertinent to bird strike on turbofans is provided. Section 1.3.1 describes numerical and experimental techniques to predict the damaged fan configuration. Section 1.3.2 describes three unique studies that examine the aerodynamic behavior and aeroelastic response of a bird damaged fan.

### 1.3.1 Approaches for Analyzing Bird Impact on Fan Blades

The ability of a fan blade design to withstand bird impact is examined using a combined numerical and experimental approach. Numerical bird impact analyses are employed to simulate the bird impact and predict the resulting fan blade deformations. These simulations offer a cost effective means to examine the effects of bird impact for a wide range of bird strike conditions and are useful to fine-tune fan blade designs prior to experimental testing. Once the numerical analyses identify a promising design, experimental bird impact tests are used for design refinement. An accurate numerical bird impact analysis is desirable to reduce the number of design iterations that require experimental testing.

Several studies have employed FEM codes to simulate bird-to-blade impact and predict the resulting fan blade deformations [4, 10–14, 16, 54]. Such analyses require accurate treatment of the bird material model, the bird and fan blade geometries, the bird and blade material laws at high velocities and strain rates, and the bird-to-blade contact algorithm [13]. The structural dynamics of the fan blades is modeled using nonlinear FEM,

which can accommodate high strain rates, large deformations, and plastic strains [13]. The bird material is represented by a fluid with negligible viscosity, based on findings that the high-speed impact forces greatly exceed the tissue strength of the bird [13, 55]. Furthermore, the bird geometry usually assumes the form of a cylinder, a cylinder with hemispherical ends, an ellipsoid, or a sphere [15]. Solution strategies include a pure Lagrangian, pure Eulerian, Arbitrary Lagrangian-Eulerian, and Smooth Particle Hydrodynamics type frameworks [10, 15, 56].

Experimental bird-strike tests include static blade impact tests, spinning rig impact tests, and full-engine bird ingestion tests [8, 9, 57, 58]. In static blade tests, a bird is fired at a stationary single blade to confirm the basic structural design of the blade [9]. Spinning rig tests consist of an artificial bird fired at a single blade or complete fan assembly rotating in vacuum. These spinning rig tests are used to explore minor geometric modifications and offer an cost effective means for investigating the effects of bird weight, strike location, and fan speed [8]. Single blade spinning tests provide greater experimental control over the bird impact and offer a more unobstructed view of the impact dynamics. Complete assembly tests in vacuum yield the bird damaged fan that is subsequently installed in an otherwise undamaged engine to examine the effect of bird induced damaged on engine performance [8, 9]. Full-engine bird ingestion tests demonstrate the structural integrity of the entire engine and provide the means for determining the sustained thrust loss due to bird ingestion [9]. In these full-engine tests, carcasses of real birds are fired into a running test stand mounted engine [9, 57]. It is important to note that complete engine bird ingestion tests are used mainly to demonstrate compliance with the FAA regulations as these tests are quite expensive [9].

### 1.3.2 Aerodynamic and Aeroelastic Studies of a Bird-Damaged Fan

Despite its importance, only a limited number of computational studies have examined the aerodynamic behavior and aeroelastic response of a bird-damaged fan. Bohari and Sayma [59] presented a CFD approach for analyzing the aerodynamic characteristics of a bird-damaged NASA rotor 67 containing a single blade with "assumed" leading edge damage. A RANS solver is utilized for steady aerodynamic calculations with the Spallart-Allmaras and k-$\epsilon$ turbulence models. Two damaged configurations were analyzed at 100%, 80% and 60% design rotational speed. The fan characteristic curves were mapped for the three rotational speeds, and the stall boundary was identified for both damaged configurations. The steady CFD results conclude that the stall margins deteriorate for the damaged fan with stall occurring below the design operating line. However, the mass flow rate and total pressure ratio produced by the fan prior to stall were unaffected by the damage.

Imregun et al. [17, 18] conducted two unique studies that examine the aeroelastic response and stability of a bird-damaged bladed disk using a fully coupled CFD/CSD formulation to determine the time-dependent response. A bladed disk containing two bird-damaged blades identified as the "heavy-damaged" and "medium-damaged" blades is considered. The RANS equations, with the Baldwin and Barth turbulence model, are solved in the time-domain. The structural model utilizes a linear modal representation obtained using a FE formulation where large-deflection nonlinearities and gyroscopic effects are neglected. A plastic deformation of the damaged blades is assumed, and a linear FE model is used to represent the damaged fan. Furthermore, due to the loss of cyclic symmetry in the bird-damaged assembly, the structural model includes the entire bladed assembly, including the hub disk and shaft. The FEM analysis indicates that the hub disk stiffness couples

the individual blade modes and the resulting assembly modes are clearly different from the single cantilevered blade modes. This difference depends on the relative disk/blade stiffness.

In Ref. [17], steady aerodynamic calculations indicate a change in the shock structure of the damaged blades as well as full flow separation and a strong recirculation area indicative of a wake being released from the damaged blade. Considerable blockage of the flow field is caused by the "heavy-damaged" blade, and the mass-flow rate dropped 8% compared to the undamaged fan assembly. The unsteady aerodynamic calculations show a rotating stall cell that is periodically released from the damaged area and is likely to affect the entire fan. The fully coupled analysis demonstrates an instability of the first torsion mode of the "medium-damaged" blade; however, it is unclear if the growth in modal displacement is the result of a flutter mechanism or the strong wake shed by the upstream "heavy-damaged" blade. These findings are inconclusive since the fully-coupled calculations were only performed for 1/3 fan revolution due limitations on the available computer resources.

In a follow-up study, Kim et al. [18] examined the sensitivity of the rotating stall instability to flight conditions and further examined the aeroelastic response of the damaged fan. The calculations were performed at two points on the characteristic curve; one at higher mass flow/lower pressure ratio and the other at lower mass flow/higher pressure ratio. The aerodynamic calculations at high pressure ratios exhibited rotating stall that produced unsteady aerodynamic forces on the blades. For the low pressure ratio calculations, the flow separation was restricted to the damaged blades, and the unsteady aerodynamic forces were small. The aeroelastic stability of the damaged fan operating at 70% engine

speed was computed and compared to the undamaged configuration. Overall, the aeroelastic stability of a bird-damaged assembly was found to be significantly lower than the undamaged fan. Furthermore, aeroelastic stability was found to be sensitive to flight conditions with flutter margins being reduced at low pressure ratios and rotating stall occurring at high pressure ratios.

These studies provide insight into the aerodynamic behavior and aeroelastic response of a bird-damaged fan. However, the damage considered was not representative of realistic blade damage required by bird-strike certification tests, where leading edge damage over a large region of the blade span is accompanied by global bending and twist of the blade. Also, the turbofan geometries employed in these studies were not representative of high-bypass turbofans and the damaged sector is limited to one or two blades. Furthermore, the aeroelastic response calculations of Refs. [18] and [17] were performed at 70% engine rotational speed, and the aeroelastic behavior of the damaged fan at other engine speeds was not considered.

## 1.4 Objectives of this Dissertation

From the introduction and literature review presented it is evident that a computational aeroelastic study of a bird damaged commercial turbofan, with the bird damage representative of experimental bird strike tests or accurate numerical simulation of the bird-strike event, is required to improve our fundamental understanding of the bird-strike problem. Therefore, the overall objective of this dissertation is to investigate and characterize the aeroelastic behavior of a bird-damaged turbofan using a coupled CFD/CSD framework.

An aerodynamic model suitable for use in an aeroelastic study of a bird-damaged commercial turbofan engine is presented together with the steady and unsteady flow fields associated with the bird-damaged fan. A combined CFD and CSD framework is implemented to compare the blade response resulting from one-way forced response and fully-coupled aeroelastic response calculations and thus assess the role of complete aeroelastic coupling on the response. The aerodynamic and aeroelastic response calculations are performed at the 100%, 75%, and 60% throttle settings on the skyline chart to examine the effect of engine speed on the fan response. The specific objectives of this study are to:

1. Describe an aerodynamic model suitable for calculating the nonlinear, unsteady aerodynamic behavior of a bird damaged fan.

2. Present a coupled CFD/CSD framework for one-way forced response and fully-coupled aeroelastic response calculations of a bird damaged fan.

3. Investigate the steady and unsteady flow associated with a fan sector consisting of five bird-damaged blades that are representative of a practical bird strike configuration.

4. Study in detail the forced response and aeroelastic response of a bird-damaged fan stage under post bird strike conditions at 100%, 75%, and 60% throttle setting.

5. Compare the aerodynamic work calculated from the forced response and aeroelastic response calculations to identify the potential for aeroelastic instability.

## 1.5 Principal Contributions of this Dissertation

Accomplishing the stated objectives provides a substantial contribution toward improved understanding of the bird strike problem and it also demonstrates the feasibility of performing computational aeroelastic predictions of a bird-damaged turbofan. The following contributions are unique to this study:

1. This study represents the first comprehensive aerodynamic and aeroelastic analysis of a modern commercial turbofan where the damaged configuration consists of a sector of 5 damaged blades obtained from comprehensive numerical simulation of the bird-strike event.

2. Development of an automated mesh deformation scheme based on Radial Basis Function (RBF) interpolation to deform and transform an undamaged CFD mesh into a mesh that represents the damaged geometry accurately.

3. Detailed results for the aerodynamic and aeroelastic response of the damaged fan sector in a complete engine at conditions representing engine operation at the 100%, 75%, and 60% throttle settings.

4. Identification of the dominant unsteady aerodynamic features of the damaged fan that drive the blade response.

5. Comparison of the forced response and aeroelastic response of the blades to determine the importance of aeroelastic coupling in predicting the post bird strike fan response. This study is the first to consider the forced response of the damaged fan.

6. Assessment of the aeroelastic stability of the fan blades by comparison of the aerodynamic work from the forced response and aeroelastic response calculations.

## 1.6 Outline of the Dissertation

This dissertation has nine chapters. An introduction to the bird strike problem in turbofans, motivations for this study, a literature review, and objectives of this dissertation are provided in Chapter 1. The undamaged and damaged fan geometry is presented in detail in Chapter 2. Chapter 3 provides a thorough description of the aerodynamic model including a new approach for generating the computational mesh of a bird-damaged fan. In Chapter 4, the CFD-based aerodynamic model is verified against results from an industry CFD solver for an undamaged and damaged fan. Chapter 5 describes the structural dynamic required for coupling with the aerodynamic model for aeroelastic response calculations using the frameworks described in Chapter 6. In Chapter 6.4, the aerodynamic model is used to perform steady and unsteady CFD calculations of a bird-damaged fan at the 100%, 75%, and 60% throttle settings. The flow field is compared to that of an undamaged fan, and the effects of the bird-damage is examined in detail. In Chapter 8 the structural dynamic model is coupled to the aerodynamic model, and the forced response and aeroelastic response calculations of a bird-damaged fan are presented. The aerodynamic work due to the aerodynamic loads is compared for the forced response and aeroelastic response calculations so as to assess the aeroelastic stability of the damaged blades. Finally, Chapter 9 provides conclusions and directions for future research on the bird strike problem.

# CHAPTER 2

## Details of the Bird-Damaged Fan Configuration

The turbofan geometry examined in this study resembles a modern, commercial high-bypass ratio turbofan engine. Figure 2.1(a) depicts a section of a representative commercial turbofan engine where the fan stage, core duct, and bypass duct are identified. The aerodynamic and aeroelastic calculations are performed for an isolated fan stage consisting of 24 fan blades that is appropriate and compatible with the objectives of this dissertation. The fan stage begins downstream of the engine inlet and extends into the bypass and core ducts. Figure 2.1(b) depicts the simplified model of the fan stage considered in this study.

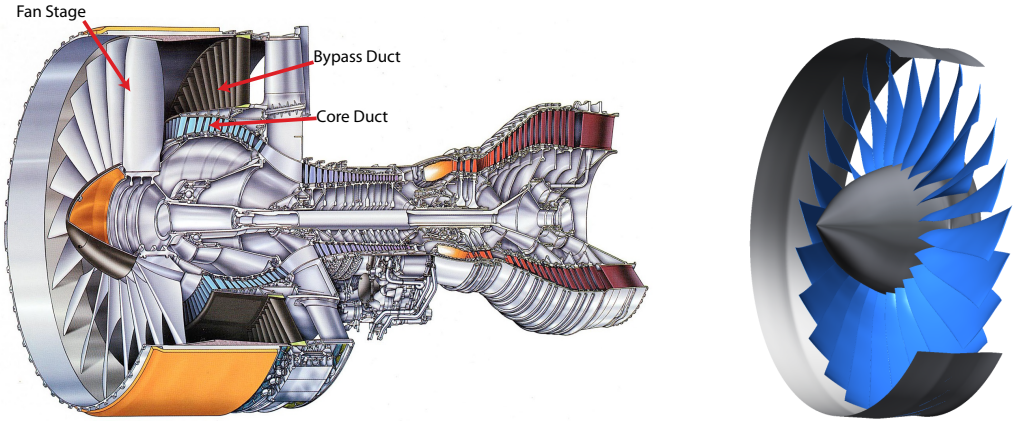


(a) Pratt & Whtiney PW4000 turbofan engine. (b) Isolated fan stage.

Figure 2.1: Representative commercial turbofan.

The aerodynamic geometry of the fan blades is described by a set of constant-span cross-sections referred to as blade profiles, as shown in Fig. 2.2(a). These blade profiles define the blade geometry in turbomachinery-specific CFD mesh generators and solvers. In contrast, a Computer Aided Design (CAD) model defines the structural geometry for generation of the FE mesh and the corresponding structural dynamic model of the fan blades. The CAD model, illustrated by Fig. 2.2(b), contains the three-dimensional blade geometry together with additional features such as the dovetail and hub plate. The blade profiles and CAD model in Fig. 2.2 were provided by the sponsor organization.

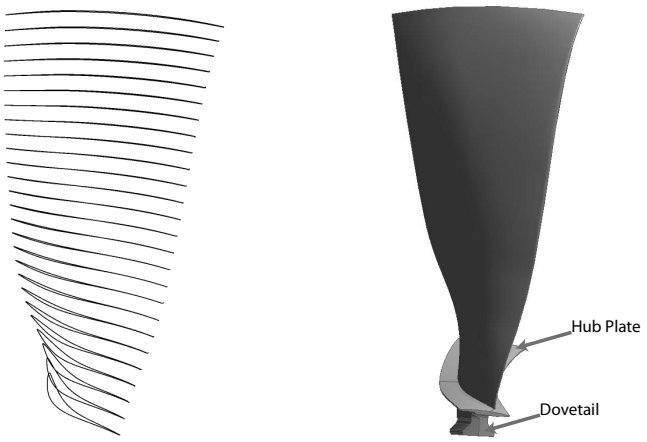


(a) Aerodynamic blade profiles.

(b) Original CAD model.

Figure 2.2: Aerodynamic blade profiles and the original CAD model for an undamaged blade.

Alignment of the aerodynamic and structural computational meshes at the wetted surface of the fan blade is essential for the accurate transfer of the aerodynamic loads and structural displacements during aeroelastic response calculations. Small geometric discrepancies between the blade profiles and the CAD model cause problems for aeroelastic coupling algorithms. To ensure alignment of the aerodynamic and structural geometries, a modified CAD model of the blade was constructed. The new CAD model is defined by

the aerodynamic blade profiles together with two-dimensional cross-sections of the blade dovetail. This method can also generate a new CAD model corresponding to a different blade geometry, such as a damaged blade, in a straightforward manner by modifying the aerodynamic blade profiles. The hub plate does not have a significant role in the structural response calculations and is neglected from the updated CAD model for convenience. Figure 2.3 depicts the new CAD models of an undamaged and a representative damaged blade constructed using the aerodynamic blade profiles.

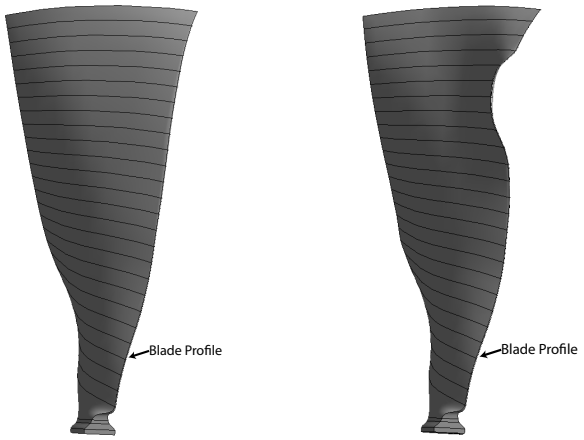


(a) Undamaged blade. (b) Damaged blade.

Figure 2.3: New CAD model of an undamaged and a damaged blade, defined by aerodynamic blade profiles.

## 2.1 Bird Strike Impact Analysis

The LS-DYNA code is employed to numerically simulate the bird impact and determine the bird damaged configuration considered in this study. The LS-DYNA code is a general purpose FEM code used for a variety of impact problems. The code has been extensively used to model bird strike problems and has proven itself a reliable tool for computing the damaged blade configurations [10, 16]. Details of the LS-DYNA code are provided

in LS-DYNA Theory Manual [60]. The LS-DYNA bird strike impact analysis described in this section was developed and validated at the sponsor organization, and the damaged bird configuration was provided for this study. The procedure followed for generating the bird-damaged fan geometry is briefly described in this section.

The LS-DYNA bird strike calculation is restricted to a subset of 5 blades, and the remaining fan blades are assumed to be undamaged by the bird strike event. The calculations are performed using a FE mesh of the fan blades and bird model. Figure 2.4 depicts a frontal view and isometric projection of the 5 fan blades and bird model used in the bird impact calculation. Each blade is cantilevered at the root such that the translational and rotational degrees of freedom of the blade root nodes are constrained. The fan material is assumed to be titanium and is modeled as an elasto-plastic material with a piecewise linear stress-strain relationship where the yield stress is dependent on the strain rate. The bird model takes the form of an ellipsoid, and a viscous material model is employed to capture the impact properties of a real bird.

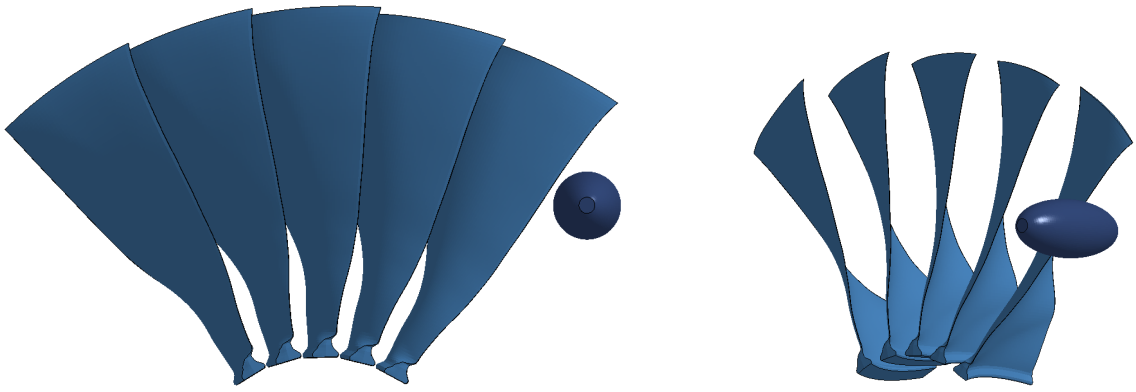

(a) Frontal view. (b) Isometric projection.

Figure 2.4: Fan blades and bird model for bird impact calculation (direction of rotation: clockwise).

The LS-DYNA bird strike simulation computes a typical bird strike experimental test sequence performed in vacuum. The test sequence consists of several steps: spin the fan stage at a specified engine rotational speed, fire a bird at the fan stage, continue to spin the engine until the transient response of the blades subsides, slow the fan stage to zero engine rotational speed. In this process, the rotating fan stage is referred to as "hot" and differs from the non-rotating "cold" fan stage due to centrifugal loads. Furthermore, the fan stage prior to bird strike is referred to as "undamaged" where as the fan stage in the post bird strike condition is referred to as "damaged".

The LS-DYNA calculation is performed in four separate steps: the prestress calculation, bird impact calculation, transient response calculation, and fan stage unload calculation:

1. Prestress calculation- centrifugal effects are introduced to obtain the hot, undamaged geometry and associated stress of the rotating blade.

2. Bird impact calculation- the time-dependent impact forces due to the bird model are applied to the structure and the resulting time-dependent blade response is calculated. The bird impact duration lasts until the bird "clears" the fan stage.

3. Transient response calculation- structural damping is introduced during the transient response calculation to suppress oscillations resulting from the bird strike and achieve a steady-state geometry for the damaged blades.

4. Fan stage unload calculation- the rotational effects are removed to yield the post bird strike damaged configuration for the non-rotating fan.

The bird strike conditions for the LS-DYNA analysis correspond to the single largest medium bird test in which a single 2.5 lb bird is ingested at take-off conditions with a strike

location of 70% blade span. Due to the large bird weight and outer span location, the damage sustained by the single largest medium bird test at these conditions is expected to have a significant influence on the aeroelastic behavior of the bird-damaged fan. The FE mesh of the damaged fan blades are depicted in Fig. 2.5(a), where the blades are numbered for convenience. The blade damage includes substantial leading edge deformation in all 5 blades as well as global bending and twist. Furthermore, the damage covers a significant portion of the blade span, with the largest deformation occurring for blade 2. Figure 2.5(b) depicts the CAD models of 5 undamaged blades (colored in blue) overlaid with the 5 damaged blades (colored in orange).

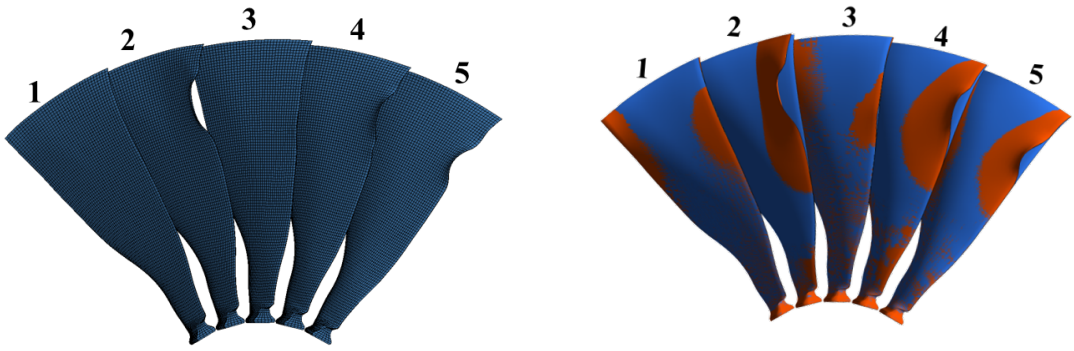


(a) FE mesh of the damaged fan blades.

(b) Comparison of damaged and undamaged blade geometries.

Figure 2.5: Bird damaged fan resulting from the bird-impact simulation (direction of rotation: clockwise).

To quantify the damaged sustained by the bird impact, the change in leading edge passage gaps and the cross-sectional twist angle are examined as a function of blade span. The percentage change in leading edge is calculated using Eq. 2.1, where $S_{LE}$ is the circumferential displacement of the leading edge. The cross-sectional twist angle is calculated using Eq. (2.2), where $\lambda$ and $\lambda_D$ are the angles between the straight line connecting the leading edge and trailing edge and the $z$-axis for the undamaged and damaged blade, respectively.

Figure 2.6 depicts $S_{LE}$, $\lambda$, and $\lambda_D$ for a representative damaged (red) and undamaged (green) blade profile at 75% span.

$$\%\Delta S_{LE} = \frac{S_{LE} N_b}{2\pi ||\mathbf{r}||} \tag{2.1}$$

$$\Delta\lambda = \lambda_D - \lambda \tag{2.2}$$

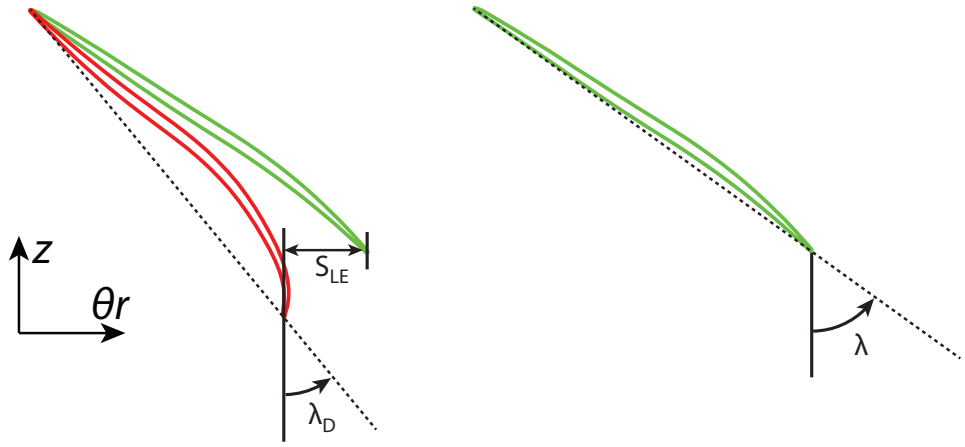


Figure 2.6: Representative damaged (red) and undamaged (green) blade profiles with passage gap and cross-sectional twist angle labeled.

Figures 2.7 and 2.8 provide the percent change in leading edge passage gaps and cross-sectional twist angle as a function of blade. A considerable change in the passage gap results from the bird impact, particularly for blade 2 where the passage gap decreases over 20%. The cross-sectional twist is also significantly affected, with the greatest twist angle exceeding 15° in magnitude for Blade 2. The significant increase in cross-sectional twist angle affects the local angle of attack of the fan blade and is expected to influence the shock structure and unsteady aerodynamic loading of the damaged fan.

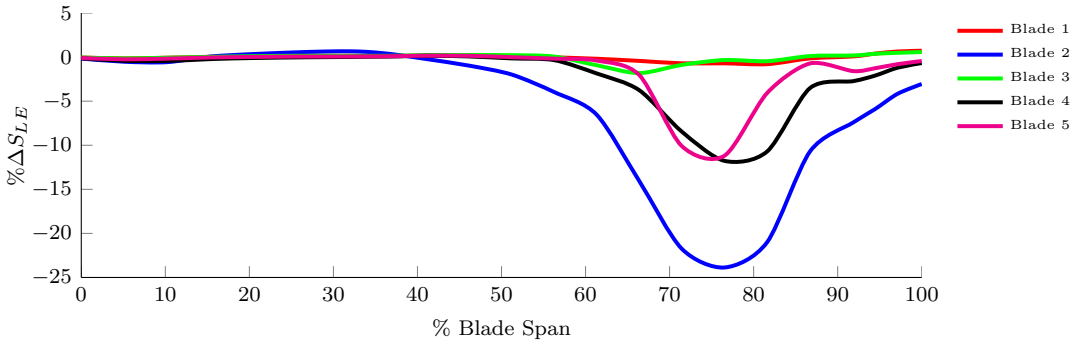


Figure 2.7: Normalized change in leading edge passage gap due to bird damage.

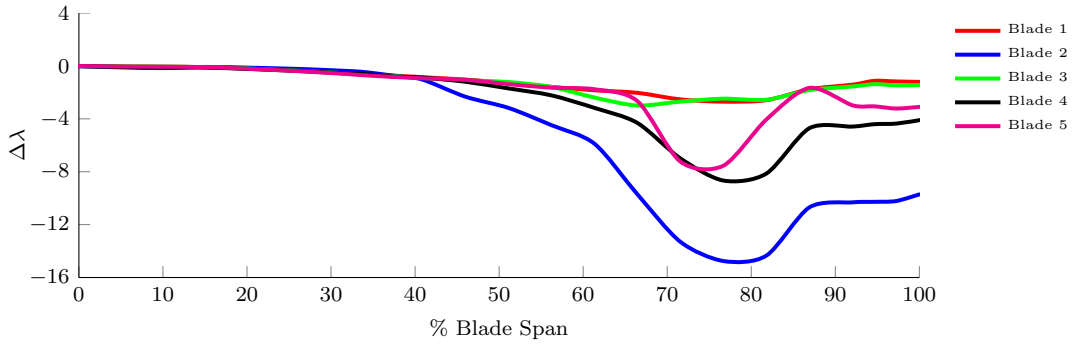


Figure 2.8: Cross-sectional twist angle due to bird damage.

## 2.2 Damaged Fan Geometry

Blade profiles corresponding to the damaged blades are needed to define the aerodynamic geometry and the CAD-based structural geometry of the fan. The FE mesh of the damaged blades from the LS-DYNA bird impact analysis contains a coarse resolution of the leading edge and trailing edge; therefore, it is not suitable for extracting the blade profiles directly from the FE mesh. Instead, an RBF-based interpolation scheme was developed to deform the blade profiles of an undamaged blade to coincide with the damaged geometry. This procedure employs a Radial Basis Function Network (RBFN) to interpolate the deformation from the LS-DYNA impact calculations to the undamaged blade profiles.

A RBFN consists of a linear combination of RBFs that are used to generate an inter-

polant of the deformation field. A RBF, $\phi$, is a scalar function whose value depends only on the distance from the evaluation point, $\mathbf{x}^e$, to the origin, such that $\phi = \phi(||\mathbf{x}^e||)$. Provided a set of $N_D$ driver points at which the deformation is known, the RBF interpolant of the deformation field is constructed in the form given by Eq. (2.3). The RBF fitting coefficients, $\mathbf{A}$, are uniquely determined by ensuring that the deformation evaluated with the RBF interpolant at the driver points is equal to the prescribed deformation, as given in Eq. (2.4). The RBF defined by $\phi(||\mathbf{x}^e||) = ||\mathbf{x}^e||$ is used, and the norm is evaluated as the Euclidean distance: $||\mathbf{x}|| = \sqrt{x^2 + y^2 + z^2}$.

$$\hat{\boldsymbol{\varsigma}}(\mathbf{x}^e) = \sum_{l=1}^{N_D} \mathrm{A}_l \phi(||\mathbf{x}^e - \mathbf{x}_l^d||) \tag{2.3}$$

$$\boldsymbol{\varsigma}_l(\mathbf{x}_m^d) = \hat{\boldsymbol{\varsigma}}(\mathbf{x}_m^d) = \sum_{l=1}^{N_D} \mathrm{A}_l \phi(||\mathbf{x}_m^d - \mathbf{x}_l^d||) \quad 1 \leq m \leq N_D \tag{2.4}$$

Equation (2.3) is used to construct the interpolant and map the deformation from the FE mesh of the damaged blades to the undamaged blade profiles. The FE nodes on the surface of an undamaged blade are chosen as the driver points, and the corresponding deformation vector is extracted from the LS-DYNA bird impact analysis. The RBF fitting coefficients, $\mathrm{A}_l$ are uniquely determined by ensuring that the deformation evaluated with the RBF interpolant at the driver points is equal to the prescribed deformation, as given in Eq. (2.4). A separate RBF interpolant is created for each damaged blade, and the deformation at each point on the corresponding undamaged blade profiles is evaluated using Eq. (2.3). The damaged blade profiles are then calculated by applying this deformation to the undamaged blade profiles. Figure 2.9 illustrates the procedure to calculate the damaged blade profiles

using RBF interpolation.

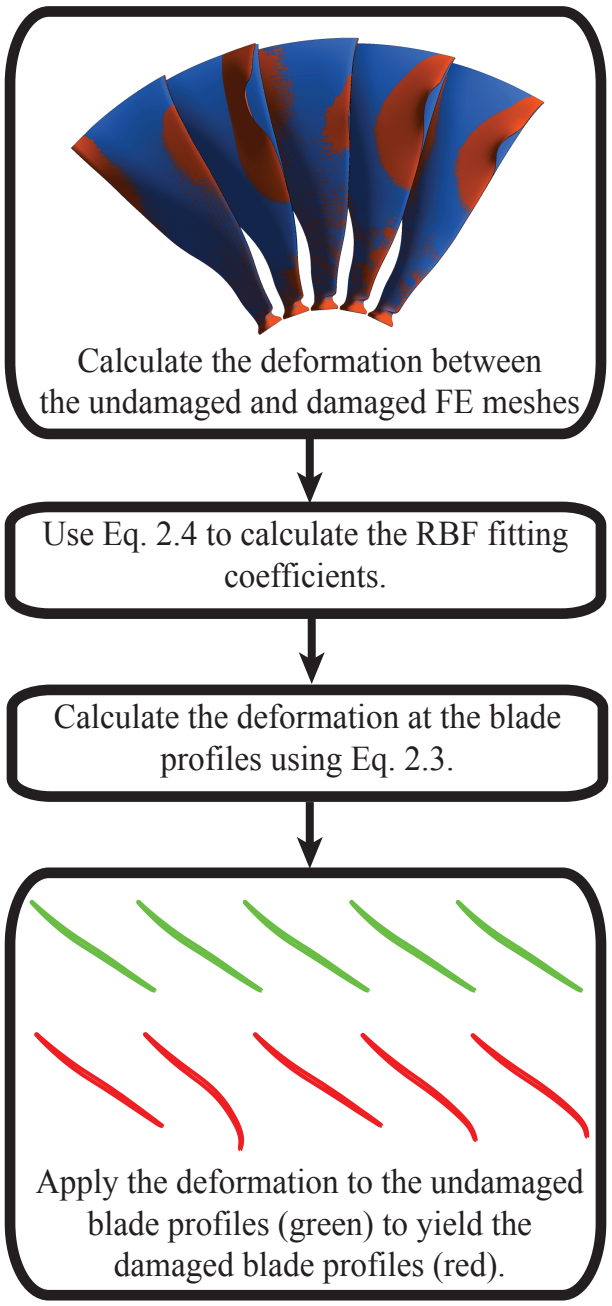


Figure 2.9: Flow chart of the RBF interpolation scheme used to calculate the damaged blade profiles.

Figure 2.10(a) depicts the 5 undamaged blade profiles at 75% span, Fig. 2.10(b) depicts the corresponding damaged blade profiles obtained with the RBF interpolation scheme, and Fig. 2.10(c) shows a comparison of the undamaged and damaged blade profiles. The

RBF interpolation scheme yields blade profiles that describe exactly the damaged geometry while retaining important aerodynamic properties of the blades such as leading edge and trailing edge curvature.

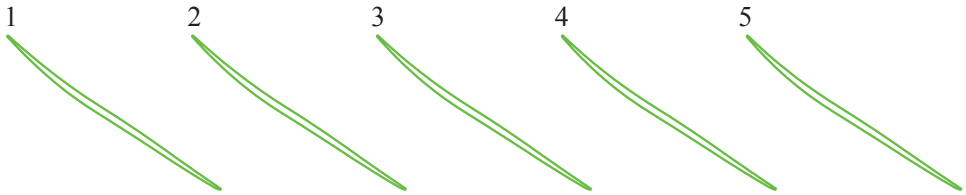


(a) Undamaged blade profiles at 75% span.

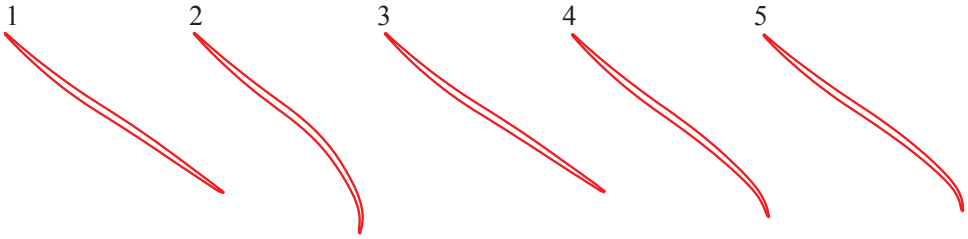


(b) Damaged blade profiles at 75% span.

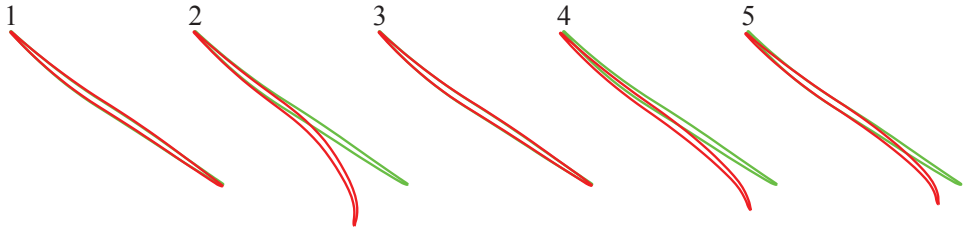


(c) Comparison of damaged and undamaged blade profiles at 75% span.

Figure 2.10: Blade profiles of undamaged and damaged fan blades at 75% span.

The aerodynamic and CAD geometries of the damaged blades are defined by the damaged blade profiles, as described previously. Figure 2.11 shows the CAD model of the damaged fan considered in this study, where the damaged blades are highlighted in orange and the blades are numbered. The procedure detailed in this chapter ensures the blade profiles that define the aerodynamic geometry coincide exactly with the CAD-based structural geometry, which is essential for the aeroelastic calculations performed in this study.

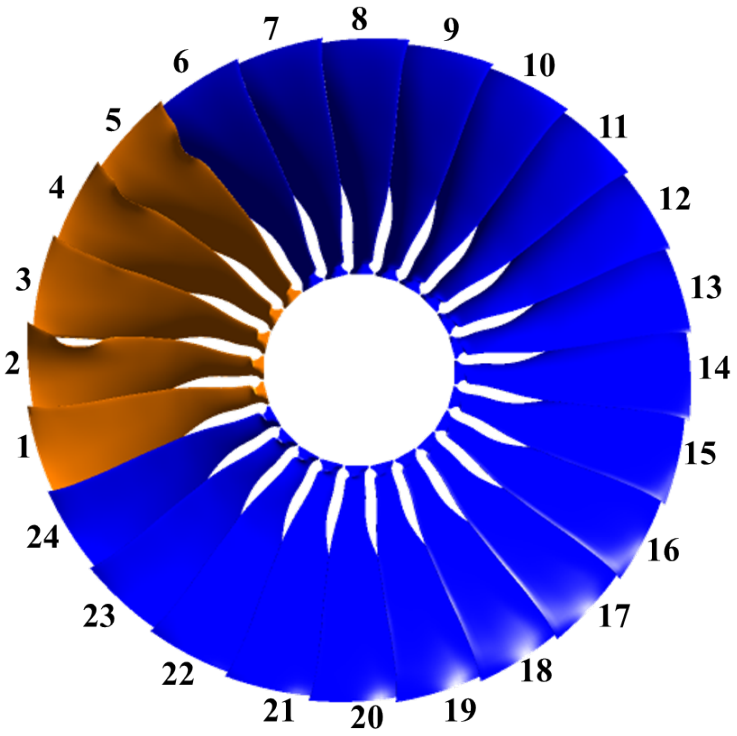


Figure 2.11: Bird-damaged fan with damaged blades highlighted in orange.

# CHAPTER 3

# CFD-Based Aerodynamic Model

A key component of the aeroelastic response calculation is an accurate representation of the unsteady aerodynamic loads. The aerodynamic model must represent a balance between accuracy in flow prediction and computational efficiency. Modern advances in computer processor speeds and parallelization have enabled numerical solutions of the equations that govern fluid dynamics of industrial scale problems to become practical. This chapter describes the RANS equations that are solved numerically to model the aerodynamic behavior of the bird-damaged fan. Implementation of ANSYS CFX, the commercially available RANS solver employed to perform the aerodynamic calculations in this study, is described. An innovative scheme developed in this thesis that automatically generates the CFD mesh of the damaged fan is also presented.

## 3.1 Governing Equations

The equations governing fluid dynamics describe the conservation of mass, momentum, and energy as expressed in Eqs. (3.1)-(3.3) [61, 62]. Equations (3.1)-(3.3) are denoted the continuity equation, the momentum equation, and the energy equation, respectively. These equations accurately represent time-dependent laminar and turbulent flows in the

subsonic, transonic, or supersonic regime and are suitable for modeling the complex flow environment present in turbofans.

$$\frac{\partial \rho}{\partial t} + \frac{\partial}{\partial \mathrm{x}_i}\left(\rho \mathrm{V}_i\right) = 0 \tag{3.1}$$

$$\frac{\partial}{\partial t}(\rho \mathrm{V}_i) + \frac{\partial}{\partial \mathrm{x}_j}\left(\rho \mathrm{V}_i \mathrm{V}_j\right) + \frac{\partial P}{\partial \mathrm{x}_i} = \frac{\partial \tau_{ji}}{\partial \mathrm{x}_j} + \mathrm{S}_{M_i} \tag{3.2}$$

$$\begin{aligned} \frac{\partial}{\partial t}\left[\rho\left(h + \frac{1}{2}\mathrm{V}_i\mathrm{V}_i\right) - P\right] &+ \frac{\partial}{\partial \mathrm{x}_j}\left[\rho \mathrm{V}_j\left(h + \frac{1}{2}\mathrm{V}_i\mathrm{V}_i\right)\right] \\ &= \frac{\partial}{\partial \mathrm{x}_j}\left(\mathrm{V}_i \tau_{ij}\right) - \frac{\partial \mathrm{q}_j}{\partial \mathrm{x}_j} \end{aligned} \tag{3.3}$$

For a Newtonian fluid, the viscous stress is assumed to vary linearly with strain rate, resulting in the expression for the viscous stress tensor, $\boldsymbol{\tau}$, given by Eq. (3.4). The bulk viscosity, $\zeta$, of a monatomic gas is related to the dynamic viscosity, $\mu$, using Eq. (3.5). The specific enthalpy, $h$, is a measure of the total energy of the fluid per unit mass and is expressed as the sum of the internal energy, $e$, and the pressure work, as given by Eq. (3.6). The heat-flux vector, $\mathbf{q}$, is expressed using Fourier's law as given in Eq. (3.7), where $\kappa$ is the thermal conductivity for the specific fluid.

$$\tau_{ij} = \mu\left(\frac{\partial \mathrm{V}_i}{\partial \mathrm{x}_j} + \frac{\partial \mathrm{V}_j}{\partial \mathrm{x}_i}\right) + \zeta \frac{\partial \mathrm{V}_k}{\partial \mathrm{x}_k}\delta_{ij} \tag{3.4}$$

$$\zeta = -\frac{2}{3}\mu \tag{3.5}$$

$$h = e + \frac{P}{\rho} \tag{3.6}$$

$$\mathrm{q}_j = -\kappa \frac{\partial T}{\partial \mathrm{x}_j} \tag{3.7}$$

For an ideal and calorically perfect gas, the specific internal energy, temperature, pressure, and density are related using Eqs. (3.8) and (3.9). The dynamic viscosity is related to the temperature by Sutherland's formula expressed in Eq. (3.10). In Eq. (3.10), $\mu_0$ is the reference viscosity, $T_0$ is the reference temperature, and $C$ is Sutherland's constant, all of which are specified for the fluid of interest. The heat-flux vector can also be expressed in terms of $\mu$, $h$, and the laminar Prandtl number, $Pr$ defined by Eq. (3.12).

$$P = \rho R T \tag{3.8}$$

$$e = C_V T = C_V \frac{P}{\rho R} = \frac{C_P}{\gamma_f} T \tag{3.9}$$

$$\mu = \mu_0 \frac{T_0 + C}{T + C} \left( \frac{T}{T_0} \right)^{3/2} \tag{3.10}$$

$$\mathrm{q}_j = -\frac{\mu}{Pr} \frac{\partial h}{\partial \mathrm{x}_j} \tag{3.11}$$

$$Pr = \frac{C_P \mu}{\kappa} \tag{3.12}$$

### 3.1.1 Introduction of the RANS Equations

Numerical solution of Eqs. (3.1)-(3.3) is obtained through spatially and temporally discretization. The spatial and temporal discretization necessary to accurately capture turbulent flow is of higher resolution than can be solved efficiently for large fluid domains. However, the fluid time-scale of interest is often significantly larger than the turbulent fluctuations. Therefore, turbulent flow can be assumed to exhibit time-averaged characteristics with an additional time-dependent component used to account for the impact of flow fluctuations on the mean flow field. Since time-averaged flow quantities are typically of primary interest, the fluid equations can be time-averaged to obtain the RANS equations in density-weighted variables. The presentation of the RANS equations and the $k - \epsilon$ turbulence model provided below follow from Refs. [61, 63], which provide a useful treatment of the RANS equations and turbulence modeling.

The RANS equations, expressed in Eqs. (3.13)-(3.15), mathematically represent the mean flow behavior and significantly reduce the computer cost required to model numerically the turbulent flow [61–63]. The RANS equations take the form of the original governing equations expressed in mean flow variables with several additional terms: the symmetric Reynolds stress tensor, $\tau_{T_{ij}}$; the kinetic energy of the turbulence fluctuations, $k$; and the Reynolds heat flux, $\mathrm{q}_{T_j}$. In order to provide closure to the system of equations, turbulence models have been developed to associate these quantities to the remaining mean flow

variables.

$$\frac{\partial \rho}{\partial t} + \frac{\partial}{\partial \mathrm{x}_i}(\rho \mathrm{V}_i) = 0 \tag{3.13}$$

$$\frac{\partial}{\partial t}(\rho \mathrm{V}_i) + \frac{\partial}{\partial \mathrm{x}_j}(\rho \mathrm{V}_j \mathrm{V}_i) = -\frac{\partial P}{\partial \mathrm{x}_i} + \frac{\partial}{\partial \mathrm{x}_j}\left[\tau_{ij} + \tau_{T_{ij}}\right] + \mathrm{S}_{M_i} \tag{3.14}$$

$$\begin{aligned} \frac{\partial}{\partial t}\left[\rho\left(h + \frac{\mathrm{V}_i \mathrm{V}_i}{2} + k\right) - P\right] &+ \frac{\partial}{\partial \mathrm{x}_j}\left[\rho \mathrm{V}_j \left(h + \frac{\mathrm{V}_i \mathrm{V}_i}{2} + k\right)\right] \\ &= -\frac{\partial}{\partial \mathrm{x}_j}\left(\mathrm{q}_j + \mathrm{q}_{T_j}\right) + \frac{\partial}{\partial \mathrm{x}_j}\left[\mathrm{V}_i\left(\tau_{ij} + \tau_{T_{ij}}\right)\right] \end{aligned} \tag{3.15}$$

### 3.1.2 $k - \epsilon$ Turbulence Model

Turbulence models are employed to provide closure to the RANS equations by prescribing a means to compute the Reynolds stress tensor and the Reynolds heat flux from the mean flow variables. A category of turbulence models, termed eddy viscosity models, utilize the Boussinesq approximation that relates the Reynolds stress to the mean strain-rate tensor and the turbulent viscosity, $\mu_T$, as given in Eq. (3.16). Furthermore, eddy viscosity models assume the Reynolds heat flux is proportional to the mean temperature gradient, as given in Eq. (3.17) [62, 63].

$$\tau_{T_{ij}} = \mu_T \left(\frac{\partial \mathrm{V}_i}{\partial \mathrm{x}_j} + \frac{\partial \mathrm{V}_j}{\partial \mathrm{x}_i}\right) - \frac{2}{3}\left(\rho k + \mu_t \frac{\partial \mathrm{V}_k}{\partial x_k}\right)\delta_{ij} \tag{3.16}$$

$$q_{T_i} = -\frac{\mu_T C_P}{Pr_T}\frac{\partial T}{\partial \mathrm{x}_j} = -\Gamma_T \frac{\partial h}{\partial \mathrm{x}_j} \tag{3.17}$$

In Eqs. (3.16) and (3.17), the turbulent viscosity must be modeled, and $Pr_T$ is the turbulent Prandtl number defined as the ratio between momentum eddy diffusivity and heat transfer eddy diffusivity. Therefore, the ratio $\mu_T/Pr_T$ can be defined as the eddy diffusivity, denoted by $\Gamma_T$.

Eddy viscosity turbulence models are often categorized by the number of differential transport equations required to provide closure to the RANS equations. Algebraic (zero-equation) models, such as the Baldwin-Lomax model (Ref. [64]), are very simple turbulence models that directly calculate turbulent viscosity from the mean flow quantities and are straightforward to implement. However, they rely on a turbulent mixing length scale and only work well with flows for which they have been previously tuned. Therefore, algebraic models are considered to be incomplete and are only useful for preliminary studies. One-equation models, such as the Spalart-Allmaras model [65], are based on more accurate physical approximations of the turbulence viscosity, including processes such as convection, diffusion, production, etc.. However, such models are also incomplete. The turbulence length scale has to be related to a user-specified flow dimension. Two-equation models, such as the $k-\epsilon$ and $k-\omega$ models, are more complete by providing the computation of the kinetic energy of turbulence fluctuations and the turbulence length scale. Two-equation models represent the simplest complete turbulence models in the sense of more accurately representing the fluctuating velocity field.

The $k-\epsilon$ turbulence model is an industry standard eddy viscosity model in which the turbulent viscosity is modeled in terms of the turbulence kinetic energy, $k$, and the turbulence dissipation rate, $\epsilon$. The $k-\epsilon$ turbulence model is based on the eddy viscosity concept where $\mu_T$ is assumed to be related to $k$ and $\epsilon$ by Eq. (3.18).

$$\mu_T = C_\mu \rho \frac{k^2}{\epsilon} \tag{3.18}$$

In Eq. (3.18), $C_\mu$ is a constant, the value of which is given in Table 3.1, and the values of $k$ and $\epsilon$ are determined by solution of the differential transport equations for turbulence kinetic energy and turbulence dissipation rate given by Eqs. (3.19) and (3.20), respectively [62]. Eqs. (3.19) and (3.20) includes several constants, namely $C_{\epsilon 1}$, $C_{\epsilon 2}$, $C_\mu$, $\sigma_k$, and $\sigma_\epsilon$, whose values are given in Table 3.1.

$$\frac{\partial}{\partial t}(\rho k) + \frac{\partial}{\partial \mathrm{x}_j}(\rho \mathrm{V}_i k) = \tau_{T_{ij}} \frac{\partial \mathrm{V}_i}{\partial \mathrm{x}_j} - \rho\epsilon + \frac{\partial}{\partial \mathrm{x}_j}\left[\mu + \frac{\mu_T}{\sigma_k}\frac{\partial k}{\partial \mathrm{x}_j}\right] \tag{3.19}$$

$$\frac{\partial}{\partial t}(\rho \epsilon) + \frac{\partial}{\partial \mathrm{x}_j}(\rho \mathrm{V}_i \epsilon) = C_{\epsilon 1}\frac{\epsilon}{k}\tau_{T_{ij}} \frac{\partial \mathrm{V}_i}{\partial \mathrm{x}_j} - C_{\epsilon 2}\rho\frac{\epsilon^2}{k} + \frac{\partial}{\partial \mathrm{x}_j}\left[\mu + \frac{\mu_T}{\sigma_k}\frac{\partial \epsilon}{\partial \mathrm{x}_j}\right] \tag{3.20}$$

Table 3.1: Constants for the $k - \epsilon$ turbulence model.

| Constant | Value |
|---|---|
| $C_{\epsilon 1}$ | 1.44 |
| $C_{\epsilon 2}$ | 1.92 |
| $C_\mu$ | 0.09 |
| $\sigma_k$ | 1.0 |
| $\sigma_\epsilon$ | 1.3 |

## 3.2 Description of the ANSYS CFX Solver

The ANSYS CFX code is a commercial, high performance, three-dimensional solver for the RANS equations. The ANSYS CFX code uses a finite volume numerical approach that yields a near second-order accurate spatial discretization. A second-order accurate back-

ward Euler time-integration scheme is used for the unsteady calculations. Furthermore, the k-$\epsilon$ turbulence model is used with scalable wall functions to resolve the near-wall boundary layer, and the fluid is assumed to be ideal and calorically perfect. The ANSYS CFX code also interfaces with the ANSYS Mechanical APDL structural solver for Fluid Structure Interaction (FSI) calculations by employing a moving mesh capability. The ANSYS CFX solver is briefly described in this section. A more detailed description of ANSYS CFX is provided in Ref. [62].

### 3.2.1 The RANS Equations in the Rotating Frame

The RANS equations in ANSYS CFX, given by (3.13)-(3.15), are solved in a rotating Cartesian reference frame that is fixed to the rotating blades. The stationary velocity $\mathbf{V}$ in Eqs. (3.13)-(3.15) is replaced by the velocity relative to the rotating frame, $\mathbf{V}^R$, defined by Eq. (3.21). Body force terms are added to the right hand side of Eq. (3.14) to account for the Coriolis and centrifugal effects. The Coriolis and centrifugal terms in ANSYS CFX are given by Eq. (3.22) and Eq. (3.23), respectively.

$$\mathbf{V}^R = \mathbf{V} - \boldsymbol{\Omega} \times \mathbf{r} \tag{3.21}$$

$$\mathbf{S}_{\text{Cor}} = -2\rho\boldsymbol{\Omega} \times \mathbf{V}^R \tag{3.22}$$

$$\mathbf{S}_{\text{cfg}} = -\rho\boldsymbol{\Omega} \times (\boldsymbol{\Omega} \times \mathbf{r}) \tag{3.23}$$

### 3.2.2 Numerical Discretization

In the ANSYS CFX code, Eqs. (3.13)-(3.15) are discretized using an element-based finite volume numerical approach that is near second-order accurate. The fluid domain is spatially discretized by employing a CFD mesh composed of nodes and elements. The conservation of mass, momentum, and energy are enforced within control volumes that are constructed around each node of the CFD mesh. The solution variables are stored at the nodes. The portion of a CFD mesh element within a control volume is referred to as an element sector. The number of element sectors comprising a control volume is equal to the number of elements that share the surrounded node. Figure 3.1 depicts a representative two-dimensional CFD mesh and the control volume corresponding to the center node. The control volume is shaded in gray and is composed of four element sectors. A representative element sector is enclosed in red and the corresponding element to which it belongs is enclosed in green.

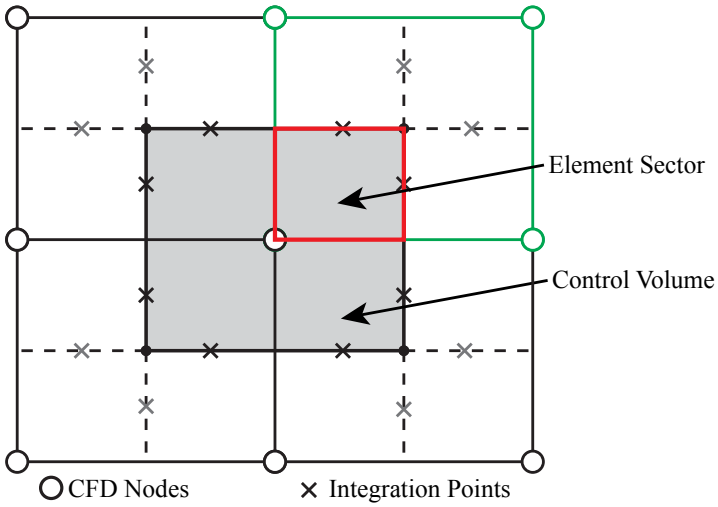


Figure 3.1: Representative computational control volume.

The governing RANS equations given by Eqs. (3.13)-(3.15) are integrated over each

control volume of the CFD mesh. The volume integrals represent contributions from sources within the control volume, and the surface integral terms represent contributions from fluxes through the control volume surface. The volume integrals are evaluated by averaging the contributions from each element sector that comprise the control volume. Surface integration is performed by summing the surface fluxes calculated at the integration points for each element sector of the control volume. The numerical discretization implemented in ANSYS CFX is demonstrated for the conservation equation of a passive scalar, $\varphi$, given by Eq. (3.24). Equation (3.25) illustrates the discretized form of Eq. (3.24) where a first-order backward Euler time-integration scheme with a time-step of $\Delta t_f$ is used for simplicity.

$$\frac{d}{dt}\int_{V_f} \rho\varphi dV_f + \underbrace{\int_{S_f} \mathrm{V}_j \varphi \mathrm{n}_{a_j} dS_f}_{\text{Advection Term}} = \underbrace{\int_{S_f} \Gamma_{\text{eff}} \left(\frac{\partial \varphi}{\partial \mathrm{x}_j}\right) \mathrm{n}_{a_j} dS_f}_{\text{Diffusion Term}} \tag{3.24}$$

$$V_f \left(\frac{(\rho\varphi) - (\rho^{\varphi})^0}{\Delta t_f}\right) + \underbrace{\sum_{ip} (\rho \mathrm{V}_j \mathrm{n}_{a_j})_{ip} \varphi_{ip}}_{\text{Advection Term}} = \underbrace{\sum_{ip} \left(\Gamma_{\text{eff}} \frac{\partial \varphi}{\partial \mathrm{x}_j} \mathrm{n}_{a_j}\right)_{ip}}_{\text{Diffusion Term}} \tag{3.25}$$

Shape functions are employed for evaluating the solution variable fields or solution variable gradients at the integration points, denoted by $ip$. Standard tri-linear finite-element shape functions are employed in which the variation of a representative flow variable, $\varphi$, within an element is given by Eq. (3.26).

$$\varphi = \sum_{i=1}^{N_{Nodes}} N_i \varphi_i \tag{3.26}$$

For the hexahedral CFD element shown in Fig. 3.2, $N_{Nodes} = 8$, $\varphi_i$ is the value of

$\varphi$ at node $i$, and $N_1 \ldots N_8$ are the trilinear basis functions expressed in the local element coordinate system $< \xi, \eta, \zeta >$.

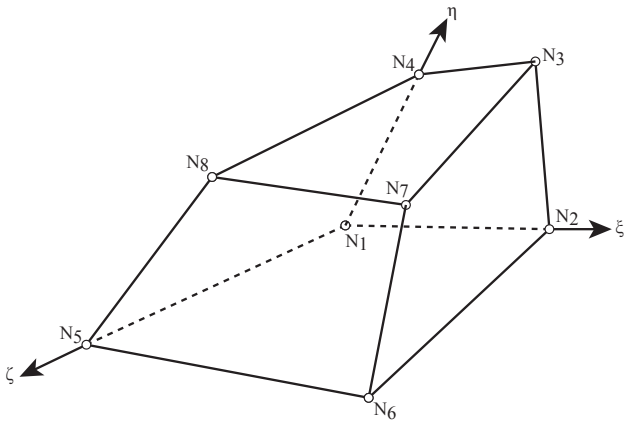


Figure 3.2: CFD element with local element coordinate system.

#### 3.2.2.1 Advection Scheme

The advection terms in Eq. (3.25) are evaluated in ANSYS CFX using the stored values of $\varphi$ at neighboring nodes, as given by in Eq. (3.27).

$$\varphi_{ip} = \varphi_{up} + \vartheta \nabla \varphi \cdot \mathbf{r}_{up} \tag{3.27}$$

In Eq. (3.27), $\varphi_{ip}$ is the approximated value at an integration point, $\varphi_{up}$ is the value at the upwind node, and $\mathbf{r}_{up}$ is the position vector from the upwind node to the integration point. Particular choices of $\vartheta$ and $\nabla\varphi$ yield different numerical schemes available to discretize the advection term in ANSYS CFX. The first-order Upwind Difference Scheme is obtained by setting $\vartheta = 0$ and it is numerically robust. However, the associated discretization errors can introduce numerical diffusion that tends to smooth out flow variables in regions of steep spatial gradients. The second-order Central Difference Scheme is obtained by setting

$\vartheta = 1$ and $\nabla\varphi$ equal to the variable gradient evaluated at the local element and is equivalent to the interpolation given in Eq. (3.26) when evaluated at the integration point. The Central Difference Scheme may result in non-physical oscillations of the flow variable near steep spatial gradients.

A high-resolution advection scheme that utilizes a nonlinear algorithm for calculating the value of $\vartheta$ based on the work of Barth and Jespersen (Ref. [66]) is also available in ANSYS CFX. In this algorithm, $\varphi_{min}$ and $\varphi_{max}$ are computed using a stencil of neighboring nodes, and the value of $\vartheta$ is chosen such that $\varphi_{ip}$ calculated by Eq. (3.27) is within the bounds set by $\varphi_{min}$ and $\varphi_{max}$. The value of $\vartheta$ is constrained so as not to exceed 1. In flow regions with small gradients, the value of $\vartheta$ will be close to 1 producing improved second-order accuracy. In regions where the flow variable gradients are steep, $\vartheta$ will be closer to 0 to avoid non-physical oscillations. In one-dimension, this high-resolution scheme is equivalent to the Total Variation Diminishing scheme [67]. The high-resolution advection scheme is implemented in this study.

#### 3.2.2.2 Diffusion Scheme

The tri-linear element shape functions, $N_1 \ldots N_8$, are employed for evaluating spatial derivatives in the diffusion term in Eq. (3.25). The spatial derivative of $\varphi$ with respect to $x$ at a given integration point is given by Eq. (3.28).

$$\left.\frac{\partial\varphi}{\partial x}\right|_{ip} = \sum_{i=1}^{N_{Nodes}} \left.\frac{\partial N_i}{\partial x}\right|_{ip} \varphi_i \tag{3.28}$$

In Eq. (3.28), $\varphi_i$ is the value of $\varphi$ evaluated at node $i$ of the local element. The shape function spatial derivatives in Eq. (3.28) are evaluated at the element integration points.

The spatial derivatives of the shape functions with respect to the global coordinates system $(x, y, z)$ can be expressed in terms of derivatives in the local element coordinate system $< \xi, \eta, \zeta >$ by way of the Jacobian transformation matrix, as shown in Eq. (3.29).

$$\begin{bmatrix} \frac{\partial N_i}{\partial x} \\ \frac{\partial N_i}{\partial y} \\ \frac{\partial N_i}{\partial z} \end{bmatrix} = \begin{bmatrix} \frac{\partial x}{\partial \xi} & \frac{\partial y}{\partial \xi} & \frac{\partial z}{\partial \xi} \\ \frac{\partial x}{\partial \eta} & \frac{\partial y}{\partial \eta} & \frac{\partial z}{\partial \eta} \\ \frac{\partial x}{\partial \zeta} & \frac{\partial y}{\partial \zeta} & \frac{\partial z}{\partial \zeta} \end{bmatrix}^{-1} \begin{bmatrix} \frac{\partial N}{\partial \xi} \\ \frac{\partial N}{\partial \eta} \\ \frac{\partial N}{\partial \zeta} \end{bmatrix} \tag{3.29}$$

#### 3.2.2.3 Time-Stepping Scheme

For control volumes that do not deform in time, the discretized time derivative for the $n^{th}$ time step is given by Eq. (3.30), where $\Delta t_f$ is the time-step and the superscripts $n + \frac{1}{2}$ and $n - \frac{1}{2}$ denote values at the start and end of the time-step.

$$\frac{d}{dt} \int_{V_f} \rho\varphi dV_f \approx V_f \frac{(\rho\varphi)^{n+\frac{1}{2}} - (\rho\varphi)^{n-\frac{1}{2}}}{\Delta t_f} \tag{3.30}$$

The second-order backward Euler scheme is utilized for unsteady aerodynamic calculations. The start and end values are approximated using values at the two previous time steps, denoted by $0$ and $00$, and the current time step, as given in Eqs. (3.31)-(3.32). Introduction of these expressions into Eq. (3.30) yields the discretization given in Eq. (3.33).

$$(\rho\varphi)^{n-\frac{1}{2}} = (\rho\varphi)^{0} + \frac{1}{2}((\rho\varphi)^{0} - (\rho\varphi)^{00}) \tag{3.31}$$

$$(\rho\varphi)^{n+\frac{1}{2}} = (\rho\varphi) + \frac{1}{2}((\rho\varphi) - (\rho\varphi)^{0}) \tag{3.32}$$

$$\frac{d}{dt}\int_{V_f}\rho\varphi dV_f = V_f\frac{1}{\Delta t_f}\left(\frac{3}{2}(\rho\varphi) - 2(\rho\varphi)^0 + \frac{1}{2}(\rho\varphi)^{00}\right) \tag{3.33}$$

For steady calculations, pseudo time-stepping is used to artificially time-march the solution to convergence using the first-order backward Euler scheme. The start and end values are approximated using values at the previous time step, denoted by $0$, and the current time step. The resulting discretization is given by Eq. (3.34).

$$\frac{d}{dt}\int_{V_f}\rho\varphi dV_f = V_f\frac{\rho\varphi - (\rho\varphi)^0}{\Delta t_f} \tag{3.34}$$

### 3.2.3 Numerical Treatment of the Boundary Layer Flow

In the vicinity of a wall, the no-slip boundary condition introduces strong gradients in the flow and viscous effects dominate. Proper representation of viscous effects at the wall and resolution of the rapid variation of flow variables near the wall in a numerical solution presents difficulties. The near-wall boundary layer region can be subdivided into two layers: the innermost viscous sublayer and the outer logarithmic layer. Within the viscous sublayer, the flow is predominantly laminar and viscosity dominates momentum and heat transfer. In contrast, turbulence effects dominate momentum and heat transfer in the logarithmic layer.

To capture the rapid flow variations occurring near the boundary, a fine CFD mesh resolution is required for stability of the numerical solution and accuracy of the flow representation. A fine mesh resolution permits a direct integration at the wall the boundary layer. However, the computational demands of the numerical solution can be significant. The wall function method available in ANSYS CFX is a suitable alternative to wall inte-

gration. The wall function method is based on the "law of the wall" that assumes that the mean velocity of a turbulent flow at a point near a wall is proportional to the logarithmic distance of that point to the wall. The wall function method approach utilizes empirical formulas to impose flow conditions near the wall without the need to resolve the boundary layer with a fine CFD mesh.

When using the wall function method, the near wall tangential velocity profile, $V^+$, is related to the wall shear stress, $\tau_w$ by means of the logarithmic relation given in Eq. (3.35). The unknown tangent velocity at a distance $\Delta y$ from the wall, $V_t$, and the friction velocity, $V_\tau$, are given by Eq. (3.37), where $y^+$ represents the dimensionless distance from the wall. The von Karman constant, $\kappa_w$ is set to be $\approx 0.51$ based on experiments, and the log-layer constant $C_w$ is set to $5.2$ for smooth walls. Scalable wall functions are implemented in ANSYS CFX when the CFD mesh near the wall is not sufficiently fine, typically when the $y^+$ value of the node closest to the wall exceeds 2.

$$V^+ = \frac{V_t}{V_\tau} = \frac{1}{\kappa_w} \ln\left(y^+\right) + C_w \tag{3.35}$$

$$y^+ = \frac{\rho \Delta y V_\tau}{\mu} \tag{3.36}$$

$$V_\tau = \sqrt{\frac{\tau_w}{\rho}} \tag{3.37}$$

## 3.3 Implementation of ANSYS CFX For Fan Stage Computations

The computational domain for the CFD calculations consists of an isolated fan stage, which is suitable for prediction of the performance characteristics and unsteady aerodynamic behavior of a bird-damaged fan. The fan stage begins downstream of the engine inlet, extends into the bypass duct and core duct, and includes a set of fan blades, a rotating hub, a stationary shroud, and a stationary splitter, as shown in Fig. 3.3. The fan stage geometry is given in cylindrical coordinates $< r, \theta, z >$. The hub, shroud, and splitter geometries are defined by two-dimensional curves in the $r$-$z$ plane, and the three-dimension hub, shroud, and splitter surfaces are obtained by full revolution of these curves about the engine centerline. The surfaces connecting the edges of the hub, shroud, and splitter define the inflow, bypass duct outflow, and core duct outflow boundaries of the computational domain. A clearance between the blade tip and shroud is specified to accurately account for the influence of the tip gap on flow losses and shock structure.

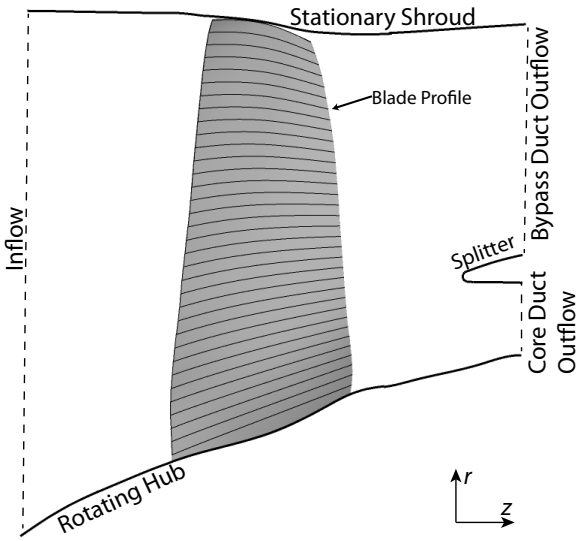


Figure 3.3: Meridional cross-section of the fan stage computational domain.

The computational domain consists of three sub-domains: the inlet, the passage, and the outlet, as depicted in Fig. 3.4(a) for a single blade passage of an undamaged fan and Fig. 3.4(b) for the full wheel. The full wheel computational domain consists of $N_b$ single blade passages copied and rotated about the engine centerline. The inlet sub-domain includes the downstream portion of the engine inlet nacelle and the engine nose cone. The passage sub-domain surrounds the fan blades, and the outlet sub-domain begins just downstream of the blade, extends into the bypass duct and core duct, and includes the upstream portion of the splitter. For an undamaged fan, radial symmetry is exploited to reduce the computational domain. However, bird-damage destroys this symmetry and the whole-wheel fan stage must be modeled.

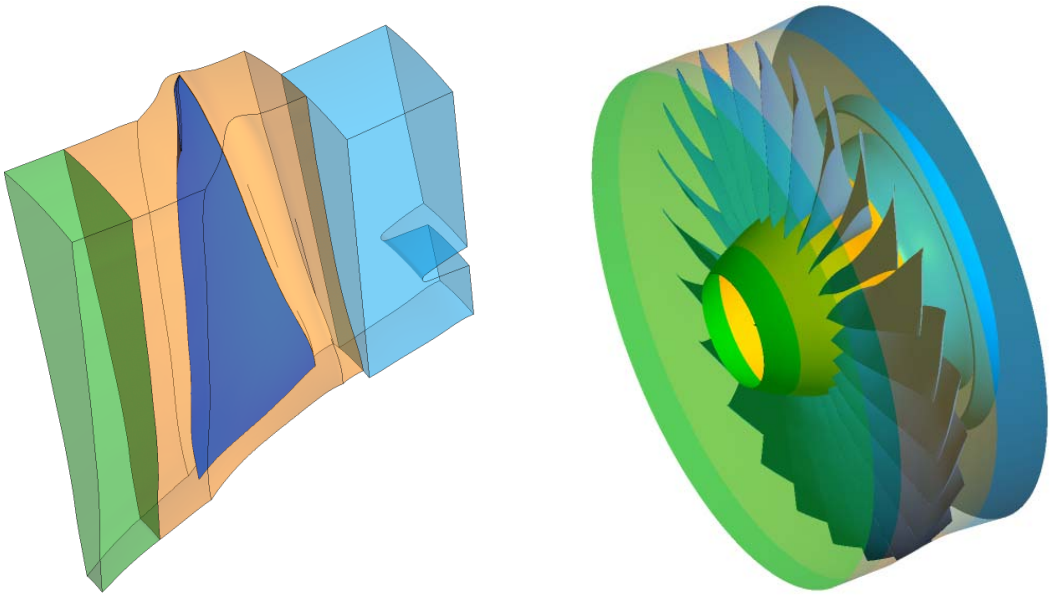

(a) Single blade passage computational domain.

(b) Full wheel computational domain.

Figure 3.4: Fan stage computational domains: inlet (green), passage (orange), outlet (blue).

### 3.3.1 Fluid Properties Prescribed in ANSYS CFX

Solution of Eqs. (3.13)-(3.14) requires specification of several flow properties. Table 3.2 provides the flow properties used in this study, where the fluid corresponds to air and is modeled as an ideal, calorically perfect gas.

Table 3.2: Flow properties for the CFD calculations.

| Fluid Property | Variable | Quantity |
|---|---|---|
| Sutherland's Constant | $C$ | 216 [R] |
| Specific heat at constant volume | $C_V$ | 4290 [ft lbf slug$^{-1}$ R$^{-1}$] |
| Specific heat at constant pressure | $C_P$ | 6006 [ft lbf slug-1 R-1] |
| Ideal gas constant | $R$ | 15783.5 [lb in$^1$ s$^{-2}$ R$^{-1}$ mol$^{-1}$] |
| Sutherland's reference temperature | $T_0$ | 524.07 [R] |
| Ratio of specific heats | $\gamma_f$ | 1.4 |
| Turbulent Prandtl number | $\mathrm{Pr}_T$ | 0.9 |
| Thermal conductivity | $\kappa$ | 3.25973$\times 10^{-3}$ [lbf s$^{-1}$ R$^{-1}$] |
| Sutherland's reference viscosity | $\mu_0$ | 2.64984$\times 10^{-9}$ [lbf in$^{-2}$ s] |

### 3.3.2 Boundary Conditions

Boundary conditions prescribe the aerodynamic properties of the flow on the external surfaces of the computational domain and provide closure to the RANS equations. Proper specification of the boundary conditions is essential for accurate representation of a fan operating in a complete engine using a CFD model of an isolated fan stage. The boundary conditions enforced in this study aim to simulate the behavior of the fan stage installed in a test stand mounted engine operating at standard day +27°F freestream conditions where the freestream Mach number (flight Mach Number) is zero. The engine rotational speed corresponds to the first three throttle settings on the skyline chart depict in Fig. 1.2: 100%, 75%, 60%. Table 3.3 provides the freestream conditions and engine rotational speed for the 100%, 75%, and 60% throttle settings conditions.

Table 3.3: Freestream conditions and engine rotational speed for the 100%, 75%, and 60% throttle settings conditions.

| Throttle Setting | 100% | 75% | 60% |
|---|---|---|---|
| Total Temperature | 545.7 [R] | 545.7 [R] | 545.7 [R] |
| Total Pressure | 14.7 [psi] | 14.7 [psi] | 14.7 [psi] |
| Flight Mach Number | 0 | 0 | 0 |
| Engine Rotation Speed | 5894.7 [RPM] | 5260.2 [RPM] | 4841.7 [RPM] |

At the domain inflow, the radial distributions of total pressure and flow direction are enforced to provide boundary information for the conservation of mass and momentum equations. The total pressure distribution normalized by freestream reference pressure is depicted in Fig. 3.5(a) and includes flow losses due to the upstream engine inlet nacelle. The incoming flow angle relative to the engine centerline is depicted in Fig. 3.5(b). The circumferential component of the flow direction is small and negligible. A constant total temperature equal to the freestream total temperature is specified at the inflow to provide boundary information for the conservation of energy equation. Finally, the turbulence kinetic energy, $k$, and turbulence dissipation, $\epsilon$, are specified as boundary conditions for the turbulence model by prescribing a turbulence intensity of 0.005 and an eddy length scale of 0.0005 [in], which correspond to a low degree of turbulence in the incoming flow.

Outflow boundary conditions are specified at the core duct outflow and bypass duct outflow surfaces. At the core duct outflow, the mass flow rate is prescribed with the assumption that the engine core "pulls" a fixed mass flow rate through the fan for a given operating condition (free-stream condition and engine rotation speed). Static pressure is enforced at the bypass duct outflow using the radial-equilibrium condition in ANSYS CFX that permits the static pressure to vary radially while maintaining the specified static pressure on average. To implement the radial-equilibrium condition, the ANSYS CFX solver

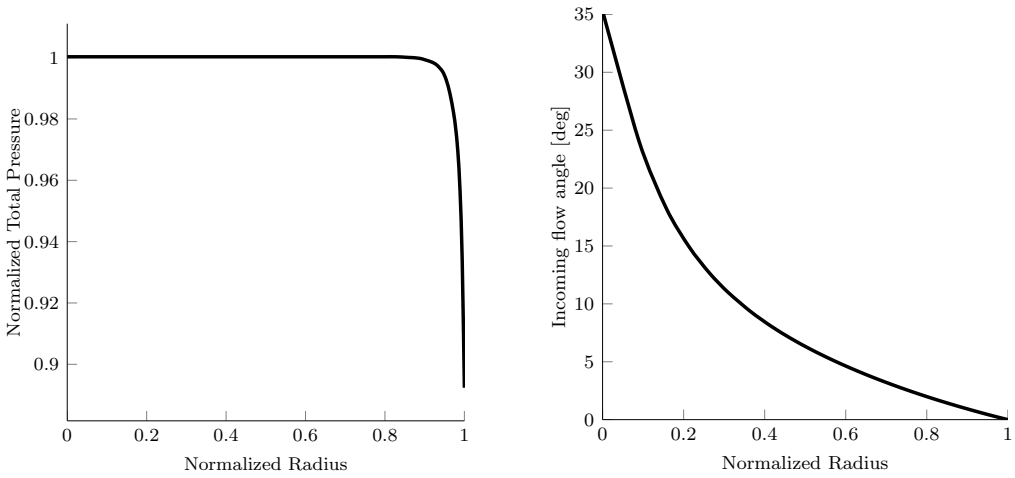


(a) Normalized total pressure distribution.

(b) Incoming flow angle distribution.

Figure 3.5: Inflow boundary total pressure and flow angle distributions.

divides the bypass duct outflow into $N_r$ radially-oriented circumferential bands. The pressure within each band is allowed to vary in the circumferential direction, and the average pressure within each band, $\bar{P}$, is constrained by the radial-equilibrium condition given in Eq. (3.38) [62].

$$\frac{d\bar{P}}{dr} = \bar{\rho}\frac{\bar{u_\theta}^2}{r_r} \tag{3.38}$$

Solid wall boundary conditions are enforced at the fan blades, hub, shroud, and splitter. At these boundaries, the velocity of the flow is set to match that of the rotating wall through specification of a no-slip condition. The shroud and splitter constitute the stationary components of the domain in which a zero wall velocity is prescribed. The fan blades and hub constitute the rotating components of the domain in which a non-zero wall velocity equivalent to the engine rotation speed is prescribed.

### 3.3.3 Operating Condition

The performance of a fan stage is characterized by the total pressure ratio and referred mass flow rate. The total pressure ratio is defined as the ratio of the mass flow averaged total pressure at the bypass duct outflow to the mass flow averaged total pressure just upstream of the fan blades. The referred mass flow rate, calculated using Eq. (3.39), is the mass flow rate through the domain corrected for non-standard day inflow conditions and represents the mass flow that would pass through the fan if the inflow total pressure and total temperature corresponded to standard day conditions. The operating point of a fan stage is described by the total pressure ratio and referred mass flow rate resulting from operation at a particular condition defined by the engine rotation speed, inflow conditions, and bypass duct static pressure. The inflow total pressure and total temperature correspond to freestream conditions, and the outflow static pressure represents the back-pressure produced by downstream engine components.

$$\dot{m}_R = \dot{m}\sqrt{\frac{T^T}{T^T_{STD}}}\left(\frac{P^T_{STD}}{P^T}\right) \tag{3.39}$$

A fan map depicts the operating points obtained using numerical simulations and experimental tests of an isolated fan stage for a variety of operating conditions. The operating points obtained with various outflow static pressures at a fixed engine speed and inflow conditions are connected to form characteristic curves. The stall point is identified by the peak in total pressure ratio along a characteristic curve and indicates the onset of stall. Stall is an undesirable, unsteady flow phenomenon produced by flow separation that occurs typically at low mass flow rates and high bypass duct static pressure. A stall line connects the stall

points on each characteristic curve and identifies the boundary of steady flow, where operating points to the left of the stall line are unsteady. A fan map also includes the fan operating line that consists of the unique set of operating points produced by the fan stage when installed in a complete engine. The operating line is measured during an infinitesimally slow throttle sweep of a complete-engine operating at a particular freestream condition. A representative fan map that includes several characteristic curves, the associated stall points, and the stall line is shown in Fig. 3.6.

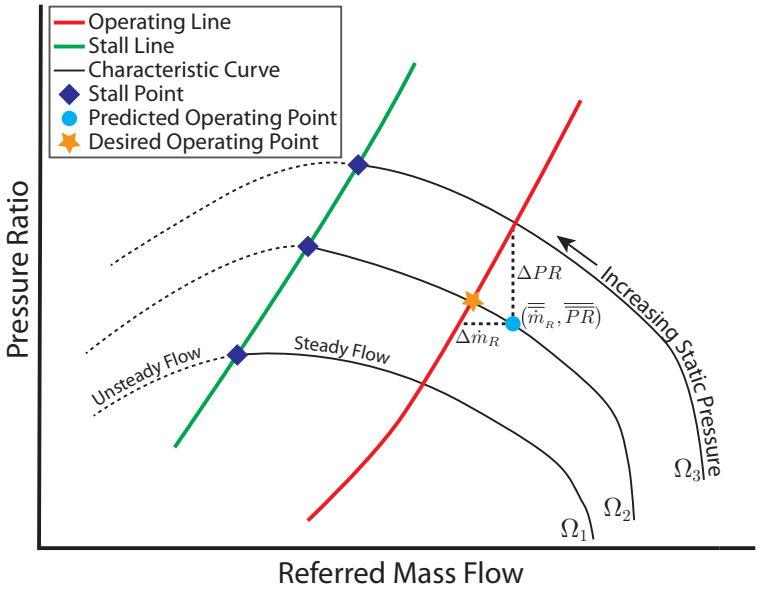


Figure 3.6: Representative fan map.

The bypass duct static pressure boundary condition is specified so that the predicted operating point coincides with a point on the operating line. The bypass duct static pressure necessary to achieve the desired operating point at the intersection of the characteristic curve and the operating line is unknown a priori. Therefore, an iterative procedure is utilized to map the characteristic curve and determine the bypass duct static pressure that yields an operating point within 1% error of the operating line. The error is calculated using Eq. (3.40) where the predicted operating point is denoted by $\left(\overline{\dot{m}}_R, \overline{PR}\right)$, and $\Delta \dot{m}_R$ and

$\Delta PR$ denote the horizontal and vertical distance of the operating point from the operating line, as shown in Fig. 3.6.

$$\%\Delta\text{OL} = 100\sqrt{\left(\frac{\Delta\dot{m}_R}{\overline{\dot{m}}_R}\right)^2 + \left(\frac{\Delta PR}{\overline{PR}}\right)^2} \tag{3.40}$$

The characteristic curves and stall line calculated with a bird-damaged fan operating in an otherwise undamaged engine differ from those obtained with an undamaged fan. The damaged fan is still able to achieve the total pressure ratios and mass flow rates specified by the operating line. However, the operating point on this operating line will differ from that of the undamaged fan due to flow disturbances induced by the bird damage.

### 3.3.4 Computational Mesh

A CFD computational mesh consisting of nodes and elements is required to numerically solve the RANS equations. Careful generation of the CFD mesh is necessary to accurately capture the complex phenomena of the fan. The ANSYS TurboGrid program is employed to generate a high-quality, structured CFD mesh of hexahedral elements for the inlet and passage sub-domains of an undamaged single blade passage. A set of constant-span CFD mesh cross-sections are created based on a specified mesh topology and the three-dimensional mesh is constructed using spline fits and interpolation between each cross-section. The ANSYS TurboGrid program cannot accommodate geometries with a splitter that bisects the domain outflow. Instead ANSYS Meshing is used to create an unstructured hexahedral mesh for the outlet sub-domain. The CFD mesh of a single blade passage is copied and rotated to construct the full wheel CFD mesh of an undamaged fan.

Conventional mesh topologies, including H-Grid, J-Grid, C-Grid, L-grid, and O-grid,

typically require a substantial amount of user manipulation to construct a CFD mesh of acceptable quality, particularly for complex blade geometries. Furthermore, these conventional topologies often result in an excessive mesh resolution within the blade passage in order to ensure a sufficient boundary layer resolution. Figure 3.7 depicts a representative CFD mesh constructed using a combination of an O-Grid surrounding the blade and an H-Grid topology in the blade passage. This topology results in a overly fine mesh resolution upstream and downstream of the blade leading and trailing edges, as evident in Fig. 3.7, along with distorted elements on the upper surface near the leading edge, as depicted in Fig. 3.8.

The ANSYS TurboGrid program employs an Automatic Topology and Meshing (ATM)) optimized topology method that generates a structured mesh of higher-quality than easily obtained using conventional topologies. For this reason, the ATM topology is used to generate a structured, hexahedral mesh of the inlet and passage domains of an undamaged single blade passage. Details of ANSYS TurboGrid and the ATM topology are available in the ANSYS TurboGrid product documentation [68]. Figure 3.9 depicts a constant-span cross-section of the mesh at 75% blade span for a single blade passage. Figure 3.10 depicts an overall meridional view of the computational mesh.

The selection of mesh topology, mesh density, and boundary layer resolution for the undamaged CFD mesh are motivated by the physical flow phenomena expected and the degree of accuracy desired from the CFD solution. Proper resolution of the boundary layer and tip gap is essential to accurately capture the shock structure and flow losses due to viscosity in the boundary layer and flow leakage through the tip gap. Additionally, the mesh topology must avoid substantially skewed elements, areas of large expansion in

element size, or elements with large aspect ratio to ensure numerical accuracy and solution convergence.

In this study, three mesh resolutions are considered: "coarse", "medium", and "fine". The overall topology of the coarse, medium, and fine mesh correspond with the CFD mesh in Figs. 3.9 and 3.10. The primary difference between the three meshes is the boundary layer refinement and tip gap resolution. Figure 3.11 provides a comparison of the leading-edge boundary layer refinement at 75% blade span for the coarse, medium, and fine meshes. The fine mesh is constructed with an average $y+$ value of 2.6 for direct wall integration of the boundary layer. The coarse and medium mesh feature a larger $y+$ value and utilize scalable wall functions to reduce the computational expense associated with resolving the boundary layer flow. Table 3.4 lists the number of nodes in the CFD mesh, the number of nodes in the radial direction between the blade tip and the shroud, and the minimum, maximum, and area-averaged $y+$ value of the first node from the blade surface. A mesh sensitivity study to determine the role of boundary layer refinement and tip gap resolution is discussed in Chapter 4.

Table 3.4: Details of the coarse, medium, and fine meshes.

| Mesh | # of Nodes | # Tip Nodes | Min. $y+$ | Max. $y+$ | Avg. $y+$ |
|---|---|---|---|---|---|
| Coarse | 435,546 | 4 | 1.76 | 400.86 | 101.6 |
| Medium | 625,485 | 9 | 0.91 | 129.0 | 24.6 |
| Fine | 1,278,743 | 43 | 0.08 | 15.2 | 2.6 |

| Mesh | % $y+ > 2$ | % $y+ > 10$ | % $y+ > 50$ | % $y+ > 150$ | % $y+ > 250$ |
|---|---|---|---|---|---|
| Coarse | 100% | 98.1% | 73.1% | 15.0% | 1.62% |
| Medium | 99.2% | 81.3% | 13.8% | 0.0% | 0.0% |
| Fine | 48.3% | 0.63% | 0.0% | 0.0% | 0.0 |

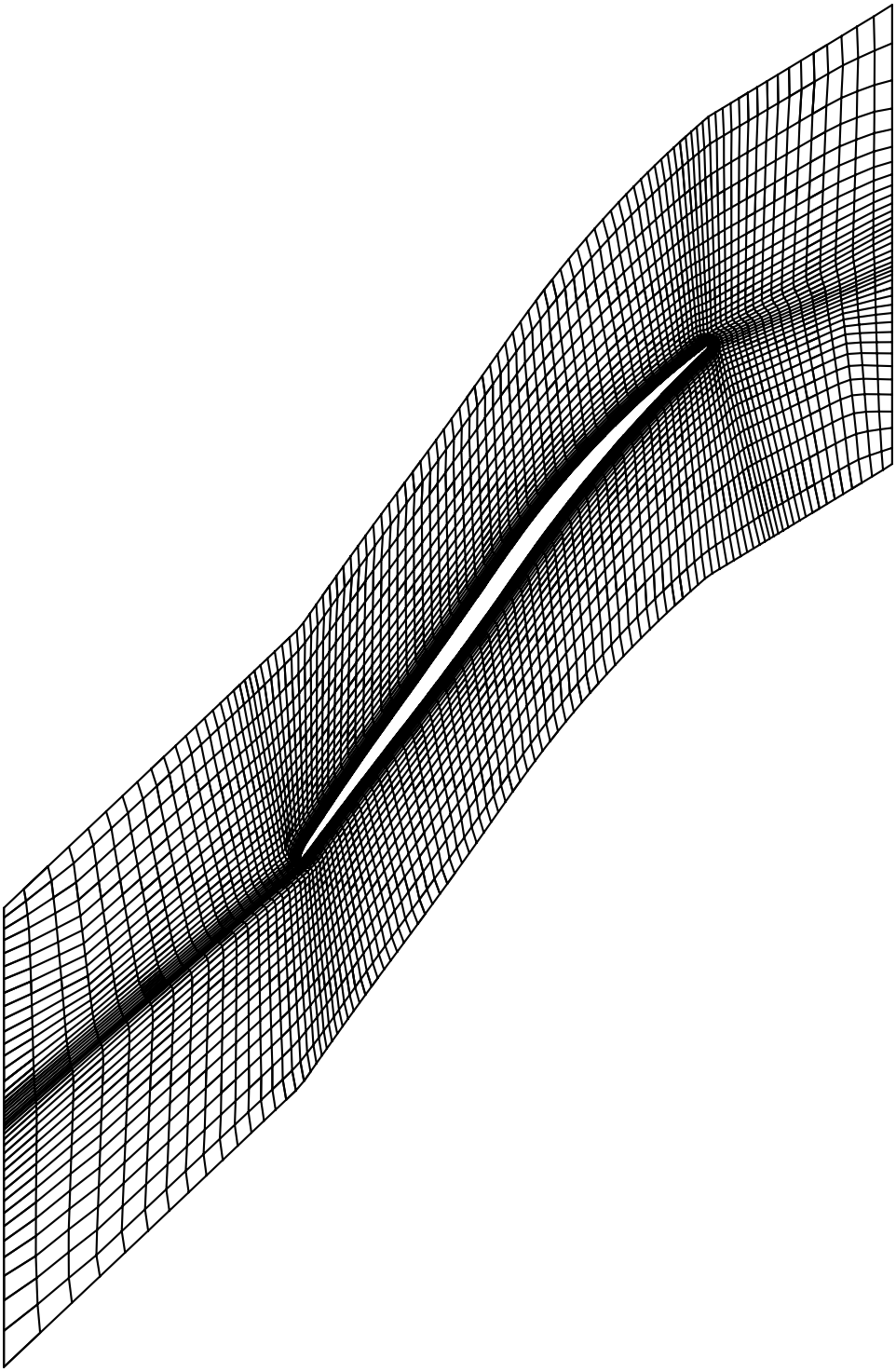

Figure 3.7: CFD mesh constructed with conventional mesh topologies at 75% blade span.

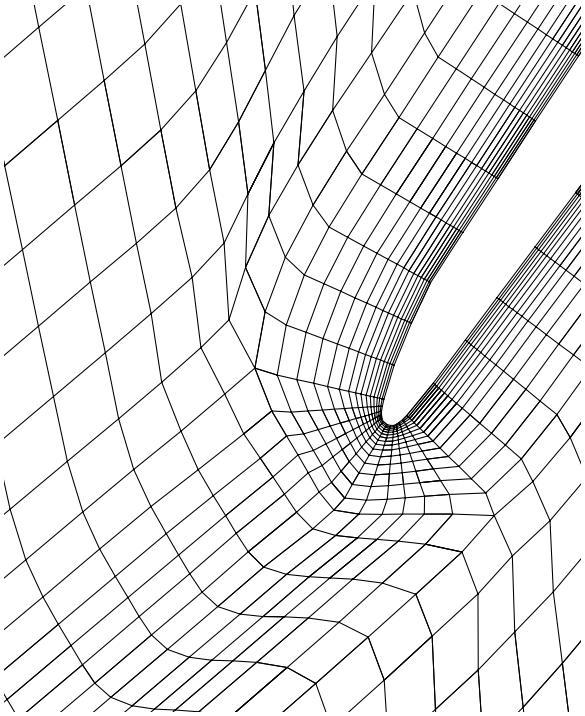

Figure 3.8: Leading edge of CFD mesh constructed with conventional mesh topologies at 75% span.

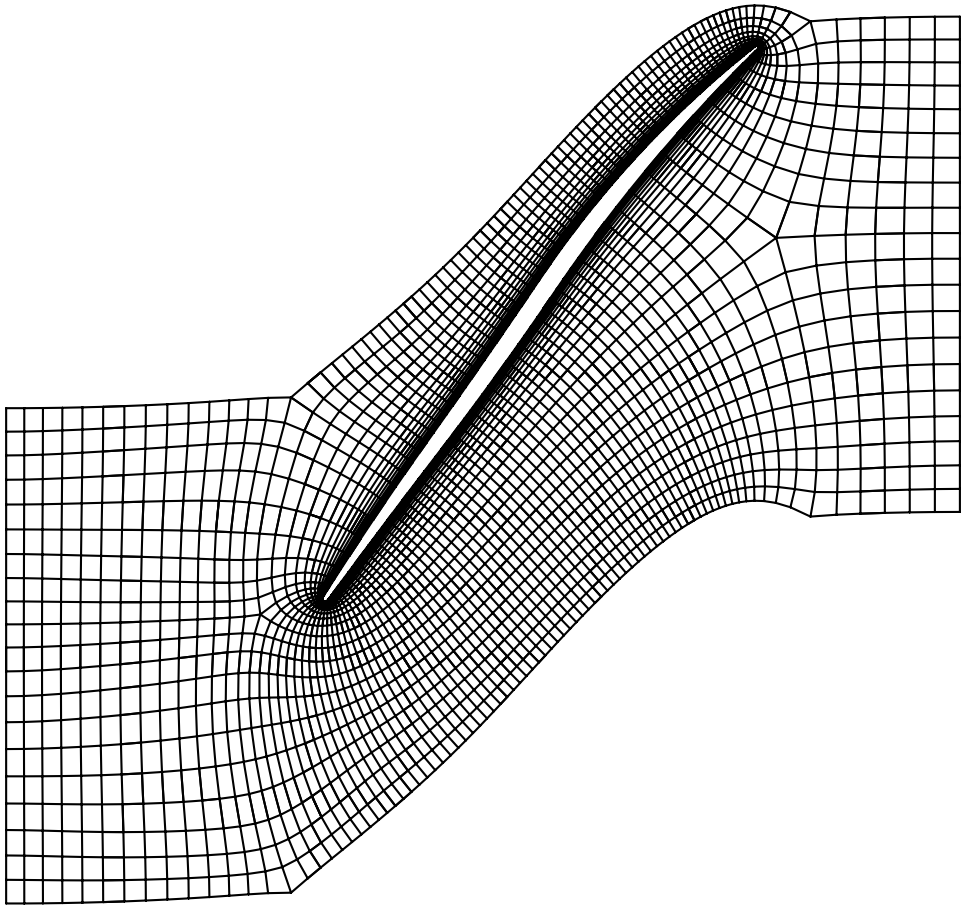

Figure 3.9: CFD mesh constructed with the ANSYS ATM topology at 75% blade span.

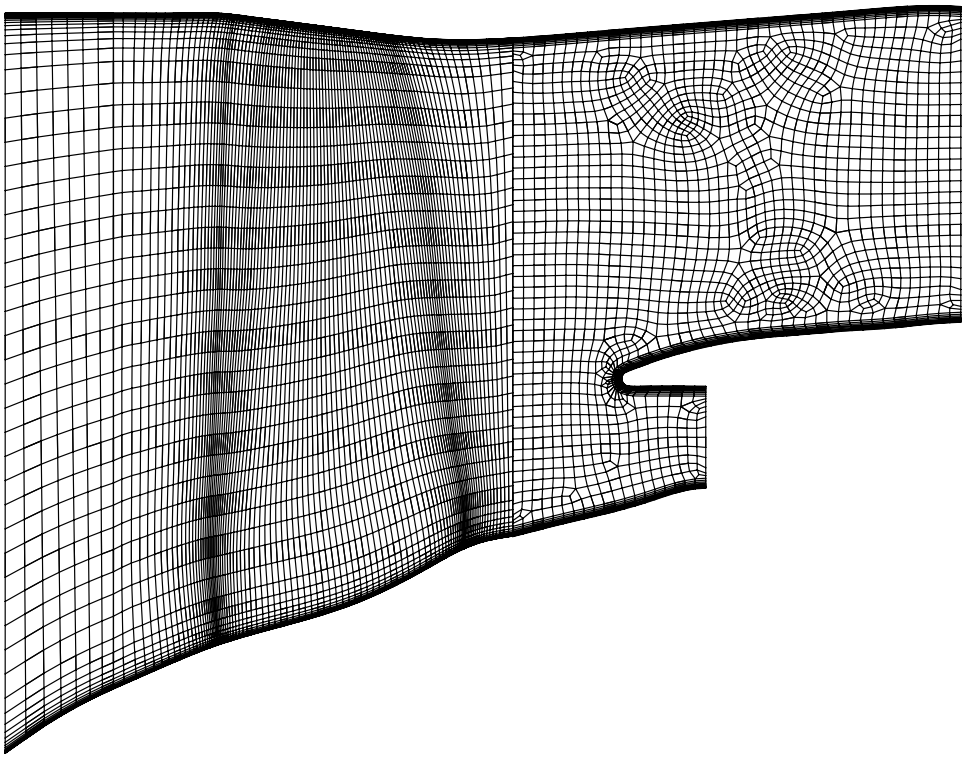

Figure 3.10: Meridional view of CFD mesh constructed with the ANSYS ATM topology.

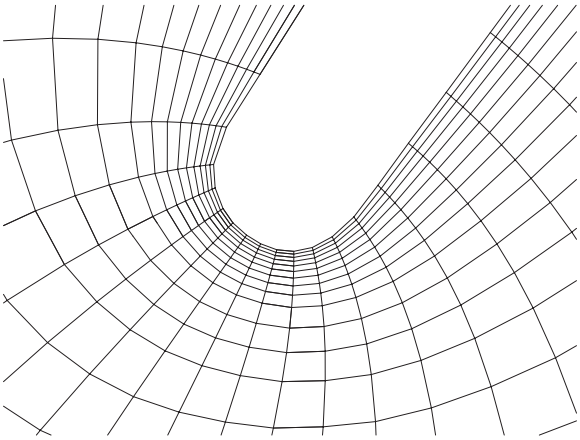

(a) Coarse mesh leading edge at 75% blade span.

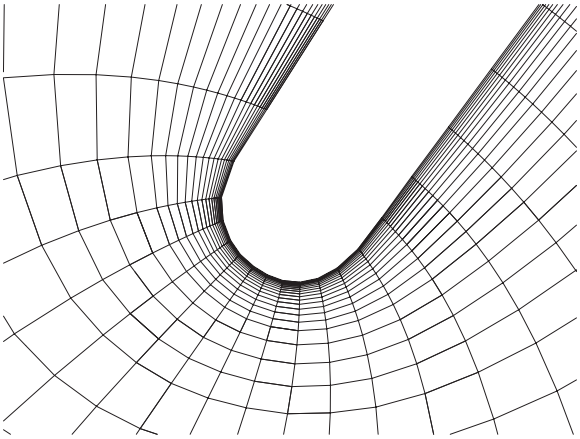

(b) Medium mesh leading edge at 75% blade span.

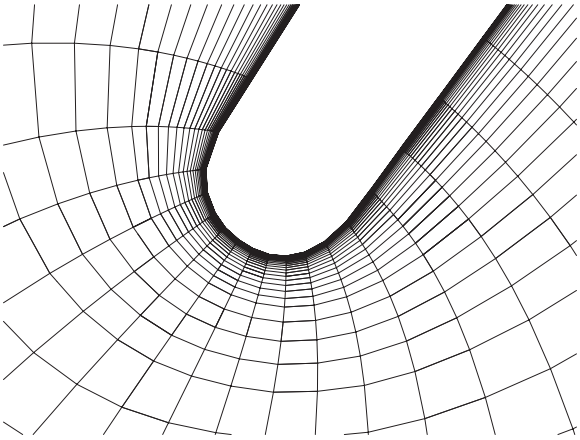

(c) Fine mesh leading edge at 75% blade span.

Figure 3.11: Comparison of leading-edge boundary layer resolution for the coarse, medium, and fine mesh at 75% span.

### 3.3.5 Computational Mesh for the Damaged Geometry

The ANSYS TurboGrid ATM topology is not applicable for full wheel geometries that include a set of damaged blades. To extend the high mesh quality produced by the ANSYS Turbo Grid ATM mesh topology to the damaged fan geometry, an automated mesh deformation procedure was developed. This procedure employs a RBFN, introduced in Section 2.2, to interpolate the deformation of the bird damaged blade profiles to the CFD mesh of the undamaged wheel. The RBFN interpolation is an effective tool for multivariate interpolation and has been successfully utilized for large-amplitude mesh deformation in aeroelastic applications and CFD-based aerodynamic shape optimization studies [69–76].

A RBFN consists of a linear combination of RBF's, $\phi$, whose value depends only on the distance from the evaluation point, $\mathbf{x^e}$, to the origin, such that $\phi = \phi(||\mathbf{x^e}||)$. Provided a set of $N_D$ driver points at which the deformation is known, the RBF interpolant of the deformation field takes the form given by Eq. (2.3) and expressed in matrix form by Eq. (3.41).

$$\hat{\boldsymbol{\varsigma}}(\mathbf{x}^e) = \left\{ \begin{array}{cccc} \phi(||\mathbf{x}^e - \mathbf{x}_1^{\mathrm{d}}||) & \phi(||\mathbf{x}^e - \mathbf{x}_2^{\mathrm{d}}||) & \cdots & \phi(||\mathbf{x}^e - \mathbf{x}_{N_D}^{d}||) \end{array} \right\} \left\{ \begin{array}{c} \mathrm{A}_1 \\ \mathrm{A}_2 \\ \vdots \\ \mathrm{A}_{N_D} \end{array} \right\} \tag{3.41}$$

The choice of RBF is important to ensure the best possible representation of the deformation field and resulting mesh quality. Reference [74] demonstrated that the volume spline defined by $\phi(||\mathbf{x}^e||) = ||\mathbf{x}^e||$ is an ideal RBF for CFD mesh deformation; therefore,

the volume spline is used in this study where the norm is evaluated as the Euclidean distance: $||\mathbf{x}^e|| = \sqrt{x^2 + y^2 + z^2}$. The fitting coefficients, $\mathbf{A}$, are uniquely determined by solving the linear system given by Eq. (3.42), where $\phi(\mathbf{x}^e, \mathbf{x}_l^d) = \phi(||\mathbf{x}^e - \mathbf{x}_l^d||)$ notation is introduced for simplicity.

$$\begin{bmatrix} \phi(\mathbf{x}_1^{\mathrm{d}}, \mathbf{x}_1^{\mathrm{d}}) & \phi(\mathbf{x}_1^{\mathrm{d}}, \mathbf{x}_2^{\mathrm{d}}) & \cdots & \phi(\mathbf{x}_1^{\mathrm{d}}, \mathbf{x}_{N_D}^{d}) \\ \phi(\mathbf{x}_1^{\mathrm{d}}, \mathbf{x}_1^{\mathrm{d}}) & \phi(\mathbf{x}_2^{\mathrm{d}}, \mathbf{x}_2^{\mathrm{d}}) & \cdots & \phi(\mathbf{x}_2^{\mathrm{d}}, \mathbf{x}_{N_D}^{d}) \\ \vdots & \vdots & \ddots & \vdots \\ \phi(\mathbf{x}_{N_D}^{d}, \mathbf{x}_1^{\mathrm{d}}) & \phi(\mathbf{x}_{N_D}^{d}, \mathbf{x}_2^{\mathrm{d}}) & \cdots & \phi(\mathbf{x}_{N_D}^{d}, \mathbf{x}_{N_D}^{d}) \end{bmatrix} \begin{Bmatrix} \mathrm{A}_1 \\ \mathrm{A}_2 \\ \vdots \\ \mathrm{A}_{N_D} \end{Bmatrix} = \begin{Bmatrix} u(\mathbf{x}_{d1}) \\ u(\mathbf{x}_{d2}) \\ \vdots \\ u(\mathbf{x}_{dD}) \end{Bmatrix} \tag{3.42}$$

The general procedure for generating the CFD mesh of the damaged geometry employs Eqs. (3.41) to map the deformation described by the damaged blade profiles onto the undamaged CFD mesh. The points that define the undamaged blade profiles are chosen as the driver points, and the deformation vector at each driver point is determined by calculating the difference between the points on the undamaged blade profiles and the corresponding points on the damaged profiles. The deformation is constrained at the inflow, outflow, hub, and shroud to preserve the profiles of these surfaces in the $(r, z)$ plane.

The inputs to the RBF mesh deformation procedure include the undamaged CFD mesh of the passage domain for a single blade passage, the damaged and undamaged blade profiles of the corresponding blade, and the damaged and undamaged blade profiles of the adjacent upstream and downstream blades. Figure 3.12 depicts a cross-section of the undamaged CFD mesh and the corresponding blade profiles that describe the deformation. In Fig. 3.12, the undamaged profiles are green and the damaged profiles are red. The deforma-

tion is performed for the passage surrounding blade A. The upstream blade and downstream blade are referred to as blade A+1 and blade A-1, respectively.

The RBF mesh deformation procedure is implemented in steps to reduce the computational requirement of the RBF mesh deformation procedure and ensure the quality of the resulting mesh. The following describes the step-by-step procedure to deform the CFD mesh of the representative blade A, shown in Fig. 3.12:

**Step 1:** The CFD nodes on the surface of blade A are deformed using the damaged and undamaged blade profiles of blade A as the driver points.

**Step 2:** The lower periodic surface is deformed using the blade profiles of blade A and blade A-1 as the driver points. Similarly, the upper periodic surface is deformed using the blade profiles of blade A and blade A+1. The deformation of the lower periodic and upper periodic surfaces is restricted to circumferential displacement to preserve the profiles of these surfaces in the $(r, z)$ plane. The deformation from the blade A+1 profiles and blade A-1 profiles is included to ensure the periodic surfaces between adjacent blade passages match.

**Step 3:** The inflow and outflow surfaces are deformed in the circumferential direction. The nodes common with the lower periodic and upper periodic surfaces serve as the driver points.

**Step 4:** The hub and shroud are deformed in the circumferential and axial direction using the nodes common to lower periodic, upper periodic, inflow, and outflow surface along with the blade profiles of blade A as driver points.

**Step 5:** The radial deformation of the hub and shroud nodes is calculated to restore the

original profile in the $(r, z)$ plane.

**Step 6:** The deformed nodes on the CFD mesh exterior and blade surface serve as the driver points for the interior nodes of the CFD mesh.

Table 3.5 summarizes the driver points used to deform each component of the CFD mesh and the corresponding displacement that is applied. Figure 3.13 depicts a cross-section of the damaged CFD mesh at 75% span, where the low periodic, high periodic, inflow, and outflow surfaces are labeled. A key benefit of the automated mesh deformation procedure developed for this study is that a CFD mesh can be generated for a variety of damaged configurations using the same undamaged CFD mesh.

Table 3.5: Driver points and displacement components for the RBF mesh deformation scheme.

| Surface | Driver Points | Displacement |
|---|---|---|
| Blade | Blade A Profiles | All |
| Lower Periodic | Blade A Profiles<br>Blade A-1 Profiles | Circumferential |
| Upper Periodic | Blade A Profiles<br>Blade A+1 Profiles | Circumferential |
| Inflow | Nodes shared with lower/upper periodic surfaces | Circumferential |
| Outflow | Nodes shared with lower/upper periodic surfaces | Circumferential |
| Hub | Blade surface nodes<br>Nodes shared with lower/upper periodic surfaces<br>Nodes shared with inflow/outflow surfaces | Circumferential/axial then radial |
| Shroud | Blade surface nodes<br>Nodes shared with lower/upper periodic surfaces<br>Nodes shared with inflow/outflow surfaces | Circumferential/axial then radial |
| Interior | Blade surface nodes<br>Low/high periodic surface nodes<br>Inflow/outflow surface nodes<br>Hub/shroud surface nodes | All |

Figure 3.14 depicts a cross-section of the undamaged and damaged coarse CFD mesh at 75% span. The damaged CFD mesh produced by the RBF mesh deformation procedure

retains the high mesh quality of the original mesh, particularly near the leading edge, as demonstrated for blade 2 in Figs. 3.14(c) and 3.14(d). Several metrics are examined to quantitatively assess the high mesh quality preservation in the mesh deformation scheme: the minimum and maximum face angle, the element volume ratio, and the minimum element volume. The face angle is a measure of mesh skewness and is calculated as the angle between two element faces that share a common node. The element volume ratio is a measure of the local element expansion and is defined as the ratio of the maximum element volume to the minimum element volume of all elements that share the same. Finally, the minimum volume is the smallest element volume in the mesh and must be greater than 0. Table 3.6 provides the limit for each mesh metric, as recommended by the ANSYS CFX-Solver Modeling Guide [77], the extremum value of that metric within the mesh, as well as the percentage of elements in the damaged mesh that violate the metric. Only a small percentage of elements violate the recommended limits for maximum and minimum face angle in the damaged medium and fine meshes.

Table 3.6: Mesh quality metrics for the undamaged and damaged coarse, medium, and fine meshes.

| | | Coarse Mesh | | Damaged Coarse Mesh | |
|---|---|---|---|---|---|
| Metric | Criteria | Max. Value | % Over | Max. Value | % Over |
| Max. Face Angle | $<170°$ | 146° | 0.0% | 140° | 0.0% |
| Min. Face Angle | $>10°$ | 29.6° | 0.0% | 44.1° | 0.0% |
| El. Volume Ratio | $<30$ | 12.6 | 0.0% | 11.7 | 0.0% |
| Min. Volume | $>0in^3$ | 3.31E-8$in^3$ | 0.0% | 2.37E-8$in^3$ | 0.0% |
| Edge Length Ratio | $<100$ | 459 | 1.0% | 480 | 1.1% |

| | | Medium Mesh | | Damaged Medium Mesh | |
|---|---|---|---|---|---|
| Metric | Criteria | Max. Value | % Over | Max. Value | % Over |
| Max. Face Angle | $<170°$ | 153° | 0.0% | 176° | 0.1% |
| Min. Face Angle | $>10°$ | 29.6° | 0.0% | 3.92° | 0.1% |
| El. Volume Ratio | $<30$ | 18.1 | 0.0% | 34.1 | $\sim$0.0% |
| Min. Volume | $>0in^3$ | 1.97E-9$in^3$ | 0.0% | 8.26E-10$in^3$ | 0.0% |
| Edge Length Ratio | $<100$ | 1,981 | 9.7% | 2,622 | 10.5% |

| | | Fine Mesh | | Damaged Fine Mesh | |
|---|---|---|---|---|---|
| Metric | Criteria | Max. Value | % Over | Max. Value | % Over |
| Max. Face Angle | $<170°$ | 154° | 0.0% | 140° | 0.3% |
| Min. Face Angle | $>10°$ | 26.2° | 0.0% | 44.1° | 0.3% |
| El. Volume Ratio | $<30$ | 34.7 | $\sim$0.0% | 11.7 | 0.0% |
| Min. Volume | $>0in^3$ | 2.08E-8$in^3$ | 0.0% | 2.37E-8$in^3$ | 0.0% |
| Edge Length Ratio | $<100$ | 20,420 | 52.2% | 36,340 | 54.1% |

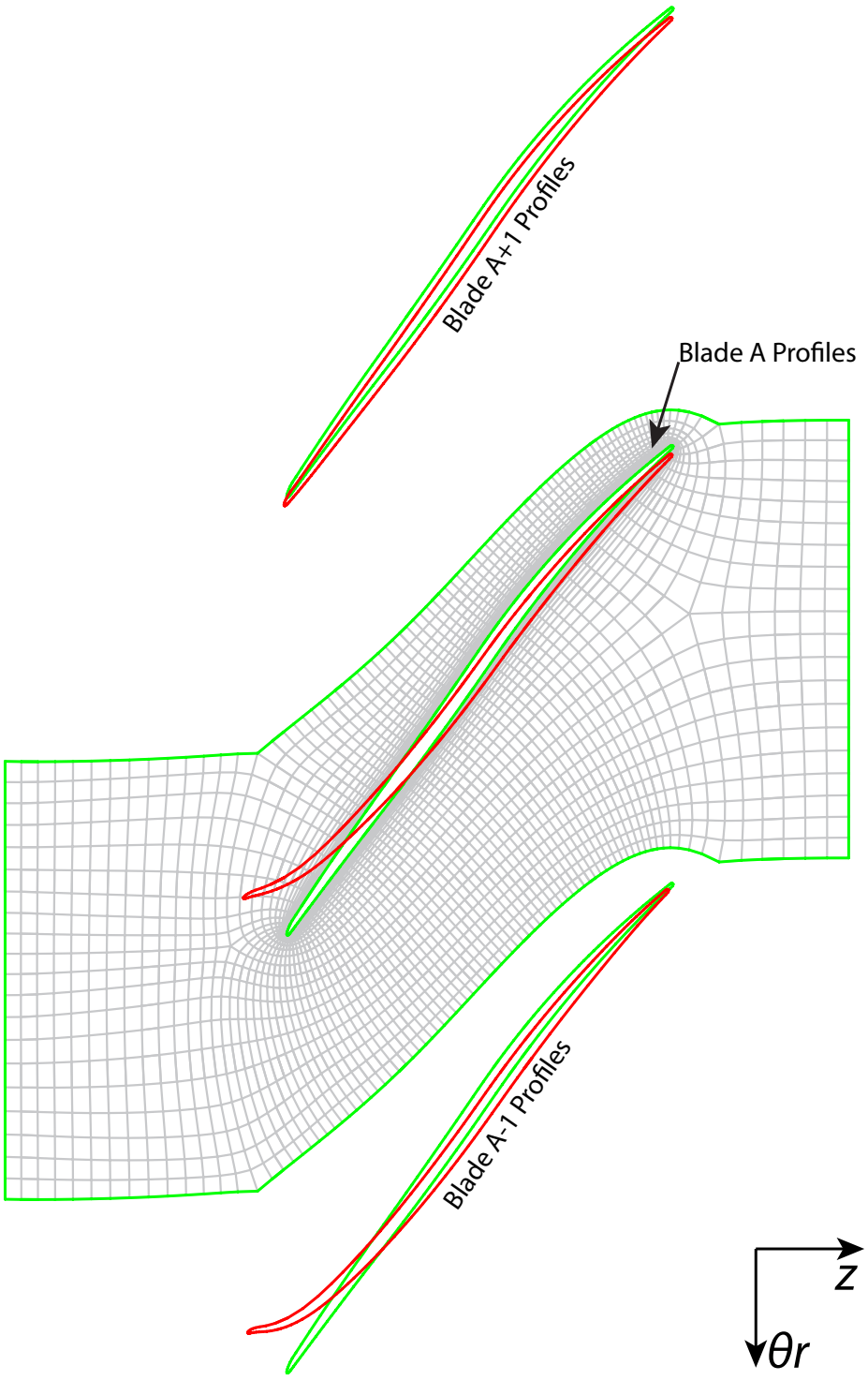


Figure 3.12: Cross-section of undamaged CFD mesh and corresponding blade profiles that describe the deformation.

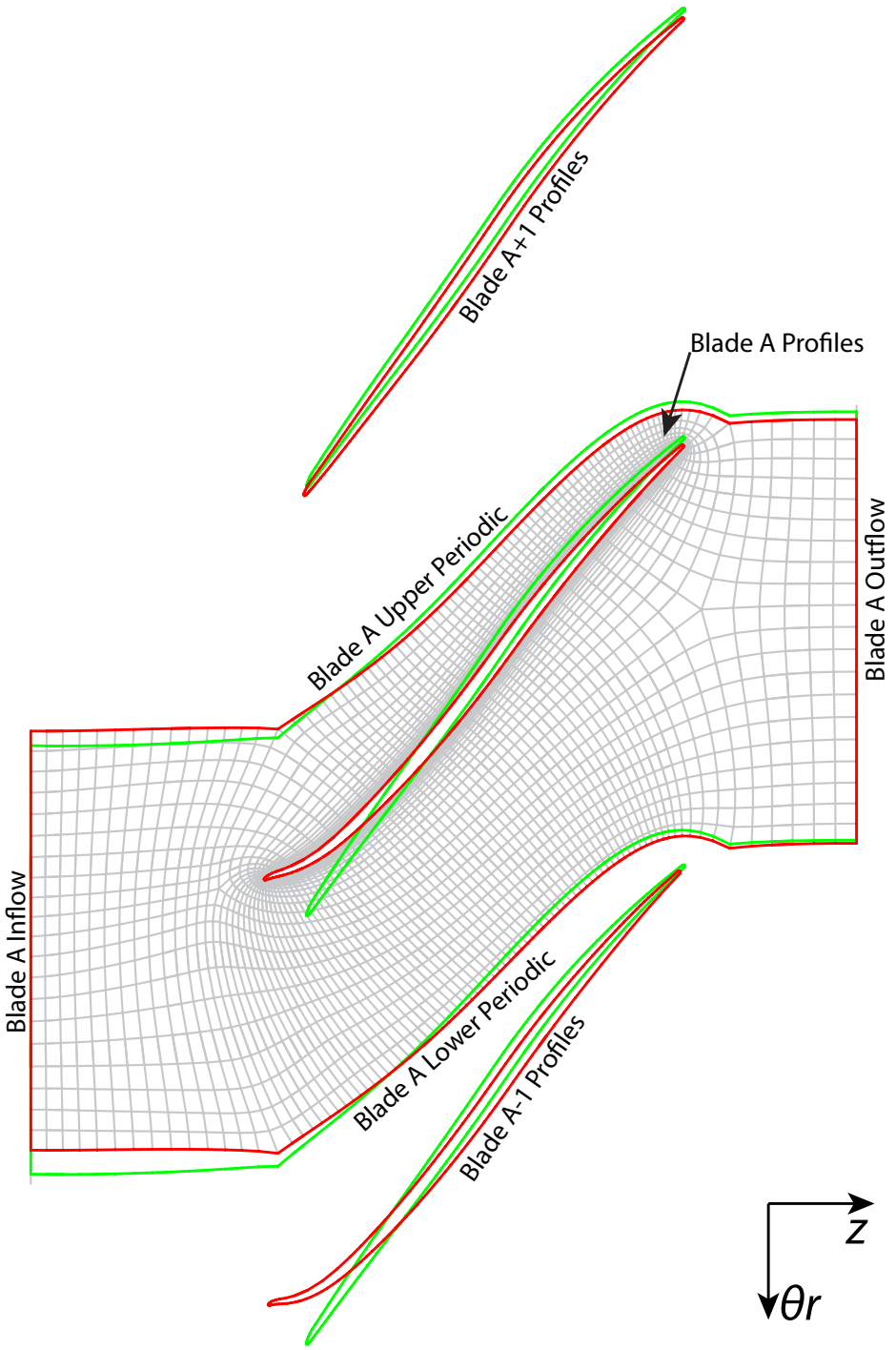


Figure 3.13: Cross-section of damaged CFD mesh with the low periodic, high periodic, inflow, and outflow surfaces labeled.

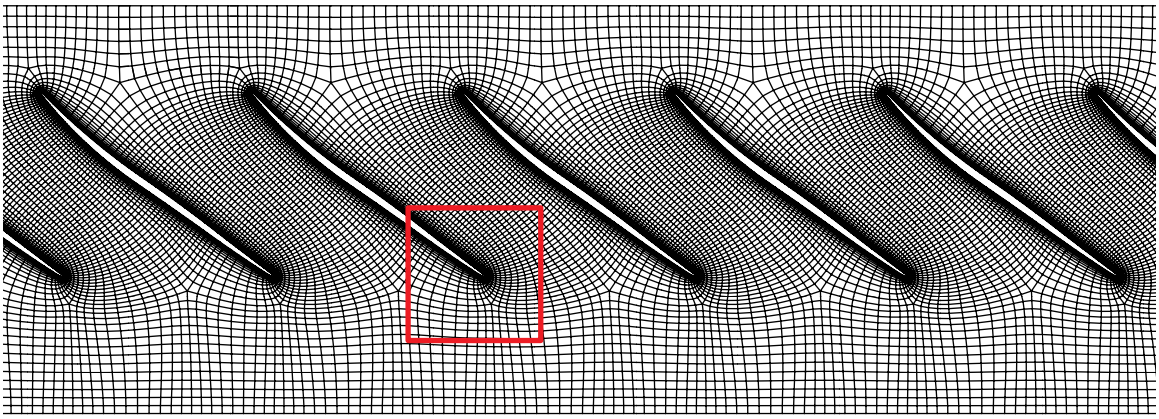

(a) Undamaged CFD mesh.

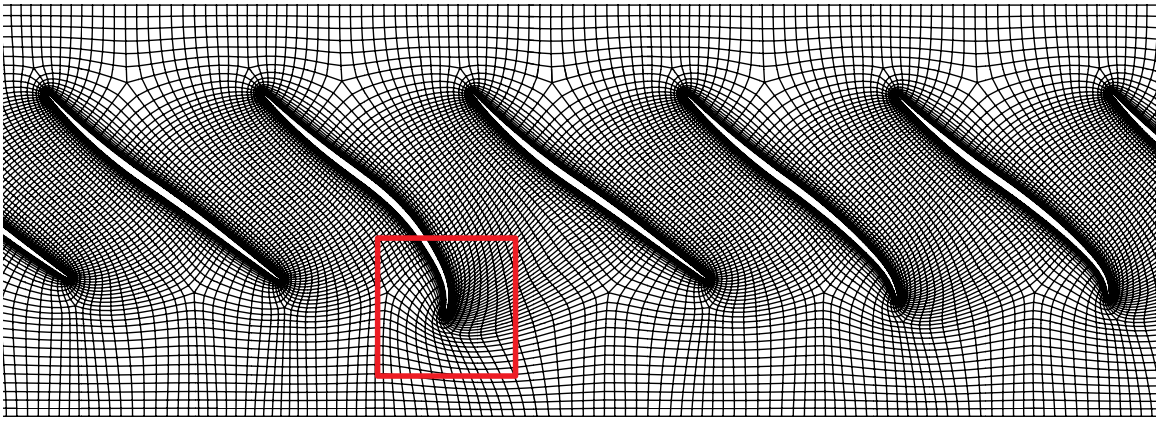

(b) Damaged CFD mesh.

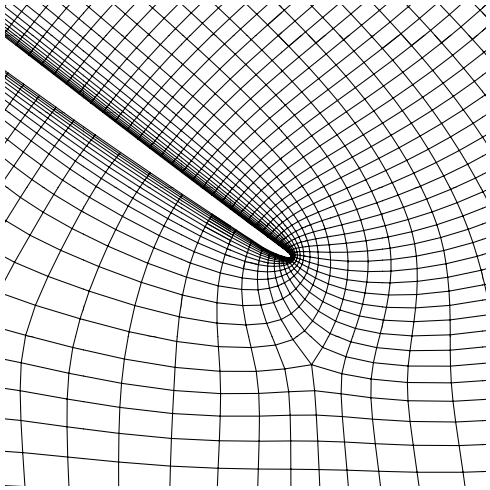

(c) Undamaged blade 2 leading edge CFD mesh.

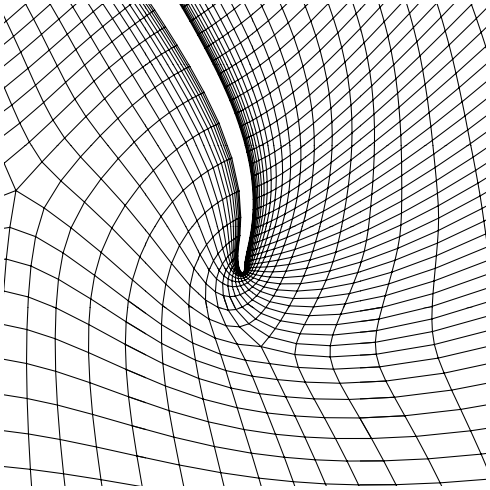

(d) Damaged blade 2 leading edge CFD mesh.

Figure 3.14: Comparison of the undamaged and damaged CFD mesh at 75% span.

# CHAPTER 4

# Verification of the Aerodynamic Model

In this chapter, the aerodynamic calculations obtained with the CFD-based aerodynamic model described in Chapter 3 are verified by comparing with results from an industry CFD solver for an undamaged fan. Subsequently, aerodynamic calculations performed with ANSYS CFX and the industry solver are compared for a representative damaged fan configuration to confirm the capabilities of the ANSYS CFX aerodynamic model for this type of calculation. The industry CFD solver is a RANS solver that has been extensively validated for fan and compressor design calculations. The aerodynamic calculations from the industry CFD solver were performed at the sponsor organization independent of this study, and the results were provided for comparison purposes. The ANSYS CFX calculations are performed using the coarse, medium, and fine mesh to identify the appropriate CFD mesh density for the objectives of this study. For the calculations presented in this chapter, the freestream conditions correspond to standard day +27°F conditions, the engine rotational speed is set to the 100% throttle setting, and the flight Mach number is zero.

Overall, the aerodynamic calculations performed with ANSYS CFX for an undamaged fan stage agree well with the industry CFD solver and confirm the CFD-based aerodynamic model. Furthermore, the increased boundary layer and tip gap resolution of the medium

and fine meshes show negligible effect on the steady solutions of an undamaged fan and damaged fan. Therefore, the coarse mesh is employed for the aerodynamic and aeroelastic response calculations presented in Chapters 6.4 and 8.

## 4.1 Verification of Undamaged Fan Aerodynamic Calculations

The undamaged fan configurations were provided by the sponsor organization and correspond to the commercial turbofan engine described in Chapter 2. The undamaged fan calculations from ANSYS CFX are verified by comparing with results from the industry CFD solver. The quantities compared are overall flow parameters, radial flow distributions at various axial locations, and blade cross-section pressure distributions. Results obtained with the coarse, medium, and fine meshes are included to determine the importance of the boundary layer and tip gap resolution. The aerodynamic calculations are compared for the single blade passage computational domain depicted in Fig. 3.4(a). The blade geometry corresponds to the take-off design configuration and includes the centrifugal and steady aerodynamic loads resulting from operating the fan at take-off conditions. The calculations with the industry solver are performed with a structured H-grid CFD mesh composed of hexahedral elements, similar to the mesh illustrated by Fig. 3.7, that consists of 2.4 million nodes per passage and employs a fine boundary layer resolution for direct integration of the near-wall flow. This mesh differs in mesh topology and resolution from the coarse, medium, and fine mesh used in the ANSYS CFX calculations. Identical boundary conditions are enforced for all CFD calculations to ensure that the comparison is conducted for

an identical situation.

The ANSYS CFX calculations were performed for 400 iterations utilizing a pseudo time-stepping procedure with a time-step of $\Delta t_f = 0.1/\Omega$. Convergence of the ANSYS CFX calculations includes monitoring of the solution residuals for the governing equations and convergence of the overall flow properties, including total pressure ratio $PR$, referred mass flow rate $\dot{m}_R$, and total temperature at the bypass duct outflow $T_B^T$. Convergence of the solution is identified when the overall flow properties change less than 0.01% over several iterations. The calculations were performed using parallel Intel Xeon X5650 2.67 GHz processors assembled on a high-performance computing cluster composed of 12-processor nodes with 48 GB of Random Access Memory (RAM) per node. The number of processors utilized for the coarse, medium, and fine mesh calculation varied based on the cluster availability and RAM requirements. The total Central Processing Unit (CPU) time, defined as sum of the CPU time consumed by all of the processors, is used to compare the computational expense of these calculations.

Table 6.3 provides the total CPU time for the 400 iterations, the number of iterations required to obtain a solution within 0.01% of the converged values of $PR$, $\dot{m}_R$, and $T_B^T$, and the associated total CPU time to obtain a solution within 0.01% of the converged values. The flow solution converges in $\sim$170 iterations for all three meshes; however, the CPU time required of the medium and fine meshes is considerably greater than that of the coarse mesh. Therefore, it is desirable to identify the mesh density that accurately captures the flow field while minimizing the computational expense. Figure 4.1(a) shows the convergence of $PR$, $\dot{m}_R$, and $T_B^T$, normalized by the converged values, as a function of solver iterations for the coarse mesh solution. Figure 4.1(b) provides the Root Mean

Square (RMS) residuals corresponding to the conservation of mass, momentum, and energy equations for the coarse mesh solution, where residuals below $10^{-4}$ indicate a suitably converged solution.

Table 4.1: Convergence details for the coarse, medium, and fine meshes.

| Mesh | Total CPU Time (hours) | # of Iterations to within 0.01% | CPU Time (hours) |
|---|---|---|---|
| Coarse | 6.5 | 162 | 2.75 |
| Medium | 12 | 174 | 5 |
| Fine | 26 | 159 | 10 |

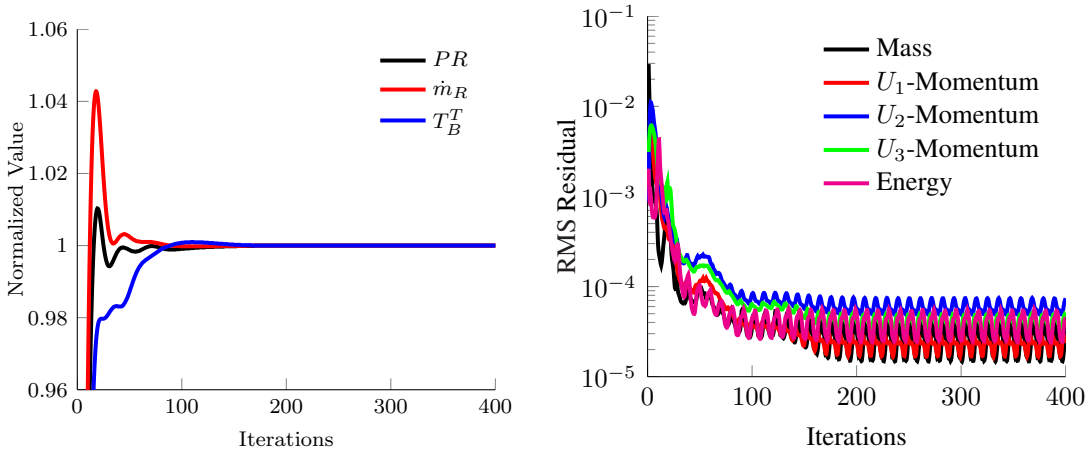


(a) Convergence of overall flow parameters.

(b) Solver residuals history.

Figure 4.1: Convergence of overall flow parameters and solver residuals history for coarse mesh undamaged fan calculations.

### 4.1.1 Comparison of Overall Flow Parameters

Several flow parameters are compared at various axial stations within the computational domain. Station $LE$ refers to the axial location immediately upstream of the fan blade leading edge, and Station $B$ refers to the outflow of the computational domain in the bypass duct. Station $LE$ is composed of two sub-stations: Station $LE_C$ and Station $LE_B$. Station

$LE_C$ is the portion of Station $LE$ through which flow travels into the core duct, and Station $LE_B$ is the remaining portion of Station $LE$ through which flow travels into the bypass duct. The overall flow parameters, listed in Table 4.2, provide a picture of the overall flow field and are useful for comparison purposes. The flow parameters are mass-flow average or area averaged at the axial station as indicated in Table 4.2 and compared between the two solvers. The Table 4.2 also provides the $L^1$ relative error norm for comparison of the ANSYS CFX results with the industry CFD solver solution. The general form of the $L^1$ relative error norm between two sets of data is obtained using Eq. (4.1) where $N_p$ indicates the number of data points for comparison, $\varphi$ is the baseline data, and $\hat{\varphi}$ is the data provided by the industry solver and used for comparison. The ANSYS CFX results agree very well with the industry CFD solver solution, with the maximum discrepancy being less than 1%.

Table 4.2: Comparison of overall flow parameters.

| Parameter | Definition | Coarse % Error | Medium % Error | Fine % Error |
|---|---|---|---|---|
| $P^T_{LE}$ | Total pressure at $LE$ (mass-flow averaged) | 0.14% | 0.14% | 0.14% |
| $P^T_{LE_C}$ | Total pressure at $LE_C$ (mass-flow averaged) | 0.14% | 0.07% | 0.14% |
| $T^T_{LE_C}$ | Total temperature at $LE_C$ (mass-flow averaged) | 0.04% | 0.04% | 0.04% |
| $P^T_{LE_B}$ | Total pressure at $LE_B$ (mass-flow averaged) | 0.28% | 0.28% | 0.28% |
| $T^T_{LE_B}$ | Total temperature at $LE_B$ (mass-flow averaged) | 0.01% | 0.01% | 0.01% |
| $P^T_B$ | Total pressure at $B$ (mass-flow averaged) | 0.54% | 0.54% | 0.58% |
| $T^T_B$ | Total temperature at $B$ (mass-flow averaged) | 0.03% | 0.02% | 0% |
| $\dot{m}_{LE}$ | Mass flow at $LE$ | 0.22% | 0.19% | 0.21% |
| $\dot{m}_{LE_B}$ | Mass flow at $LE_B$ | 0.11% | 0.07% | 0.09% |
| $\dot{m}_{LE_C}$ | Mass flow at $LE_C$ | 0.76% | 0.76% | 0.76% |
| $\dot{m}_{R_{LE}}$ | Referred mass flow at $LE$ | 0.76% | 0.76% | 0.76% |
| $BPR$ | $\dot{m}_{LE_B}/\dot{m}_{LE_C}$ | 0.63% | 0.63% | 0.63% |
| $PR$ | $P^T_B/P^T_{LE_B}$ | 0.56% | 0.56% | 0.56% |

$$\% \text{ Error} = 100\frac{1}{N_p}\frac{\sum_{i=1}^{N_p}|\hat{\varphi}_i - \varphi_i|}{|\varphi_i|} \tag{4.1}$$

### 4.1.2 Comparison of Radial Flow Distributions

Radial distributions of several normalized flow quantities calculated with ANSYS CFX are compared to the industry CFD solver results. These radial distributions are calculated at the domain inflow (*IN*), 5% of the blade chord upstream of the blade leading edge (*LE5*), 5% of the blade chord downstream of the blade trailing edge (*TE5*), and the domain outflow (*OUT*). Figures 4.2 depicts the radial distributions of circumferentially-averaged axial velocity (density-averaged), static pressure (area-averaged), total pressure (mass-flow averaged), and total temperature (mass-flow averaged), normalized by their respective average values, at the four axial locations for ANSYS CFX using the coarse mesh and the industry CFD solver. The $L^1$ relative error norm between the three ANSYS CFX solutions (coarse, medium, and fine) are below 1%; therefore, the radial distributions for the medium and fine mesh are not presented. The $L^1$ relative error norm between the ANSYS CFX results and industry CFD solver solution is provided in Table 4.3 for the coarse, medium, and fine meshes.

Overall, the ANSYS CFX solutions agree very well with the solution from the industry CFD solver, with an average error of $\sim$0.65% for all radial distributions. The largest discrepancy occurs in the axial velocity and static pressure distribution at the *OUT* location in the core duct. This discrepancy is attributed to differences in the implementation of the core duct mass flow boundary condition in the CFD solvers. This discrepancy is deemed acceptable, since the maximum error in the axial velocity and static pressure distributions at *OUT* is less than 4%.

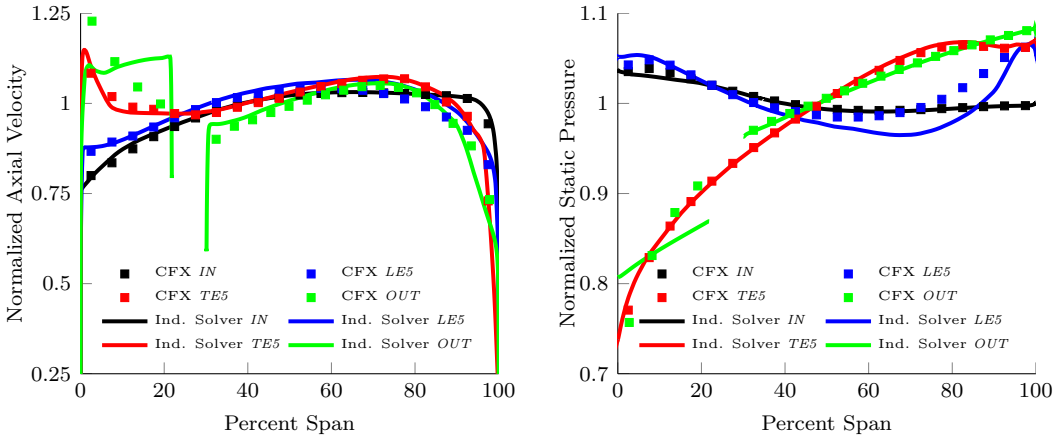


(a) Normalized axial velocity distributions at various axial locations.

(b) Normalized static pressure distributions at various axial locations.

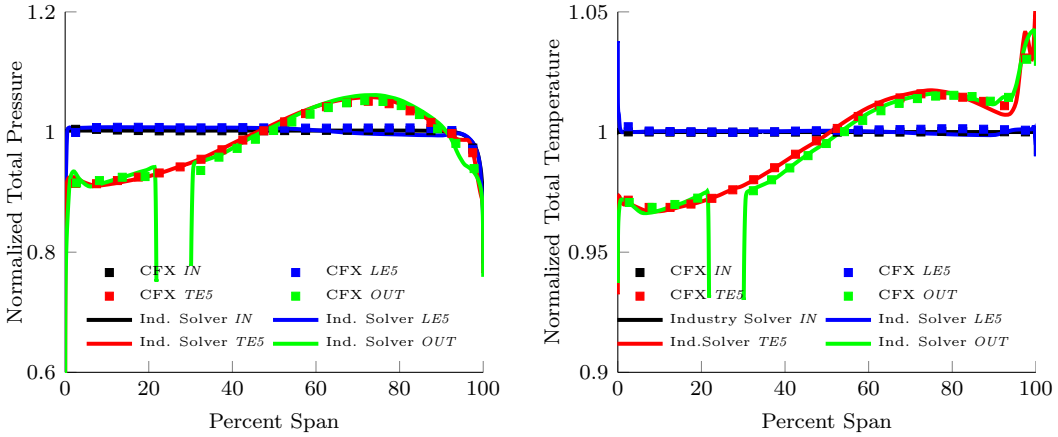


(c) Normalized total pressure distributions at various axial locations.

(d) Normalized total temperature distributions at various axial locations.

Figure 4.2: Comparison of radial distributions of several normalized flow quantities between the coarse mesh and the industry solver.

### 4.1.3 Comparison of Blade Cross-Sectional Pressure Distribution

The final component in this verification effort is comparison of the chord-wise static pressure distributions at several blade cross-sections. Figure 4.3 depicts the chord-wise static pressure distribution, normalized by the average value, obtained with ANSYS CFX and the industry CFD solver at 30%, 60%, and 90% blade span. The pressure distribution obtained with ANSYS CFX using the coarse, medium, and fine mesh are very similar, with a $L^1$

Table 4.3: Radial flow distribution errors.

| Parameter | Location | Coarse % Error | Medium % Error | Fine % Error |
|---|---|---|---|---|
| $U_z$ | (*IN*) | 0.49% | 0.49% | 0.43% |
| $U_z$ | (*LE5*) | 1.75% | 1.77% | 1.74% |
| $U_z$ | (*TE5*) | 0.77% | 0.79% | 0.80% |
| $U_z$ | (*OUT*) | 3.18% | 3.19% | 3.19% |
| $P$ | (*IN*) | 0.15% | 0.13% | 0.12% |
| $P$ | (*LE5*) | 1.23% | 1.23% | 1.22% |
| $P$ | (*TE5*) | 0.29% | 0.27% | 0.26% |
| $P$ | (*OUT*) | 0.92% | 0.93% | 0.93% |
| $P^T$ | (*IN*) | 0.09% | 0.09% | 0.09% |
| $P^T$ | (*LE5*) | 0.42% | 0.41% | 0.42% |
| $P^T$ | (*TE5*) | 0.36% | 0.37% | 0.37% |
| $P^T$ | (*OUT*) | 0.80% | 0.81% | 0.81% |
| $T^T$ | (*IN*) | 0.01% | 0.01% | 0.01% |
| $T^T$ | (*LE5*) | 0.08% | 0.08% | 0.08% |
| $T^T$ | (*TE5*) | 0.13% | 0.13% | 0.13% |
| $T^T$ | (*OUT*) | 0.11% | 0.12% | 0.13% |
| Average Error | | 0.61% | 0.65% | 0.65% |

relative error norm between the three mesh solutions of less than 1%. Therefore only the results from the coarse mesh are presented in Fig. 4.3. The $L^1$ relative error norm between the ANSYS CFX and the industry CFD solver result is provided in Table 4.4 for the coarse, medium, and fine meshes.

Table 4.4: Comparison of chord-wise static pressure distributions.

| Span | Surface | Coarse % Error | Medium % Error | Fine % Error |
|---|---|---|---|---|
| 30% Span | Pressure | 0.43% | 0.42% | 0.41% |
| 30% Span | Suction | 0.13% | 0.13% | 0.13% |
| 60% Span | Pressure | 1.4% | 1.4% | 1.5% |
| 60% Span | Suction | 3.2% | 3.2% | 3.2% |
| 90% Span | Pressure | 2.2% | 2.3% | 2.3% |
| 90% Span | Suction | 2.6% | 2.5% | 2.5% |

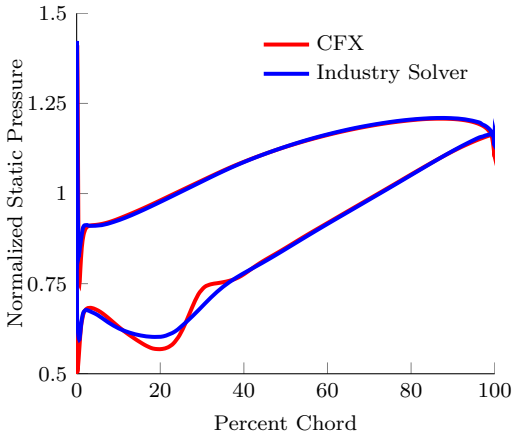


(a) Normalized chord-wise static pressure distributions at 30% blade span.

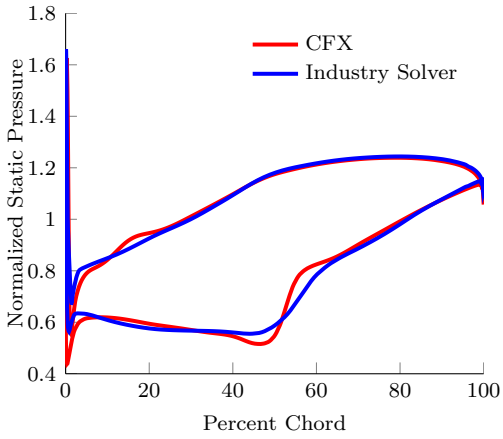


(b) Normalized chord-wise static pressure distributions at 60% blade span.

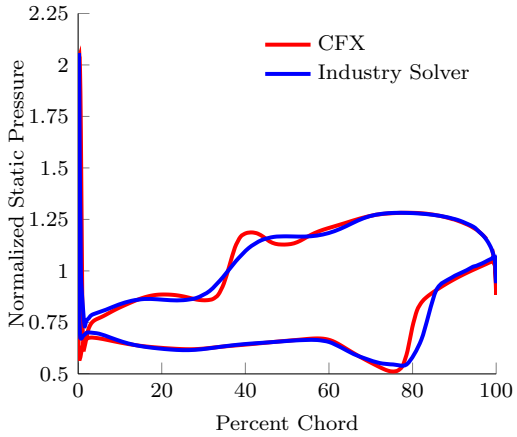


(c) Normalized chord-wise static pressure distributions at 90% blade span.

Figure 4.3: Comparison of normalized chord-wise static pressure distributions.

Good agreement in the chord-wise static pressure distributions between the ANSYS CFX and the industry CFD solver results is evident, with the minimum and maximum error being 0.13% and 3.2%, respectively. There is also agreement in the chord-wise location of the passage shock, which influences the cross-section moment and thus could affect the aeroelastic behavior of the blade [8, 34, 45, 52]. The largest discrepancies occur in the leading edge and trailing edge pressure spikes and the pressure gradient at the passage shock. The main source of these discrepancies is attributed to differences in numerical dissipation

and diffusion between the two CFD solvers. The discrepancies may also result from differences in mesh resolutions along the blade, which significantly affect the resolution of steep pressure gradients. Specifically, the static pressure jump across the passage shock in the industry CFD solver solution is somewhat smeared out due to the coarse chord-wise mesh resolution used in the industry CFD solver. The mesh used with ANSYS CFX has a finer chord-wise mesh resolution, and the static pressure jump across the passage shock is more sharply defined. This is especially apparent at 90% blade span.

## 4.2 Comparison of Damaged Fan Aerodynamic Calculations

The aerodynamic calculations for the bird-damaged fan performed with ANSYS CFX and the industry solver are compared in this section. The damaged fan operating point obtained with ANSYS CFX and the industry solver are compared first. Subsequently, Mach contours at 77% span and mid-chord are compared. Results obtained with the coarse, medium, and fine meshes are included to determine the importance of mesh resolution. The damaged configuration provided by the sponsor organization consists of 5 bird-damaged fan blades located in an otherwise undamaged fan. The blade damage results from an experimental bird strike test of a commercial turbofan in which a single 2.5 pound bird was ingested at take-off conditions with a strike location of 70% span. Figure 4.4 depicts the damaged fan for which the comparison of ANSYS CFX and the industry solver is performed. This damaged configuration differs slightly from the damaged configuration described in Chapter 2. The damaged fan results presented in this section confirm the

CFD-based aerodynamic model through comparison with the industry solver. Chapter 6.4 provides a thorough presentation and discussion of the steady and unsteady aerodynamic behavior of the bird-damaged fan considered in this study.

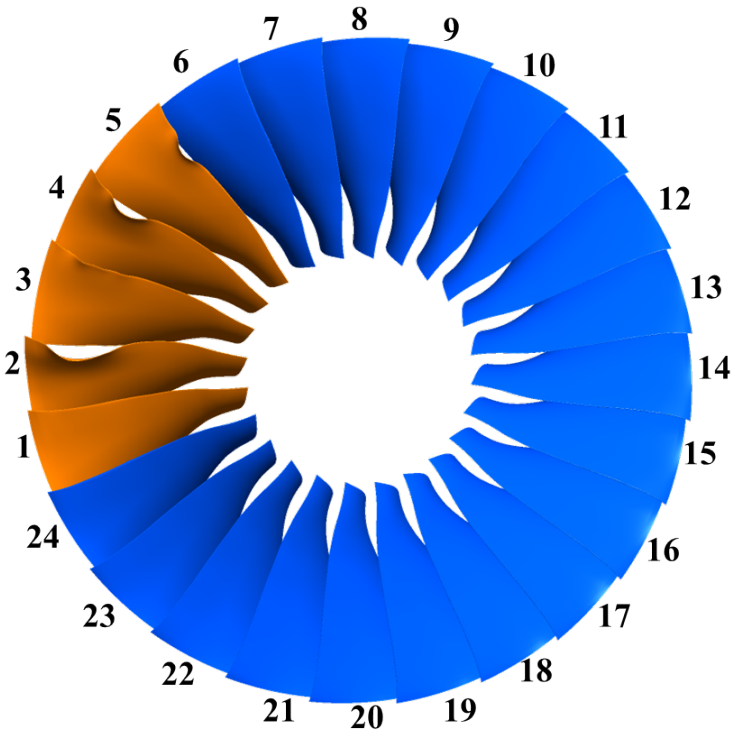


Figure 4.4: Bird damaged fan for verification effort with damaged blades highlighted in orange.

The bird-damaged configuration represents an off-design condition for which numerical convergence of the CFD solution is difficult to achieve. To facilitate numerical stability of the solution, a pseudo time-step of $\Delta t_f = 0.01/\Omega$ is specified for the first 400 iterations, after which the pseudo time-step is increased to $\Delta t_f = 0.1/\Omega$. Furthermore, the lack of symmetry caused by the bird-damage requires a full-wheel CFD calculation that significantly increases the computational requirements associated with the CFD solution. The coarse mesh calculations of the damaged fan require 2000 iterations for convergence of $PR$, $\dot{m}_R$, and $T_B$. The calculations performed with the medium and fine meshes were

initialized from the coarse mesh solution to enhance convergence and were performed for an additional 500 iterations.

Table 4.5 provides the number of iterations and the total CPU time for each calculation. In addition, the iterations required to obtain a solution within 1% of the converged values of $PR$, $\dot{m}_R$, and $T_B^T$, and the associated CPU time is provided for the coarse mesh. The convergence criteria for $PR$, $\dot{m}_R$, and $T_B^T$ is increased from 0.01% to 1% for the damaged fan since a steady solution is difficult to obtain due to the inherent unsteadiness caused by the damaged blades. The medium and fine mesh calculations were initialized by the coarse mesh solution, and the values of $PR$, $\dot{m}_R$, and $T_B^T$ did not vary outside the 1% convergence criteria. Therefore, the number of iterations and the associated CPU time required for convergence of the medium and fine mesh calculations are not provided in Table 4.5. Figure 4.5(a) shows the convergence of $PR$, $\dot{m}_R$, and $T_B^T$, normalized by the converged values, as a function of solver iterations for the coarse mesh. Figure 4.5(b) provides the RMS residuals corresponding to the conservation of mass, momentum, and energy equations for the coarse mesh. The convergence for the damaged fan is inferior when compared to the RMS residuals for the undamaged fan calculations.

Table 4.5: Convergence details for the damaged fan calculations.

| Mesh | # of Iterations | Total CPU Time (hours) | # of Iterations to within 1% | CPU Time to within 1% |
|---|---|---|---|---|
| Coarse | 2000 | 85 | 958 | 49.5 |
| Medium | 2000+500 | 85+34 | N/A | N/A |
| Fine | 2000+500 | 85+70 | N/A | N/A |

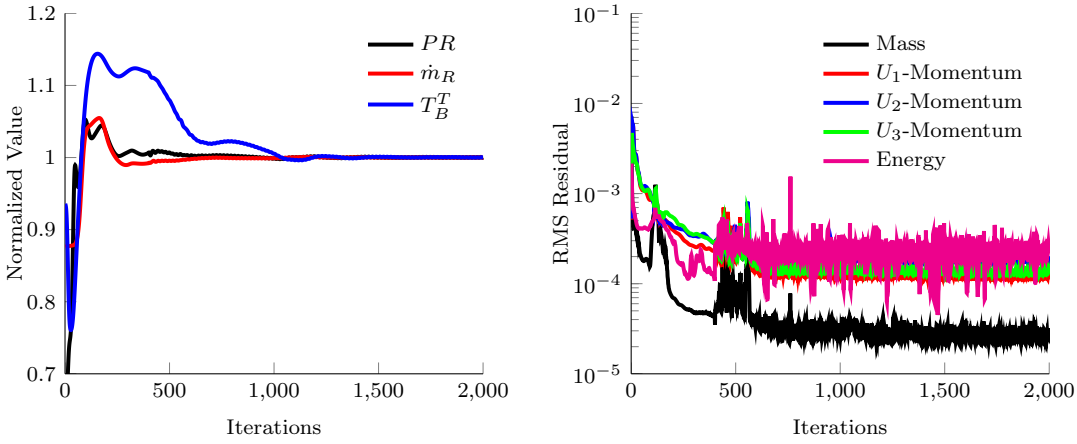


(a) Convergence of overall flow parameters.

(b) Convergence of solver residuals.

Figure 4.5: Convergence of overall flow parameters and solver residuals for coarse mesh damaged fan calculations.

### 4.2.1 Comparison of the Damaged Fan Operating Point

The damaged fan operating point calculated with ANSYS CFX is compared with the steady analysis obtained using the industry CFD solver. The characteristic curve of the damaged fan was mapped by varying the bypass duct static pressure to identify the operating point within 2% error of the fan operating line. A characteristic curve was not calculated using the medium or fine meshes due to the increased computational costs required to compute multiple operating points with these meshes. Instead, the bypass duct static pressure associated with the coarse mesh operating point was used to calculate the operating point with the medium and fine meshes. Figure 4.6 provides the fan operating line normalized by the undamaged operating point along with the damaged fan characteristic curve and the damaged fan operating points calculated with the coarse, medium, and fine mesh and the industry solver. The damaged operating points calculated with the coarse, medium, and fine mesh all lie within 1% error of the operating line.

Table 4.6 lists the undamaged and damaged operating points obtained with the coarse,

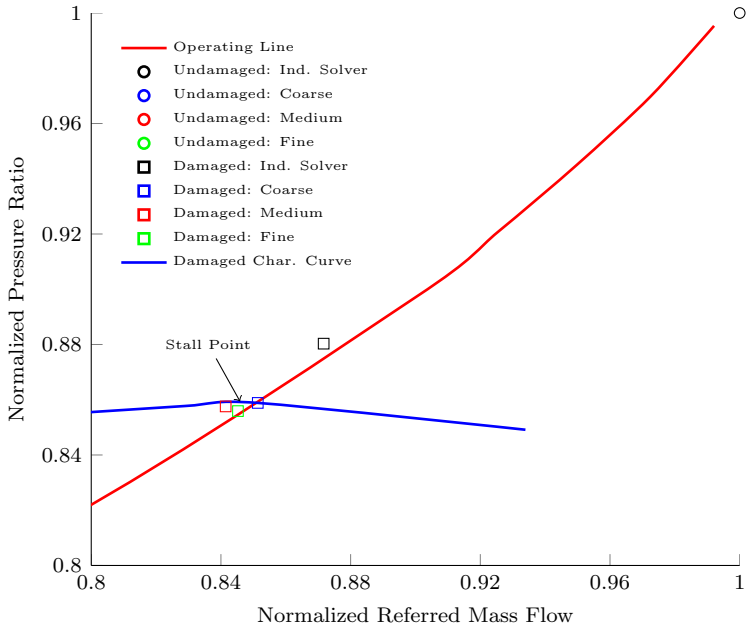


Figure 4.6: Normalized fan map including the operating line, undamaged operating points, damaged operating points, and damaged characteristic curve.

medium, and fine meshes and the industry CFD solver, where the values are normalized by the referred mass flow rate and total pressure ratio of an undamaged fan. Table 4.6 also provides the percent mass flow loss relative to the undamaged fan, where the mass flow loss is costly related to the thrust loss resulting from the bird strike. The coarse, medium, and fine meshes predict a mass flow loss that is 1.9%-2.9% greater than the industry solver. The slightly larger flow loss associated with the medium and fine meshes relative to the coarse mesh is attributed to the increased flow losses captured by the increased mesh resolution in the boundary layer and tip gap. Considering the inherent unsteadiness associated with the damaged fan operating near the stall point, the minor variations in operating point between the ANSYS CFX solver and the industry CFD solver are acceptable.

Table 4.6: Comparison of operating points for the undamaged and damaged fan.

| Solver | Configuration | Normalized $\dot{m}_R$ | Normalized $PR$ | % Flow Loss | %$\Delta$OL |
|---|---|---|---|---|---|
| Industry Solver | Undamaged | 1.000 | 1.000 | N\A | 0.72% |
| ANSYS CFX | Undamaged: Coarse | 1.000 | 0.996 | N\A | 1.3% |
| ANSYS CFX | Undamaged: Medium | 1.000 | 0.996 | N\A | 1.3% |
| ANSYS CFX | Undamaged: Fine | 1.000 | 0.996 | N\A | 1.3% |
| Industry Solver | Damaged | 0.872 | 0.880 | 12.8% | 0.87% |
| ANSYS CFX | Damaged: Coarse | 0.851 | 0.859 | 14.9% | 0.36% |
| ANSYS CFX | Damaged: Medium | 0.842 | 0.858 | 15.9% | 0.84% |
| ANSYS CFX | Damaged: Fine | 0.845 | 0.856 | 15.5% | 0.05% |

### 4.2.2 Comparison of the Damaged Fan Mach Contours

Mach contours at 77% span and mid-chord are presented to qualitatively compare the overall aerodynamic behavior predicted by ANSYS CFX and the industry solver. Figure 4.7 provides a Mach number contour of the damaged fan at 77% span, the location of greatest damage, obtained with the industry CFD solver and ANSYS CFX using the coarse, medium, and fine mesh. The five damaged blades are labeled as blade 1 through blade 5 where blade numbers correspond with those in Fig. 4.4. Overall, the ANSYS CFX solutions agree well with the industry solver in predicting the complex flow field associated with the damaged fan sector, and the increased mesh resolutions of the medium and fine mesh have negligible effect on the solution at 77% span. Both solvers predict a separation bubble caused by the leading edge deformation of blade 2, 4, and 5 that blocks the flow through the downstream passages. For these blades, a greater degree of separated flow and flow blockage is apparent in the ANSYS CFX solutions, which is likely responsible for the greater flow loss predicted by the ANSYS CFX solutions.

Figures 4.8 show Mach number contours on a constant-axial slice of the wheel at mid

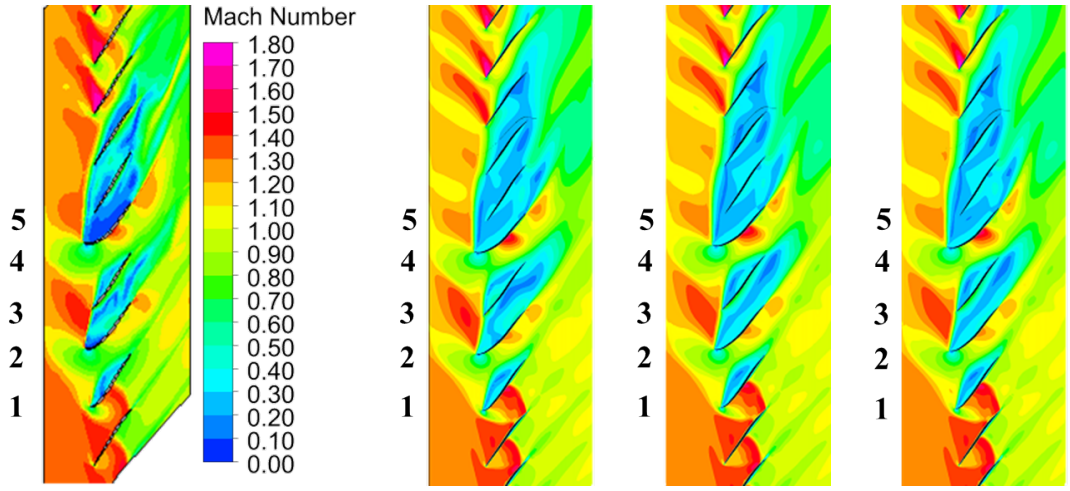


(a) Industry CFD solver. (b) ANSYS CFX: Coarse mesh. (c) ANSYS CFX: Medium mesh. (d) ANSYS CFX: Fine mesh.

Figure 4.7: Comparison of steady Mach number contours of the damaged fan at 77% span.

blade chord obtained with the ANSYS CFX and industry solvers. Again, the ANSYS CFX solutions obtained with the coarse, medium, and fine mesh show a negligible effect of the boundary layer and tip gap mesh resolution. Furthermore, when compared to the industry solver, the ANSYS CFX solutions predict the same overall flow features, especially in the blade passages adjacent to the damaged blades. However, the industry solver predicts a region of stalled flow at the blade tips that covers roughly 3/4 of the fan wheel. In contrast, the ANSYS CFX solutions predict stalled flow for a larger spanwise portion of the blade tips but for only half of the fan wheel. As a result, the flow loss predicted by the industry solver is more evenly distributed across the fan, whereas the flow loss predicted by ANSYS CFX is concentrated at half of the fan wheel.

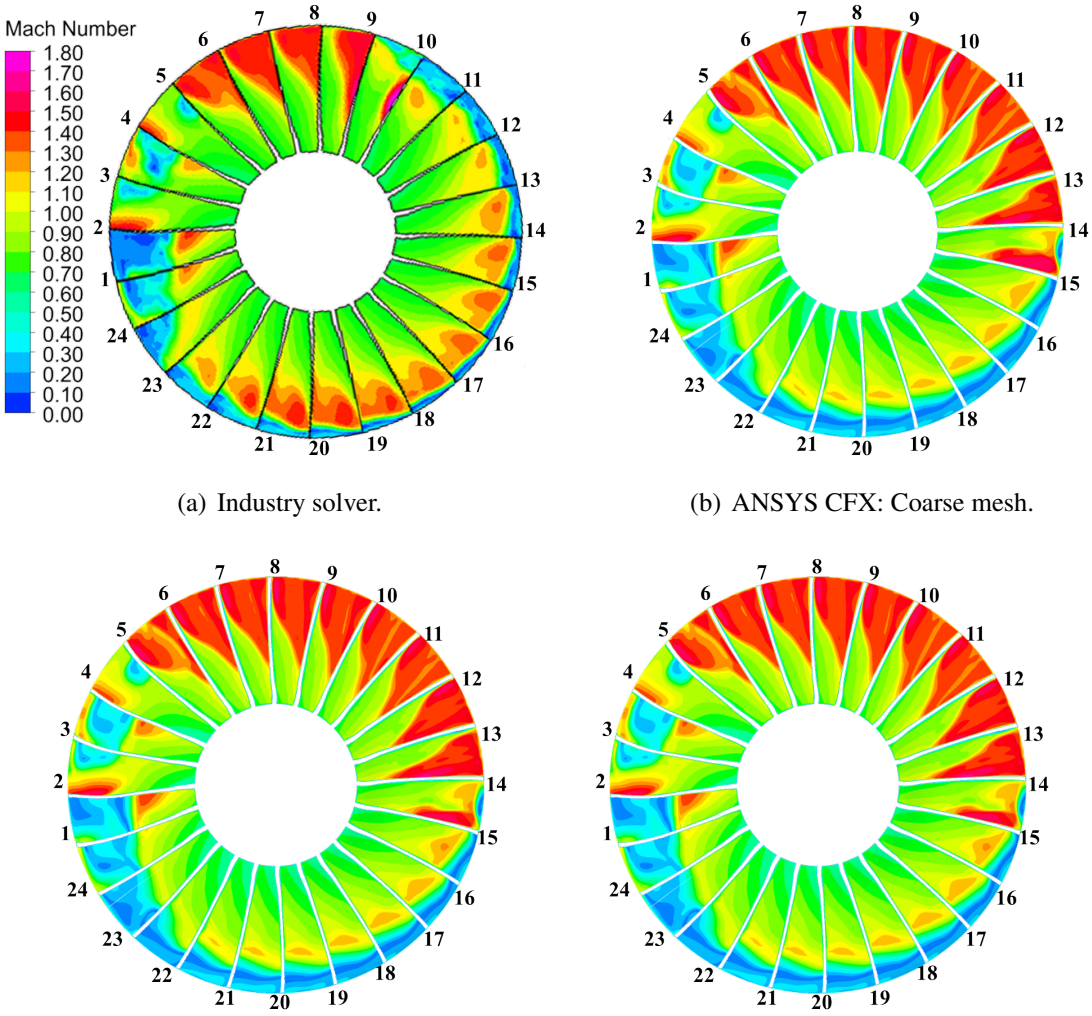


(a) Industry solver.

(b) ANSYS CFX: Coarse mesh.

(c) ANSYS CFX: Medium mesh.

(d) ANSYS CFX: Fine mesh.

Figure 4.8: Comparison of steady Mach contours of the damaged fan at mid-chord (direction of rotation: clockwise).

# CHAPTER 5

# FE-Based Structural Dynamic Model

This chapter describes the structural dynamic model employed to predict the blade response to the unsteady aerodynamic loads associated with damaged fan. The structural dynamic model is implemented in ANSYS Mechanical APDL, a commercially available FE-based structural solver that accommodates one-way and two-way coupling with ANSYS CFX for the forced response and aeroelastic response calculations performed in this study. The ANSYS Mechanical APDL can model nonlinear material behavior, geometric nonlinearities associated with large deformations, and centrifugal effects associated with rotating structures. Further details of ANSYS Mechanical APDL are available in the ANSYS Mechanical APDL Theory Reference Guide [78].

## 5.1 Equations of Motion

The equations of motion for the structural dynamic model are formulated from the principle of virtual work. The principle of virtual work states that a structure initially in equilibrium remains in equilibrium while subject to compatible virtual displacements if the virtual work of the applied forces equals the virtual strain energy [79]. The principle of virtual work for an elastic body subject to inertial forces, body forces, and external forces is given by

Eq. (5.1), where $\delta$ is the variational operator and $V_s$ is the volume of structural body. In Eq. (5.1), $\rho_s \ddot{\mathbf{w}}$ is the inertia force resulting from dynamic motion of the structure, $c\dot{\mathbf{w}}$ is the internal damping force, and $\mathbf{f}$ is the external force [78, 79].

$$\underbrace{\int_{V_s} \delta\boldsymbol{\varepsilon}^T \boldsymbol{\sigma} dV_s}_{\text{Virtual Strain Energy}} = \underbrace{-\int_{V_s} \delta\mathbf{w}^T(\rho_s \ddot{\mathbf{w}} + c\dot{\mathbf{w}})dV_s + \delta\mathbf{w}^T\mathbf{f}}_{\text{Virtual Work of Applied Forces}} \tag{5.1}$$

The Finite Element Method is employed to solve Eq. (5.1) by discretizing the structural body into an assembly of nodes and elements. The displacement field within each element is expressed in terms of the nodal displacements using shape functions defined in the element-fixed coordinate system $< \xi, \eta, \zeta >$ as expressed in Eq. (5.2). In Eq. (5.2), $\mathbf{w}$ represents the displacement field of an element, $\mathbf{N}$ is the vector of element shape functions, and $\mathbf{u}$ is the vector of nodal displacements.

$$\mathbf{w} = \mathbf{N}\mathbf{u} \tag{5.2}$$

The elastic strain is related to the nodal displacements using the strain-displacement matrix, $\mathbf{B}$, as given in Eq. (5.3). The stress is related to the elastic strain through the compliance matrix, $\mathbf{D}$, as expressed in Eq. (5.3).

$$\boldsymbol{\varepsilon} = \mathbf{B}\mathbf{u} \tag{5.3}$$

$$\boldsymbol{\sigma} = \mathbf{D}\boldsymbol{\varepsilon} \tag{5.4}$$

Each element within the structural domain must satisfy Eq. (5.1), which is expressed

for a single element by Eq. (5.5). The external force vector in Eq. (5.1) is replaced by the nodal force vector, $\mathbf{f_a}$, and the last term in Eq. (5.5) is the virtual work associated with the forces applied at the nodes.

$$\int_{V_s} \delta\mathbf{u}^T\mathbf{B}^T\mathbf{D}\mathbf{B}\mathbf{u}dV_s = -\int_{V_s} \mathbf{N}^T\delta\mathbf{u}^T\left(\rho_s\mathbf{N}\ddot{\mathbf{u}} + c\mathbf{N}\dot{\mathbf{u}}\right)dV_s + \delta\mathbf{u}^T\mathbf{f_a} \tag{5.5}$$

The virtual displacement vector, $\delta\mathbf{u}$, represents an arbitrary set of displacements common to each term in Eq. (5.5). Therefore, Eq. (5.5) can be reduced to the form given in Eq. (5.6), where $\rho_s$ and $c$ are assumed constant throughout each element. The element mass, damping, and stiffness matrices in Eq. (5.6) are calculated using Eqs. (5.7), (5.8), and (5.9), respectively.

$$\mathbf{m}\ddot{\mathbf{u}} + \mathbf{c}\dot{\mathbf{u}} + \mathbf{k}\mathbf{u} = \mathbf{f_a} \tag{5.6}$$

$$\mathbf{m} = \rho_s\int_{V_s} \mathbf{N}^T\mathbf{N}dV_s \tag{5.7}$$

$$\mathbf{c} = c\int_{V_s} \mathbf{N}^T\mathbf{N}dV_s \tag{5.8}$$

$$\mathbf{k} = \int_{V_s} \mathbf{B}^T\mathbf{D}\mathbf{B}dV_s \tag{5.9}$$

The equations of motion for the structural dynamics system are given by Eq. (5.10), where the global mass, damping, and stiffness matrices are assembled from the respective element matrices. In Eq. (5.10), $\mathbf{U}$ is the nodal displacement vector, in global coordinates,

for the entire FE mesh and $\mathbf{F_a}$ is the applied nodal force vector.

$$\mathbf{M\ddot{U}} + \mathbf{C\dot{U}} + \mathbf{KU} = \underbrace{\mathbf{F_\Omega} + \mathbf{F}_{\text{aero}}}_{\mathbf{F_a}} \tag{5.10}$$

Equation (5.10) is solved in a stationary reference frame. To account for the centrifugal effects due to engine rotation, centrifugal forces are applied to the element nodes. The centrifugal force vector for a single element is given by Eq. (5.11), and the assembled centrifugal force vector is denoted by $\mathbf{F_\Omega}$ in Eq. (5.10). Equation (5.10) focuses on the structural dynamic portion of the aeroelastic system and it is not aware of the aerodynamic module. The assembled aerodynamic force vector, $\mathbf{F}_{\text{aero}}$, represents the aerodynamic force transferred to the FE nodes from the CFD calculations during the forced response and aeroelastic response calculations.

$$\mathbf{f_\Omega} = \rho_s \int_{V_S} \mathbf{N}^T [\mathbf{\Omega} \times (\mathbf{\Omega} \times \mathbf{r})] dV_s \tag{5.11}$$

## 5.2 Implementation of the Structural Dynamic Model in ANSYS Mechanical APDL

The computational domain for the structural dynamic model of the damaged fan consists of 24 individual blades, as shown in Fig. 2.11. The hub flexibility is assumed to be negligible compared to that of the fan blades; therefore, the hub disk is not modeled. The blades are cantilevered at the blade root and boundary conditions are imposed to mimic the manner in which the fan blades are fastened to the hub disk. The damaged and un-

Table 5.1: Titanium blade material properties.

| Material Property | Property Value |
|---|---|
| $\rho_s$ | $0.414\times10^{-3}$ [lb/in$^3$] |
| $E$ | $16.00\times10^{6}$ [lb/in$^2$] |
| $\nu$ | 0.33 |

damaged blades are assumed to be elastic. The residual stress and strain hardening of the damaged blades that results from the bird impact analysis is neglected. The fan blade material is titanium and is modeled with a linearly elastic, isotropic material law where the stress-strain relationship is given by Eq. (5.12). Table 5.1 provides the material properties of the blade. In practice, fan blades include several sources of structural damping such as material damping and interfacial damping. For simplicity of the structural dynamic model, no structural damping is implemented and the damping matrix in Eq. (5.10) is zero. The blade responses presented in Chapter 8 neglect the influence of structural damping, and future studies should examine the role of structural damping in the blade response.

$$\underbrace{\begin{Bmatrix} \varepsilon_{11} \\ \varepsilon_{22} \\ \varepsilon_{33} \\ \varepsilon_{12} \\ \varepsilon_{23} \\ \varepsilon_{13} \end{Bmatrix}}_{\varepsilon} = \underbrace{\begin{bmatrix} 1/E & -\nu/E & -\nu/E & 0 & 0 & 0 \\ -\nu/E & 1/E & -\nu/E & 0 & 0 & 0 \\ -\nu/E & -\nu/E & 1/E & 0 & 0 & 0 \\ 0 & 0 & 0 & E/2(1+\nu) & 0 & 0 \\ 0 & 0 & 0 & 0 & E/2(1+\nu) & 0 \\ 0 & 0 & 0 & 0 & 0 & E/2(1+\nu) \end{bmatrix}}_{\mathbf{D}^{-1}} \underbrace{\begin{Bmatrix} \sigma_{11} \\ \sigma_{22} \\ \sigma_{33} \\ \sigma_{12} \\ \sigma_{23} \\ \sigma_{13} \end{Bmatrix}}_{\sigma} \tag{5.12}$$

Equation (5.10) is solved using a FE mesh that is generated from the CAD model pre-

sented in Fig. 2.11. The FE mesh of the fan blades is composed of 8-noded, solid, hexahedral elements (ANSYS SOLID185 element type) with three translational degrees of freedom at each node. The displacement field within the element is obtained using trilinear basis functions expressed in the element-fixed $< \xi, \eta, \zeta >$ coordinate system shown in Fig. 5.1 [80].

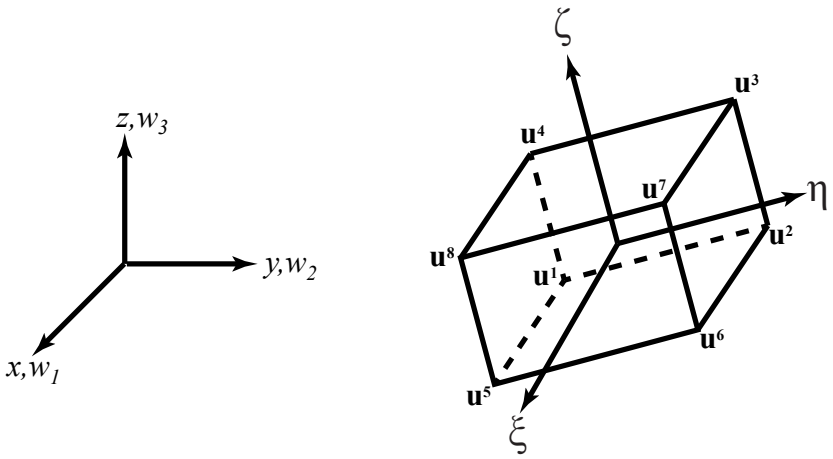


Figure 5.1: ANSYS SOLID185 hexahedral element with element-fixed coordinate system.

The implementation of the structural dynamic model in ANSYS Mechanical APDL includes a large deflection formulation that is limited to geometric nonlinearity. In the case of the rotating system, the geometric nonlinearity allows a systematic representation of the centrifugal loads. This is accomplished by a geometric stiffness matrix where the radial loading depends on the speed of rotation and the distance of the element from the axis of rotation. A Newton-Raphson iterative procedure is implemented to update the stiffness matrix within each time-step.

The HHT-$\alpha$ (Ref. [81]) time-integration scheme is implemented to integrate Eqs. (5.10) in time. The HHT-$\alpha$ method assumes the form of the equations of motion given in Eqs. (5.13) [81]. Equations (5.14) and (5.15) provide the time-integration formulas for $\mathbf{U}_{t+\Delta t_s}$ and

$\dot{\mathbf{U}}_{t+\Delta t_s}$, where $\beta$ and $\gamma$ are integration parameters [81]. The HHT-$\alpha$ is unconditionally stable and second-order accurate if the integration parameters meet the criteria described by Eqs. (5.16)-(5.18). For this study, the ANSYS default values for the HHT-$\alpha$ integration parameters are used: $\gamma = 0.6$, $\beta = 0.3025$, and $\alpha = -0.1$.

$$\mathbf{M}\ddot{\mathbf{U}}_{t+\Delta t_s} + (1+\alpha)\mathbf{K}\mathbf{U}_{t+\Delta t_s} - \alpha\mathbf{K}\mathbf{U}_t = \mathbf{F}_{\mathbf{a}t+\Delta t_s} \tag{5.13}$$

$$\mathbf{U}_{t+\Delta t_s} = \mathbf{U}_t + \dot{\mathbf{U}}_t\Delta t_s + [(1/2 - \beta)\ddot{\mathbf{U}}_t + \beta\ddot{\mathbf{U}}_{t+\Delta t_s}]\Delta t_s^2 \tag{5.14}$$

$$\dot{\mathbf{U}}_{t+\Delta t_s} = \dot{\mathbf{U}}_t + [(1-\gamma)\ddot{\mathbf{U}}_t + \gamma\ddot{\mathbf{U}}_{t+\Delta t_s}]\Delta t_s \tag{5.15}$$

$$\gamma = 1/2 - \alpha \tag{5.16}$$

$$\beta = (1-\alpha)^2/4 \tag{5.17}$$

$$-1/3 \leq \alpha \leq 0 \tag{5.18}$$

## 5.3 FE Mesh Sensitivity Study

A mesh sensitivity study was conducted to identify the FE mesh resolution required for this study. The FE mesh follows a structure topology, as depicted in Fig. 5.2 for a single blade. In Fig. 5.2, the wetted surface of the blade is highlighted in green. The FE mesh

also features a curved leading edge and trailing edge to improve mapping between the FE mesh and CFD mesh for transfer of the aerodynamic force and structural displacements during the coupled calculations. The FE mesh was parameterized using the number of span-wise elements, number of chord-wise elements, and number of through-the-thickness elements. Six candidate meshes were considered to assess the effects of mesh density on modal frequencies and displacements for a rotating, undamaged blade. Table 5.2 provides the number of chord-wise, span-wise, and thickness elements as well as the total number of nodes and elements per blade. Mesh A represents the finest mesh resolution considered and is the mesh in which all others are compared.

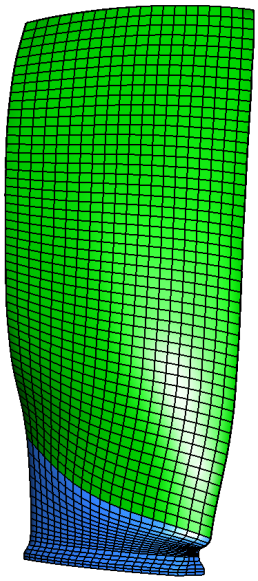

Figure 5.2: General mesh topology for an undamaged blade with the wetted surface highlighted in green.

The modal frequencies of a fan blade rotating at 100% take-off engine RPM are compared in Table 5.3. Table 5.6 lists the first 5 modal frequencies obtained with Mesh A and the percent error corresponding to the modal frequencies calculated with the other candidate meshes. The coarser meshes are deemed to be acceptable if they reproduce the first

Table 5.2: FE mesh parameters for the mesh sensitivity study.

| | Chord | Span | Thickness | # Nodes | # Elements |
|---|---|---|---|---|---|
| Mesh A | 40 | 106 | 6 | 30709 | 25440 |
| Mesh B | 40 | 106 | 3 | 17548 | 12720 |
| Mesh C | 20 | 67 | 3 | 5712 | 4020 |
| Mesh D | 20 | 56 | 2 | 3591 | 2240 |
| Mesh E | 10 | 346 | 2 | 1584 | 960 |
| Mesh F | 10 | 346 | 1 | 726 | 320 |

five modal frequencies with an error of less than 1%, when compared to the solution based on Mesh A. The main reason for using the first 5 modal frequencies is due to the expectation that these modes will dominate the response of the damaged fan. Based on this requirement, Meshes B, C, and D are identified as suitable meshes for this study.

Table 5.3: First 5 modal frequencies of a rotating, undamaged blade.

| | 1st Bending 1B | 2nd Bending 2B | 1st Torsion 1T | 3rd Bending 3B | 2nd Torsion 2B |
|---|---|---|---|---|---|
| Mesh A | 126.5 [Hz] | 261.5 [Hz] | 380.2 [Hz] | 530.0 [Hz] | 709.73 [Hz] |
| Mesh B | 0.25% | 0.32% | 0.08% | 0.20% | 0.07% |
| Mesh C | 0.37% | 0.55% | 0.27% | 0.50% | 0.41% |
| Mesh D | 0.63% | 0.81% | 0.42% | 0.79% | 0.81% |
| Mesh E | 0.91% | 1.32% | 0.91% | 1.97% | 2.00% |
| Mesh F | 1.22% | 1.76% | 1.35% | 2.86% | 3.87% |

The total displacement at the blade surface calculated with meshes A, B, C, and D at 100% take-off RPM are also compared. Accurate calculation of the rotating blade geometry is necessary to define the hot blade geometry for the aerodynamic computations. The total displacement, defined as the magnitude of the displacement vector, is calculated with Eq. (5.19). Table 5.4 presents the maximum total displacement for each mesh, along with the percent error compared to Mesh A. All meshes capture the maximum displacement,

which occurs at the blade tip leading edge, with less than 1% error.

$$||\mathbf{u}^n|| = \sqrt{u_1^{n2} + u_2^{n2} + u_3^{n2}} \tag{5.19}$$

Table 5.4: Total displacement for the rotating, undamaged blade.

| | $max(\|\|\mathbf{u}^n\|\|)$ | % Error |
|---|---|---|
| Mesh A | 0.370 [in] | N/A |
| Mesh B | 0.370 [in] | -0.1% |
| Mesh C | 0.369 [in] | -0.5% |
| Mesh D | 0.368 [in] | -0.6% |

Based on the mesh sensitivity study, Mesh C was selected as an acceptable compromise between mesh size and accuracy of solution. The final mesh used in this study is shown for a single undamaged blade in Fig. 5.3(a). Figure 5.3(b) depicts the computational mesh of the damaged fan, where the damaged blades are highlighted in orange. The same FEM mesh topology and mesh resolution is used for the undamaged and damaged blades.

## 5.4 Rotating Mode Shapes and Frequencies

The centrifugal effects due to rotation have a significant influence on the steady-state displacement and modal frequencies of a rotating blade. A static structural analysis starting from the non-rotating, denoted "cold", geometry is performed to obtain the rotating, denoted "hot", geometry that includes the centrifugal loads. The structural displacement field resulting from rotation is depicted in Fig. 5.4 for the 100%, 75% and 60% throttle settings. The engine RPM for each thrust level and the corresponding maximum displacement, which occurs at the blade tip leading edge, is provided in Table 5.5. The hot blade

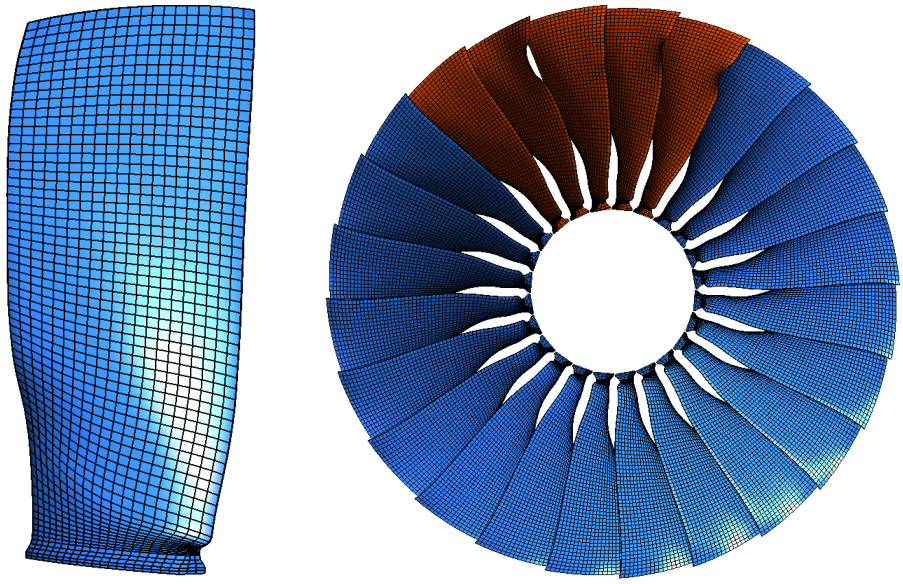

(a) Final FE mesh for an undamaged blade.

(b) Bird-damaged FE mesh with damaged blades highlighted in orange.

Figure 5.3: Final FE mesh: 137,088 total nodes, 96,480 total elements.

configuration defines the blade geometry for the CFD mesh generation.

Table 5.5: Maximum tip displacement for the 100%, 75%, and 60% throttle settings.

| Throttle Setting | 100% | 75% | 60% |
|---|---|---|---|
| Engine Rotation Speed | 5894.7 [RPM] | 5260.2 [RPM] | 4841.7 [RPM] |
| $max(\|\|\mathbf{u}^n\|\|)$ | 0.37 [in] | 0.31 [in] | 0.27 [in] |

The first 5 mode shapes of a rotating, undamaged fan blade at 100% take-off engine rotational speed are shown in Figs. 5.5. The mode shapes of a rotating, undamaged blade at 75% and 60% take-off thrust are similar in shape. The natural frequencies of the first 5 mode shapes of a rotating, undamaged blade at the 100%, 75% and 60% throttle settings are listed in Table 5.6 along with the natural frequencies of a non-rotating blade. The mode shapes of the damaged blades are similar to those of the undamaged blade, and the natural frequencies for each damaged blade are provided in Table 5.6. Note that the frequencies and mode shapes described in Fig. 5.5 and Table 5.6 have been identified as "1st Bending

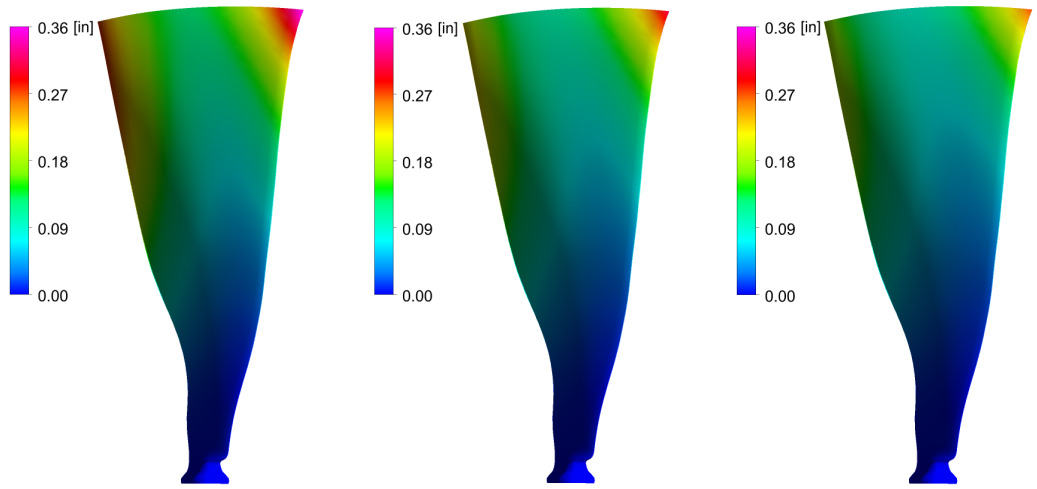


(a) Hot geometry at 100% throttle setting.

(b) Hot geometry at 75% throttle setting.

(c) Hot geometry at 60% throttle setting.

Figure 5.4: Total displacement from cold-to-hot calculation.

Mode", "2nd Bending Mode", etc.. However, due to the built-in twist of the blade and the effect of rotation, these modes are coupled where all three degrees of freedom (bending out of the plane of rotation, bending in the plane of rotation, and torsion) participate. By identifying the mode as "1st Bending Mode" it is impled that the primary contribution to the mode shape comes from bending.

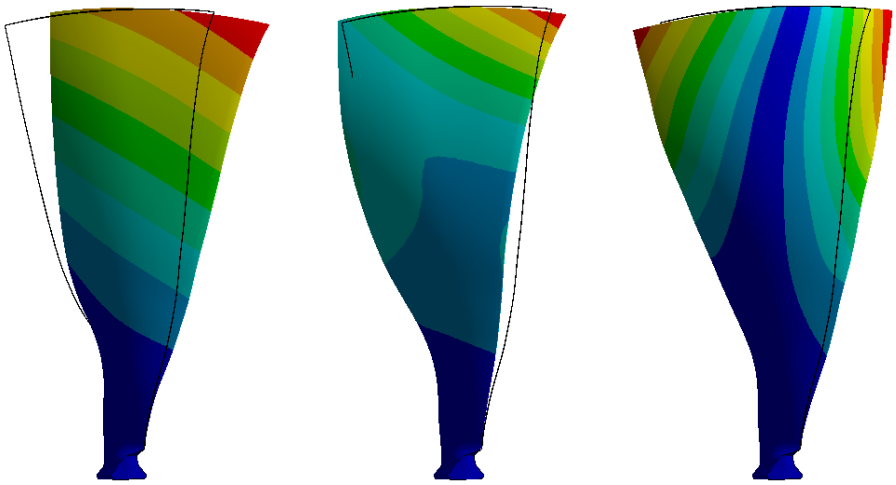

(a) Mode 1, 1st Bending Mode (1B).

(b) Mode 2, 2nd Bending Mode (2B).

(c) Mode 3, 1st Torsion Mode (1T).

(d) Mode 4, 3rd Bending Mode (3B).

(e) Mode 5, 2nd Torsion Mode (2T).

Figure 5.5: First 5 mode shapes of a rotating, undamaged blade.

Table 5.6: Natural frequencies of the first 5 modes of undamaged and damaged blades.

| **100% Throttle Setting** | | | | | |
|---|---|---|---|---|---|
| | 1B [Hz] | 2B [Hz] | 1T [Hz] | 3B [Hz] | 2T [Hz] |
| Undamaged | 126.97 | 262.95 | 381.21 | 532.65 | 712.65 |
| Blade 1 | 126.98 | 263.61 | 373.44 | 537.52 | 699.62 |
| Blade 2 | 126.70 | 264.81 | 301.22 | 574.09 | 656.77 |
| Blade 3 | 127.00 | 263.69 | 374.25 | 534.29 | 717.84 |
| Blade 4 | 126.85 | 263.37 | 330.25 | 560.51 | 654.37 |
| Blade 5 | 127.03 | 264.11 | 339.39 | 560.24 | 677.24 |

| **75% Throttle Setting** | | | | | |
|---|---|---|---|---|---|
| | 1B [Hz] | 2B [Hz] | 1T [Hz] | 3B [Hz] | 2T [Hz] |
| Undamaged | 118.11 | 236.51 | 379.31 | 510.31 | 710.63 |
| Blade 1 | 118.12 | 247.15 | 370.82 | 515.66 | 696.66 |
| Blade 2 | 117.83 | 251.10 | 293.06 | 554.54 | 647.20 |
| Blade 3 | 118.14 | 247.28 | 371.39 | 513.13 | 714.93 |
| Blade 4 | 117.99 | 247.70 | 324.12 | 536.80 | 651.86 |
| Blade 5 | 118.17 | 246.57 | 334.12 | 537.62 | 673.94 |

| **60% Throttle Setting** | | | | | |
|---|---|---|---|---|---|
| | 1B [Hz] | 2B [Hz] | 1T [Hz] | 3B [Hz] | 2T [Hz] |
| Undamaged | 112.22 | 235.99 | 378.26 | 496.05 | 709.39 |
| Blade 1 | 112.23 | 236.51 | 369.51 | 501.72 | 694.81 |
| Blade 2 | 111.94 | 241.77 | 288.51 | 541.70 | 641.80 |
| Blade 3 | 112.25 | 236.68 | 369.64 | 499.60 | 713.03 |
| Blade 4 | 112.10 | 237.50 | 320.40 | 521.78 | 650.39 |
| Blade 5 | 112.28 | 237.31 | 330.84 | 523.19 | 671.97 |

| **Non-rotating** | | | | | |
|---|---|---|---|---|---|
| | 1B [Hz] | 2B [Hz] | 1T [Hz] | 3B [Hz] | 2T [Hz] |
| Undamaged | 57.27 | 161.23 | 369.82 | 404.86 | 695.27 |
| Blade 1 | 57.17 | 161.29 | 353.99 | 414.80 | 677.23 |
| Blade 2 | 58.42 | 173.56 | 263.66 | 455.62 | 612.55 |
| Blade 3 | 57.32 | 161.81 | 352.73 | 415.40 | 692.51 |
| Blade 4 | 58.18 | 165.65 | 294.93 | 425.70 | 641.10 |
| Blade 5 | 57.35 | 162.81 | 307.07 | 430.98 | 658.97 |

# CHAPTER 6

# Framework for Aeroelastic Response Computations

The ANSYS Multi-field solver (ANSYS MFX) is used to couple the ANSYS CFX aerodynamic solver and ANSYS Mechanical APDL structural solver for the forced response and aeroelastic response calculations performed in this study. The following sections describe the computational frameworks for the forced response and aeroelastic response calculations. Details of the aerodynamic load and structural displacement transfer between the ANSYS CFX and ANSYS Mechanical APDL at the wetted surface of the blade are also provided. A sample aeroelastic response calculation is also presented to demonstrate the aeroelastic response framework. Further information regarding the coupling algorithm and mapping scheme is available in the ANSYS documentation [82].

## 6.1 One-way Forced Response Framework

For the one-way forced response calculation, the unsteady aerodynamic loads are calculated and applied on the structural model at each time-step to obtain the structural response. For this case, the CFD mesh is not deformed as the structure deforms; therefore, the feedback mechanism of the structural response on the unsteady aerodynamic loading is not captured. The aerodynamic load for the forced response is time dependent and thus it

captures only the transient nature of the aerodynamic loading. Equation (6.1) governs the forced response calculations.

$$\mathbf{M}\ddot{\mathbf{U}} + \mathbf{K}\mathbf{U} = \mathbf{F}_{\mathbf{\Omega}} + \mathbf{F}_{\text{aero}}(t) \tag{6.1}$$

A flow chart of the force response analysis is shown in Fig. 6.1. The mapping between the hot FE mesh and the CFD mesh at the wetted surface is performed to establish the fluid structure interface. Next, a steady CFD calculation is carried out to generate the initial conditions for the unsteady CFD calculations that are subsequently used in the forced response calculation. During each time-step of the forced response calculation, the aerodynamic pressure and viscous loads from the unsteady CFD analysis are transferred to the surface of the FE mesh and the structural dynamic response is calculated.

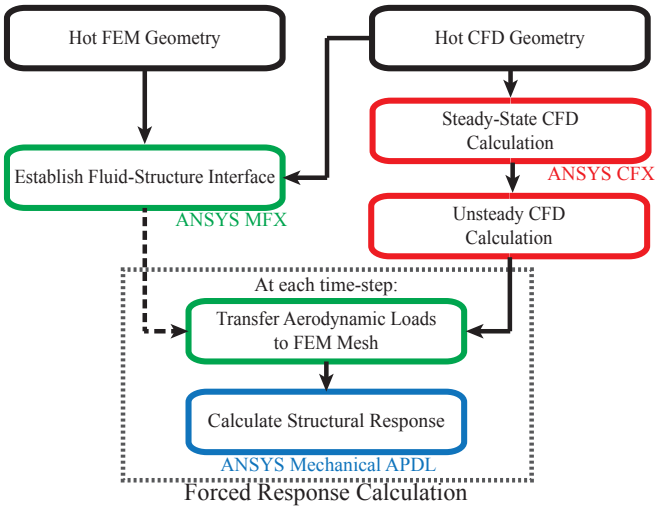


Figure 6.1: Schematic of the forced response framework.

## 6.2 Fully-Coupled Aeroelastic Framework

To obtain the coupled fluid-structure aeroelastic response, an implicit coupling algorithm is employed where the aerodynamic and structural components representing the fan are solved iteratively in each time-step. The CFD mesh is deformed with the structure such that the time-varying displacement at the blade surface influences the aerodynamic loads on the structure. The aerodynamic load varies with time due to transient effects in the aerodynamic calculation caused by both the bird damage and the blade motion. The equations of motion for the aeroelastic response calculations are provided by Eq. 6.2.

$$\mathbf{M}\ddot{\mathbf{U}} + \mathbf{K}\mathbf{U} = \mathbf{F}_{\mathbf{\Omega}} + \mathbf{F}_{\text{aero}}(t, \mathbf{U}, \dot{\mathbf{U}}, \ddot{\mathbf{U}}) \tag{6.2}$$

A flow chart of the coupled aeroelastic framework is shown in Fig. 6.2. The mapping between the FE mesh and the CFD mesh at the wetted surface is performed to establish the fluid structure interface. Next, the aerodynamic forces from a steady CFD calculation of the damaged fan are applied to a static structural model to initialize the structural and aerodynamic models for the aeroelastic response calculations. Within each time-step of the aeroelastic response calculation, the aerodynamic state is calculated and the associated aerodynamic loads are transferred to the FE mesh. The resulting structural displacements are then transferred to the CFD mesh blade surface and the interior CFD nodes are displaced by the amount mandated by the structural deformation.

Coupling sub-steps within each physical time-step are also introduced so as to ensure convergence of the aerodynamic loads and structural displacements as required by the implicit solution procedure. Convergence occurs when the changes in loads and dis-

placements between two consecutive sub-steps are smaller than a specified tolerance level. Equation (6.3) represents the convergence criterion enforced in ANSYS CFX, where the default convergence tolerance of $\varepsilon = 0.01$ (1%) is specified [82].

$$\log(||\varphi_{new} - \varphi_{old}||/||\varphi_{new}||) - log(\varepsilon) \leq 0 \tag{6.3}$$

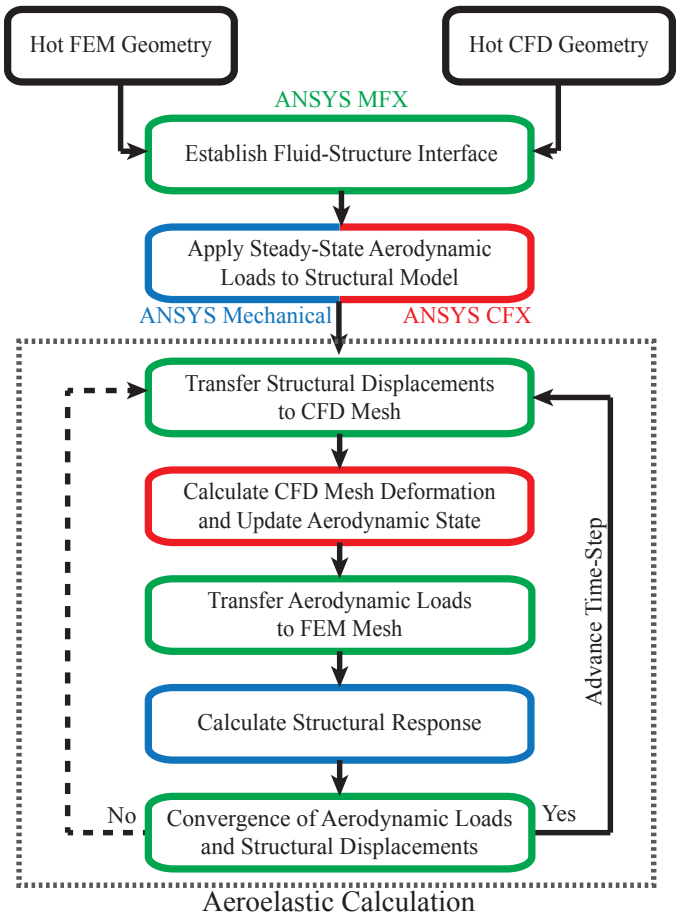


Figure 6.2: Schematic of the aeroelastic response framework.

## 6.3 Aerodynamic Force and Structural Displacement Transfer

The aerodynamic forces, or loads, have to be transferred from the CFD mesh to the FEM mesh at the wetted surface of the fan blade to obtain $\mathbf{F}_{\text{aero}}$ in Eq. (5.10). This is a requirement for both the forced response as well as the coupled aeroelastic calculations. The aerodynamic forces are calculated at each CFD node on the blade surface using Eq. (6.4) and include contributions from the aerodynamic pressure and viscous wall stresses. The aerodynamic forces are transferred to the FE nodes on the blade surface using the conservative interpolation scheme in ANSYS MFX. When the blade surface on the CFD mesh and FE mesh match exactly, the conservative interpolation scheme guarantees the conservation of the overall force transfer. In addition, the conservative interpolation scheme generally preserves the local aerodynamic load distribution transferred from the CFD mesh to the FE mesh.

$$F_f^n(t) = \int_{S_f^n} (P(t) + \tau(t)) \cdot \mathbf{n_a} dS_f^n \tag{6.4}$$

For the aeroelastic calculations, the structural displacements are transferred from the FE mesh to the CFD mesh using the profile-preserving interpolation scheme in ANSYS MFX. Each CFD node on the blade surface is mapped to a structural FE on the blade surface. The shape functions of the associated FE are used to interpolate the displacement at corresponding CFD node. This interpolation scheme preserves the local distributions of displacements transferred from the coarse FE mesh to the finer CFD mesh. If a mismatch between the blade surfaces exist, the displacement transferred to the CFD mesh is

interpolated from the nearest FE node.

The CFD mesh displacement is prescribed on the blade surface based on the structural displacement and is set to zero on the inlet, outlet bypass, outlet core, and splitter surfaces. The CFD nodes on the hub and shroud are permitted to slide on the boundaries so that the original surfaces of revolution are maintained. The displacement of the interior CFD nodes is governed by the displacement-diffusion equation represented by Eq. (6.5). In Eq. (6.5), $\Gamma_M$ is the mesh diffusivity and is analogous to the mesh stiffness, and $\mathbf{\Psi}$ is the mesh displacement relative to the mesh at the previous time-step.

$$\nabla \cdot (\Gamma_M \nabla \mathbf{\Psi}) = 0 \tag{6.5}$$

A spatially dependent mesh diffusivity is useful for preserving the initial mesh distribution and element quality. A large mesh diffusivity restricts movement of the nodes relative to each other, with regions of lower mesh diffusivity absorbing a larger amount of the mesh displacement. In this study, a mesh diffusivity inversely proportional to the element volume is specified so that the larger elements in the blade passages absorb most of the displacement and the small elements near the blade surface do not become highly skewed. Equation (6.6) provides the expression for mesh diffusivity, where the exponent controls how quickly the mesh diffusivity changes with element volume.

$$\Gamma_M = \left( \frac{V_{f\text{ref}}}{V_f} \right)^2 \tag{6.6}$$

## 6.4 Example of an Aeroelastic Response Calculation

An aeroelastic response calculation is illustrated for an undamaged fan containing a single flexible blade. For this calculation, a full-wheel aerodynamic model is coupled to a structural dynamic model of a single cantilevered blade using the aeroelastic response framework illustrated by Fig. 6.2. The aerodynamic forces and structural displacements are transferred between the CFD mesh and FE mesh for the flexible blade, and the remaining blades in the aerodynamic model are assumed to be rigid. The aerodynamic environment of the undamaged fan is steady; therefore, an initial disturbance is introduced to initialize the aeroelastic response. The freestream conditions for this calculation correspond to standard day +27°F conditions, the engine rotational speed is set to the 100% throttle setting, and the flight Mach number is zero.

The aeroelastic response calculation is initialized by the following procedure. A static structural analysis starting from the cold geometry is performed to obtain the hot geometry that accounts for the centrifugal effects. This hot structural geometry defines the blade geometry for the CFD mesh. The mapping between the hot FE mesh and the CFD mesh at the wetted surface is performed to establish the fluid structure interface. The number of unmapped CFD and FE nodes and the associated area on the blade surface is presented in Table 6.1. Approximately 10% of the CFD nodes on the blade surface are not mapped to the FE mesh. However, these nodes represent only 2.76% of the blade surface and are primarily located on the blade leading edge, trailing edge, and near the blade root.

A static aeroelastic equilibrium calculation is the final initialization step required before the aeroelastic response calculations. Aeroelastic equilibrium represents the blade configuration due to equilibrium between the steady aerodynamic loads and the static structural

Table 6.1: Details of the CFD/FE mesh mapping.

| | CFD Mesh | FEM Mesh |
|---|---|---|
| Total area | 302.25 [$in^2$] | 302.76 [$in^2$] |
| Non-matching area | 8.41 [$in^2$] | 2.19 [$in^2$] |
| Non-matching area fraction | 2.78% | 0.72% |
| Total surface nodes | 15092 | 2384 |
| Unmapped nodes | 1452 | 4 |

displacements. Determining the static aeroelastic equilibrium usually requires several iterations between the aerodynamic and structural solvers. For fan blades, the displacement resulting from the steady aerodynamic loads is small and does not result in a significant change in the aerodynamic loads. Therefore, a single iteration between the aerodynamic and structural solver is sufficient to obtain the aeroelastic equilibrium configuration. During this calculation, the aerodynamic loads from the steady CFD calculation are applied to the static structural model and the resulting structural displacements are transferred to the CFD mesh. The resulting blade configuration is denoted by the term "running" blade geometry and includes both centrifugal loads and steady aerodynamic loads. A steady CFD calculation is performed for the running geometry to generate the initial conditions for the unsteady CFD calculation used in the subsequent aeroelastic response calculation.

The aeroelastic response calculation is initialized from the running blade configuration and the associated steady aerodynamic loading. The aerodynamic and structural calculations for the aeroelastic response are transient. The magnitude of blade tip leading edge displacement for the static aeroelastic equilibrium calculation and the aeroelastic response calculation is provided in Fig. 6.3. The first increase in tip displacement during the static aeroelastic equilibrium calculation results from the centrifugal loads and the subsequent

increase results from the steady aerodynamic loads. An initial disturbance is applied at $t = 0$ that results in a transient response of the blade shown by the black line in Fig. 6.3. The figure also includes the tip displacement for an uncoupled blade subject to the same initial disturbance denoted by the blue curve in the figure. Thus the two lines represent a comparison between the aeroelastic and the free vibration response. The amplitude of the blade tip displacement from the aeroelastic response that decays in time clearly illustrates the effect of the aeroelastic coupling.

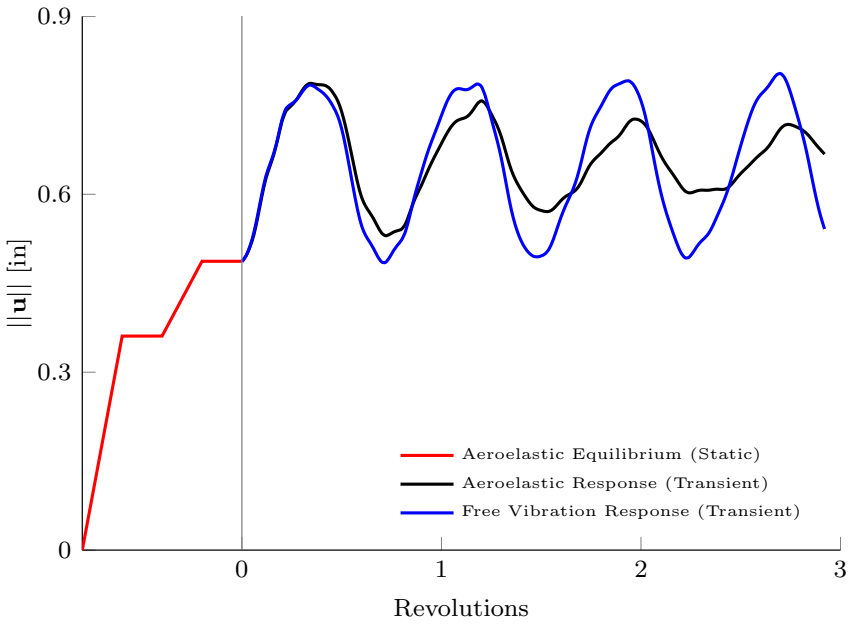


Figure 6.3: Total displacement of blade tip leading edge from the example aeroelastic response calculation.

The resultant aerodynamic force obtained from the aerodynamic calculation is compared to the resultant aerodynamic force applied to the structural dynamic model to determine the accuracy of the force transfer. Figures 6.4(a)-6.4(c) presents the $x$, $y$, and $z$ components of the resultant aerodynamic force acting on the blade from the aerodynamic calculations, normalized by the initial value. The resultant aerodynamic force components are calculated by summing the force components from each CFD node on the blade surface.

Table 6.2: Error between the resultant aerodynamic force from the aerodynamic calculations and the resultant aerodynamic forced applied to the structure.

| | $L^1$ Error | Max. Error |
|---|---|---|
| $\sum F_x$ | 0.60% | 0.77% |
| $\sum F_y$ | 0.16% | 0.35% |
| $\sum F_z$ | 0.25% | 0.45% |

Figures 6.4(a)-6.4(c) also present the $x$, $y$, and $z$ components of the resultant force applied to the structural dynamic model and are calculated by summation of the components of the applied load vector at the blade surface. Table 6.2 presents the $L^1$ relative error norm and maximum error between the resultant aerodynamic force components from the aerodynamic calculations and the resultant aerodynamic forced applied to the structure. Overall, excellent agreement is noted.

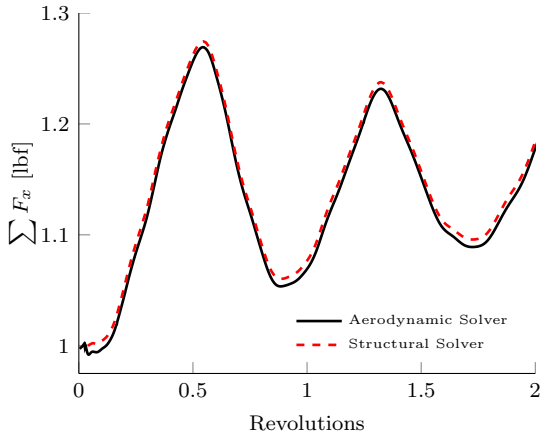


(a) Comparison of $\sum F_x$

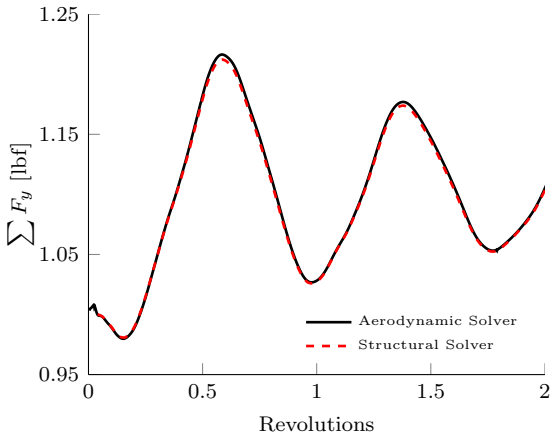


(b) Comparison of $\sum F_y$

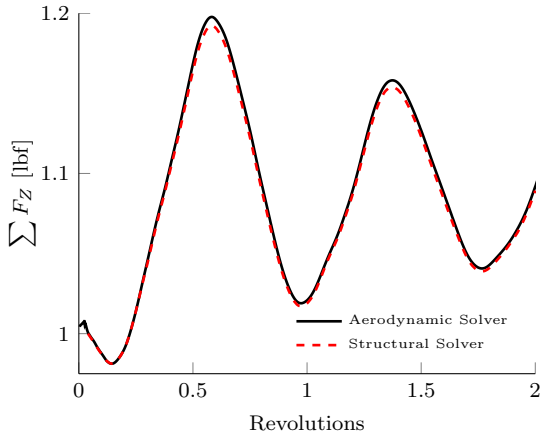


(c) Comparison of $\sum F_z$

Figure 6.4: Comparison of the resultant aerodynamic force from the aerodynamic calculations and the resultant aerodynamic forced applied to the structure.

# CHAPTER 7

# Aerodynamic Characteristics of a Bird-Damaged Fan Stage

The steady and unsteady aerodynamic calculations of the bird-damaged fan are examined to provide insight into the principal aerodynamic characteristics at three different operating conditions. The freestream conditions correspond to standard day +27°F conditions, the freestream flight Mach number is zero, and the engine rotation speeds for each throttle setting are provided in Table 3.3. The damaged configuration, described in Chapter 2, consists of a sector of 5 damaged blades located in an otherwise undamaged fan. The coarse CFD mesh given in Chapter 3 is used for all aerodynamic calculations, as justified by the mesh-sensitivity study provided in Chapter 4. The calculations were performed using parallel Intel Xeon X5650 2.67 GHz processors assembled on a high-performance computing cluster composed of 12-processor nodes with 48 GB of RAM per node. The computational cost of the steady CFD calculations is discussed in Chapter 4. The computational requirements for the unsteady CFD computations, used in the forced response calculations, are given in Chapter 8.

## 7.1 Steady Aerodynamic Calculations of the Undamaged Fan

Steady aerodynamic calculations were performed for an undamaged fan at the 100%,

75%, and 60% throttle settings and the results are compared with the corresponding result for the damaged fan. The single passage fluid domain was used for these calculations, and the blade geometry corresponds to the undamaged hot configuration where centrifugal effects are included. A characteristic curve for each throttle setting was mapped by varying the bypass duct static pressure. Initially a small bypass duct static pressure is specified to obtain an operating point well below the operating line. The bypass duct pressure is subsequently gradually increased. Steady-state convergence is difficult to achieve near the stall point where unsteady flow begins to dominate. The operating points at the intersection of the operating line and the characteristic curves are significant because they represent operation of the undamaged fan stage in a complete engine.

Figure 7.1 provides the fan map for the undamaged fan and includes fan operating line provided by the sponsor organization and the characteristic curves corresponding to the 100%, 75%, and 60% throttle settings. The values in Figs. 7.1 are normalized by the referred mass flow rate and total pressure ratio at the intersection of the 100% throttle characteristic curve and the operating line. Figure 7.1 also includes an approximate stall line that connects the stall points on each characteristic curve. The distance between the operating line and the stall line indicates that the undamaged fan, when installed in a complete engine, operates well away from stall. Table 7.1 provides the normalized referred mass flow rate and total pressure ratio for each point on the characteristic curves shown in Fig. 7.1. The bypass duct static pressure and the distance from the operating line, calculated using Eq. (3.40), are also provided for each operating point. The operating point nearest the operating line is identified by bold text in Table 7.1.

Table 7.1: Operating points for the undamaged fan at the 100%, 75%, and 60% throttle settings.

| Throttle Setting | Normalized $P_B$ | Normalized $\dot{m}_R$ | Normalized $PR$ | %ΔOL |
|---|---|---|---|---|
| 100% | 0.818 | 1.013 | 0.884 | 19.6% |
| 100% | 0.909 | 1.011 | 0.937 | 10.5% |
| **100%** | **1.000** | **1.000** | **1.000** | **0.22%** |
| 100% | 1.027 | 0.983 | 1.017 | 4.8% |
| 100% | 1.055 | 0.924 | 1.030 | 15.8% |
| 75% | 0.727 | 0.953 | 0.793 | 30.5% |
| 75% | 0.800 | 0.941 | 0.825 | 20.2% |
| 75% | 0.873 | 0.915 | 0.859 | 9.0% |
| **75%** | **0.909** | **0.887** | **0.880** | **0.70%** |
| 75% | 0.945 | 0.829 | 0.892 | 9.7% |
| 75% | 0.964 | 0.772 | 0.898 | 18.9% |
| 60% | 0.655 | 0.897 | 0.729 | 43.4% |
| 60% | 0.727 | 0.885 | 0.755 | 31.9% |
| 60% | 0.800 | 0.862 | 0.784 | 19.1% |
| **60%** | **0.873** | **0.797** | **0.814** | **0.74%** |
| 60% | 0.909 | 0.725 | 0.825 | 12.0% |
| 60% | 0.927 | 0.690 | 0.829 | 17.8% |

## 7.2 Steady Aerodynamic Calculations of the Damaged Fan

Steady aerodynamic calculations were performed to gain insight into the aerodynamic behavior of the damaged fan and also to provide the initial conditions for the unsteady aerodynamic calculations. The full-wheel computational domain is required for these calculations, and the blade geometry corresponds to the hot configuration including centrifugal effects. The characteristic curves of the damaged fan were mapped for each throttle setting by varying the bypass duct static pressure. The bypass duct static pressure was gradually increased to reach an operating point near the operating line that represents operation of the damaged fan installed in a complete engine.

Figure 7.2 provides the fan map of the damaged fan and includes the fan operating line

and the characteristic curves corresponding to the 100%, 75%, and 60% throttle settings. The values in Figs. 7.2 are normalized by the referred mass flow rate and total pressure ratio at the intersection of the 100% throttle characteristic curve and the operating line. Table 7.2 provides the normalized referred mass flow rate and total pressure ratio and the corresponding bypass duct static pressure together with the distance from the operating line. Steady-state convergence of the damaged fan at operating points near the operating line was difficult to achieve, indicating that the damaged fan is operating in the vicinity of stall. For the 100% throttle setting, the steady calculations at $P_B$=0.938 and $P_B$=0.898 exhibit an operating point that oscillates with solver iteration, and the values in Table 7.2 represent the mean values over the last 500 iterations. The operating points corresponding to $P_B$=0.854 for the 75% throttle setting and $P_B$=0.836 for the 60% throttle setting represent the highest bypass duct static pressure for which the steady solution converged. It is important to note that the steady calculations converge at a "snap-shot" of the unsteady behavior that may not represent completely the time-averaged behavior of the unsteady solution.

Comparison of the undamaged and damaged fan maps clearly illustrates the significant influence of the bird damage on the steady aerodynamic behavior of the damaged fan. The damaged fan characteristic curves are much flatter near the operating line, indicating that the damaged fan is operating very near the stall point where unsteady flow phenomena may be significant. The operating point of the damaged fan is also significantly affected by the bird damage. Table 7.3 compares the undamaged and damaged operating points, normalized by the operating point of the undamaged fan at the 100% throttle setting. Table 7.3 also provides the percent mass flow loss relative to the undamaged fan at the corresponding throttle setting, where the mass flow loss is related to the thrust loss resulting from the bird

Table 7.2: Operating points for the damaged fan at the 100%, 75%, and 60% throttle settings.

| Throttle Setting | Normalized $P_B$ | Normalized $\dot{m}_R$ | Normalized $PR$ | %$\Delta$OL |
|---|---|---|---|---|
| 100% | 0.855 | 0.969 | 0.902 | 9.2% |
| 100% | 0.864 | 0.967 | 0.907 | 7.9% |
| 100% | 0.873 | 0.964 | 0.912 | 6.7% |
| 100% | 0.880 | 0.962 | 0.917 | 5.6% |
| 100% | 0.887 | 0.958 | 0.921 | 4.4% |
| 100% | 0.895 | 0.944 | 0.923 | 1.9% |
| **100%** | **0.898** | **0.936** | **0.924** | **0.63%** |
| 75% | 0.800 | 0.895 | 0.818 | 14.7% |
| 75% | 0.809 | 0.890 | 0.821 | 13.3% |
| 75% | 0.818 | 0.883 | 0.824 | 11.6% |
| 75% | 0.827 | 0.874 | 0.828 | 9.5% |
| 75% | 0.836 | 0.870 | 0.833 | 7.7% |
| 75% | 0.845 | 0.864 | 0.839 | 5.7% |
| **75%** | **0.854** | **0.853** | **0.842** | **3.3%** |
| 60% | 0.773 | 0.836 | 0.767 | 20.0% |
| 60% | 0.782 | 0.831 | 0.770 | 18.1% |
| 60% | 0.791 | 0.824 | 0.774 | 16.1% |
| 60% | 0.800 | 0.816 | 0.776 | 14.0% |
| 60% | 0.809 | 0.806 | 0.779 | 11.5% |
| 60% | 0.827 | 0.774 | 0.783 | 5.9% |
| **60%** | **0.836** | **0.757** | **0.784** | **2.5%** |

strike. To calculate the mass flow loss for the 75% and 60% throttle settings, the characteristic curve is extrapolated to the operating line assuming a constant pressure ratio (i.e. flat characteristic curve). The largest mass flow loss occurs for the 100% and 60% throttle settings followed by the 75% throttle setting.

To gain insight into the flow behavior resulting from the damaged fan sector, a constant-span circumferential slice of the wheel is examined and compared to the undamaged case. Figures 7.3 provides Mach number contours of the undamaged and damaged fan at 75% span, the location of greatest damage, for each throttle setting. The five damaged blades are labeled as 1 through 5 where the blade numbers correspond to those in Fig. 2.11. When

Table 7.3: Comparison of operating points for the undamaged and damaged fan.

| Throttle Setting | Configuration | Normalized $\dot{m}_R$ | Normalized $PR$ | % Flow Loss | %$\Delta$OL |
|---|---|---|---|---|---|
| 100% | Undamaged | 1.000 | 1.000 | N\A | 0.22% |
| 100% | Damaged | 0.931 | 0.933 | 7.33% | 0.63% |
| 75% | Undamaged | 0.881 | 0.889 | N\A | 0.70% |
| 75% | Damaged | 0.847 | 0.850 | 5.90% | 3.3% |
| 60% | Undamaged | 0.793 | 0.822 | N\A | 0.74% |
| 60% | Damaged | 0.752 | 0.791 | 7.20% | 2.5% |

compared with the Mach number contour at 75% span for the undamaged fan, Figs. 7.3(a)-7.3(c) clearly illustrate the significant effect of the bird damage on the flow field. The moderate leading edge deformation of blade 5 creates a separation bubble on the suction side of the blade that partially blocks the flow through the downstream passage. The larger leading edge deformation and global bending of blade 2 and blade 4 result in a more substantial flow disruption in which the flow through several downstream passages is blocked. Furthermore, the mass flow through the blade passages downstream of the damaged sector experience a loss of mass flow due to increased angles of attack and flow separations, and the passages upstream of the damaged sector compensate for this loss with an increased mass flow and a stronger passage shock.

Figures 7.4 provide Mach number contours on a constant-axial slice of the wheel at mid blade chord for the undamaged and damaged fans at each throttle setting. The significant effect of the damaged sector on the aerodynamic environment of the entire fan wheel is evident. The damaged sector produces stalled flow, identified by the blue regions in Fig. 7.4, for a large spanwise portion of the damaged blade passages. The Mach contours in the damaged blade passages are similar for all three throttle settings with a strong region of stalled flow downstream of blades 1, 2, and 4. Stalled flow is also present at the undamaged blade

tips over approximately half of the fan wheel. The flow loss associated with the stalled blade tips is compensated by the increased flow through the unstalled blade passages, as is evident by the increased Mach number distribution through these blade passages. The extent of the stalled flow at the blade tips varies between the three throttle settings. For the 100% and 60% throttle settings, the stalled flow extends counterclockwise from blade 24 to blade 17. In contrast, the stalled flow for the 75% throttle setting extends to a lesser extent from blade 24 counterclockwise to blade 20.

## 7.3 Unsteady Aerodynamic Calculations of the Damaged Fan

The unsteady aerodynamic calculations for the 100%, 75%, and 60% throttle settings are initialized from the corresponding steady solution. A physical time-step of $\Delta t_f = \frac{1}{500\Omega}$ is specified, and 3 CFD-solver sub-iterations are performed at each time-step to ensure convergence of the solution. The unsteady calculations were performed for 5,000 time-steps corresponding to 10 revolutions of the fan.

### 7.3.1 Unsteady Operating Point

Figures 7.5(a), 7.5(c), and 7.5(e) show the unsteady total pressure ratio and referred mass flow rate for the 100%, 75%, and 60% throttle settings, respectively. The values in Figs. 7.5(a), 7.5(c), and 7.5(e) are normalized by the referred mass flow rate and total pressure ratio of the undamaged fan at the corresponding throttle setting. Considerable unsteadiness in the operating point is apparent, where the mass flow rate and total pressure rate exhibit an oscillatory behavior. The unsteady operating point at 100% throttle setting oscillates with

a period of $\sim$4 revolutions. The unsteady operating point for the 75% and 60% throttle settings oscillate with a larger period of $\sim$6 revolutions and $\sim$7 revolutions, respectively. The unsteady operating point is plotted on the fan map in Figs. 7.5(b), 7.5(d), and 7.5(f), where the values are normalized by the referred mass flow rate and total pressure ratio of the undamaged fan at the same throttle setting. For the 100% and 60% throttle settings, the unsteady operating point oscillates about the steady operating point, and the unsteady operating point for the 75% throttle setting oscillates about a point below the steady value indicating that unsteadiness contributes to additional flow losses.

Table 7.4 provides the mean referred mass flow rate and total pressure ratio normalized by the corresponding values from the undamaged fan at the same throttle setting. Table 7.4 also provides the amplitude of the unsteady referred mass flow rate and total pressure ratio as a percent of the mean value along with the mean flow loss for each case. The referred mass flow rate varies approximately $\pm$3.4% about its mean value and the total pressure ratio varies approximately $\pm$1.2% about its mean value. Furthermore, the mean flow loss is approximately 8% for each case, and is greater than that predicted by the steady calculations for the 75% and 60% throttle settings. The 75% throttle setting exhibits the largest flow loss of 8.4% and is considerably greater than the 5.9% flow loss predicted by the steady solution. Therefore, it is clear that unsteady effects are important in predicting the flow loss of the damaged fan, and the steady aerodynamic calculation of the damaged fan tends to under-predict the flow loss.

Table 7.4: Unsteady operating points for the damaged fan.

| Throttle Setting | Normalized avg($\dot{m}_R$) | Normalized avg($PR$) | Amplitude $\dot{m}_R$ | Amplitude $PR$ | % Flow Loss |
|---|---|---|---|---|---|
| 100% | 0.926 | 0.919 | $\pm$3.1% | $\pm$1.3% | 7.28% |
| 75% | 0.930 | 0.942 | $\pm$3.7% | $\pm$1.3% | 8.40% |
| 60% | 0.941 | 0.957 | $\pm$3.4% | $\pm$1.1% | 8.05% |

### 7.3.2 Unsteady Mach Contours

Mach contours at mid-chord are examined to provide insight into the unsteady behavior of the damaged fan. Figures 7.6 depicts the unsteady Mach number contours at the mid-chord for 9 equally spaced time-steps spanning one representative oscillation of the unsteady solution at the 100% throttle setting. The corresponding total pressure ratio and referred mass flow rate at these time-steps are indicated by the fine vertical lines in Fig. 7.5(a). Only a small amount of unsteadiness is observed in the vicinity of the damaged blades where the flow remains largely separated, and the flow through the damaged blade passages is partially or totally blocked. By contrast, considerable unsteadiness is evident in much of the undamaged sector, with the greatest level of flow unsteadiness occurring in the blade passages between blade 16 clockwise to blade 21.

The stalled flow emanating from the damaged sector, denoted a stall cell and identified by the blue regions, is the dominant unsteady flow effect in Figs. 7.6. At 0.8 revolutions, the stall cell covers roughly a third of the fan wheel, from blade 21 clockwise to blade 5, and the mass flow rate is near its maximum. From 1.4 revolutions to 3.8 revolutions, the stall cell regresses slightly before propagating opposite the direction of rotation until half of the blade tips are stalled, from blade 15 clockwise to blade 5. At this point, the mass flow rate is at a minimum due to the partially blocked blade passages associated with the stalled

flow. Subsequently from 4.4 revolutions to 5.6 revolutions, the stall cell detaches from the damaged sector, progresses opposite the direction of rotation, and dissipates as the flow recovers and the mass flow rate increases to the maximum value. Furthermore, as the stall cell propagates at the blade tips, the Mach number in the inner span of the corresponding blade passage also decreases, indicating a loss of mass flow through a majority of the blade passages.

The unsteady Mach contours at mid-chord for the 75% and 60% throttle settings are provided in Figs. 7.7 and 7.8. The unsteady flow behavior of these throttle settings is very similar to the 100% case, where the dominant unsteady feature is the stalled flow emanating from the damaged sector. For these cases, the stall cell at the blade tips propagates opposite the direction of rotation until the mass flow rate is at a minimum. As the mass flow rate recovers, the stall cell regresses in the direction of rotation. The stall cell does not detach from the damaged sector, as is the case for the 100% throttle setting, and the stall cell extends counterclockwise to blade 12. The Mach number of the unstalled blade passages between blades 6 and 11 also varies considerably with the progression and regression of the stall cell.

The cyclic progression and regression of the stall cell emanating from the damaged sector is similar to the rotating stall phenomenon experienced by undamaged fans and compressors. The separated flow originating from the damaged sector initiates a progressing stall cell similar to a rotating stall cell; however, the substantial leading edge deformation of the damaged blades prevents the flow from reattaching to the upstream blades. As a result, the flow is blocked at an increasing number of blade passages as the stall cell propagates, causing a decrease in the overall mass flow rate. As the mass flow rate decreases, the angle

of attack of the blades is decreased such that the flow reattaches and the mass flow rate recovers.

### 7.3.3 Unsteady Blade Forces

After each time-step of the unsteady CFD calculations the resultant aerodynamic force on each blade is calculated from summation of the pressure and viscous loads acting on the CFD elements at the blade surface. The resultant unsteady aerodynamic forces acting on the damaged blades (blades 1-5) and five representative undamaged blades are shown in Fig. 7.9(a) for the 100% throttle setting. The values in Figs. 7.9 are normalized by the resultant aerodynamic force acting on a blade in an undamaged fan at the same conditions. The largest unsteadiness is evident for the undamaged blades where the unsteady forces are due to the stall cell emanating from the damaged sector. The unsteady forces acting on the damaged blades exhibit a higher frequency that is attributed to the unsteady wake shed by the damaged blades. A Fast Fourier Transformation (FFT) of the unsteady blade forces is presented to determine the amplitude and frequency content of the unsteady aerodynamic loading and to provide insight as to which of the fan blades may be excited by the unsteady aerodynamic loads. The unsteady forces acting on the damaged and undamaged blades for frequencies up to 200 [Hz] is shown in Fig. 7.9(b) for the 100% throttle setting. Figure 7.9(c) provides the FFT of unsteady force for frequencies between 600 [Hz] and 800 [Hz]. The resultant force amplitudes at frequencies between 200 [Hz] and 600 [Hz] and above 800 [Hz] are negligible and are not presented.

The significantly larger unsteady aerodynamic loading on the undamaged blades at frequencies below 200 [Hz] is evident in Fig. 7.9(b). The dominant forcing frequencies for

the undamaged blades range from 19.1 [Hz] to 191.5 [Hz], with the largest force component acting on blades 16, 20, 24 at 57.4 [Hz] with a normalized amplitude of 0.047, 0.044, 0.038, respectively. Blade 16 also exhibits a dominant force component at 114.9 [Hz] with an normalized amplitude of 0.039. The dominant forcing frequencies for the damaged blades ranges from 19.1 [Hz] to 57.4 [Hz], with the largest force component occurring for blade 1 with a normalized amplitude of 0.009 at 57.4 [Hz]. Components of the unsteady forces acting on the undamaged blades occur at frequencies near the first bending mode of the rotating blades ($\sim$126.97 [Hz]) and may excite a structural mode and result in a large amplitude response. The dominant forcing amplitudes acting on the damaged blades are substantially smaller than those acting on the undamaged blades and occur at a frequency much lower than that of the first natural mode. Therefore, the structural response of the undamaged blades is expected to be much larger than that of the damaged blades.

The force component amplitudes for the damaged and undamaged blades become somewhat similar at higher frequencies between 600 [Hz] and 800 [Hz]. Blade 4 exhibits the largest force component, which occurs at 708.5 [Hz] with a normalized amplitude of 0.008. The dominant force component acting on the undamaged blades occurs for blade 24 also at 708.5 [Hz] with a normalized amplitude of 0.004. The aerodynamic forces acting on the undamaged and damaged blades at frequencies between 600 [Hz] and 800 [Hz] are smaller than those at lower frequencies; however, they occur at frequencies that may excite the second torsional mode of the rotating blades ($\sim$712.65 [Hz]).

The resultant unsteady aerodynamic forces and corresponding FFT for the 75% and 60% throttle settings are shown in Figs. 7.10 and 7.11. When compared to the 100% throttle setting, the dominant forcing frequencies for the 75% and 60% throttle settings

are lower as a result of the slower progression and regression of the stall cell emanating from the damaged sector. For the 75% throttle setting, the dominant forcing frequencies for the damaged and undamaged blades range from 17.1 [Hz] to 51.4 [Hz]. Blade 20 exhibits the largest normalized amplitude of 0.110 at 17.1 [Hz], followed by blades 12, 16, and 24 at the same frequency. Blades 12, 16, and 20 are the only blades with dominant forcing frequencies above 17.1 [Hz]. The FFT of the unsteady aerodynamic forces for the 60% throttle setting are similar, with the dominant forcing frequencies ranging from 15.8 [Hz] to 78.8 [Hz]. Blades 3 and 24 exhibit the largest normalized amplitude of $\sim$0.055 occurring at 15.8 [Hz]. The dominant forcing frequencies for the 75% and 60% throttle settings are well below that of the first bending mode of the rotating blades; therefore, the structural response is expected to be smaller than that at the 100% throttle setting. Similar to the 100% throttle setting, the unsteady forces for the 75% and 60% throttle settings also exhibit a peak in force amplitude near 600 [Hz], as shown in Figs. 7.10(c) and 7.11(c). At these higher frequencies, the dominant forcing occurs for the damaged blades 3 and 4 and the undamaged blade 20 and may excite the higher structural modes of the rotating blades.

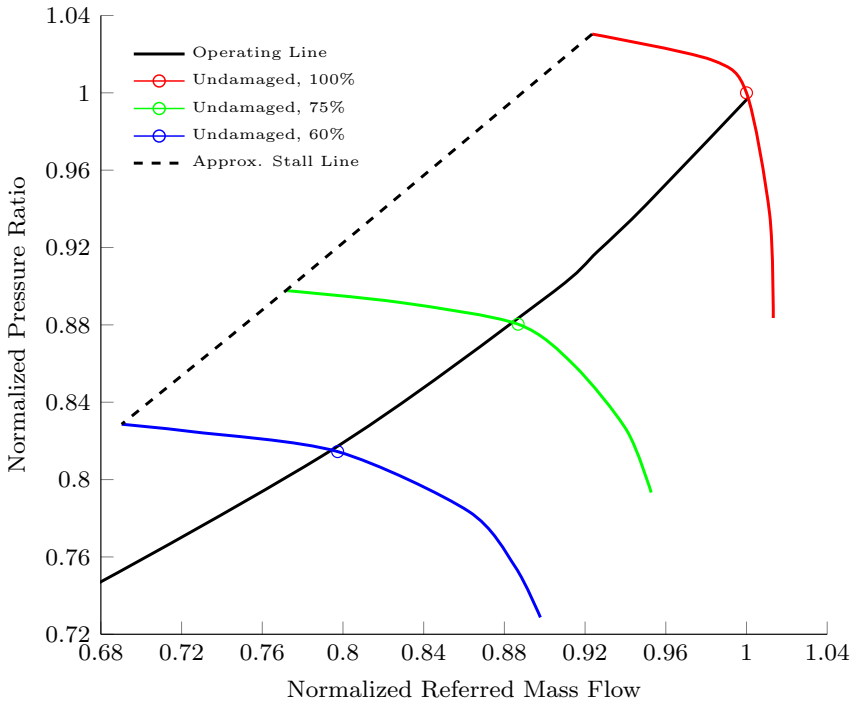


Figure 7.1: Undamaged fan map for 100%, 75%, and 60% throttle settings.

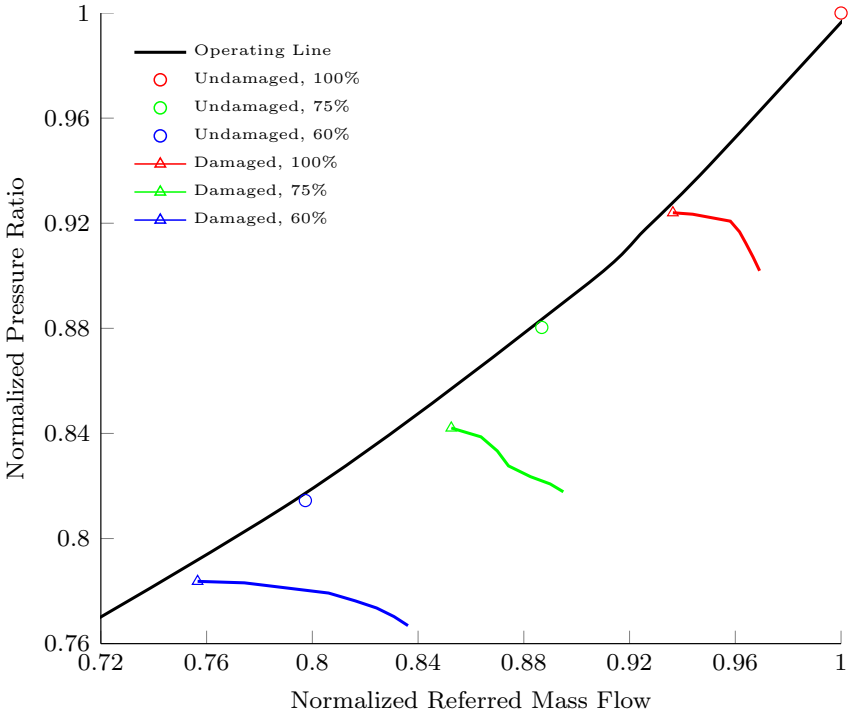


Figure 7.2: Damaged fan map for 100%, 75%, and 60% throttle settings.

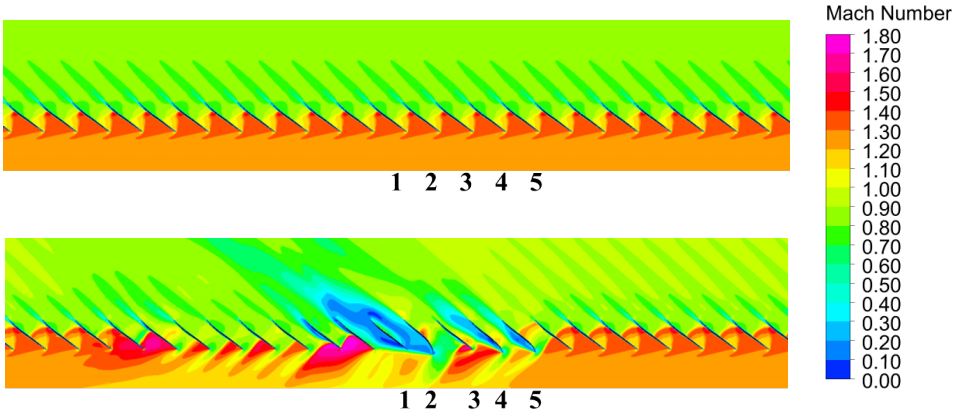


(a) Undamaged and damaged fan at the 100% throttle settings.

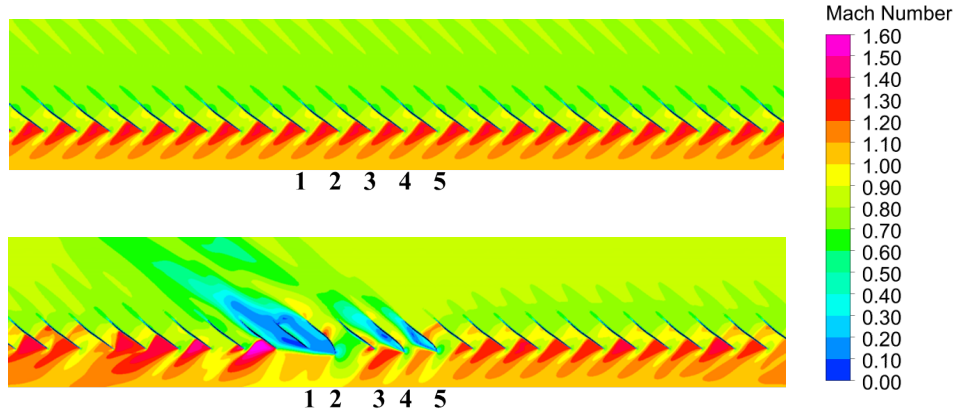


(b) Undamaged and damaged fan at the 75% throttle settings.

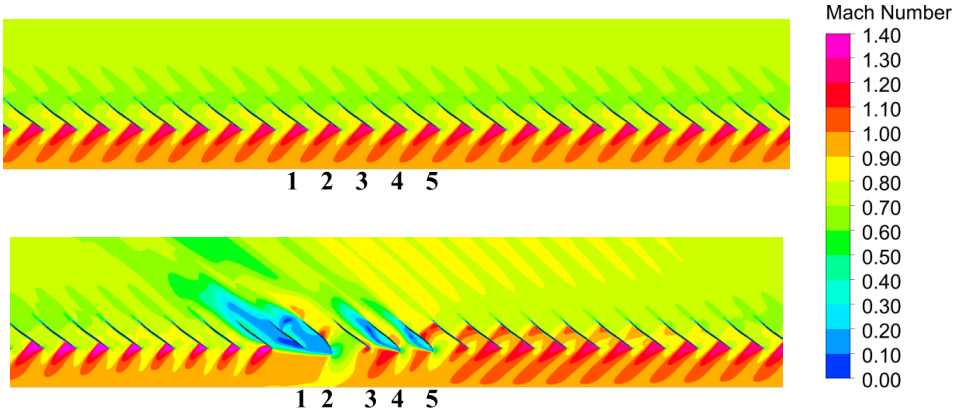


(c) Undamaged and damaged fan at the 60% throttle settings.

Figure 7.3: Steady Mach number contours of the undamaged and damaged fan at 75% span (direction of rotation: left to right).

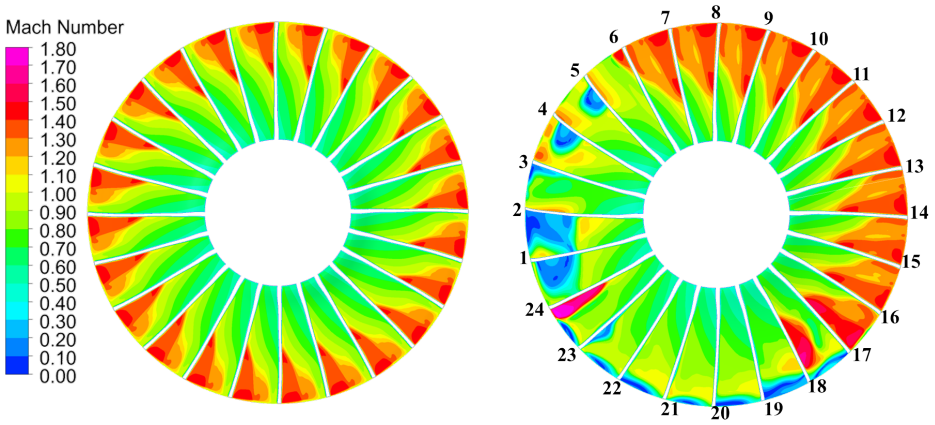


(a) Undamaged and damaged fan at the 100% throttle settings.

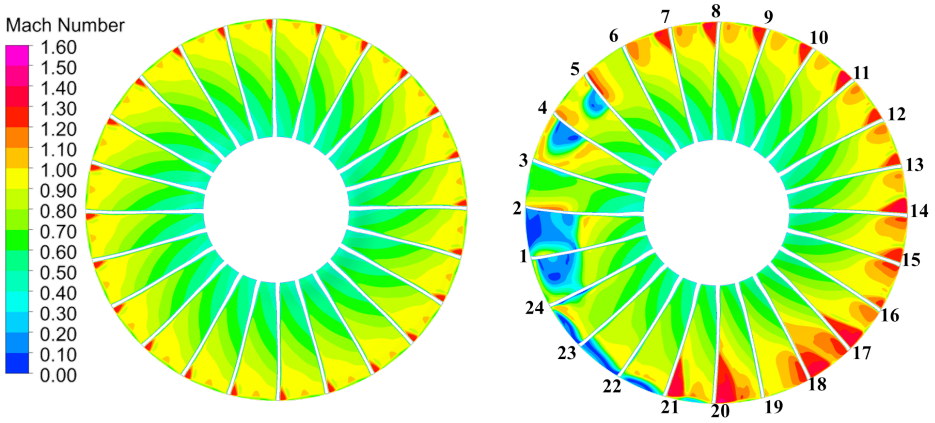


(b) Undamaged and damaged fan at the 75% throttle settings.

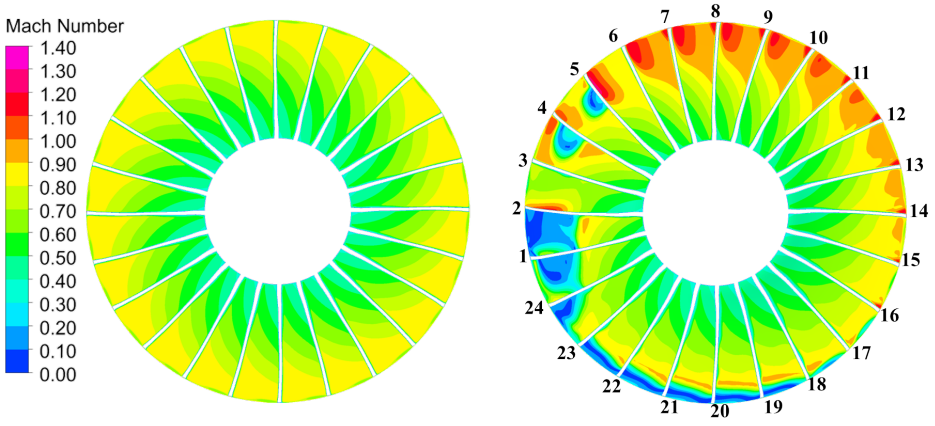


(c) Undamaged and damaged fan at the 60% throttle settings.

Figure 7.4: Steady Mach number contours of the undamaged and damaged fan at mid-chord (direction of rotation: clockwise).

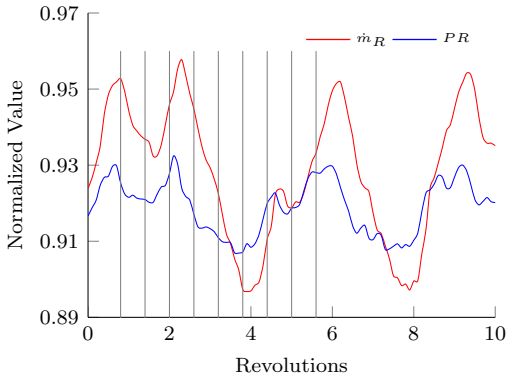


(a) Referred mass flow rate and total pressure ratio time history at the 100% throttle setting.

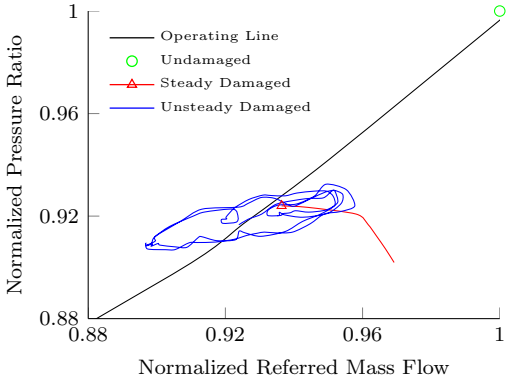


(b) Fan map with characteristic curve and steady and unsteady operating points at the 100% throttle setting.

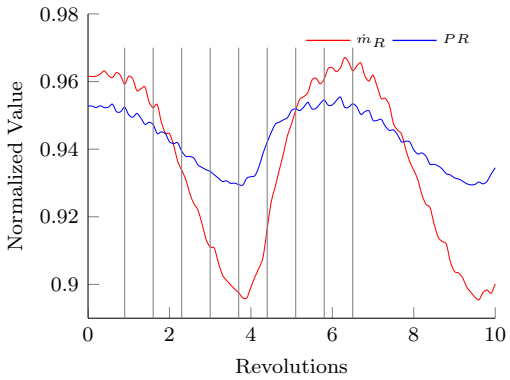


(c) Referred mass flow rate and total pressure ratio time history at the 75% throttle setting.

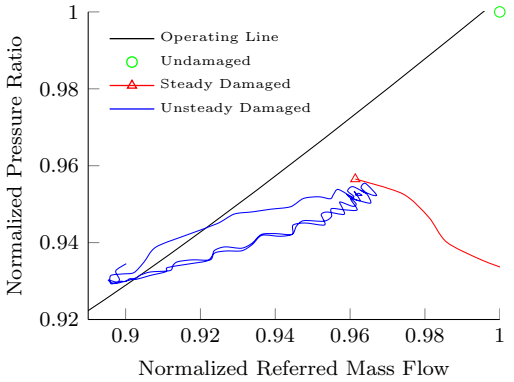


(d) Fan map with characteristic curve and steady and unsteady operating points at the 75% throttle setting.

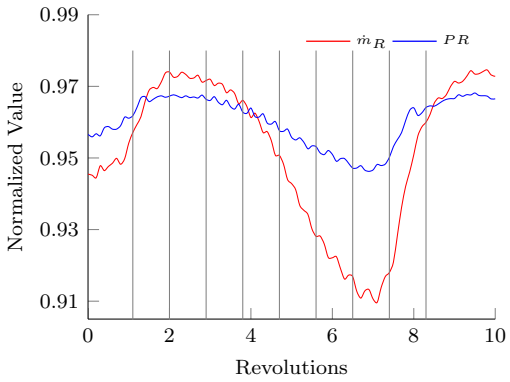


(e) Referred mass flow rate and total pressure ratio time history at the 60% throttle setting.

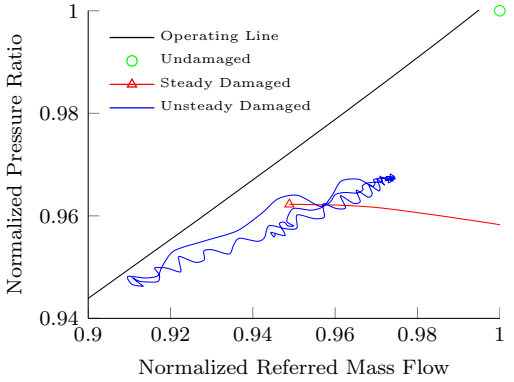


(f) Fan map with characteristic curve and steady and unsteady operating points at the 60% throttle setting.

Figure 7.5: Unsteady total pressure ratio and referred mass flow rate.

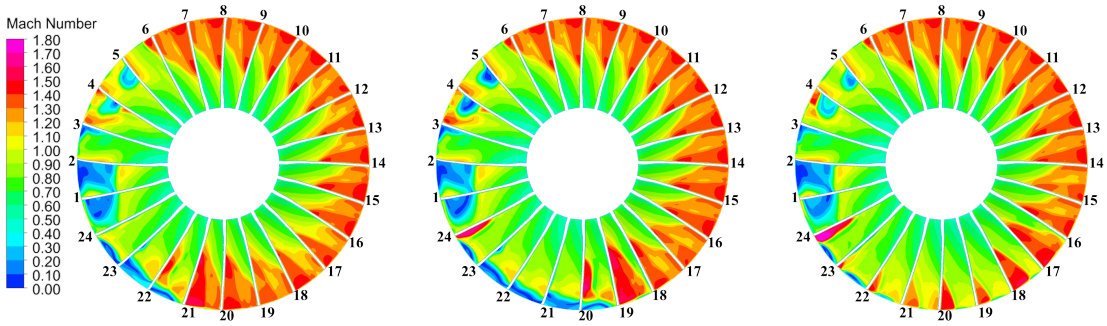


(a) 0.8 revolutions. (b) 1.4 revolutions. (c) 2.0 revolutions.

(d) 2.6 revolutions. (e) 3.2 revolutions. (f) 3.8 revolutions.

(g) 4.4 revolutions. (h) 5.0 revolutions. (i) 5.6 revolutions.

Figure 7.6: Unsteady mid-chord Mach number contours of the damaged fan at the 100% throttle setting (direction of rotation: clockwise).

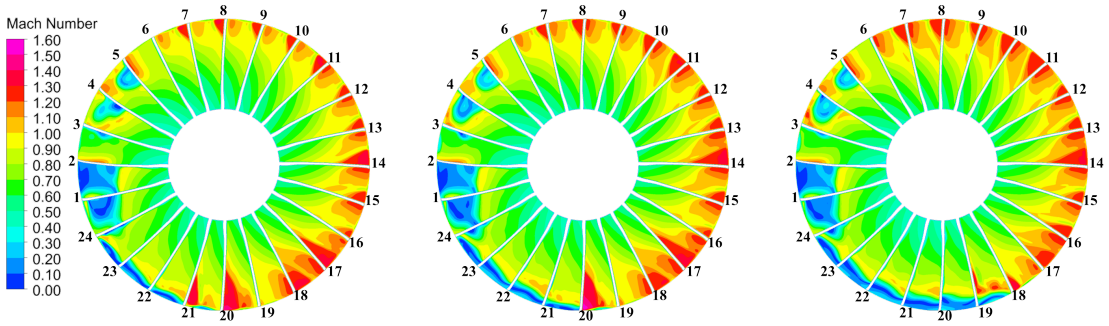


(a) 0.9 revolutions. (b) 1.6 revolutions. (c) 2.3 revolutions.

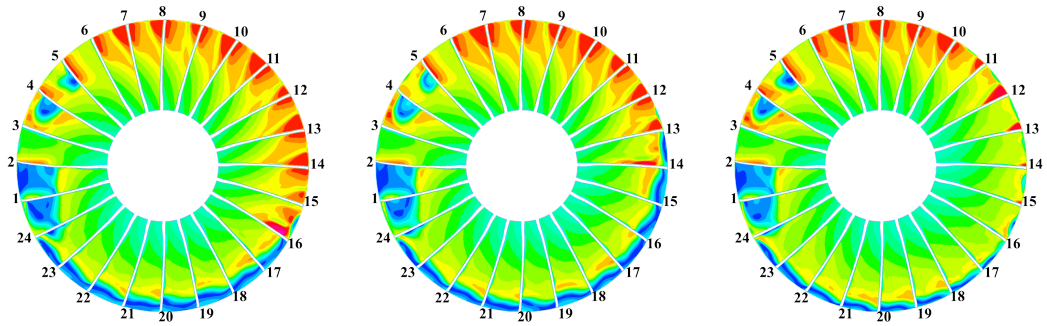

(d) 3.0 revolutions. (e) 3.7 revolutions. (f) 4.4 revolutions.

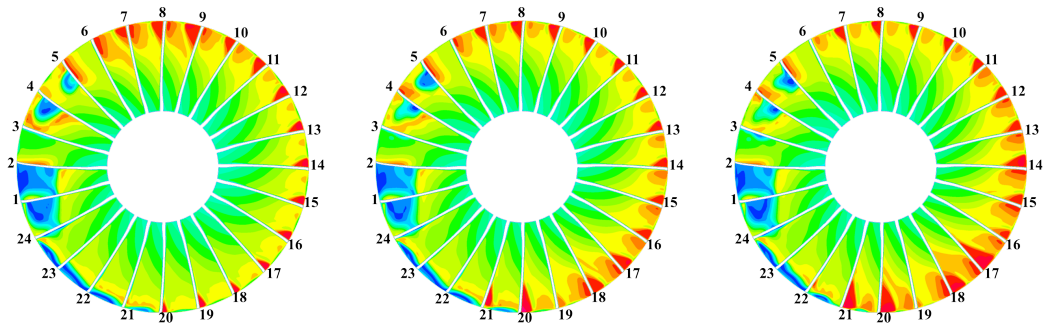

(g) 5.1 revolutions. (h) 5.8 revolutions. (i) 6.5 revolutions.

Figure 7.7: Unsteady mid-chord Mach number contours of the damaged fan at the 75% throttle setting (direction of rotation: clockwise).

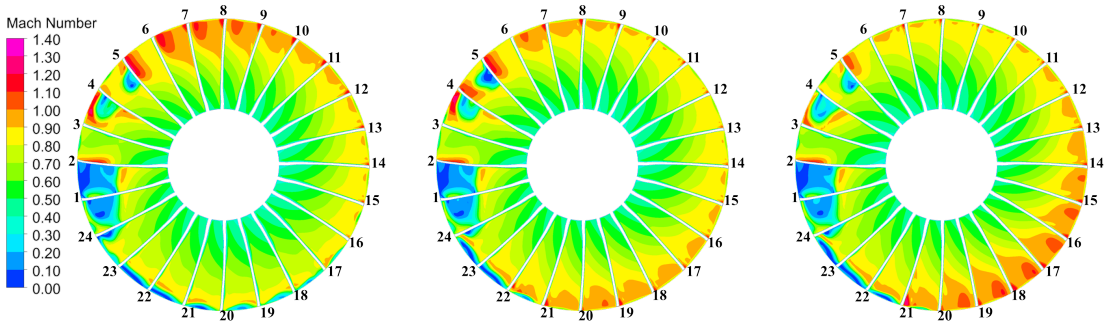


(a) 1.1 revolutions. (b) 2.0 revolutions. (c) 2.9 revolutions.

(d) 3.8 revolutions. (e) 4.7 revolutions. (f) 5.6 revolutions.

(g) 6.5 revolutions. (h) 7.4 revolutions. (i) 8.3 revolutions.

Figure 7.8: Unsteady mid-chord Mach number contours of the damaged fan at the 60% throttle setting (direction of rotation: clockwise).

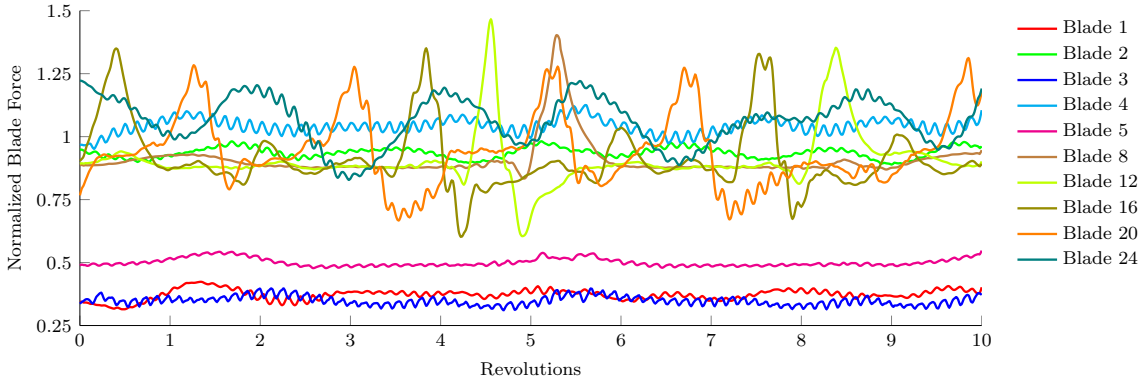


(a) Unsteady aerodynamic forces.

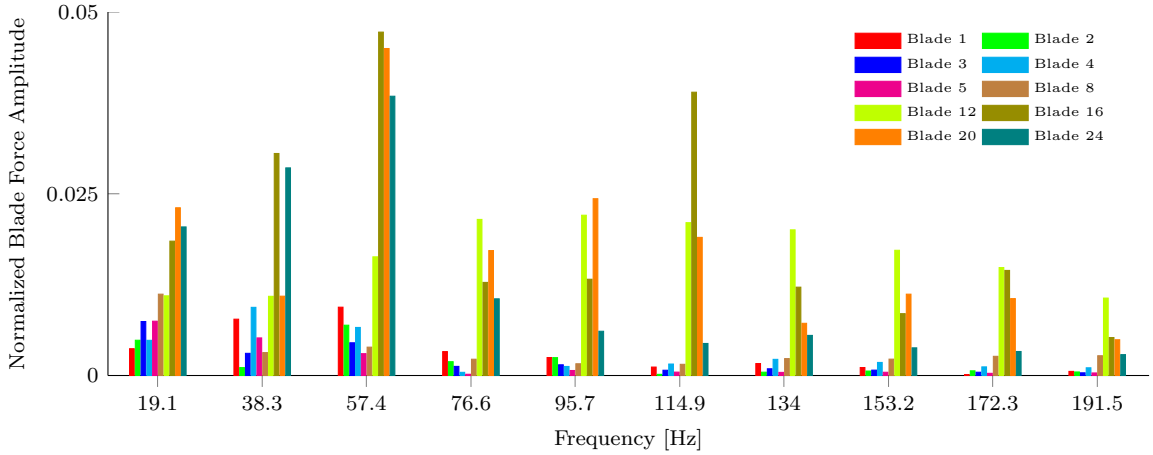


(b) Low frequency FFT of unsteady aerodynamic forces.

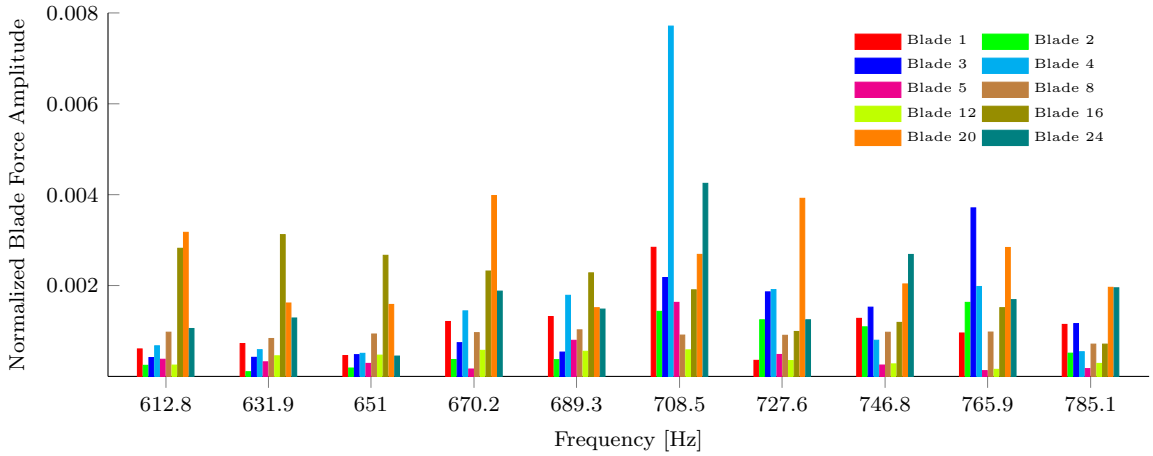


(c) High frequency FFT of unsteady aerodynamic forces.

Figure 7.9: Unsteady aerodynamic forces acting on blades at the 100% throttle setting.

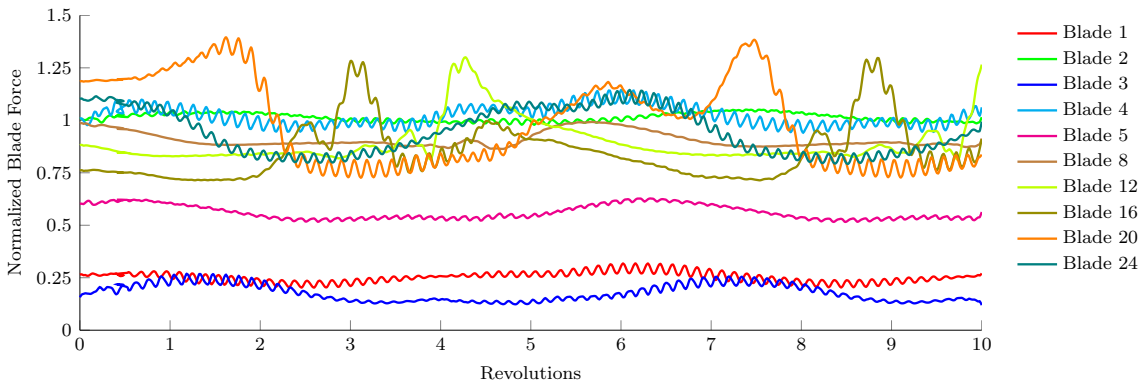


(a) Unsteady aerodynamic forces.

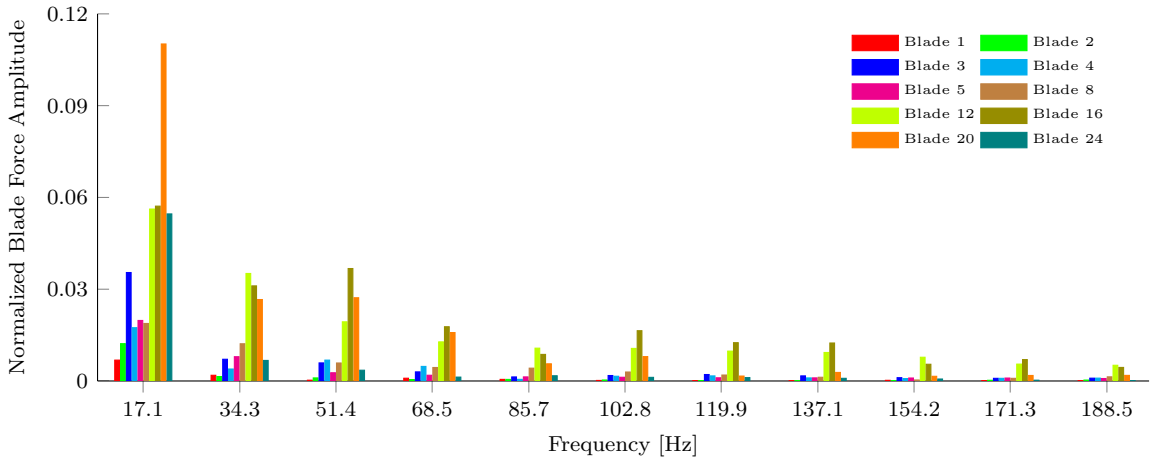


(b) Low frequency FFT of unsteady aerodynamic forces.

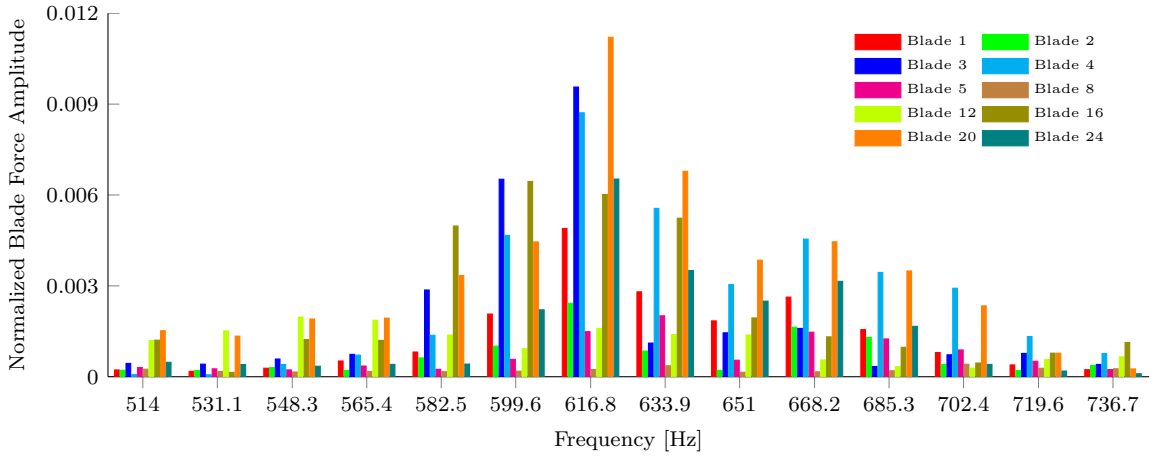


(c) High frequency FFT of unsteady aerodynamic forces.

Figure 7.10: Unsteady aerodynamic forces acting on blades at the 75% throttle setting.

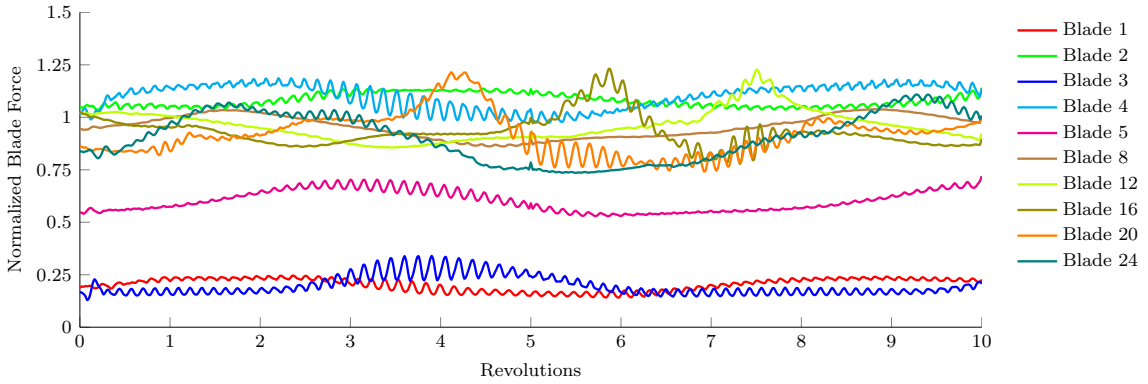


(a) Unsteady aerodynamic forces.

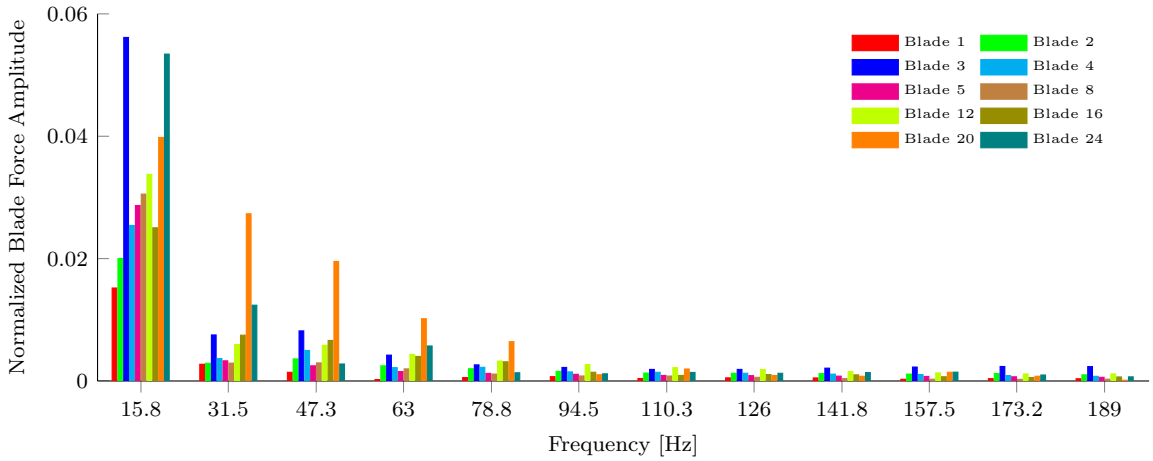


(b) Low frequency FFT of unsteady aerodynamic forces.

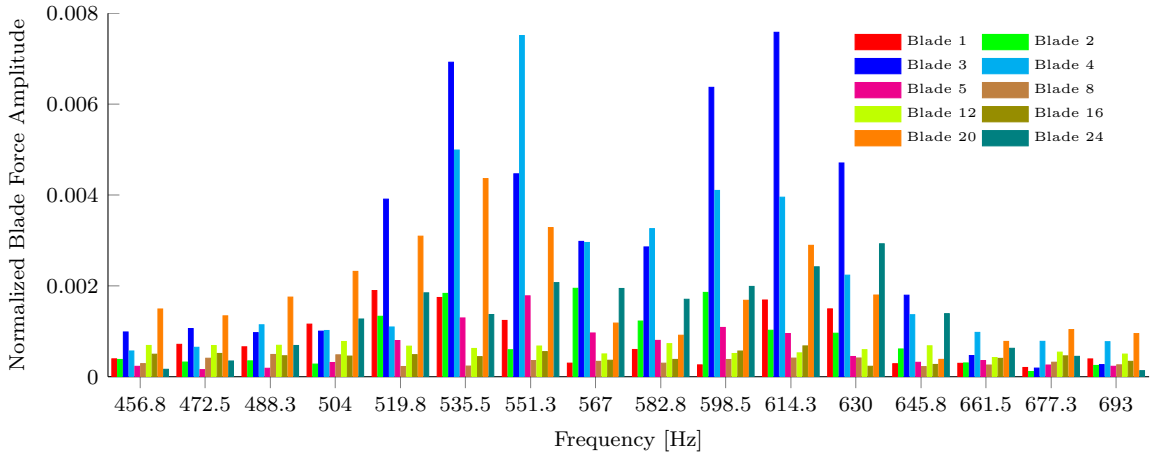


(c) High frequency FFT of unsteady aerodynamic forces.

Figure 7.11: Unsteady aerodynamic forces acting on blades at the 60% throttle setting.

# CHAPTER 8

# Aeroelastic Response of a Bird-Damaged Fan

This chapter presents the forced response and aeroelastic response calculations of the bird-damaged fan at the 100%, 75%, and 60% throttle settings. The damaged configuration is described in Chapter 2 and consists of a sector of 5 damaged blades located in an otherwise undamaged fan. The forced response and aeroelastic response calculations illustrate the effect of the unsteady aerodynamic loading on the fan blade response. The blade response from the aeroelastic calculations is compared to the forced response case to determine the role of aeroelastic coupling. The aerodynamic behavior from the aeroelastic response calculations is also presented to illustrate the effect of blade motion on the unsteady aerodynamic behavior of the damaged fan. Finally, the aerodynamic work calculated from the forced response and aeroelastic response calculations are compared to identify the potential for aeroelastic instability.

## 8.1 Forced Response of the Damaged Fan

The forced response calculations of the bird damaged fan at the 100%, 75%, and 60% throttle settings were performed using the one-way forced response framework presented in Chapter 6. The forced response calculation is initialized in a manner this is similar to

the example aeroelastic response calculation presented in Chapter 6. First, the rotational velocity is introduced during a static structural analysis to generate the hot geometry that corresponds to the CFD blade geometry. The mapping between the hot FE mesh and the CFD mesh at the wetted surface is performed to establish the fluid structure interface. The aerodynamic loads from the steady CFD calculation are applied to the static structural model to obtain the running configuration. During each time-step of the forced response calculations, the aerodynamic loads at the blade surface are extracted from the unsteady CFD calculations and transferred to the structure at the wetted surface. The forced response calculations were performed for 10 revolutions of the fan, and the time-dependent aerodynamic loads correspond to the unsteady CFD calculations presented in Chapter 6.4.

The maximum displacement for the cold-to-running configuration calculation and the forced response calculation occurs at the leading edge of the blade tip. Therefore, the displacement at the leading edge of the blade tip is a useful indicator of the blade response. Table 8.1 provides the total displacement, $||\mathbf{u}||$, at the blade tip leading edge that results from the cold-to-running configuration calculation. The leading edge tip displacement for the 100%, 75%, and 60% throttle settings are similar, with the largest displacements occurring for the 100% throttle setting. Blades 2 and 4 deform the least during the cold-to-running configuration calculation as a result of the stalled flow surrounding these blades.

Table 8.1 also provides the maximum leading edge blade tip displacement, $max(||\mathbf{u}(t)||)$, relative to the running configuration for each blade over the duration of the forced response calculation. The largest tip displacements from the forced response calculations are identified by bold text in Table 8.1 and occur for the undamaged blades opposite the damaged sector. For the 60% throttle case, the damaged blades 3 and 4 also exhibit a large maxi-

Table 8.1: Blade tip leading edge displacement from cold-to-running and forced response calculations.

| | **100% Throttle Setting** | | **75% Throttle Setting** | | **60% Throttle Setting** | |
|---|---|---|---|---|---|---|
| | $\|\|\mathbf{u}\|\|$ [in] | $max(\|\|\mathbf{u}(t)\|\|)$ [in] | $\|\|\mathbf{u}\|\|$ [in] | $max(\|\|\mathbf{u}(t)\|\|)$ [in] | $\|\|\mathbf{u}\|\|$ [in] | $max(\|\|\mathbf{u}(t)\|\|)$ [in] |
| Blade 1 | 0.495 | 0.032 | 0.415 | 0.013 | 0.361 | 0.016 |
| Blade 2 | 0.198 | 0.048 | 0.204 | 0.014 | 0.214 | 0.016 |
| Blade 3 | 0.492 | 0.020 | 0.385 | 0.043 | 0.301 | **0.099** |
| Blade 4 | 0.247 | 0.072 | 0.194 | 0.057 | 0.154 | **0.074** |
| Blade 5 | 0.423 | 0.032 | 0.361 | 0.020 | 0.305 | 0.042 |
| Blade 6 | 0.449 | 0.032 | 0.400 | 0.050 | 0.335 | 0.063 |
| Blade 7 | 0.462 | 0.089 | 0.430 | 0.037 | 0.360 | 0.051 |
| Blade 8 | 0.482 | 0.221 | 0.461 | 0.057 | 0.386 | 0.046 |
| Blade 9 | 0.482 | 0.253 | 0.457 | 0.067 | 0.390 | 0.043 |
| Blade 10 | 0.483 | 0.205 | 0.456 | 0.057 | 0.397 | 0.036 |
| Blade 11 | 0.483 | 0.223 | 0.459 | 0.065 | 0.405 | 0.040 |
| Blade 12 | 0.484 | 0.343 | 0.445 | 0.152 | 0.415 | 0.058 |
| Blade 13 | 0.485 | 0.366 | 0.438 | 0.148 | 0.421 | 0.057 |
| Blade 14 | 0.485 | 0.308 | 0.450 | **0.177** | 0.427 | **0.084** |
| Blade 15 | 0.484 | 0.260 | 0.429 | **0.182** | 0.429 | **0.080** |
| Blade 16 | 0.487 | **0.444** | 0.406 | **0.225** | 0.439 | **0.079** |
| Blade 17 | 0.577 | **0.511** | 0.439 | **0.173** | 0.439 | **0.101** |
| Blade 18 | 0.593 | **0.439** | 0.434 | **0.181** | 0.430 | **0.106** |
| Blade 19 | 0.516 | **0.328** | 0.377 | **0.221** | 0.410 | **0.088** |
| Blade 20 | 0.531 | **0.314** | 0.485 | 0.116 | 0.395 | **0.093** |
| Blade 21 | 0.545 | **0.423** | 0.512 | 0.132 | 0.386 | **0.087** |
| Blade 22 | 0.528 | 0.161 | 0.447 | 0.050 | 0.390 | **0.080** |
| Blade 23 | 0.554 | 0.123 | 0.428 | 0.011 | 0.405 | 0.038 |
| Blade 24 | 0.613 | 0.090 | 0.521 | 0.074 | 0.425 | 0.072 |

mum tip displacement from the forced response calculations. In contrast, the maximum tip displacements of the damaged blades from the 100% and 75% throttle settings are significantly smaller than those of the undamaged blades.

The circumferential displacement, $u_\theta R$, at the blade tip leading edge is used to illustrate the structural response time-history. The displacement is calculated relative to the running configuration. Figures 8.1 show the tip displacement for the duration of the forced response calculation at the 100% throttle setting, where blades with similar responses are grouped

together. The largest tip displacements occur for blades 15-21, shown in Fig. 8.1(c), which grow in time and result from the large aerodynamic loads produced by the unsteady stall cell in this region of the fan. The tip displacements for blades 7-14, shown in Fig. 8.1(b) exhibit a limited structural response for the first 4 revolutions until the stall cell releases from the damaged sector and progresses through this region of the fan producing a sudden increase in tip displacement. The behavior is repeated at $\sim$8 fan revolutions when a second stall cell is released and progresses through this region. By comparison, blades 22-24, which are located immediately downstream of the damaged sector, exhibit smaller tip displacements that remain bounded with time, as shown in Fig. 8.1(d). Finally, the tip displacements of the damaged blades 1-5, shown in Fig. 8.1(a) and the undamaged blade immediately upstream of the damaged sector are the smallest. Blade 4 exhibits the largest response among the 5 damaged blades. Overall, the most significant structural response occurs for the blades opposite the damaged sector due to the progression of the stall cell.

The circumferential displacements of the blade tips for the 75% and 60% throttle settings are shown in Figs. 8.2 and 8.3 The tip displacements are similar for the two throttle settings. The tip displacements for blades 12-19, shown in Figs. 8.2(c) and 8.3(c), are the greatest and result from the progression and regression of the stall cell in this region of the fan. For the 75% throttle setting, the tip displacements of blades 12-19 blades exhibit initially a limited structural response until the stall cell released from the damaged sector progresses through this region of the fan. The progression of the stall cell is indicated by the sequential increase in tip displacement of these blades, from blade 19 at $\sim$2 revolutions through blade 12 at $\sim$4.5 revolutions. For the 60% throttle setting, blades 18 and 19 exhibit a noticeable structural response at $\sim$1.5 revolutions as a result of the initially retreating stall

cell. The remaining blades in this sector exhibit a limited structural response until the stall cell progresses at $\sim$4 revolutions, in a manner resembling the 75% throttle case.

Comparing this case with the 100% throttle setting, it is evident that the unsteady stall cell does not detach and propagate through the undamaged blades 6-11 upstream of the damaged sector. Therefore, the tip displacements of these blades, shown in Figs. 8.2(b) and 8.3(b), are the smallest and appear to be excited primarily by the cyclic increase and decrease of mass flow through these blade passages. The tip displacements of blades 20-24, which are located immediately downstream of the damaged sector, are shown in Figs. 8.2(d) and 8.3(d). Blades 20 and 21 display a similar response to blades 12-19 that results from propagation of the unsteady stall cell. Blades 22-24 display a structural response at higher frequency and smaller amplitude that is induced by the unsteady wake shed from the damaged sector. Finally, the tip displacements of the damaged blades 1-5, shown in Fig. 8.2(a) and 8.3(a), also exhibit a higher frequency content. For both cases, blades 3 and 4 display the largest structural response among the damaged blades.

To determine the modal participation in the structural response, the blade displacements are projected onto the modal coordinates using Eq. (8.1). During post-processing of the structural response, Eq. (8.1) is solved at each time-step using a least squares approach to determine the generalized degrees of freedom, $g_M$, corresponding to each mode shape. In this process, the first 10 natural modes of each rotating blade are used and the mode shapes are normalized by the magnitude of the leading edge tip displacement. Subsequently, Eq. (8.2) is used to calculate the contribution of the $M^{\text{th}}$ natural mode to the displacement of any node in the FE mesh.

$$\mathbf{U}(\mathbf{x},t) \approx \sum_{M=1}^{10} g_M(t)\Phi_M(\mathbf{x}) \tag{8.1}$$

$$\mathbf{U}_M(\mathbf{x},t) = g_M(t)\Phi_M(\mathbf{x}) \tag{8.2}$$

The circumferential displacement together with the contributions from the first 5 rotating modes for the 100% throttle setting are shown in Figs. 8.4 for one blade that best represents the blade response from each group in Figs. 8.1. The contribution from the higher modes is negligible and is not shown. The tip displacement of blade 5, shown in Fig. 8.4(a) is dominated by the first bending mode combined with a small contribution from the first torsion mode, that decays in time, and the second torsion mode that exhibits a "beating" behavior. The tip displacement of blade 12, shown in Fig. 8.4(b) is dominated by the first bending mode and decays slightly in time following the increases in structural response at $\sim$4 and $\sim$8 revolutions. The tip displacement of blade 18 increases with and the first bending mode dominates the response, as shown in Fig. 8.4(c). The response of blade 24, shown in Fig. 8.4(d) is also dominated by the first bending mode combined with a slight contribution from the second torsion that also exhibits beating.

The circumferential displacement together with the contributions from the first 5 rotating modes for the 75% throttle setting are shown in Figs. 8.5 for a blade response that is representative of each group in Figs. 8.2. The tip displacement of blade 4, shown in Fig. 8.5(a) is dominated by the first bending mode combined with the second torsion mode that also exhibits beating. Small contributions from the first torsion and third bending mode are also present. The tip displacement of blade 11, shown in Fig. 8.5(b), is dominated by

the first bending mode and displays and increase in structural response at $\sim$4 revolutions as a result of the stall cell. The tip displacement of blade 14 displays a similar behavior with the first bending mode dominating the response, as shown in Fig. 8.5(c). The tip displacement for blade 24, shown in Fig. 8.5(d), is dominated by the first bending mode and includes contributions from the second torsion mode.

The circumferential displacement together with the contributions from the first 5 rotating modes for the 60% throttle setting are shown in Figs. 8.6 for a blade response that is representative of each group in Figs. 8.3. The tip displacement of blade 5, shown in Fig. 8.6(a) is dominated by the first bending mode, second torsion mode, and also includes beating contributions from the third bending mode. The tip displacement of blades 11, 16, and 22, shown in Figs. 8.6(b)- 8.6(d), are dominated by the first bending mode and include slight contributions from higher modes.

Table 8.2 summarizes the modal contribution of the forced response of blades 1-24 at each throttle setting. In Table 8.2, bold face type indicates the dominant modes, $\downarrow$ indicates a decaying mode, $\uparrow$ indicates a growing mode, and $^*$ indicates a mode whose amplitude displays beating. Overall, the first bending mode dominates the response of the blades at each throttle setting. In addition, the tip displacements of the damaged blades 1-5 contain contributions from the first torsion mode, which decays in time, together with the third bending and second torsion modes that exhibit beating. For the 100% throttle setting, the response of the undamaged blades is exclusively in the first bending mode, with the exception of blade 24 that includes a small contribution from the second torsion mode. The first bending mode also dominates the response of the undamaged blades for the 75% and 60% throttle cases. However, the first torsion and second bending modes also contribute

to the response of the upstream undamaged blades, and the second torsion mode displays beating in the region downstream of the damaged blades.

Table 8.2: Summary of modal contributions of the first 5 rotating modes for the forced response calculations.

| | 100% Throttle Setting | 75% Throttle Setting | 60% Throttle Setting |
|---|---|---|---|
| Blade 1 | **1B** | **1B**, 2T* | **1B**, 2T* |
| Blade 2 | **1B**, 1T↓ | **1B**, 2T*,3B* | **1B**, 1T↓, 3B*, 2T* |
| Blade 3 | **1B**, 1T↓, 2T* | **1B**, **2T*** | **1B**, 2T* |
| Blade 4 | **1B**, 1T↓, 2T* | **1B**, **2T***, 1T↓, 3B* | **1B**, **2T***, 1T↓, 3B* |
| Blade 5 | **1B**, 1T↓, 2T* | **1B**, **2T***, 1T↓, 3B* | **1B**, **2T***, 3B* |
| Blade 6-11 | **1B**↑ | **1B**↑, 2B, 1T | **1B**↑, 2B, 1T |
| Blade 12-19 | **1B**↑ | **1B**↑, 2T* | **1B**↑, 2T* |
| Blade 20 | **1B**↑ | **1B**, 2T* | **1B**, 2T* |
| Blade 21 | **1B**↑ | **1B**, 2T* | **1B**, 2T* |
| Blade 22-23 | **1B** | **1B**, 2T* | **1B**, 2T* |
| Blade 24 | **1B**, 2T* | **1B**, **2T*** | **1B**, 2T* |

## 8.2 Aeroelastic Response of the Damaged Fan

The aeroelastic response calculations of the bird damaged fan at 100%, 75%, and 60% throttle setting are presented in this section. The calculation is initialized following the procedure described in the example aeroelastic response calculation presented in Chapter 6. Specifically, the effect of rotation is introduced by a static structural analysis to obtain the hot geometry that defines the CFD blade geometry. The mapping between the hot FE mesh and the CFD mesh at the wetted surface is performed to establish the fluid structure interface. The aerodynamic loads from the steady CFD calculation are applied to the static structural model to obtain the running geometry, and the resulting structural displacements are transferred to the CFD mesh. A new steady CFD calculation is performed for the

running geometry to generate the initial conditions for the unsteady CFD calculations used in the subsequent aeroelastic response calculation.

The aeroelastic response calculations are performed with a time-step of $\Delta t_f = \frac{1}{500\Omega}$ for a duration of 10 revolutions of the fan. The aerodynamic and structural models are solved iteratively within each time-step using the fully-coupled aeroelastic framework presented in Chapter 6. Convergence of the aerodynamic loads and structural displacements, dictated by Eq. 6.3, typically requires 2 coupling sub-steps within each time-step. Furthermore, 3 CFD-solver sub-iterations are performed at each coupling sub-step to ensure convergence of the aerodynamic solution.

### 8.2.1 Unsteady Aerodynamic Results

The aerodynamic behavior of the damaged fan is presented first to illustrate the effect of blade motion. Figures 8.7(a), 8.7(c), and 8.7(e) show the unsteady total pressure ratio and referred mass flow rate from the aeroelastic response calculations at the 100%, 75%, and 60% throttle settings, respectively. The values in Figs. 8.7(a), 8.7(c), and 8.7(e) are normalized by the referred mass flow rate and total pressure ratio of the undamaged fan at the corresponding throttle setting. The unsteady operating point displays behavior similar to the case without blade motion shown in Figs. 7.5(a), 7.5(c), and 7.5(e). The unsteady operating point at 100% throttle setting oscillates with a period of $\sim$3 revolutions, which is smaller than the case without blade motion. The unsteady operating point for the 75% and 60% throttle settings oscillate with a period of $\sim$4 revolutions and $\sim$5 revolutions, which is also smaller than the case without blade motion. The unsteady operating points at 100%, 75%, and 60% throttle settings are plotted on the fan map in Figs. 8.7(b), 8.7(d), and 8.7(f)

and behave similar the case without blade motion.

Table 8.3 provides the mean referred mass flow rate and total pressure ratio normalized by the corresponding values from the undamaged fan at the same throttle setting. Table 8.3 also provides the amplitude of the unsteady referred mass flow rate and total pressure ratio as a percent of the mean value along with the mean flow loss for each case. The referred mass flow rate varies approximately $\pm 2.9\%$ about its mean value and the total pressure ratio varies approximately $\pm 1.1\%$ about its mean value. Furthermore, the mean flow loss is approximately 7.3% for each case, and is largest for the 100% throttle setting and smallest for the 60% throttle setting. Overall, the unsteady operating point for the case with blade motion in a manner similar to the rigid blade case, indicating that the blade motion has an insignificant influence on the aerodynamic behavior of the damaged fan.

Table 8.3: Unsteady operating points from the aeroelastic response calculations.

| Throttle Setting | Normalized avg($\dot{m}_R$) | Normalized avg($PR$) | Amplitude $\dot{m}_R$ | Amplitude $PR$ | % Flow Loss |
|---|---|---|---|---|---|
| 100% | 0.920 | 0.915 | $\pm 2.6\%$ | $\pm 1.1\%$ | 8.01% |
| 75% | 0.922 | 0.951 | $\pm 3.1\%$ | $\pm 1.2\%$ | 7.1% |
| 60% | 0.931 | 0.965 | $\pm 3.1\%$ | $\pm 0.9\%$ | 6.69% |

Unsteady Mach number contours at the mid-chord are shown in Figs. 8.8 at 9 equally spaced time-steps that span the first 5.6 revolutions of the aeroelastic calculation at 100% throttle setting. The corresponding total pressure ratio and referred mass flow rate at these time-steps are indicated by the fine vertical lines in Fig. 8.7(a). Similar to the case without blade motion, limited flow unsteadiness is evident in the vicinity of the damaged blades. The dominant unsteady flow feature is the stalled flow at the blade tips of the undamaged sector. In Fig. 8.8(a), the stall cell emanating from the damaged sector covers roughly

a third of the fan wheel, from blade 5 counterclockwise to blade 20, and the mass flow rate is near its maximum. Subsequently, from Fig. 8.8(b) to 8.8(g), the stall cell progresses from the damaged sector, detaches, propagates opposite the direction of rotation, and finally dissipates, as shown in Fig. 8.8(h). The unsteady Mach contours at the 75% throttle setting, shown in Figs. 8.9, are similar to the case without blade motion, where the progressing and regressing stall cell is the dominant unsteady feature. The unsteady Mach contours from the aeroelastic calculations at the 60% throttle setting, shown in Figs. 8.10, exhibit a stall cell that progresses from the damaged sector and subsequently detaches in a manner that resembles the case for the 100% throttle setting. This behavior differs from the forced response calculations where the stall cell remains attached to the damaged sector.

### 8.2.2 Aeroelastic Blade Response

The cold-to-running configuration calculation that initializes the aeroelastic response calculation yields tip displacements identical to those in Table 8.1. Table 8.4 provides the maximum leading edge blade tip displacement, $max(||\mathbf{u}(t)||)$, relative to the running configuration for each blade over the duration of the forced response calculation (labeled FR) and the aeroelastic response calculation (labeled AR). The largest tip displacements are identified by bold text in Table 8.4 and occur for the undamaged blades opposite the damaged sector. For the case of the 100% throttle setting, the force response calculation tends to yield larger tip displacements compared to those from the aeroelastic response calculation. By comparison, the aeroelastic response calculations at 75% and 60% throttle settings exhibit a larger tip displacement than the forced response calculations for a majority of the blades.

Table 8.4: Comparison of maximum leading edge blade tip displacement from the forced response (FR) and the aeroelastic response (AR) calculations.

| | **100% Throttle Setting** $max(\|\|\mathbf{u}(t)\|\|)$ [in] | | **75% Throttle Setting** $max(\|\|\mathbf{u}(t)\|\|)$ [in] | | **60% Throttle Setting** $max(\|\|\mathbf{u}(t)\|\|)$ [in] | |
|---|---|---|---|---|---|---|
| | FR | AR | FR | AR | FR | AR |
| Blade 1 | 0.032 | 0.043 | 0.013 | 0.033 | 0.016 | 0.033 |
| Blade 2 | 0.048 | 0.034 | 0.014 | 0.024 | 0.016 | 0.036 |
| Blade 3 | 0.020 | 0.067 | 0.043 | 0.055 | 0.099 | 0.059 |
| Blade 4 | 0.072 | 0.065 | 0.057 | 0.092 | 0.074 | 0.082 |
| Blade 5 | 0.032 | 0.087 | 0.020 | 0.045 | 0.042 | 0.049 |
| Blade 6 | 0.032 | 0.035 | 0.050 | 0.047 | 0.063 | 0.070 |
| Blade 7 | 0.089 | 0.044 | 0.037 | 0.047 | 0.051 | 0.079 |
| Blade 8 | 0.221 | 0.088 | 0.057 | 0.083 | 0.046 | 0.114 |
| Blade 9 | 0.253 | 0.193 | 0.067 | 0.107 | 0.043 | 0.116 |
| Blade 10 | 0.205 | 0.255 | 0.057 | 0.128 | 0.036 | 0.062 |
| Blade 11 | 0.223 | 0.212 | 0.065 | 0.137 | 0.040 | 0.058 |
| Blade 12 | 0.343 | 0.208 | 0.152 | 0.149 | 0.058 | 0.061 |
| Blade 13 | 0.366 | 0.219 | 0.148 | 0.128 | 0.057 | 0.085 |
| Blade 14 | 0.308 | **0.268** | **0.177** | **0.140** | **0.084** | **0.113** |
| Blade 15 | 0.260 | **0.261** | **0.182** | **0.144** | **0.080** | **0.120** |
| Blade 16 | **0.444** | **0.246** | **0.225** | **0.139** | **0.079** | **0.135** |
| Blade 17 | **0.511** | **0.325** | **0.173** | **0.219** | **0.101** | **0.138** |
| Blade 18 | **0.439** | **0.336** | **0.181** | **0.190** | **0.106** | **0.123** |
| Blade 19 | **0.328** | **0.290** | **0.221** | **0.245** | **0.088** | **0.103** |
| Blade 20 | **0.314** | **0.253** | 0.116 | **0.153** | **0.093** | **0.102** |
| Blade 21 | **0.423** | 0.210 | 0.132 | **0.155** | **0.087** | 0.077 |
| Blade 22 | 0.161 | 0.141 | 0.050 | 0.076 | **0.080** | 0.042 |
| Blade 23 | 0.123 | 0.160 | 0.011 | 0.038 | 0.038 | 0.044 |
| Blade 24 | 0.090 | 0.193 | 0.074 | 0.088 | 0.072 | 0.061 |

The circumferential displacement at the leading edge of the blade tips is presented in Figs. 8.11 for the duration of the aeroelastic response calculation at the 100% throttle setting. The displacement is calculated relative to the running configuration, and blades with similar responses are grouped together. Overall, the aeroelastic response of the undamaged fan blades is similar to the forced response results. The largest tip displacements occur for blades 15-21 and grow in time, as shown in Fig. 8.11(c). However, the amplitude of tip displacement for these blades is smaller than that from the forced response calculations. In

Fig. 8.11(b), blades 7-14 exhibit a limited structural response for the first $\sim$3.5 revolutions until the stall cell releases from the damaged sector and progresses through this region of the fan yielding a sudden increase in tip displacement. After the increase in blade response at $\sim$3.5 revolutions, the tip displacements decay more rapidly than the forced response case, indicating that the aeroelastic coupling introduces positive damping for these blades. In Fig. 8.11(d), blades 22-24 exhibit smaller tip displacements that remain bounded with time. When compared to the forced response results in Fig. 8.1(d), the tip displacements for blades 22-24 contain a higher frequency content that indicates higher structural modes are participating in the response of these blades. The tip displacements of blades 1-6 in Fig. 8.11(a) are the smallest; however, the aeroelastic response of these blades also contains a higher frequency component compared to the forced response calculation shown in Fig. 8.1(a).

The circumferential displacement of the blade tips for the 75% throttle setting is presented in Figs. 8.12. The largest tip displacements occur for blades 12-19 and are due to the stall cell at the blade tips, as shown in Fig. 8.12(c). The tip displacements for blades 6-11, shown in Fig. 8.12(b), are larger than those from the forced response calculations and result from the unsteady stall cell that extends further around the wheel than in the forced response case. In Fig. 8.12(d), blades 20-24 exhibit a slightly larger structural response compared to the forced response calculations. The tip displacements of the damaged blades 1-5, shown in Fig. 8.2(a), exhibit a higher frequency content, especially for blades 3 and 4, indicating the participation of a higher structural modes.

The circumferential displacement of the blade tips for the 60% throttle setting is presented in Figs. 8.13. The largest tip displacements occur for blades 12-19, as shown in

Fig. 8.13(c). The structural response of these blades exhibit a higher frequency content than the forced response calculations, particularly after the stall cell progresses at ∼3.5 revolutions. Blades 6-11, shown in Fig. 8.13(b), exhibit a limited structural response until the stall cell detaches and progresses through this region of the fan at ∼5.0 revolutions. When compared to the forced response calculations, the increase in tip displacements is larger and occurs earlier. The structural response of blades 20-24, shown in Fig. 8.3(d), are similar to the force response case with the exception of higher frequency content that appears after ∼4 revolutions. Similar to the aeroelastic response calculations at 100% and 75% throttle settings, the tip displacements of the damaged blades 1-5, shown in Fig. 8.3(a), also exhibit a higher frequency content compared to the forced response calculations, especially for blades 3 and 4.

The circumferential displacement together with the contributions from the first 5 rotating modes for the 100% throttle setting are shown in Figs. 8.14 for the same representative blades used in Figs. 8.4. Similar to the forced response cases, the tip displacement of blade 12, shown in Fig. 8.14(b), is dominated by the first bending mode and decays in time following the increase in structural response at ∼3.5 revolutions. Furthermore, the tip displacement of blade 18 in Fig. 8.14(c) grows in time with the first bending mode dominating the response. The tip displacements of blade 5 and blade 24, shown in Fig. 8.14(a) and Fig. 8.14(d), are initially dominated by the first bending mode. However, the second torsion mode grows rapidly in time and dominates the blade response after ∼2 fan revolutions. The rapid growth of the second torsion mode is unique to the aeroelastic response and may indicate an aeroelastic instability.

The circumferential displacement together with the contributions from the first 5 rotat-

ing modes for the 75% throttle setting are shown in Figs. 8.15. The influence of aeroelastic coupling is most evident for blade 4, which exhibits a rapid growth of the second torsion mode as shown in Fig. 8.15(a). The tip displacements of blades 11 and 14, shown in Figs. 8.15(b) and 8.15(c), are dominated by the first bending mode resembling the forced response case. The aeroelastic response of blade 24, shown in Fig. 8.15(d), is dominated by the first bending mode. The second torsion mode also participates but to a lesser extent than in the forced response case.

Finally, the contributions from the first 5 rotating modes for the 60% throttle setting is presented in Figs. 8.16. The effect of aeroelastic coupling on the circumferential tip displacement is evident, particularly by the appearance and increased participation of the third bending mode. This is most noticeable for the tip displacements of blade 5, shown in Fig. 8.16(a), which is dominated by the first bending mode and displays an increased contribution from the third bending mode. Similar to the forced response case, the blade response of blades 11 and 16, shown in Figs. 8.16(b) and 8.16(c), are dominated by the first bending mode. However, contribution from the third bending mode is again apparent after the increase in tip displacement at $\sim$4.5 revolutions, especially for blade 16. In Fig. 8.16(d), blade 22 is also dominated by the first bending mode and includes participation of the third bending mode with displays beating.

Table 8.2 summarizes the modal contribution for the aeroelastic response of blades 1-24 at each throttle setting. Overall, the first bending mode is dominant in the forced response and aeroelastic response of all blades, with the amplitude of this mode growing for the undamaged blades 6-18. The tip displacements from the aeroelastic response calculations also contain increased contributions from higher modes that may be significant and may

grow in time or exhibit beating. Comparison of the Tables 8.2 and 8.5 reveals some fundamental differences between the forced response and aeroelastic response of the damaged fan. For the forced response case, the primary response of the blade is in the fundamental bending mode, with occasional participation of the higher modes primarily in the second torsion mode. The participation of the higher structural modes is much more evident in the aeroelastic response column, which is not surprising when recognizing that aeroelastic behavior often exhibits a coupled bending-torsion response.

Table 8.5: Summary of modal contributions of the first 5 rotating modes for the aeroelastic response calculations.

| | 100% Throttle Setting | 75% Throttle Setting | 60% Throttle Setting |
|---|---|---|---|
| Blade 1 | **1B**, **2T**↑ | **1B**, 1T↓, 3B↓, 2T* | **1B**, 3B* |
| Blade 2 | **1B**, 3B*, 2T* | **1B**, **3B***, **2T*** | **1B**, **3B***, 2B, 1T↓, 2T* |
| Blade 3 | **1B**, **2T**↑ | **1B**, **2T***, 1T↓, 3B* | **1B**, 3B*, 2T* |
| Blade 4 | **1B**, **2T*** | **1B**, **2T**↑, 1T↓, 3B* | **1B**, **3B***, **2T***, 2B, 1T↓ |
| Blade 5 | **1B**, **2T**↑ | **1B**, **2T**↑, 3B* | **1B**, **3B***, 1T↓, 2T* |
| Blade 6-8 | **1B**↑ | **1B**↑, 2B, 1T | **1B**↑, 2B, 1T |
| Blade 9 | **1B**↑ | **1B**↑, 2B, 1T | **1B**↑, 2B, 1T, 2T |
| Blade 10-11 | **1B**↑ | **1B**↑, 2B, 1T, 2T | **1B**↑, 2B, 1T, 3B, 2T |
| Blade 12 | **1B**↑ | **1B**↑ | **1B**↑, **3B***, 2B, 1T, 2T |
| Blade 13 | **1B**↑ | **1B**↑, 3B* | **1B**↑, **3B***, 2B, 1T |
| Blade 14-18 | **1B**↑ | **1B**↑ | **1B**↑, **3B***, 2B, 1T |
| Blade 19-20 | **1B**↑, 2T↑ | **1B**↑, 2T* | **1B**↑, **3B***, 2B, 1T |
| Blade 21 | **1B**↑, 2T↑ | **1B**↑, 2T* | **1B**, **3B***, 2B, 1T |
| Blade 22 | **1B**, **2T**↑ | **1B**↑, 2T* | **1B**, **3B***, 2B, 1T, 2T |
| Blade 23 | **1B**, **2T**↑ | **1B**↑, 2T* | **1B**, 1T, 2B, 3B↑, 2T |
| Blade 24 | **1B**, **2T**↑ | **1B**↑, 2T* | **1B**, 1T, 2B, 3B↑, 2T |

## 8.3 Assessment of Aeroelastic Stability

The aeroelastic stability of the fan blades is difficult to determine due to the inherent unsteadiness of the aerodynamic environment caused by the bird damage. Common ap-

proaches to determine the aeroelastic stability of a structure often rely on calculating the aerodynamic damping associated with the growth or decay of the blade response. However, the unsteady aerodynamic loads associated with a bird damaged fan excite the blades causing a growth in blade response that may hide the aeroelastic effects.

To provide insight into the cause of the growing blade response in the aeroelastic response calculations, the work performed by the aerodynamic forces on the structure is calculated and compared to the forced response calculations. The aeroelastic stability of the aeroelastic response is inferred based on the time-history of the aerodynamic work relative to the forced response calculations. Aerodynamic work that grows relative to the forced response calculations indicates a potential aeroelastic instability. Aerodynamic work that decays relative to the forced response calculations implies positive aerodynamic damping. The aerodynamic work of the entire blade is calculated for the forced response and aeroelastic response using Eq. (8.3) and Eq. (8.4), respectively.

$$W_{FR}(t) = \int_0^t \mathbf{F}_{\text{aero}}(s) \cdot \dot{\mathbf{U}}(s) ds \tag{8.3}$$

$$W_{AR}(t) = \int_0^t \mathbf{F}_{\text{aero}}(s, \mathbf{U}, \dot{\mathbf{U}}, \ddot{\mathbf{U}}) \cdot \dot{\mathbf{U}}(s) ds \tag{8.4}$$

The aerodynamic work as a function of fan revolutions is presented in Figs. 8.17 for blades 5, 12, 18, and 24 at the 100% throttle setting. The aerodynamic work from the forced response calculations is compared to aerodynamic work from the aeroelastic response calculations to identify possible aeroelastic instabilities. In Fig. 8.17(a), the aerodynamic work on blade 5 from the aeroelastic response calculations is positive and grows at a rate

greater than that of the forced response calculations indicating the potential for aeroelastic instability of the blade. The aerodynamic work for blade 24 from the aeroelastic response calculations displays a behavior that resembles blade 5, as shown in Fig. 8.17(d), indicating a possible aeroelastic instability of this blade. For blades 12 and 18, the aerodynamic work from the aeroelastic response calculations does not increase in time when compared to the forced response case, as shown in Figs. 8.17(b) and 8.17(c). This suggests that the growth in response of these blades is due to the unsteady aerodynamic loads caused by the stall cell, and the aeroelastic effects introduce positive aerodynamic damping for these blades.

The aerodynamic work from the calculations at 75% throttle setting is presented in Fig. 8.18 for blades 4, 11, 14, and 24. Comparison of the aerodynamic work on blade 4, shown in Fig. 8.18(a), indicates that the growth of the second torsion mode in the aeroelastic response of this blade may be indicative of an aeroelastic instability. For blades 11 and 14, the aerodynamic work from the aeroelastic response calculation is similar to that from the forced response, as shown in Figs. 8.18(b) and 8.18(c). Therefore, the growth in response of these blades results from the unsteady aerodynamic loads caused by the bird damage rather than an aeroelastic instability. The aerodynamic work from the aeroelastic response calculation for blade 24, shown in Fig. 8.18(d), is smaller when compared to the forced response calculation. This suggests that aeroelastic effects introduce positive damping, which is evident by the decreased participation of the second torsion mode for the aeroelastic case.

Figs. 8.19 provides the aerodynamic work from the aeroelastic and forced response calculations at the 60% throttle setting. The aerodynamic work for blade 5 is shown in Fig. 8.19(a). The aerodynamic work from the aeroelastic response calculations increases

at a similar rate to the forced response case, which may indicate a neutrally stable case where the blade is on the flutter margin. The aerodynamic work for blades 11, 16, and 22 is shown in Figs. 8.19(b)- 8.19(d). The aerodynamic work for these blades displays similarity between the aeroelastic and forced response calculations. This behavior suggests two possible situations: (a) neutral stability of the blades, or (b) the blade response is dominated by the unsteady aerodynamic loads induced by the bird damage. Comparison of the aerodynamic work for the remaining blades at the 60% throttle setting displays similar behavior and does not indicate potential aeroelastic instabilities.

The results obtained seem to indicate that for the cases considered, bird damage does not have a major effect on aeroelastic stability. The growth in structural response for the undamaged blades opposite the damaged sector appears to be dominated by the unsteady aerodynamics caused by the damaged blades. The damaged blades and those directly downstream of the damaged sector exhibit a possible aeroelastic instability of the second torsion mode for the 100% and 75% throttle settings. For the case of 100% throttle setting, the aeroelastic response indicates an instability dominated by the second torsion mode for blades 3, 5, and 24. By comparison at 75% throttle setting the aeroelastic response in the second torsion mode of blades 4 and 5 is indicative of an aeroelastic instability. The instability of these blades likely results from interaction between the blade motion and the unsteady wake shed from the upstream damaged blades. The tip displacements of these blades appear to reach a limit-cycle amplitude that is relatively small compared to those of the undamaged blades opposite the damaged sector. Furthermore, these results should be interpreted under the assumption that structural damping is neglected. Including structural damping in the structural dynamic model may reduce or all together eliminate the

aeroelastic instability of these blades.

## 8.4 Computational Effort

The computational costs of the forced response and aeroelastic response calculations are substantial. The calculations were performed using parallel Intel Xeon X5650 2.67 GHz processors assembled on a high-performance computing cluster composed of 12-processor nodes with 48 GB of RAM per node. Table 8.6 lists the number of CPUs used by the CFD and CSD solvers and the associated wall time for the forced response and aeroelastic response calculations. The unsteady CFD calculations for the forced response calculations required 7.5 days using 48 distributed parallel CPUs. Additional processors were ineffective in decreasing the wall time since more CPU time is spent passing information between processors. The subsequent CSD calculation required 1.5 days using 12 local parallel CPUs. The ANSYS MFX code limits the number of processors for the CSD calculations. However, additional processors are not expected to significantly decrease the wall time of the CSD calculation.

Table 8.6: Computational cost of forced response and aeroelastic response calculations.

| | Number of CPUs | | Wall Time (days) | | |
|---|---|---|---|---|---|
| | CFD | CSD | CFD (days) | CSD | CFD/CSD |
| Forced Response | 48 | 12 | 7.5 | 1.5 | N/A |
| Aeroelastic Response | 60 | 12 | N/A | N/A | 34.5 |

The computational demand of the aeroelastic response calculations is considerably higher than that for the forced response calculations. Several factors contribute to the increased wall time of the aeroelastic response calculations. First, the CFD and CSD solvers

run simultaneously and exchange information during each time-step. Each solver experiences considerable "down-time" while it waits for the other solver to update and pass information for the next time-step. Second, ANSYS MFX requires the CFD and CSD solvers to utilize the same time-step, which is determined by the CFD solver. Therefore, the number of time-steps performed for the CSD calculations increases 10 fold compared to the forced response calculation. Third, several sub-steps are performed within each time-step that requires the solvers to complete additional computations compared to the forced response calculation. Finally, the CFD mesh deformation performed at each time-step is computationally expensive, and an additional 12 CPUs were utilized to provide additional computational resources.

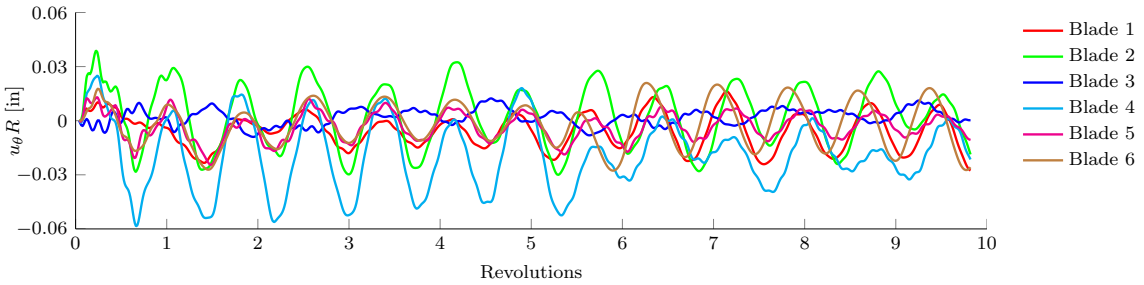


(a) Relative tip displacements for blades 1-6.

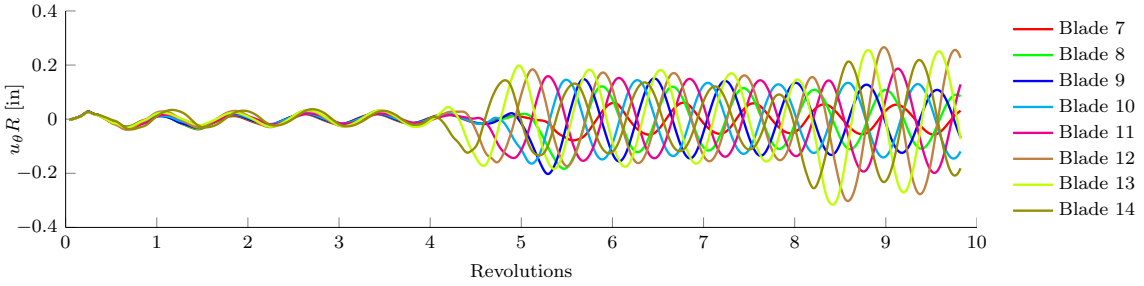


(b) Relative tip displacements for blades 7-14.

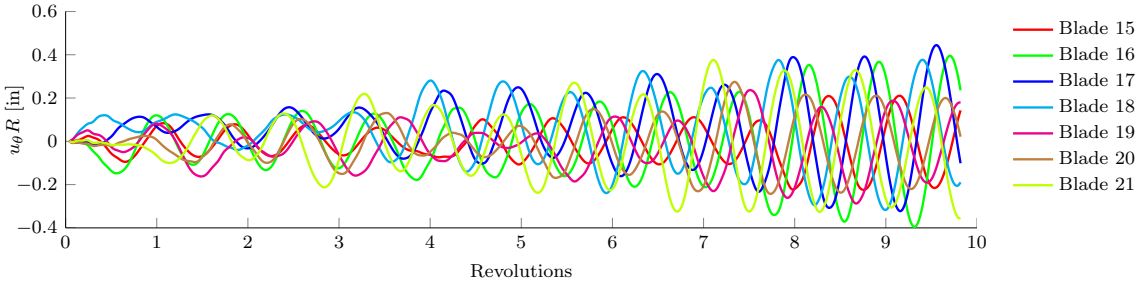


(c) Relative tip displacements for blades 15-21.

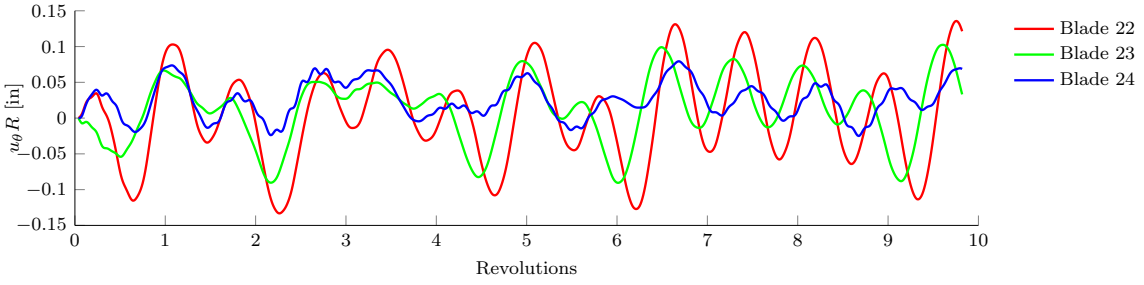


(d) Relative tip displacements for blades 22-24.

Figure 8.1: Tip displacements from the forced response calculations at the 100% throttle setting, relative to the running configuration.

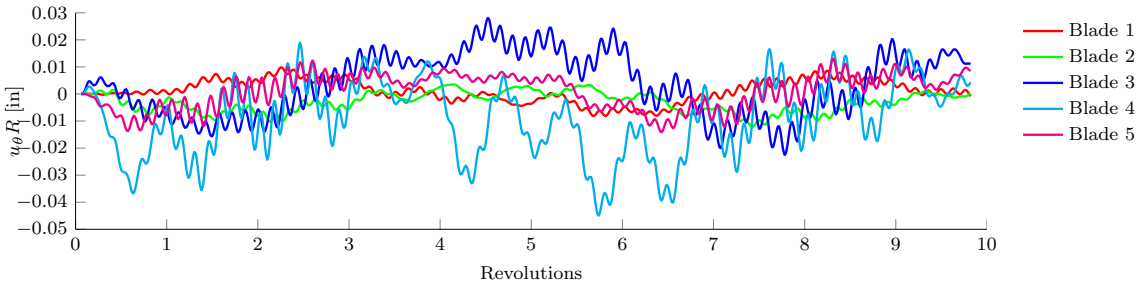


(a) Relative tip displacements for blades 1-5.

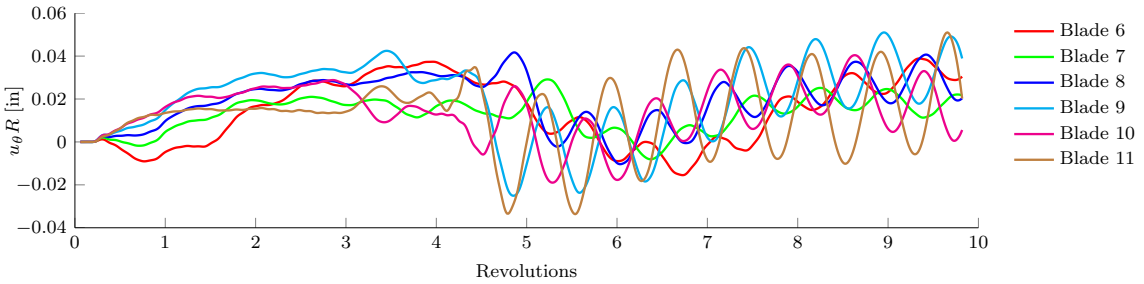


(b) Relative tip displacements for blades 6-11.

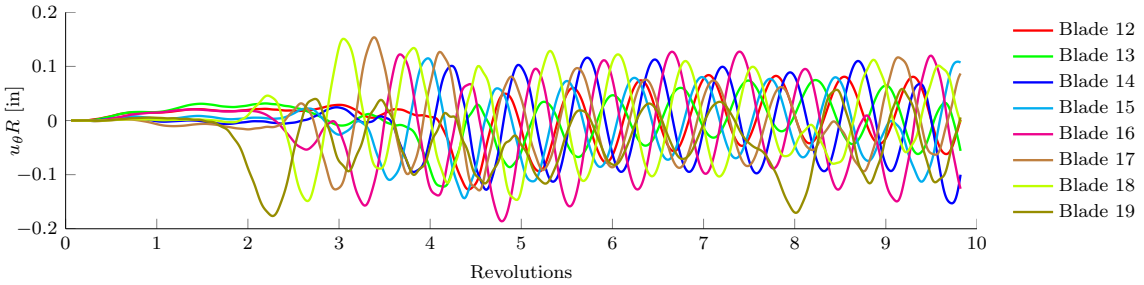


(c) Relative tip displacements for blades 12-19.

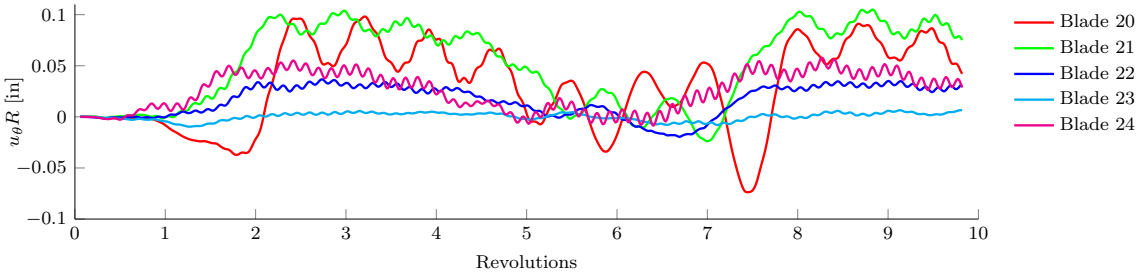


(d) Relative tip displacements for blades 20-24.

Figure 8.2: Tip displacements from the forced response calculations at the 75% throttle setting, relative to the running configuration.

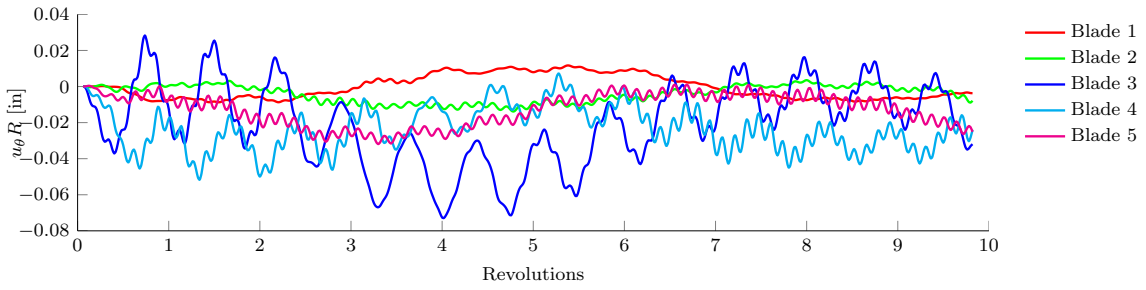


(a) Relative tip displacements for blades 1-5.

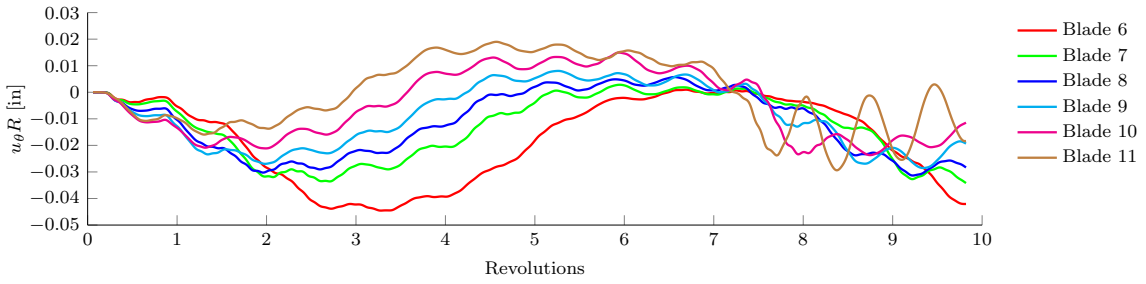


(b) Relative tip displacements for blades 6-11.

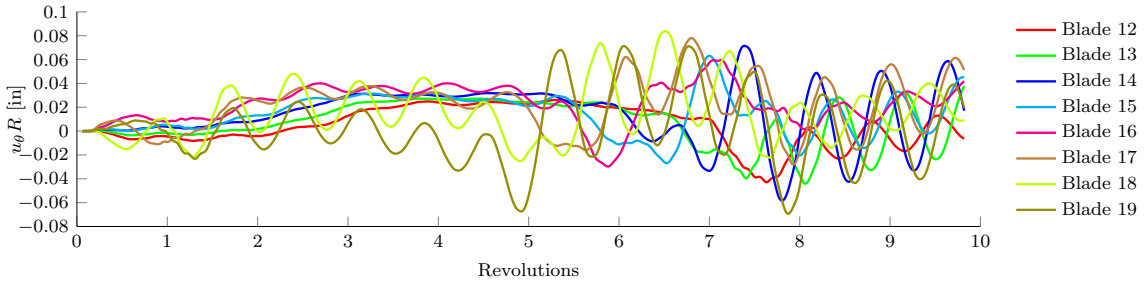


(c) Relative tip displacements for blades 12-19.

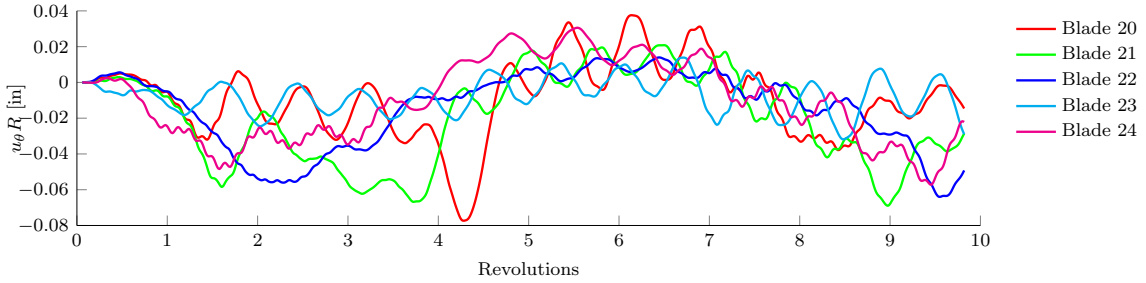


(d) Relative tip displacements for blades 20-24.

Figure 8.3: Tip displacements from the forced response calculations at the 60% throttle setting, relative to the running configuration.

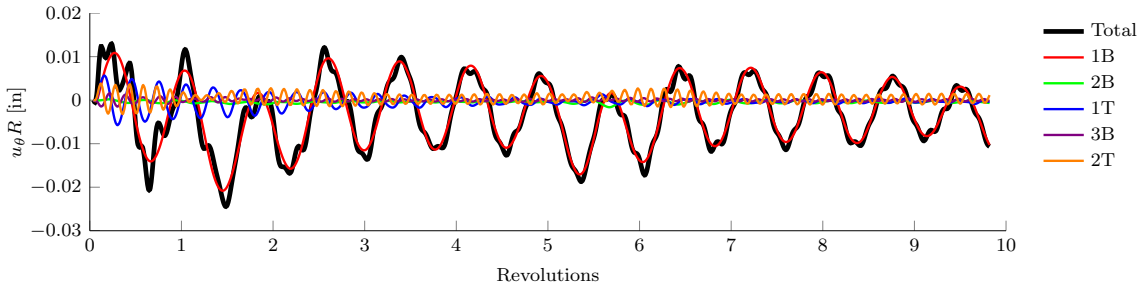


(a) Relative tip displacements for blade 5.

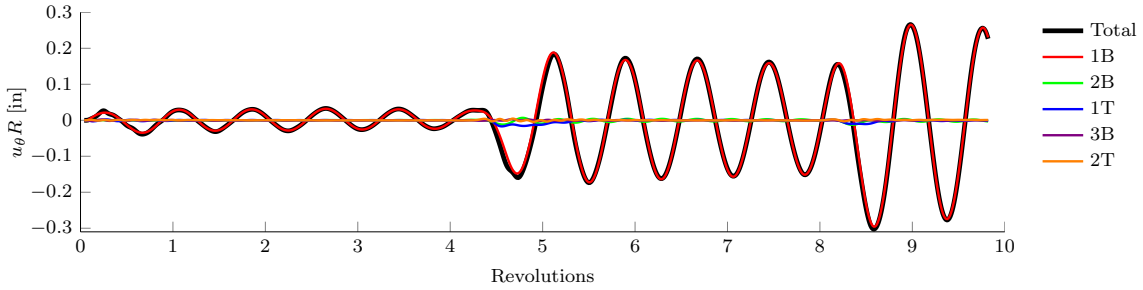


(b) Relative tip displacements for blade 12.

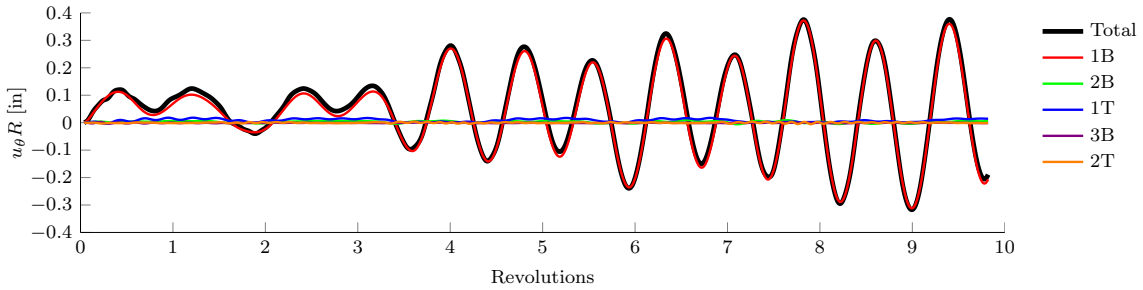


(c) Relative tip displacements for blade 18.

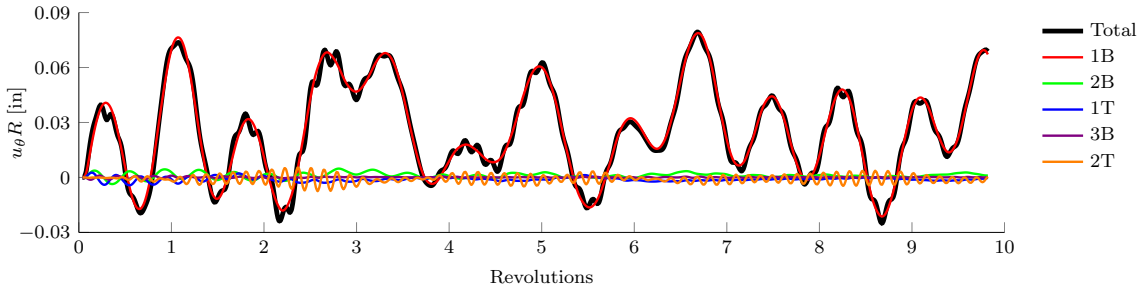


(d) Relative tip displacements for blade 24.

Figure 8.4: Forced response tip displacements and the modal contributions from the first 5 rotating modes at 100% throttle setting.

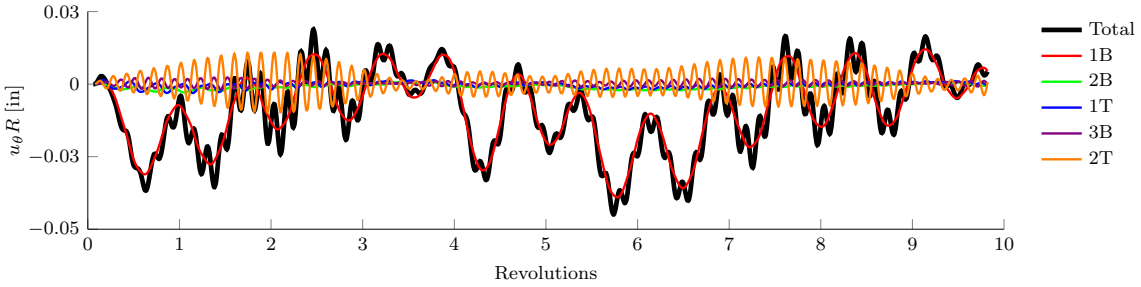


(a) Relative tip displacements for blade 4.

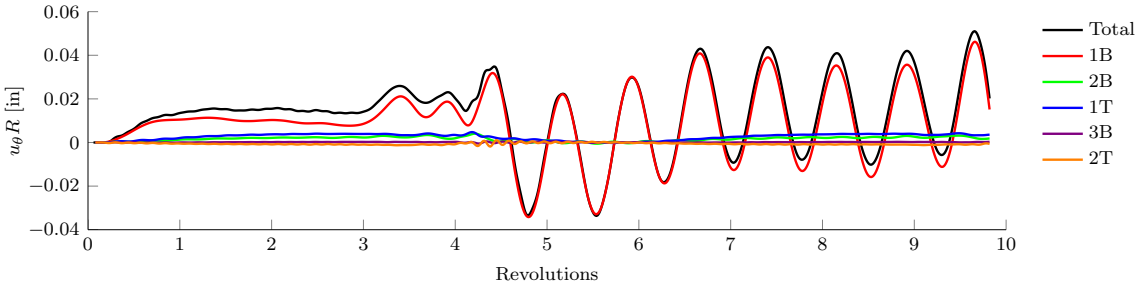


(b) Relative tip displacements for blade 11.

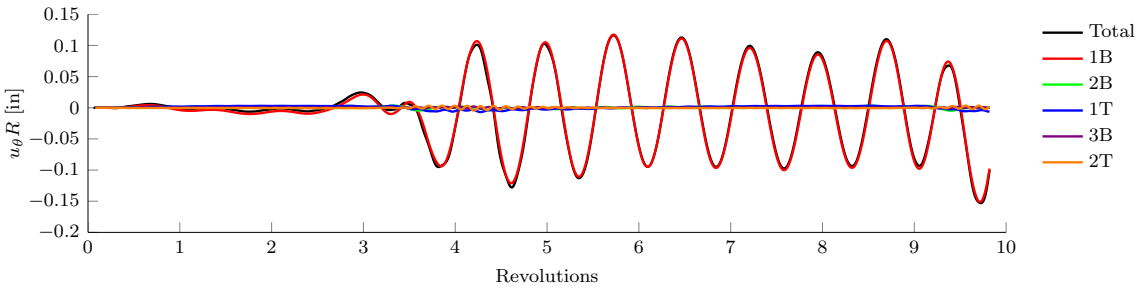


(c) Relative tip displacements for blade 14.

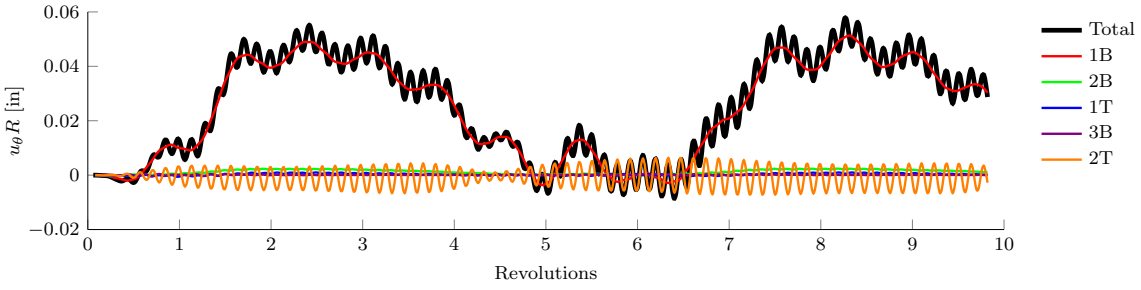


(d) Relative tip displacements for blade 24.

Figure 8.5: Forced response tip displacements and the modal contributions from the first 5 rotating modes at 75% throttle setting.

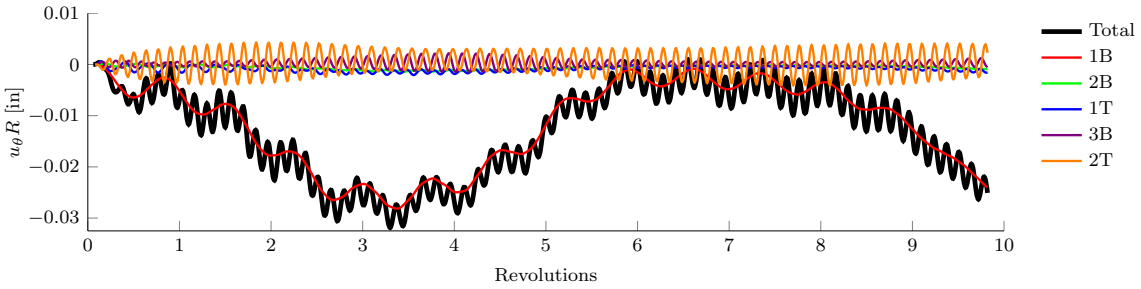


(a) Relative tip displacements for blade 5.

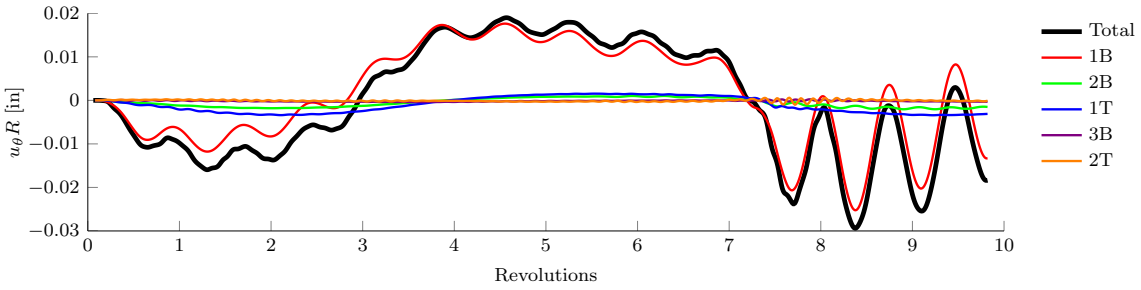


(b) Relative tip displacements for blade 11.

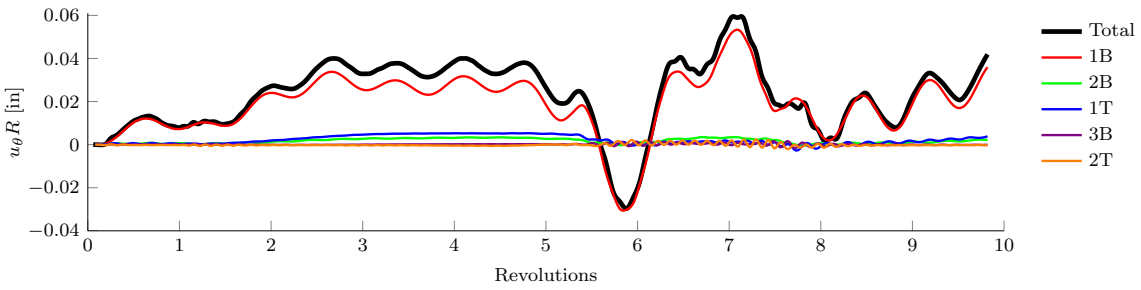


(c) Relative tip displacements for blade 16.

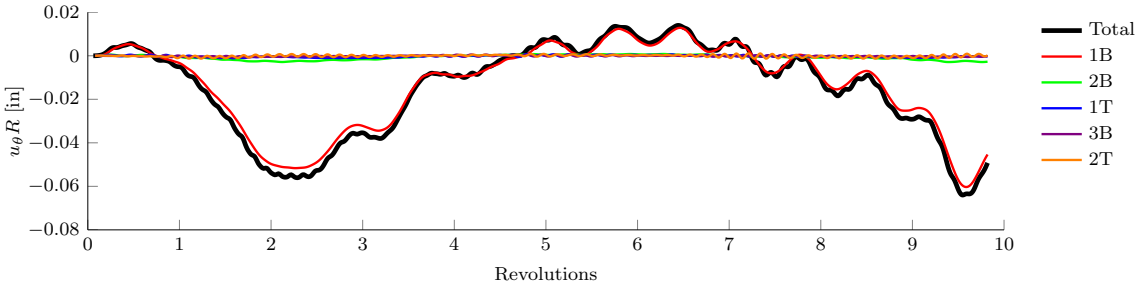


(d) Relative tip displacements for blade 22.

Figure 8.6: Forced response tip displacements and the modal contributions from the first 5 rotating modes at 60% throttle setting.

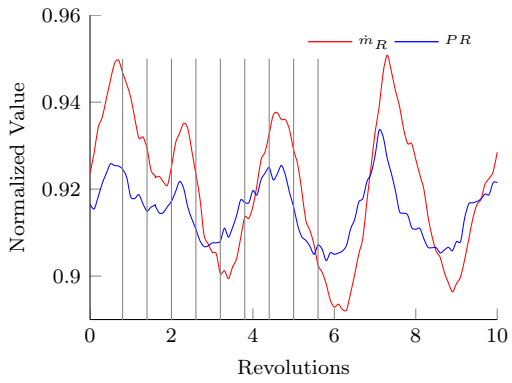


(a) Referred mass flow rate and total pressure ratio time history at 100% throttle setting.

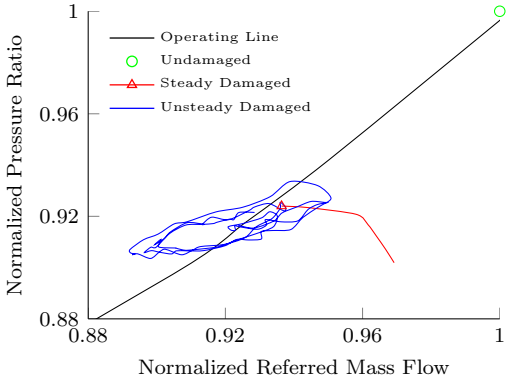


(b) Fan map with characteristic curve and steady and unsteady operating points at 100% throttle setting.

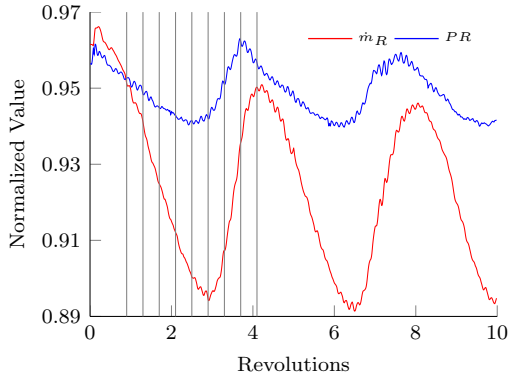


(c) Referred mass flow rate and total pressure ratio time history at 75% throttle setting.

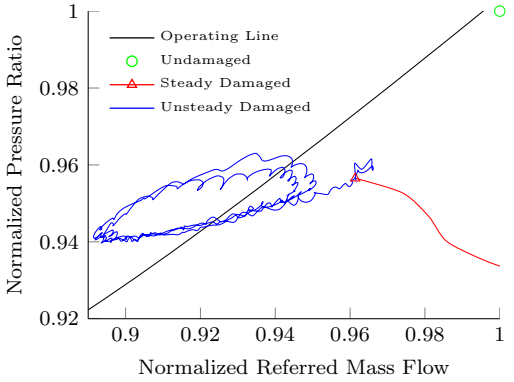


(d) Fan map with characteristic curve and steady and unsteady operating points at 75% throttle setting.

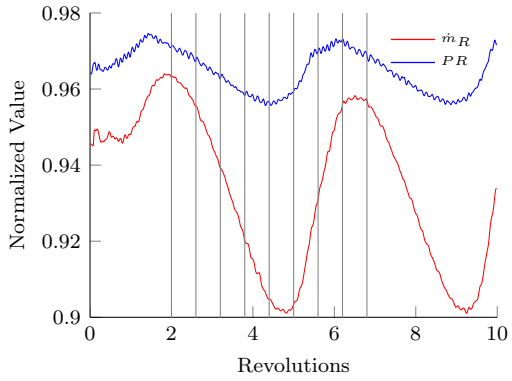


(e) Referred mass flow rate and total pressure ratio time history at 60% throttle setting.

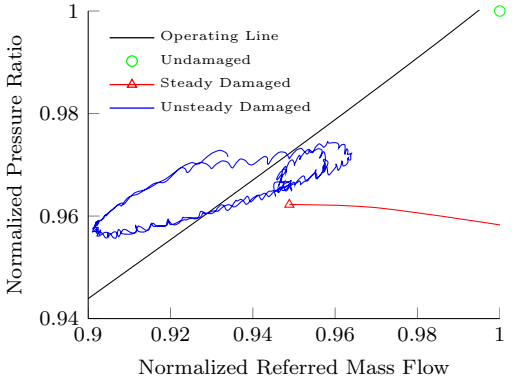


(f) Fan map with characteristic curve and steady and unsteady operating points at 60% throttle setting.

Figure 8.7: Unsteady total pressure ratio and referred mass flow rate from the aeroelastic response calculations.

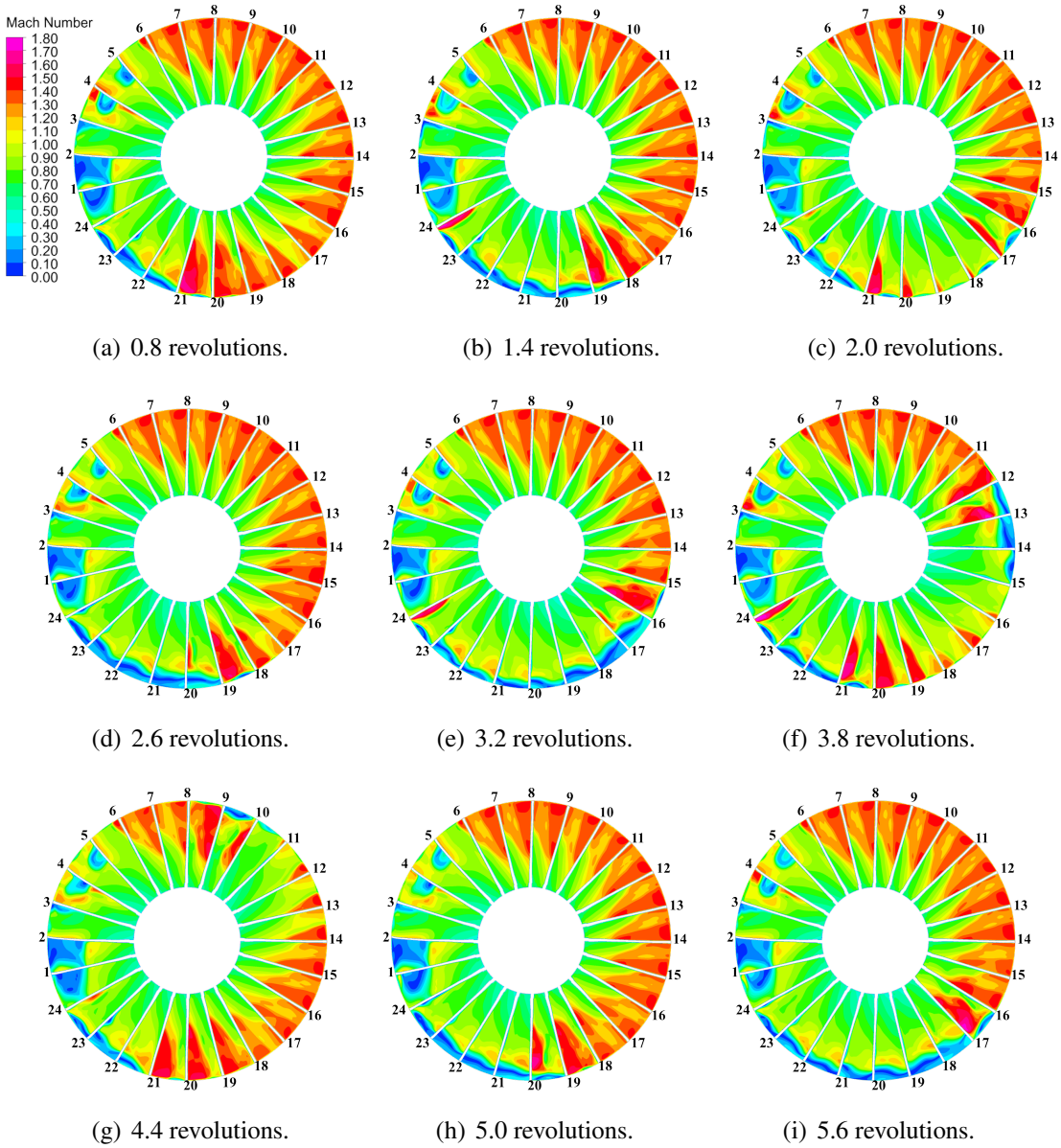


(a) 0.8 revolutions. (b) 1.4 revolutions. (c) 2.0 revolutions.

(d) 2.6 revolutions. (e) 3.2 revolutions. (f) 3.8 revolutions.

(g) 4.4 revolutions. (h) 5.0 revolutions. (i) 5.6 revolutions.

Figure 8.8: Unsteady Mach number contours of the damaged blade at mid-chord from the aeroelastic response calculations at the 100% throttle setting (direction of rotation: clockwise).

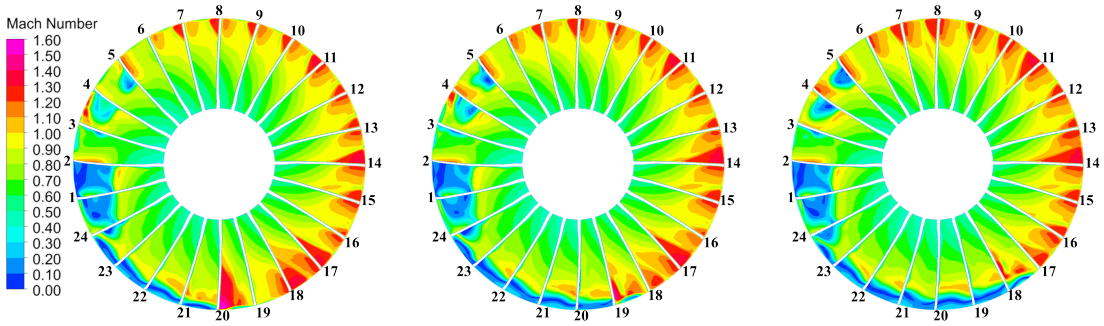


(a) 0.9 revolutions. (b) 1.3 revolutions. (c) 1.7 revolutions.

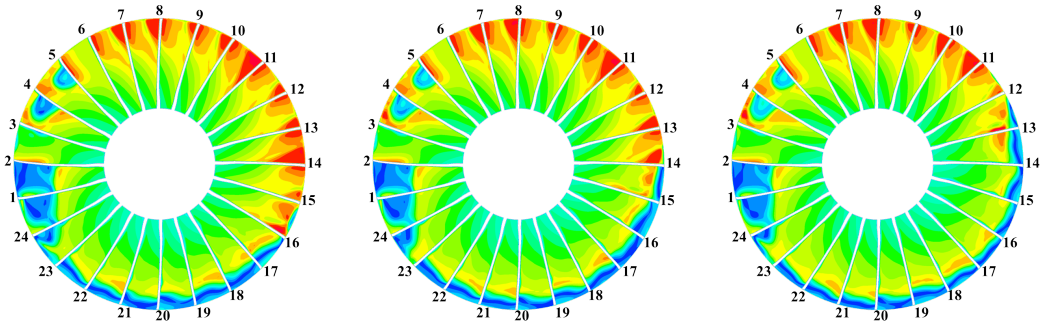

(d) 2.1 revolutions. (e) 2.5 revolutions. (f) 2.9 revolutions.

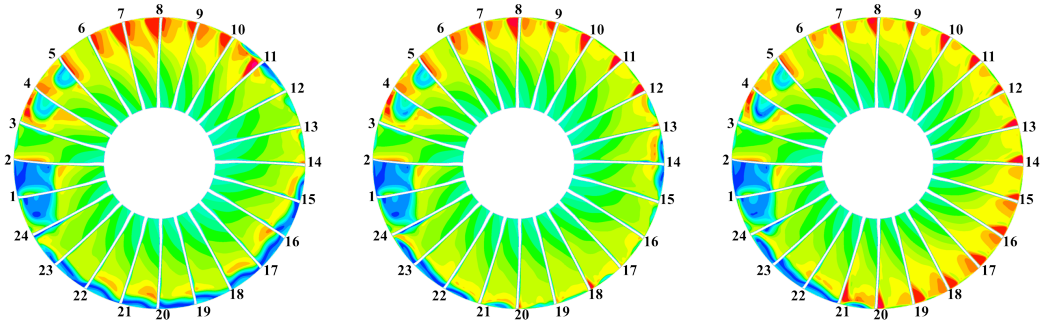

(g) 3.3 revolutions. (h) 3.7 revolutions. (i) 4.1 revolutions.

Figure 8.9: Unsteady Mach number contours of the damaged blade at mid-chord from the aeroelastic response calculations at the 75% throttle setting (direction of rotation: clockwise).

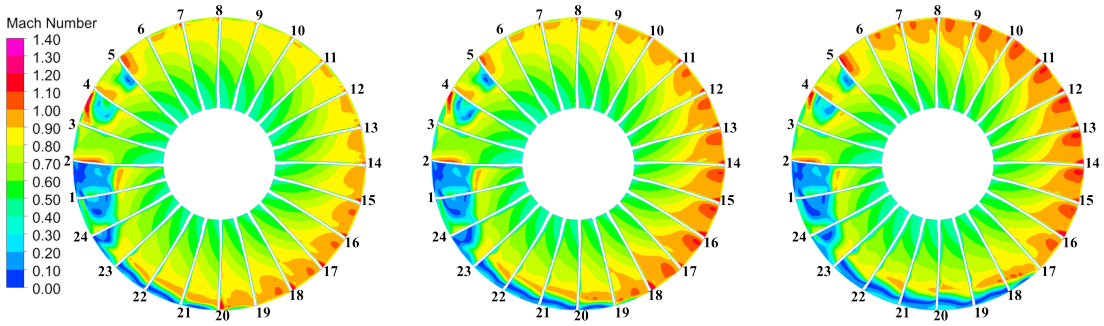


(a) 1.0 revolutions. (b) 1.6 revolutions. (c) 2.2 revolutions.

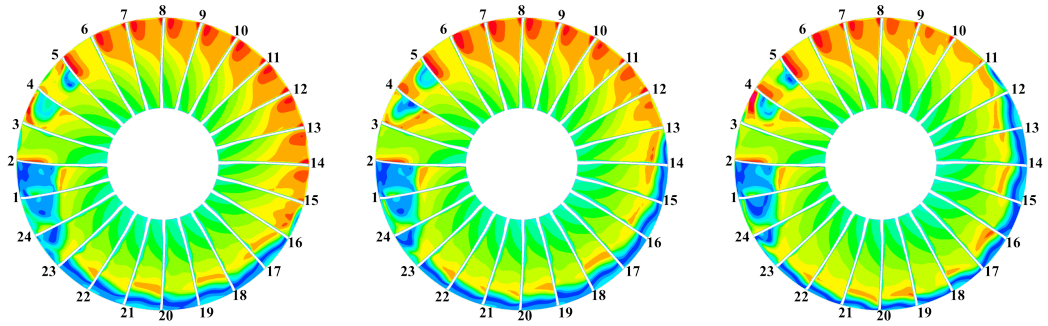

(d) 2.8 revolutions. (e) 3.4 revolutions. (f) 4.0 revolutions.

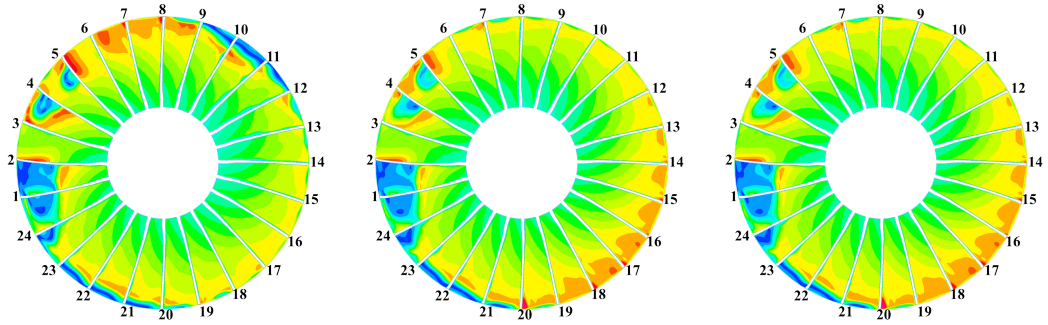

(g) 4.6 revolutions. (h) 5.2 revolutions. (i) 5.8 revolutions.

Figure 8.10: Unsteady Mach number contours of the damaged blade at mid-chord from the aeroelastic response calculations at the 60% throttle setting (direction of rotation: clockwise).

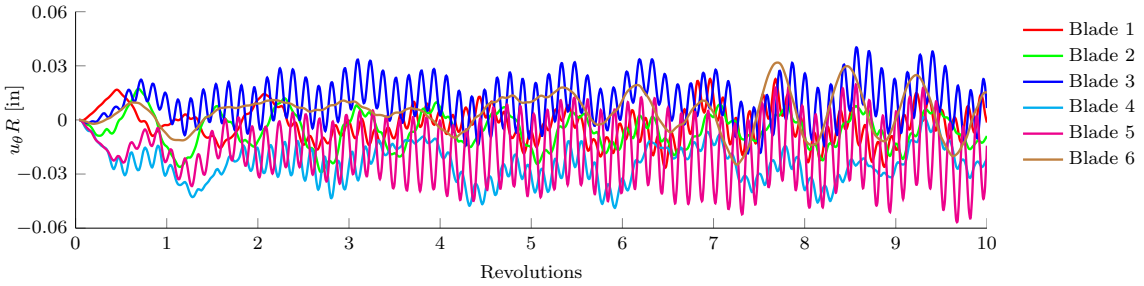


(a) Relative tip displacements for blades 1-6.

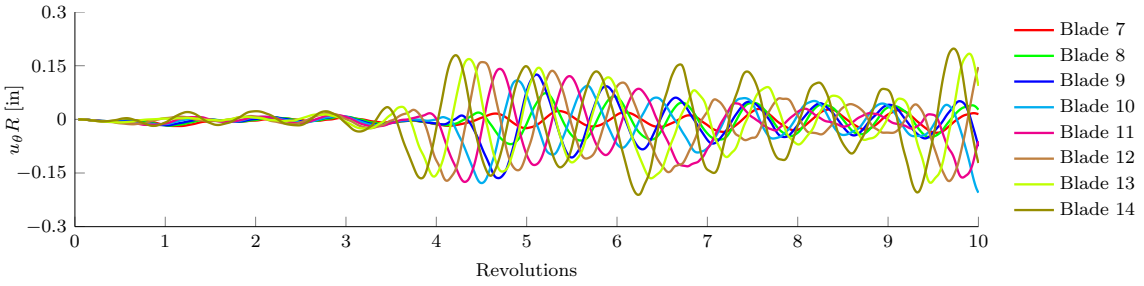


(b) Relative tip displacements for blades 7-14.

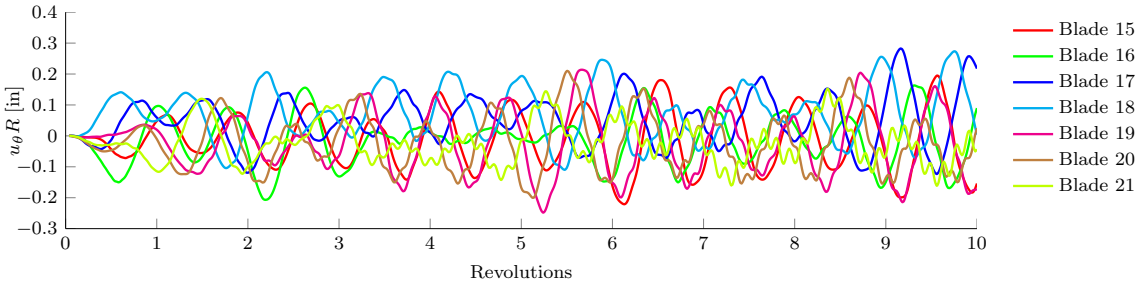


(c) Relative tip displacements for blades 15-21.

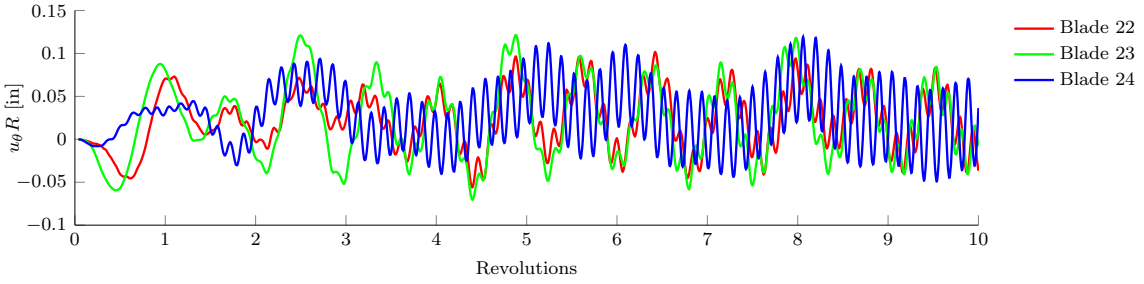


(d) Relative tip displacements for blades 22-24.

Figure 8.11: Tip displacements from the aeroelastic response calculations at 100% throttle setting, relative to the running configuration.

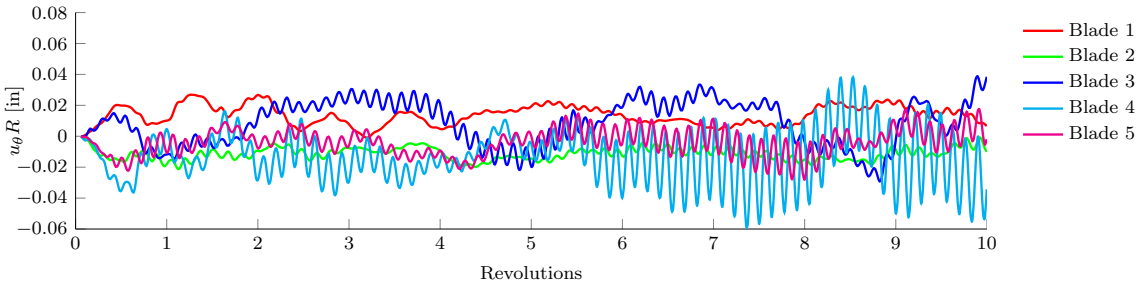


(a) Relative tip displacements for blades 1-5.

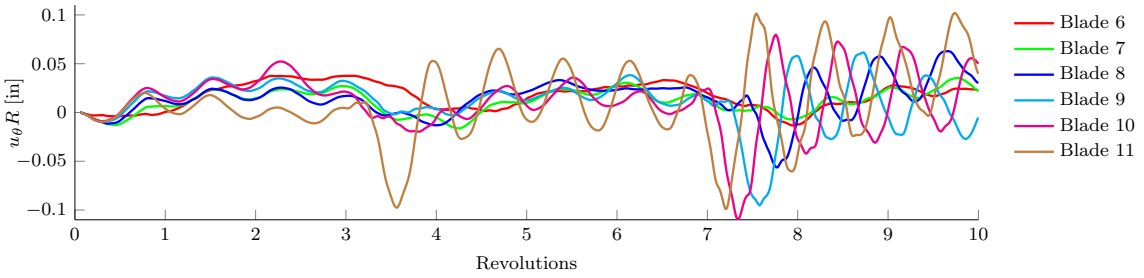


(b) Relative tip displacements for blades 6-11.

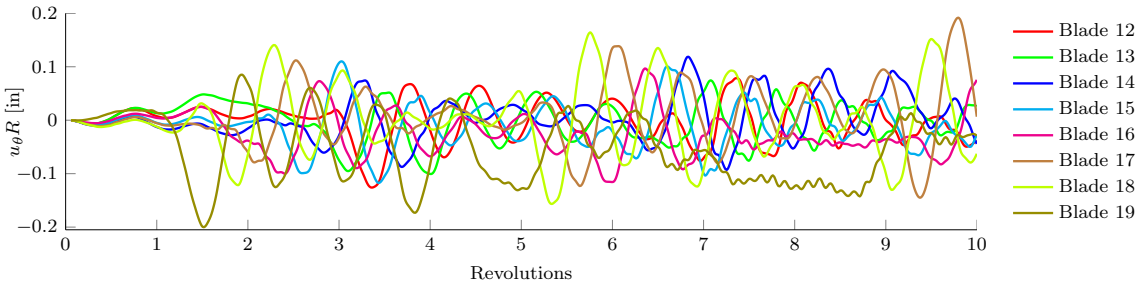


(c) Relative tip displacements for blades 12-19.

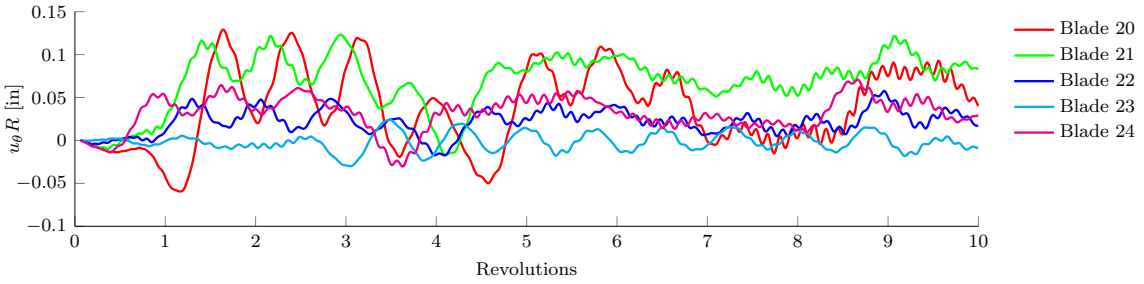


(d) Relative tip displacements for blades 20-24.

Figure 8.12: Tip displacements from the aeroelastic response calculations at the 75% throttle setting, relative to the running configuration.

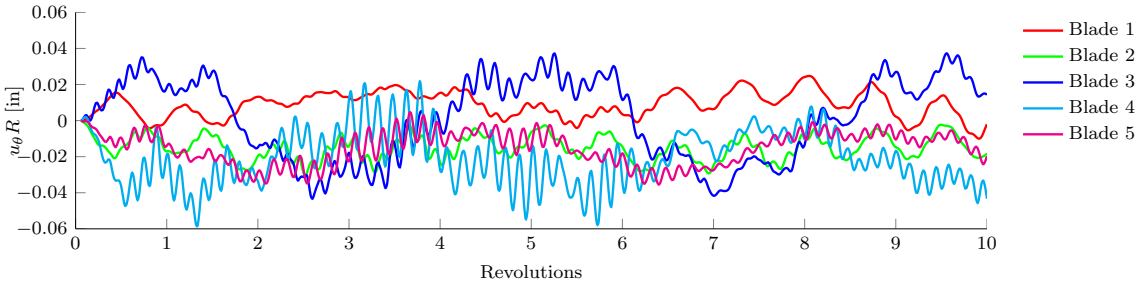


(a) Relative tip displacements for blades 1-5.

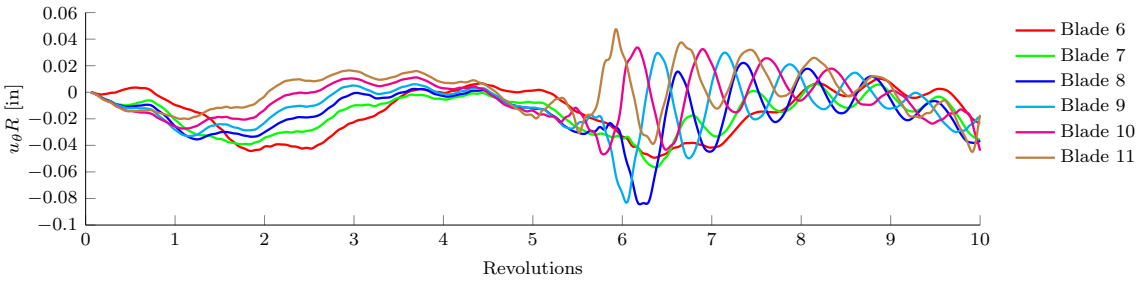


(b) Relative tip displacements for blades 6-11.

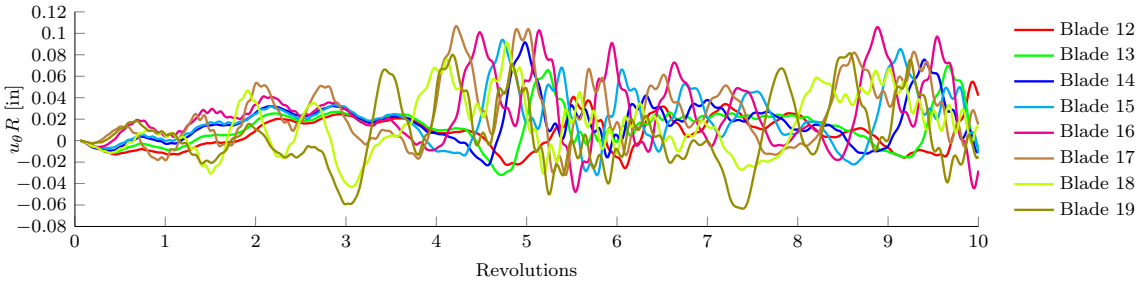


(c) Relative tip displacements for blades 12-19.

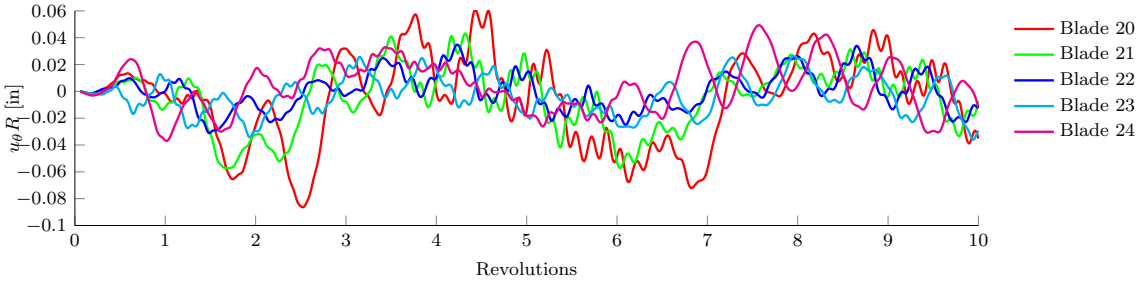


(d) Relative tip displacements for blades 20-24.

Figure 8.13: Tip displacements from the aeroelastic response calculations at the 60% throttle setting, relative to the running configuration.

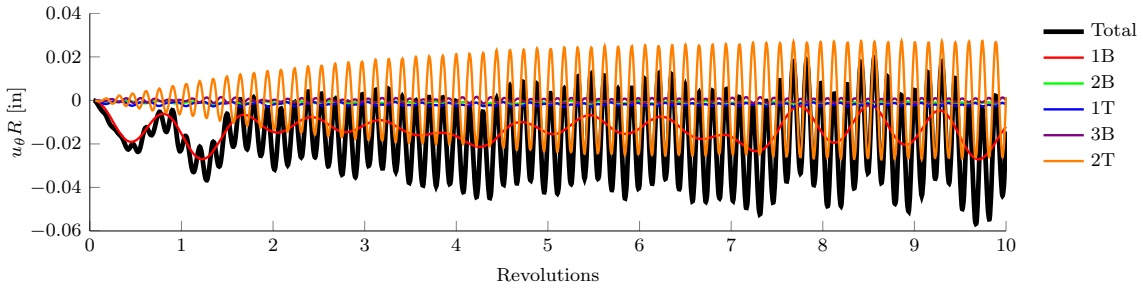


(a) Relative tip displacements for blade 5.

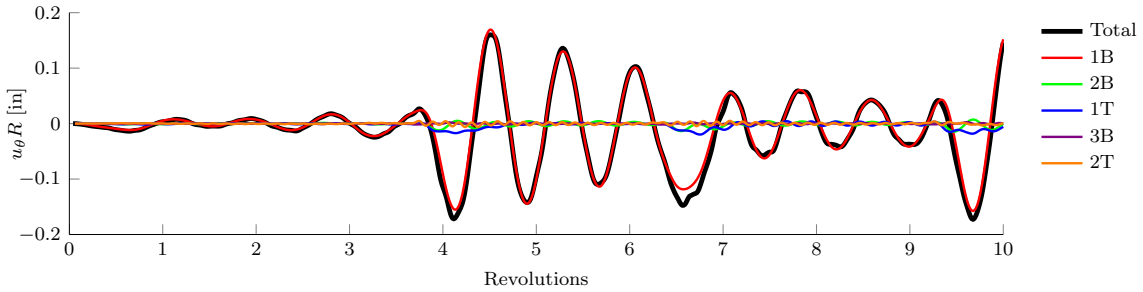


(b) Relative tip displacements for blade 12.

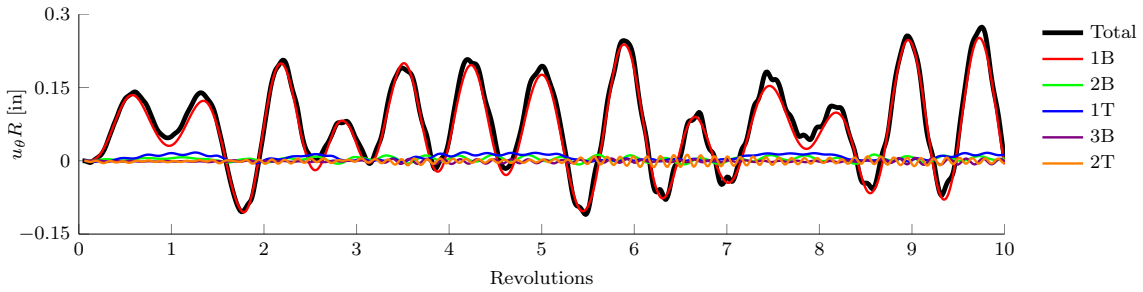


(c) Relative tip displacements for blade 18.

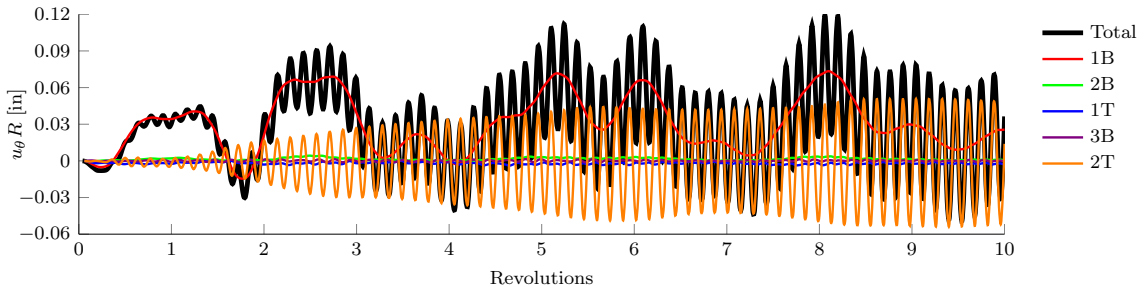


(d) Relative tip displacements for blade 24.

Figure 8.14: Aeroelastic response tip displacements and the modal contributions of the first 5 rotating modes at the 100% throttle setting.

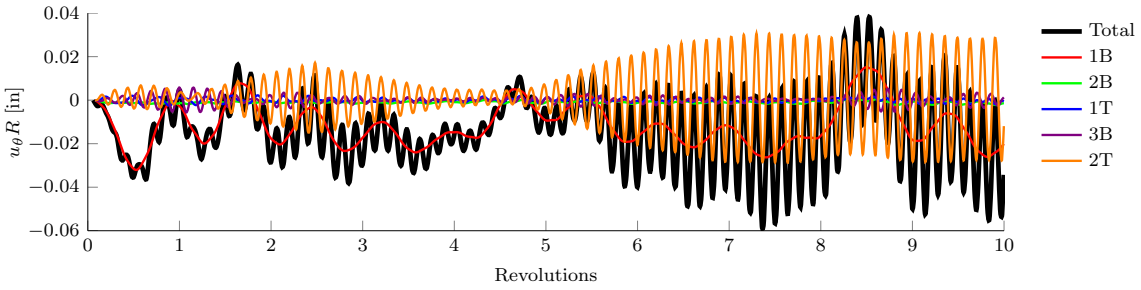


(a) Relative tip displacements for blade 4.

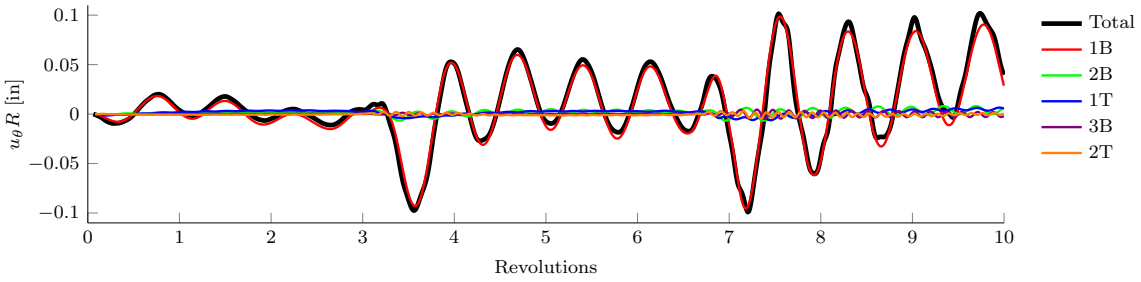


(b) Relative tip displacements for blade 11.

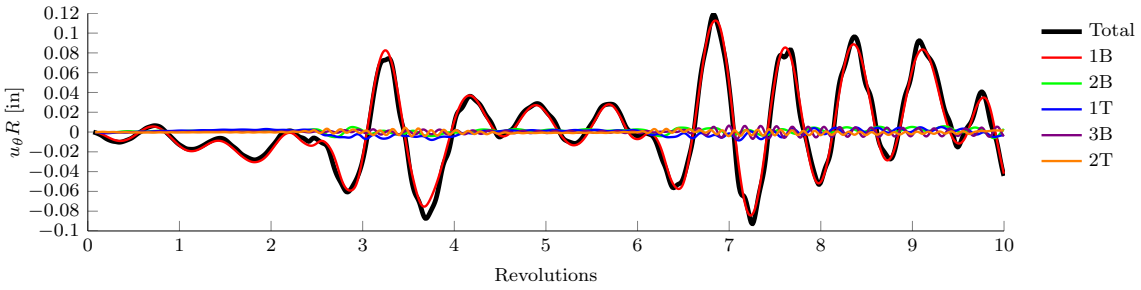


(c) Relative tip displacements for blade 14.

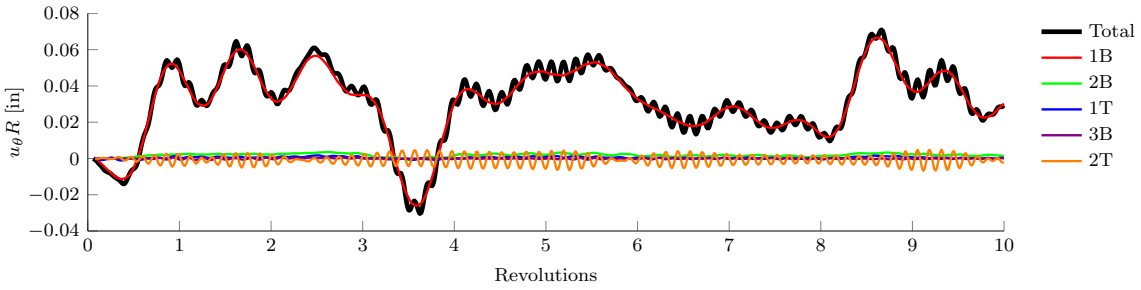


(d) Relative tip displacements for blade 24.

Figure 8.15: Aeroelastic response tip displacements and the modal contributions of the first 5 rotating modes at the 75% throttle setting.

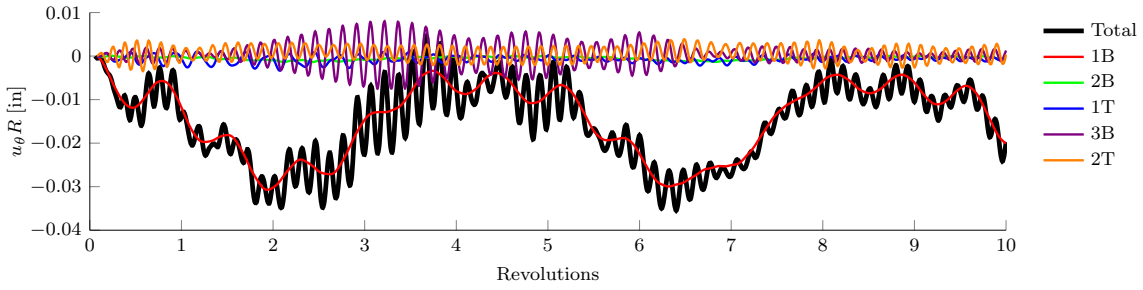


(a) Relative tip displacements for blade 5.

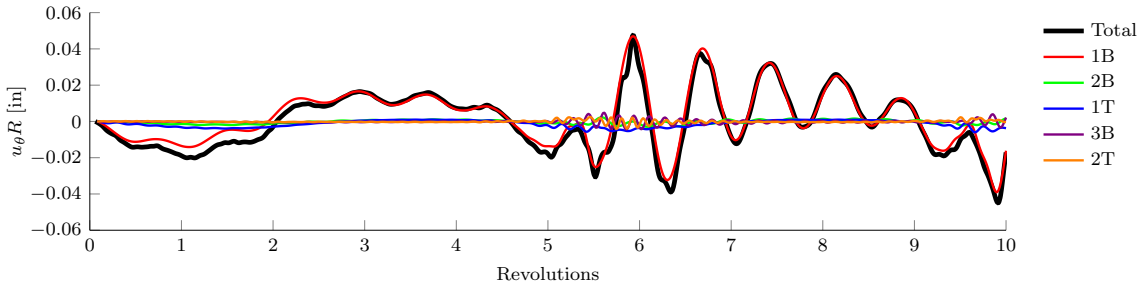


(b) Relative tip displacements for blade 11.

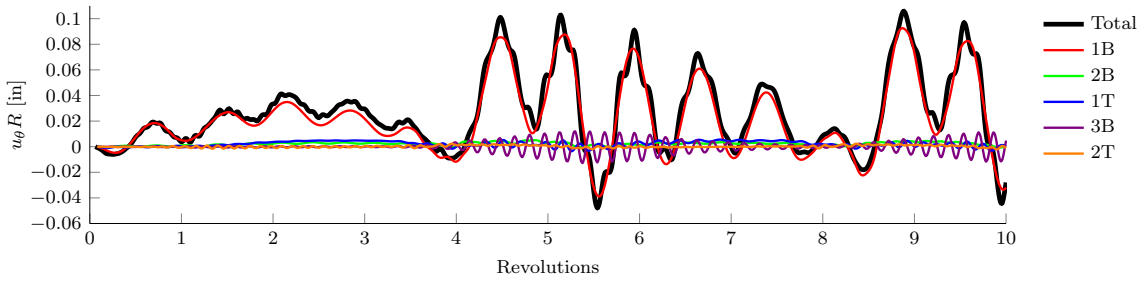


(c) Relative tip displacements for blade 16.

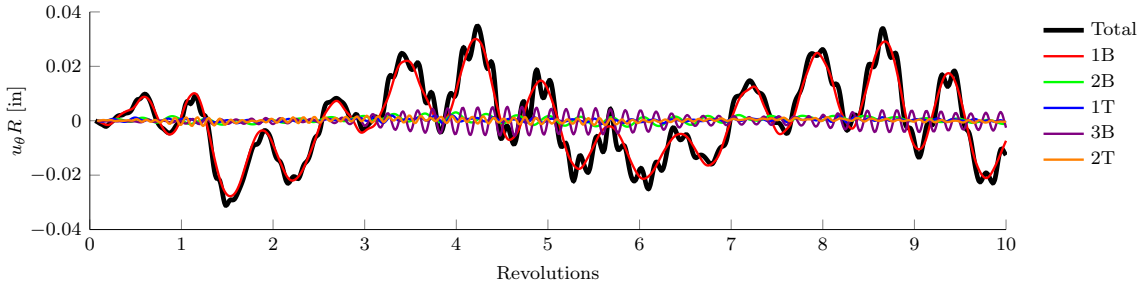


(d) Relative tip displacements for blade 22.

Figure 8.16: Aeroelastic response tip displacements and the modal contributions of the first 5 rotating modes at the 60% throttle setting.

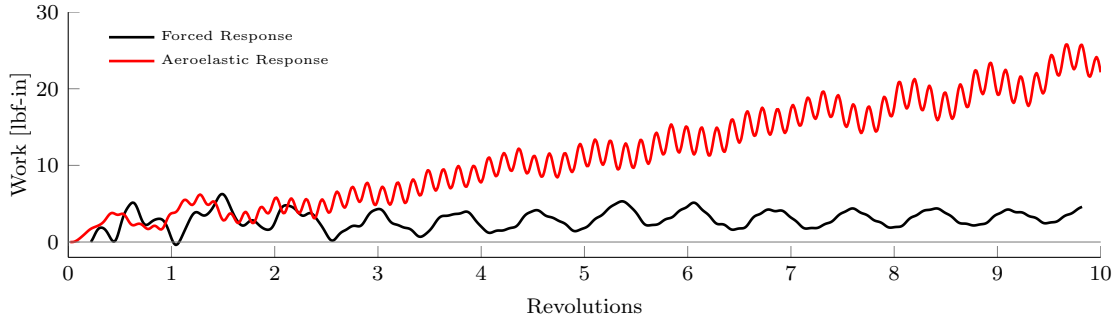


(a) Aerodynamic work for blade 5.

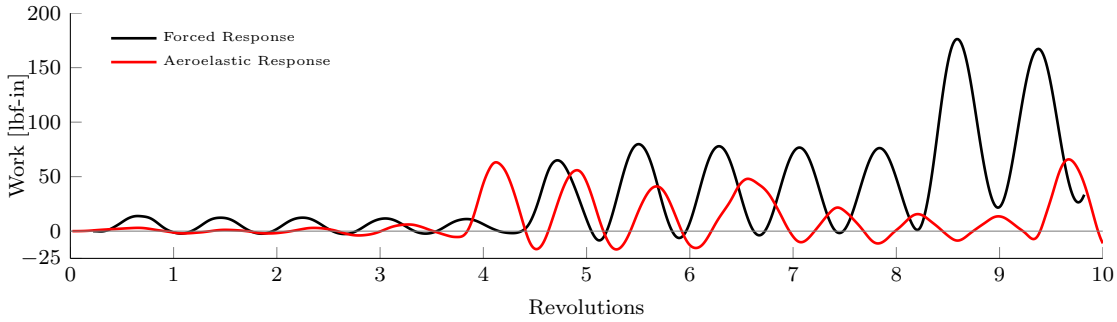


(b) Aerodynamic work for blade 12.

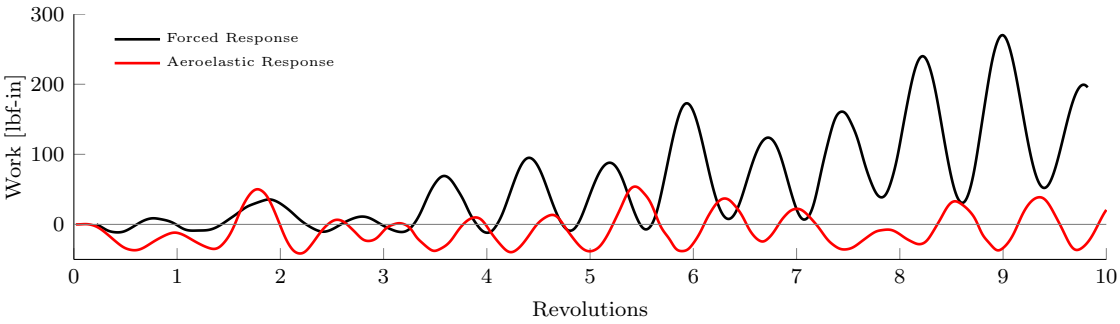


(c) Aerodynamic work for blade 18.

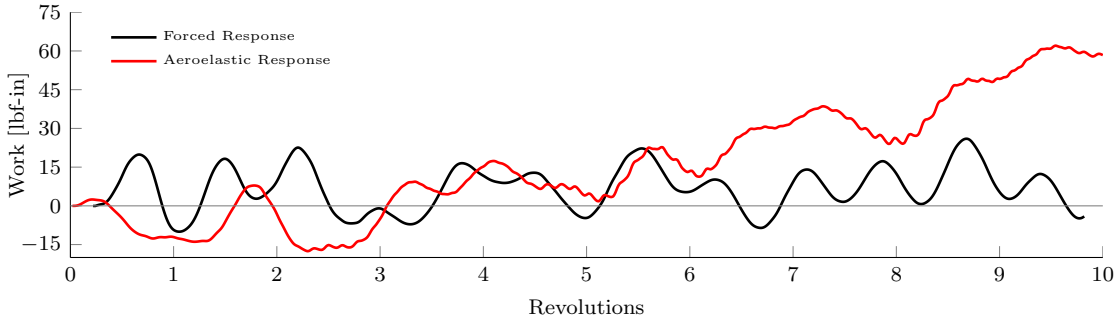


(d) Aerodynamic work for blade 24.

Figure 8.17: Comparison of aerodynamic work from the forced response and aeroelastic response calculations at the 100% throttle setting.

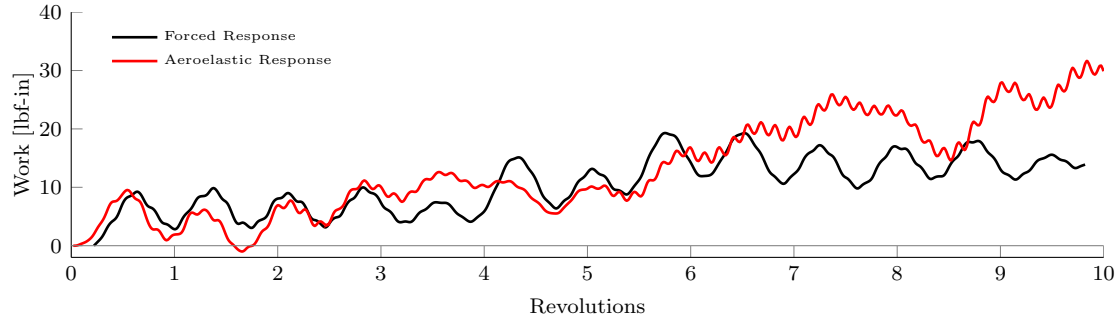


(a) Aerodynamic work for blade 4.

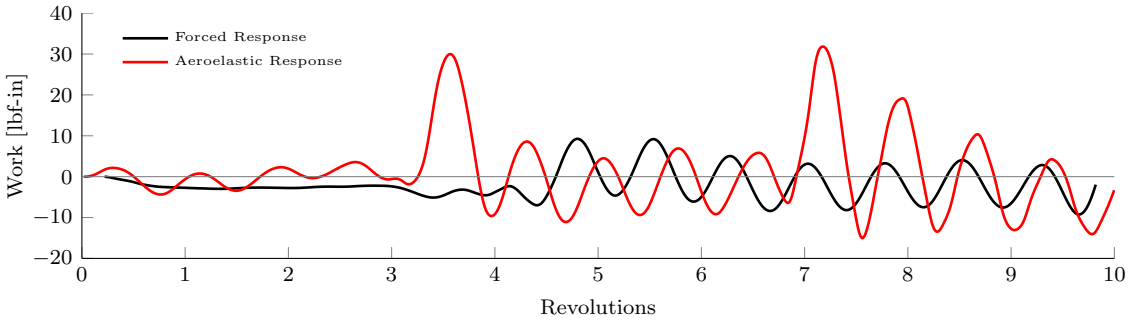


(b) Aerodynamic work for blade 11.

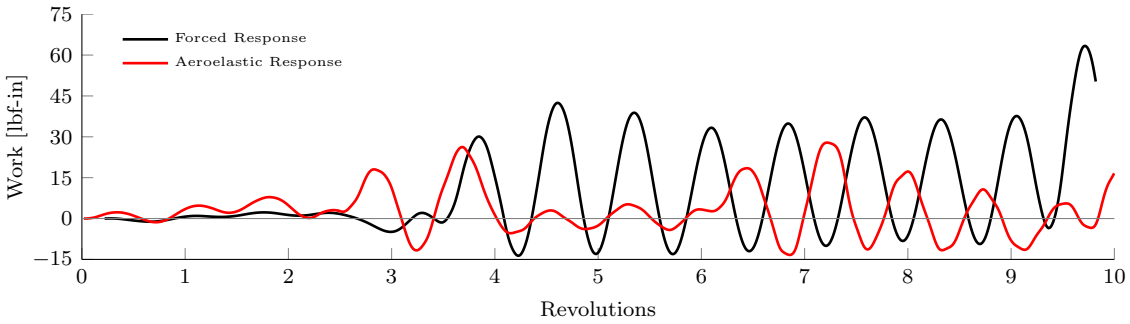


(c) Aerodynamic work for blade 14.

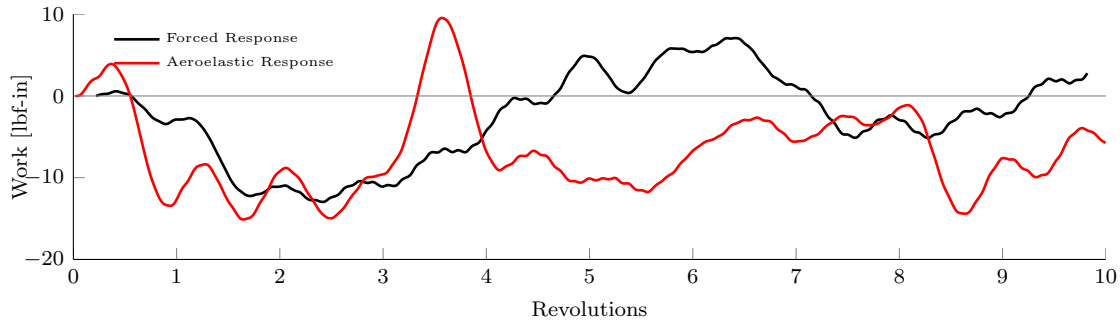


(d) Aerodynamic work for blade 24.

Figure 8.18: Comparison of aerodynamic work from the forced response and aeroelastic response calculations at the 75% throttle setting.

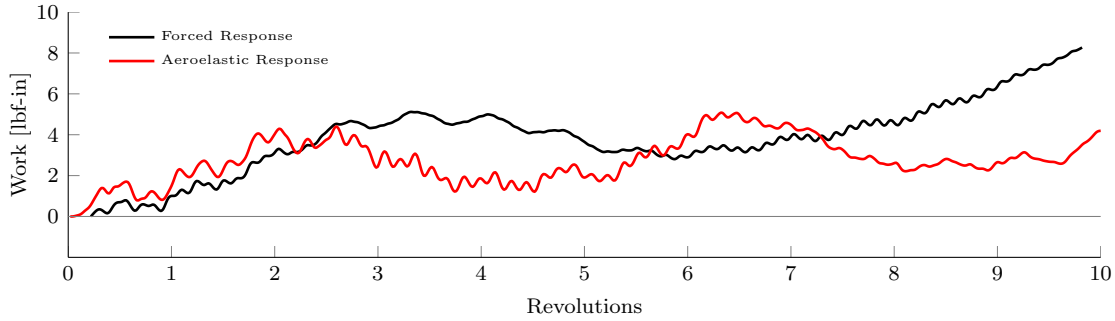


(a) Aerodynamic work for blade 5.

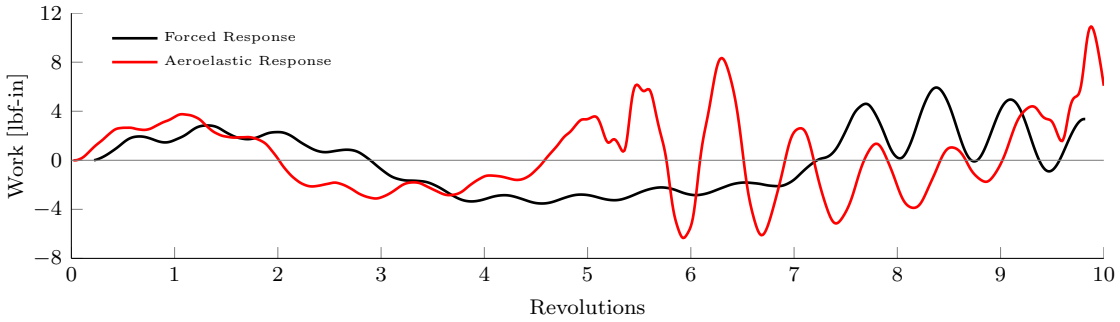


(b) Aerodynamic work for blade 11.

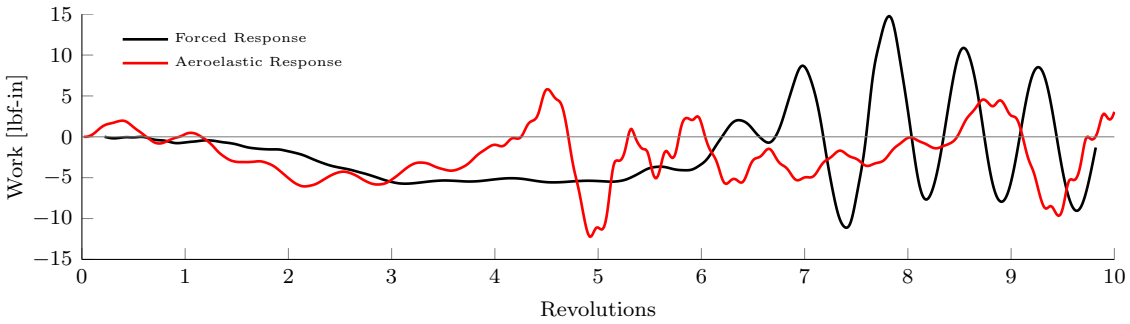


(c) Aerodynamic work for blade 16.

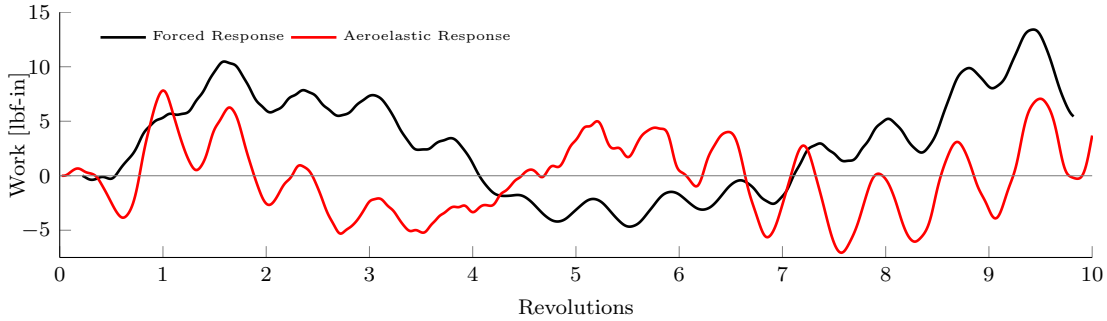


(d) Aerodynamic work for blade 22.

Figure 8.19: Comparison of aerodynamic work from the forced response and aeroelastic response calculations at the 60% throttle setting.

# CHAPTER 9

# Conclusions and Recommendations for Future Research

Predicting the aeroelastic behavior of a bird-damaged fan represents a significant barrier in the development of improved-efficiency turbofan engines. In this dissertation, computational aeroelastic predictions of a bird-damaged fan are performed for improved understanding of the bird strike problem. A coupled CFD/CSD framework is employed to investigate numerically the aerodynamic characteristics and aeroelastic response of the damaged fan. A realistic fan configuration is considered that involves a sector of 5 damaged fan blades obtained through accurate numerical simulation of the bird strike event. The primary goal was to investigate the unsteady aerodynamic loads caused by the damaged blades and predict the structural response of the fan blades. One-way forced response and fully-coupled aeroelastic response calculations of the bird-damaged fan were performed and compared to identify the importance of aeroelastic coupling. The effect of engine rotation is also explored by performing the calculations at the 100%, 75%, and 60% take-off thrust throttle settings, which correspond to FAA certification requirements for bird strike. Overall, the results emphasize several important characteristics of the damaged fan response: 1) the unsteady stall cell emanating from the damaged sector is the dominant source of the unsteady aerodynamic loads, 2) the undamaged blades opposite the damaged

sector exhibit the largest blade response that is dominated by the first bending mode, 3) comparison of the aerodynamic work illustrates the importance of aeroelastic coupling, particularly in predicting the structural response of the damaged blades.

## 9.1 Conclusions

The results presented in this dissertation provide significant insight into the aerodynamic and aeroelastic response of a bird-damaged fan. The principal conclusions and contributions of this dissertation are summarized below:

1. An automated CFD mesh deformation procedure was developed that utilizes RBF interpolation to deform an undamaged computational mesh to coincide with the damaged geometry. The mesh deformation procedure is robust and can accommodate a variety of damaged configurations while retaining a high level of mesh quality.

2. Steady aerodynamic calculations performed with ANSYS CFX for an undamaged and damaged fan stage were verified against results obtained with an industry CFD solver. Three computational mesh densities (coarse, medium, and fine) were considered to assess the effects of boundary layer and tip gap resolution. The increased boundary layer and tip gap resolution of the medium and fine meshes showed negligible effect. This indicates that the use of wall functions to resolve the boundary layer is suitable for CFD calculations of a bird-damaged fan stage.

3. Steady CFD calculations of the damaged fan exhibit a flow loss of approximately 7% compared to the undamaged fan, where the flow loss is related to the thrust loss of the engine. The characteristic curve indicates that the damaged fan is operating near

stall where unsteadiness in the flow is significant and CFD convergence is difficult to obtain. The steady calculations show substantial separation and recirculation of the flow at the damaged blades as well as stalled flow at the blade tips for a majority of the fan wheel.

4. Unsteady aerodynamic calculations of the damaged fan exhibit a periodic solution in which the mass flow rate and total pressure ratio oscillate at a rate of approximately 1/5 the engine rotation speed. The mean flow loss for the 60% and 75% throttle setting cases is slightly greater than predicted by the steady calculations, indicating that unsteady effects further contribute to the flow losses of the bird-damaged engine.

5. The unsteady flow field of the damaged fan exhibits considerable unsteadiness, particularly in the region opposite the damaged sector where a stall cell emanating from the damaged sector progresses at the blade tips once per oscillation of the unsteady solution. The unsteady solutions also indicate the presence of an unsteady wake being shed by the damaged blades.

6. The oscillating stall cell at the blade tips and the unsteady wake shed by the damaged blade exert large aerodynamics loads on the fan blades. The largest aerodynamic force components occur for the undamaged blades opposite the damaged sector. At the 100% throttle setting, significant forcing components are present at frequencies near the first bending mode. For the 75% and 60% throttle settings, the dominant forcing components occur at frequencies below the first bending mode; however, forcing components at higher frequencies also exist and can excite higher structural modes.

7. The forced response calculations show that the undamaged blades opposite the damaged sector exhibit the greatest blade tip displacement, and the amplitude of the displacement grows in time. Furthermore, the blade tip displacements for all blades are dominated by the first bending mode. The tip displacement for the damaged blades also include minor contributions from the first torsion mode that decays in time and the second torsion mode that exhibits beating.

8. The aeroelastic response calculations were compared to the forced response calculations to identify the importance of aeroelastic coupling. The largest tip displacement occurs for the undamaged blades downstream of the damaged sector and the response is dominated by the first bending mode. In contrast to the forced response, significant contributions from the higher structural modes that grow in time or exhibit beating are also present. The aeroelastic response at the 100% and 75% throttle settings show increased participation of the second torsion mode, particularly for the damaged blades and those directly downstream of the damaged sector. The 60% throttle setting calculations indicate an increased participation of the third bending mode for the damaged blades and those opposite the damaged sector.

9. The CFD results from the aeroelastic response calculations indicate that the influence of the blade motion is relatively small. The unsteady aerodynamic calculations exhibit a periodic solution where the oscillating stall cell is the dominant source of unsteadiness. When compared to the case without blade motion, the mass flow and total pressure ratio oscillate at a greater rate of approximately 1/4 the engine rotation speed.

10. Comparison of the aerodynamic work from the forced response and aeroelastic response is used to identify the mechanism driving the response and assess the aeroelastic stability of the blades. Overall, the growth in blade response appears to be due to the unsteady aerodynamic loads caused by the damaged fan blades rather than by an aeroelastic mechanism. At the 100% and 75% throttle settings, the aerodynamic work for the damaged blades and those immediately downstream of the damaged sector indicates that the rapid growth of the higher structural modes may be associated with an aeroelastic instability. At the 60% throttle setting, there is no evidence of aeroelastic instabilities of any of the blades. These conclusions are drawn for the case considered in which structural damping is neglected.

11. This study demonstrates the feasibility of performing aeroelastic response calculations of a bird-damaged fan. However, the computational expense of the aeroelastic response calculations is significant and may prevent repeated implementation for design purposes. Forced response calculations provide an affordable venue for obtaining the approximate blade response. However, this approach neglects important aeroelastic effects that may be essential in predicting blade failure.

## 9.2 Recommendations for Future Research

This study represents the most comprehensive aeroelastic investigation of a bird-damaged commercial turbofan carried out to date. However, the bird-strike problem is far from well understood and requires a significant amount of additional research. An important long-term goal in this research is a predictive capability for identifying the bird strike robustness

of potential fan designs. Such a capability could be a significant cost saver by replacing some experimental tests with simulations.

In this work, a significant amount of effort was devoted towards developing an aerodynamic model that accurately captures the unsteady flow features that drive the structural response. The structural dynamic behavior of a bird-damaged engine is equally as complex; however, a relatively simple structural model was employed for the coupled calculations. Future studies should emphasize a higher fidelity structural model of the fan. The effects of complex material properties such as damping, plasticity, strain-hardening, and strain-rate dependency on the structural response should be explored. Furthermore, the structural model of the damaged blades should include the residual stress from the bird-impact analysis. The blade-to-hub connection and hub flexibility is another aspect of the structural dynamic model that requires future attention. Specifically, fan blades are attached to the hub through a dovetail-slot connection that introduces interfacial damping that may be important in the structural response.

Improvements to the aerodynamic model should also be pursued. The aerodynamic boundary conditions specified in this study correspond to those conventionally enforced for undamaged fan calculations. The validity of these boundary conditions for damaged fan calculations is unclear, particularly as the stall point is approached. Bohari and Sayma [59] performed steady CFD calculations of a damaged fan beyond the stall line through specification of freestream conditions at a variable-area nozzle downstream of the bypass duct. This procedure, originally presented in Refs. [83, 84], could improve the accuracy and numerical stability of the unsteady CFD calculations near the operating line.

The computational expense of the aerodynamic and aeroelastic calculations limits the

use of these tools for iterative design purposes. Several cost-saving measures should be pursued to reduce the computational requirements. The CFD mesh size has a large influence on the computational expense of the aerodynamic calculations. The effect of boundary layer and tip gap resolution in the CFD mesh was investigated in this study. Further reductions in the CFD mesh resolution of the blade passage and inner-span should also be explored. A loosely-coupled aeroelastic framework in which the aerodynamic and structural solver utilize different time-steps may also reduce the computational expense of the aeroelastic response calculations while still capturing the effects of aeroelastic coupling. Development of a coupled aeroelastic analysis outside the framework of ANSYS could be a means for increasing the speed of the computations dramatically. This could be further amplified by a surrogate based approximation of the unsteady aerodynamic loading environment.

Experimental data is necessary to validate the accuracy of the calculations in this study and any subsequent research. Currently, no experimental measurements of the aerodynamic or aeroelastic behavior of a bird-damaged fan exist in the published literature. While these experiments are expensive to perform, the data would be invaluable in the development of an accurate aeroelastic analysis tool. Assumptions and simplifications in the computational model may prevent a 1-to-1 comparison with experimental data. However, a verification of the overall behavior of the damaged fan will significantly increase confidence in the aeroelastic predictions. Specifically, measurement of the mass flow rate and total pressure ratio time-history could confirm the unsteady behavior predicted by the aerodynamic calculations. Furthermore, strain-gauge measurements would be useful to confirm the computed structural response and associated modal content.

Finally, a natural extension of this work is to consider the aerodynamic behavior and

aeroelastic response for a different damaged configuration. The FAA requires successful demonstration of bird ingestion for a variety of bird strike conditions. Future studies should examine the effect of bird-size and strike location for both single bird and flocking bird impacts. Furthermore, the commercial turbofan considered in this study will soon be replaced with next-generation, improved efficiency engines. The fan blades of these engines will undoubtedly consist of advanced materials, such as carbon fiber composites, and employ complex geometries that further complicate the aeroelastic response. Therefore, any future developments of the aerodynamic and structural dynamic models should accommodate these modern designs.

# BIBLIOGRAPHY


[1] LeMieux, J., *One Bird Strike and You're Out!: Solutions to Prevent Bird Strikes*, Trafford Publishing, Bloomington, Indiana, 2009.

[2] Allan, J. R. and Orosz, A. P., "The Costs of Bird Strikes to Commercial Aviation," *Proceedings of the International Bird Strike Committee*, Calgary, August 2001, pp. 217–226.

[3] Allan, J. R., "The Costs of Bird Strikes and Bird Strike Prevention," *Human Conflicts with Wildlife: Economic Considerations*, August 2000, pp. 147–153.

[4] Tho, C. and Smith, M. R., "Accurate Bird Strike Simulation Methodology for BA609 Tiltrotor," *Journal of the American Helicopter Society*, Vol. 56, 2011.

[5] Isomura, K. and Giles, M. B., "A Numerical Study of Flutter in a Transonic Fan," *Journal of Turbomachinery*, Vol. 120, No. 3, July 1998, pp. 500–507.

[6] Eschenfelder, P., "Jet Engine Certification Standards," *Proceedings of the International Bird Strike Committee*, Amsterdam, April 2000, pp. 535–540.

[7] *Bird Ingestion*, 14 Code of Federal Regulations (CFR) §33.76 (2013).

[8] Horsley, J., "The 'Rolls-Royce' Way of Validating Fan Integrity," *AIAA Paper No. 93-2602, AIAA/SAE/ASME/ASEE 29th Joint Propulsion Conference and Exhibit*, Monterey, CA, June 1993, pp. 1–22.

[9] Teichmann, H. C. and Tadros, R. N., "Analytical and Experimental Simulation of Fan Blade Behavior and Damage Under Bird Impact," *Journal of Engineering for Gas Turbines and Power*, Vol. 113, No. 4, October 1991, pp. 582–594.

[10] Goyal, V. K., Huertas, C. A., Borrero, J. R., and Leutwiler, T. R., "Robust Bird-Strike Modeling Based on ALE Formulation Using LS-DYNA," *AIAA Paper No. 2006-1759, Proceedings of the 47th AIAA/ASME/ASCE/AHS/ASC Structures, Structural Dynamics, and Materials Conference*, Newport, RI, May 2006.

[11] Hirschbein, M. S., "Bird Impact Analysis Package for Turbine Engine Fan Blades," *AIAA Paper No. 1982-696, Proceedings of the 23rd AIAA/ASME/ASCE/AHS/ASC Structures, Structural Dynamics, and Materials Conference*, New Orleans, LA, May 1982.

[12] Mao, R., Meguid, S. A., and Ng, T. Y., "Finite Element Modeling of a Bird Striking an Engine Fan Blade," *Journal of Aircraft*, Vol. 44, No. 2, 2007, pp. 583–596.

[13] Mao, R., Meguid, S. A., and Ng, T. Y., "Transient Three Dimensional Finite Element Analysis of a Bird Striking a Fan Blade," *International Journal of Mechanics and Materials in Design*, Vol. 4, No. 1, 2008, pp. 79–96.

[14] Meguid, S. A., Mao, R., and Ng, T. Y., "FE Analysis of Geometry Effects of an Artificial Bird Striking an Aeroengine Fan Blade," *International Journal of Impact Engineering*, Vol. 35, No. 6, 2008, pp. 487–498.

[15] Nizampatnam, L. S. and Horn, W. J., "Investigation of Equation of State Models for Predicting Bird Impact Loads," *AIAA Paper No. 2008-682, Proceedings of the 46th AIAA Aerospace Sciences Meeting and Exhibit*, Reno, NV, January 2008.

[16] Shimamura, K., Shibue, T., and Grosch, D. J., "Numerical Simulation of Bird Strike Damage on Jet Engine Fan Blade," *Proceedings of the ASME/JSME Pressure Vessels and Piping Conference*, San Diego, CA, July 2004.

[17] Imregun, M. and Vahdati, M., "Aeroelastic Analysis of a Bird-Damaged Fan Assembly Using a Large Numerical Model," *The Aeronautical Journal*, Vol. 103, No. 1030, December 1999, pp. 569–578.

[18] Kim, M., Vahdati, M., and Imregun, M., "Aeroelastic Stability Analysis of a Bird-Damaged Aeroengine Assembly," *Journal of Aerospace Sciences and Technologies*, Vol. 5, No. 7, 2001, pp. 469–482.

[19] Garrick, I. E., "Aeroelasticity- Frontiers and Beyond," *AIAA Journal of Aircraft*, Vol. 13, No. 9, January-February 2001, pp. 176–184.

[20] Bisplinghoff, R. L., Ashley, H., and Halfman, R. L., *Aeroelasticity*, Addison-Wesley, Cambridge, Massachussetts, 1955.

[21] Bendkisen, O. O., Kielb, R. E., and Hall, K. C., "Structural Technology," *Encyclopedia of Aerospace Engineering*, Vol. 3, chap. Turbomachinery Aeroelasticity, John Wiley & Sons, 2010, pp. 1625–1639.

[22] Breard, C., Vahdati, M., Sayma, A. I., and Imregun, M., "An Integrated Time-Domain Aeroelasticity Model for Prediction of Fan Forced Response due to Inlet Distortion," *Transactions of the ASME*, Vol. 124, January 2002, pp. 196–208.

[23] Platzer, M. F. and Carta, F. O., *AGARD Manual on Aeroelasticity in Axial-Flow Turbomachines. Volume 1: Unsteady Turbomachinery Aerodynamics*, North Atlantic Treaty Organization Advisory Group for Aerospace Research and Development, 1987, AGARDograph No. 298.

[24] Platzer, M. F. and Carta, F. O., *AGARD Manual on Aeroelasticity in Axial-flow Turbomachines. Volume 2: Structural Dynamics and Aeroelasticity*, North Atlantic Treaty Organization Advisory Group for Aerospace Research and Development, 1988, AGARDograph No. 298.

[25] Bartels, R. E. and Sayma, A. I., "Computational Aeroelastic Modelling of Airframes and Turbomachinery: Progress and Challenges," *Philosophical Transactions of The Royal Society*, Vol. 365, No. 1859, October 2007, pp. 2469–2499.

[26] Bendiksen, O. O., "Aeroelastic Problems in Turbomachines," *AIAA Paper No. 90-1157, Proceedings of the 31st AIAA/ASME/ASCE/AHS/ASC Structures, Structural Dynamics, and Materials Conference*, Long Beach, CA, April 1990.

[27] Marshall, J. G. and Imregun, M., "A Review of Aeroelasticity Methods with Emphasis on Turbomachinery Applications," *Journal of Fluids and Structures*, Vol. 10, No. 3, 1996, pp. 237–267.

[28] Verdon, J., "Review of Unsteady Aerodynamic Methods for Turbomachinery Aeroelastic and Aeroacoustic Applications," *AIAA Journal*, Vol. 31, No. 2, February 1993, pp. 235–250.

[29] Emmons, H. W., Person, C. F., and Grant, H. P., "Compressor Surge and Stall Propagation," *Transactions of the ASME*, Vol. 79, October 1955, pp. 455–469.

[30] Day, I., "The Fundamentals of Stall and Surge in Axial Compressors," *Lecture Series-Van Karman Institute for Fluid Dynamics*, Vol. 5, 1996, pp. B1–B27.

[31] Saxer-Felici, H. M., Saxer, A. P., Inderbitzin, A., and Gyarmathy, G., "Prediction and Measurement of Rotating Stall Cells in an Axial Compressor," *ASME Journal of Turbomachinery*, Vol. 121, April 1999, pp. 365–375.

[32] Bendiksen, O. and Friedmann, P., "Coupled Bending-Torsion Flutter in Cascades," *AIAA Journal*, Vol. 18, No. 2, 1980, pp. 194–201.

[33] Bendiksen, O. and Friedmann, P., "Coupled Bending-Torsion Flutter in a Supersonic Cascade," *AIAA Journal*, Vol. 19, No. 6, 1981, pp. 774–781.

[34] Jennions, I. K. and Turner, M. G., "Three-Dimensional Navier-Stokes Computations of Transonic Fan Flow Using an Explicit Flow Solver and an Implicit k-$\epsilon$ Solver," *ASME Journal of Turbomachinery*, Vol. 116, April 1993, pp. 261–272.

[35] Rhie, C. M., Zacharais, R. M., Hobbs, D. E., Sarathy, K. P., Biederman, B. P., Lejambre, C. R., and Spear, D. A., "Advanced Transonic Fan Design Procedure Based On A Navier-Stokes Method," *ASME Journal of Turbomachinery*, Vol. 116, No. 2, April 2004, pp. 179–346.

[36] Cinnella, P., Palma, P. D., Pascazio, G., and Napolitano, M., "A Numerical Method for Turbomachinery Aeroelasticity," *Transactions of the ASME*, Vol. 126, April 2004, pp. 310–316.

[37] Whitehead, D. S., "Force and Moment Coefficients for Vibrating Aerofoils in Cascade," *Technical Report 3254, Aeronautical Research Council*, February 1960.

[38] Whitehead, D. S., "Bending Flutter of Unstalled Cascade Blades at Finite Deflection," *Technical Report 33386, Aeronautical Research Council*, October 1962.

[39] Vahdati, M., Sayma, A. I., Marshall, J. G., and Imregun, M., "Mechanisms and Prediction Methods for Fan Blade Stall Flutter," *AIAA Journal of Propulsion and Power*, Vol. 17, No. 5, September-October 2001, pp. 1100–1108.

[40] Sharma, O. P., Pickett, G. F., and Ni, R. H., "Assessment of Unsteady Flows in Turbines," *ASME Journal of Turbomachinery*, Vol. 114, No. 1, January 1992, pp. 79–90.

[41] Farhat, C., Geuzaine, P., and Brown, G., "Provably Second-Order Time-Accurate Loosely-Coupled Solution Algorithms for Transient Nonlinear Computational Aeroelasticity," *Computer Methods in Applied Mechanics and Engineering*, Vol. 195, 2006, pp. 1973–2001.

[42] Sayma, A. I., Vahdati, M., and Imregun, M., "An Integrated Nonlinear Approach for Turbomachinery Forced Response Prediction Part I: Formulation," *Journal of Fluids and Structures*, Vol. 14, No. 1, January 2000, pp. 87–101.

[43] Bendiksen, O. O., "Energy Approach to Flutter Suppression and Aeroelastic Control," *AIAA Journal of Guidance, Control, and Dynamics*, Vol. 24, No. 1, September 1976, pp. 641–657.

[44] Silkowski, P. D., Rhie, C. M., Copeland, G. S., Ely, J. A., and Bleeg, J. M., "Computational-Fluid-Dynamics Investigation of Aeromechanics," *AIAA Journal of Propulsion and Power*, Vol. 18, No. 4, July-August 2002, pp. 788–796.

[45] Aotsuka, M. and Tsuchiya, N., "Numerical Simulation of Transonic Fan Flutter with 3-D N-S CFD Code," *Proceedings of the ASME Turbo Expo 2008: Power for Land, Sea, and Air*, Berlin, Germany, June 2008.

[46] Bendiksen, O. O., "Modern Developments in Computational Aeroelasticity," *Proceedings of the Institution of Mechanical Engineers, Part G: Journal of Aerospace Engineering*, Vol. 218, No. 3, 2004.

[47] Benra, F., Dohmen, H. J., Pei, J., Schuster, S., and Wan, B., "A Comparison of One-Way and Two-Way Coupling Methods for Numerical Analysis of Fluid-Structure Interactions," *Journal of Applied Mathematics*, Vol. 2011, 2011, pp. 235–250, Article ID 853560.

[48] Farhat, C., Lesoinne, M., and LeTallec, P., "Load and Motion Transfer Algorithms for Fluid/Structure Interaction Problems With Non-Matching Discrete Interfaces: Momentum and Energy Conservation, Optimal Discretization, and Applications to Aeroelasticity," *Computer Methods in Applied Mechanics and Engineering*, Vol. 157, April 1998, pp. 94–114.

[49] Bendiksen, O. O., "A New Approach to Computational Aeroelasticity," *AIAA Paper No. 1991-0939, Proceedings of the 32nd AIAA/ASME/ASCE/AHS/ASC Structures, Structural Dynamics, and Materials Conference*, Baltimore, MD, April 8-10 1991.

[50] de Boer, A., van Zuijlen, A. H., and Bijl, H., "Review of Coupling Methods for Non-matching Meshes," *Computer Methods in Applied Mechanics and Engineering*, Vol. 196, October 2007, pp. 1515–1525.

[51] de Boer amd A. H. van Zuijlen, A. and Bijl, H., "Comparison of Conservative and Consistent Approaches for the Coupling of Non-matching Meshes," *Computer Methods in Applied Mechanics and Engineering*, Vol. 197, October 2008, pp. 4284–4297.

[52] Carstens, V., Kemme, R., and Schmitt, S., "Coupled Simulation of Flow-Structure Interaction in Turbomachinery," *Aerospace Science and Technology*, Vol. 7, 2003, pp. 298–306.

[53] Vahdati, M., Simpson, G., and Imregun, M., "Mechanisms for Wide-Chord Fan Blade Flutter," *ASME Journal of Turbomachinery*, Vol. 133, October 2011.

[54] Audic, S., Berthillier, M., Bonini, J., Bung, H., and Combescure, A., "Prediction of Bird Impact in Hollow Fan Blades," *AIAA Paper No. 2000-3201, 36th AIAA/ASME/SAE/ASEE Joint Propulsion Conference and Exhibit*, Hunstville, AL, July 2000.

[55] Wilbeck, J. S. and Rand, J. L., "The Development of a Substitute Bird Model," *ASME Paper No. 81-GT-23, ASME Gas Turbine Conference and Products Show*, Houston, TX, March 1981.

[56] Heimbs, S., "Computational Methods for Bird Strike Simulations: A Review," *Computers and Structures*, Vol. 89, 2011, pp. 2093–2112.

[57] Howard, W. D., "Turbofan Engine Bird Ingestion Testing," *AIAA Paper No. 1991-2380, Proceedings of the 27th Joint Propulsion Conference*, Sacramento, CA, June 1991.

[58] Howard, S. A., Hammer, J. T., Carney, K. S., and Pereira, J. M., "Jet Engine Bird Ingestion Simulations: Comparison of Rotating to Non-Rotating Fans," *Proceedings of the ASME Turbo Expo 2013: Turbine Technical Conference and Exposition*, San Antonio, Texas, June 2013.

[59] Bohari, B. and Sayma, A., "CFD Analysis of Effects of Damage Due to Bird Strike on Fan Performance," *Proceedings of the ASME Turbo Expo 2010: Power for Land, Sea, and Air*, Glasgow, UK, June 2010.

[60] *LS-DYNA Theory Manual*, Livermore Software Technology Corporation (LSTC), 2014.

[61] John D. Anderson, J., *Fundamentals of Aerodynamics*, McGraw-Hill, New York, NY, 2007.

[62] *Ansys CFX-Solver Theory Guide - Version 14.5*, ANSYS, Inc., 2012.

[63] Wilcox, D. C., *Turbulence Modeling for CFD*, Griffin Printing, Glendale, CA, 1993.

[64] Baldwin, B. S. and Lomax, H., "Thin Layer Approximation and Algebraic Model for Separated Flows," *AIAA Paper No. 78-257 16th AIAA Aerospace Sciences Meeting and Exhibit*, Huntsville, AL, January 1978.

[65] Spalart, P. R. and Allmaras, S. R., "A One-Equation Turbulence Model for Aerodynamic Flows," *AIAA Paper No. 92-0439 30th AIAA Aerospace Sciences Meeting and Exhibit*, Reno, NV, January 1992.

[66] Barth, T. J. and Jespersen, D. C., "The Design and Application of Upwind Schemes on Unstructured Meshes," *AIAA Paper No. 89-0366 27th AIAA Aerospace Sciences Meeting and Exhibit*, Reno, NV, January 1989.

[67] Harten, A., Engqusist, B., Osher, S., and Chakravarthy, S. R., "Uniformly High Order Accurate Essentially Non-oscillatory Schemes," *Journal of Computational Physics*, Vol. 71, No. 2, August 1987, pp. 231–303.

[68] *ANSYS TurboGrid User's Guide - Version 14.5*, ANSYS, Inc., 2012.

[69] Morris, A., Allen, C., and Rendall, T., "CFD-based Optimization of Aerofoils Using Radial Basis Functions for Domain Element Parameterization and Mesh Deformation," *International Journal for Numerical Methods in Fluids*, Vol. 58, No. 8, 2008, pp. 827–860.

[70] van Zuijlen, A., de Boer, A., and Bijl, H., "Higher-order Time Integration Through Smooth Mesh Deformation for 3D Fluid-Structure Interaction Simulations," *Journal of Computational Physics*, Vol. 224, No. 1, 2007, pp. 414–430.

[71] Jakobsson, S. and Amoignon, O., "Mesh Deformation Using Radial Basis Functions for Gradient Based Aerodynamic Shape Optimization," *Computers and Fluids*, Vol. 36, No. 6, 2007, pp. 1119–1136.

[72] Buhmann, M. D., *Radial Basis Functions: Theory and Implementations*, Cambridge University Press, Cambridge, 2003.

[73] de Boer, A., van der Schoot, M., and Bijl, H., "Mesh deformation based on radial basis function interpolation," *Computers & Structures*, Vol. 85, No. 11, 2007, pp. 784–795.

[74] Lamorte, N. and Friedmann, P. P., "Hypersonic Aeroelastic Stability Boundary Computations using Radial Basis Functions for Mesh Deformation," *AIAA Paper No. 2012-5943, Proceedings of the 18th AIAA/3AF International Space Planes and Hypersonic Systems and Technologies Conference*, Tours, France, September 2012.

[75] Rendall, T. C. S. and Allen, C. B., "Unified Fluid-Structure Interpolation and Mesh Motion Using Radial Basis Functions," *International Journal for Numerical Methods in Engineering*, Vol. 74, No. 10, 2008, pp. 1519–1559.

[76] Rendall, T. C. S. and Allen, C. B., "Efficient Mesh Motion Using Radial Basis Functions with Data Reduction Algorithms," *Journal of Computational Physics*, Vol. 228, No. 17, 2009, pp. 6231–6249.

[77] *Ansys CFX-Solver Modeling Guide - Version 14.5*, ANSYS, Inc., 2012.

[78] *Mechanical APDL Theory Reference Guide - Version 14.5*, ANSYS, Inc., 2012.

[79] Bathe, K.-J., *Finite Element Procedures*, Prentice Hall, Pearson Education, Inc., New Jersey, 2006.

[80] *Mechanical APDL Element Reference - Version 14.5*, ANSYS, Inc., 2012.

[81] Hilber, H. M., Hughes, T. J. R., and Taylor, R. L., "Improved Numerical Dissipation for Time Integration Algorithm in Structural Dynamics," *Earthquake Engineering and Structural Dynamics*, Vol. 5, No. 3, July-September 1977, pp. 283–292.

[82] *Mechanical APDL Coupled-Field Analysis Guide - Version 14.5*, ANSYS, Inc., 2012.

[83] Sayma, A. I., "Steady-Flow Analysis of Low Pressure Compression System For Turbofan Engines," *Proceedings of the ASME Turbo Expo 2007: Power for Land, Sea, and Air*, Montreal, Canada, May 2007.

[84] M. Vahdati, A. I. Sayma, C. F. and Imregun, M., "On the Use of Atmospheric Boundary Conditions for Axial-Flow Compressor Stall Simulations," *ASME Journal of Turbomachinery*, Vol. 127, April 2005, pp. 349–351.